Mathematical Modelling of Lithium Intercalation Dynamics in Battery Electrodes



Chang Wang
St Catherine's College
University of Oxford

Thesis submitted for
Doctor of Philosophy

Hilary Term 2016

This thesis is dedicated
to my parents
for their unreserved love

Acknowledgements

I am extremely grateful to the many people who have helped me in my D.Phil. research.

I would like to thank to my supervisors, Professor Peter Howell and Doctor Cameron Hall for their tremendous academic support and my valuable encouragement during these past four years. They have been extremely helpful at every stage of my D.Phil. research, guiding me through every obstacle that I encountered in research. Without their help, I would not have completed such an interesting D.Phil. that fully fulfils my intellectual curiosity. At the very last stage of my thesis preparation, I am very grateful to them for sparing the time to read and examine this thesis.

I would also like to thank Professor Colin Please for attending many of my supervision sessions and offering me numerous insightful suggestions. I thank Colin for providing me with this very interesting research topic at the very beginning of my D.Phil. journey, and for constantly inspiring me to widen from research from various perspectives.

I would like to thank Professor Jon Chapman and Professor Chris Budd for serving as examiners of my D.Phil. viva. I would also like to thank Professor Andreas Münch for serving as examiner in my transfer and confirmation viva. I want to thank them for their brilliant comments and suggestions, which always pushed me to new boundaries of research.

I thank my OCIAM colleges for the intellectual accompany and for making my D.Phil. as enjoyable as it was. I cherish the many stimulating talks that I had with you. I would like to extend this thanks to OCIAM as an institute, for providing me with the best environment for conducting research that is both mathematically motivating and critical for industry.

Thanks also go to my friends for their love and support. In particular I want to thank all my friends who inspired me to embark on a doctoral journey in applied mathematics, and who gave me tremendous support in

times of difficulty. Words in this acknowledgement session are far from sufficient, and I will take every opportunity to thank you all in person.

Finally, a special thanks to my parents for always standing by my side and giving me firm support. They are my backbone. This thesis is dedicated to them.

Abstract

This thesis discusses mathematical models for phase separation pattern in electrode materials for lithium ion batteries.

The material is assumed to be composed of discrete "compartments", which might model individual particles in nanoparticle Lithium Iron Phosphate cathode material, for example, or individual layers in graphite anode material.

We first present deterministic ODE models to describe quasi-equilibrium and out-of-equilibrium lithiation/delithiation of such systems. In sequence, we examine a single compartment under voltage-control, a multicompartment system under current-control, and a multicompartment system under voltage-control. We show that the dynamics of a single compartment can be reduced to rapid switching between an "empty" state and a "full" state, and we identify the critical voltage at which the switch occurs under both static and dynamic conditions. We also identify the critical voltages for the multicompartment system to change stage. We find that the multicompartment system supports a large number of stable states in quasi-equilibrium, and we further reveal that its dynamics may be extremely sensitive to initial conditions and control parameters.

We also explore how the dynamics are affected by discreteness and thermal noise by investigating the probability distribution of the lithium concentration. We first study a single-compartment and two-compartment systems, and then extend the analysis to more interacting compartments. We start with the discrete chemical master equations, and then derive a discrete-to-continuum model to explore the probability distribution during dynamic lithiation/delithiation. We identify distinct asymptotic regimes in which either discreteness and thermal noise are important or the dynamics is well captured by the deterministic model. We then compare the different phase-separation patterns predicted by the deterministic model

and by the stochastic model, for quasi-equilibrium and out-of-equilibrium evolutions.

Finally, we explore how different interaction laws could impact the observed phase-separation pattern.

Contents

1 Introduction **1**

1.1 Background 1

1.1.1 The lithium ion battery 1

1.1.2 A short review of the electrode materials 4

1.1.3 A short review of phase-separation 6

1.2 Phase-separation in the cathode materials 8

1.2.1 Two-phase models for bulk materials 8

1.2.2 Two-phase models for nano materials 10

1.3 Phase-separation in lithium graphite 12

1.4 Motivation 13

1.5 Overview 15

2 A deterministic model for a single compartment **20**

2.1 Model Formulation 21

2.1.1 A double-well Gibbs energy 21

2.1.2 Butler–Volmer equation 23

2.2 Equilibrium 25

2.3 Dynamics 26

2.3.1 A matched asymptotic solution 27

2.3.2 Consolidation by numerics 35

2.4 Discussions 37

2.4.1 Non-constant exchange current 37

2.4.2 The effect of charging speed 39

2.4.3 The nonlinear rescaling 41

2.5 Summary 41

3 A stochastic model for a single compartment **43**
3.1 Model formulation . . . 44
3.1.1 Chemical master equation . . . 44
3.1.2 Transition probability . . . 45
3.1.3 The Langevin equation . . . 46
3.2 Stationary behaviour . . . 47
3.2.1 Equilibrium distribution . . . 47
3.2.2 Random walk simulations under constant E . . . 51
3.3 A discrete-to-continuum model . . . 52
3.3.1 Outer layer . . . 53
3.3.2 Boundary layers . . . 54
3.4 Dynamics . . . 56
3.4.1 Distinguished limit: $\alpha = \mathcal{O}(1)$ . . . 57
3.4.2 Discrete limit: $\alpha \gg 1$ . . . 62
3.4.3 Continuum limit: $\alpha \ll 1$ . . . 63
3.4.4 Conclusion of the dynamics . . . 68
3.5 Discussions . . . 68
3.5.1 Non-constant exchange current . . . 68
3.5.2 The effect of charging speed . . . 70
3.6 Summary . . . 71

4 A deterministic multicompartment model with linear dynamics **73**
4.1 Model formulation . . . 74
4.1.1 A free energy model . . . 74
4.1.2 Gradient flow model . . . 75
4.2 Numerical simulation . . . 76
4.3 Bifurcation analysis of a three-compartment model . . . 80
4.3.1 A simple example . . . 82
4.3.2 Brief summary of the equilibria . . . 83
4.3.3 Equilibria when C is close to 0 . . . 85
4.3.4 Equilibria when C approaches 1 . . . 98
4.3.5 Equilibria when C approaches 2 . . . 100
4.3.6 Equilibria when C approaches $3 - \frac{\sigma}{1+\sigma}$ . . . 100
4.3.7 Summary of a complete intercalation/deintercalation cycle . . . 101
4.4 Summary . . . 103

5 A deterministic multicompartment model with nonlinear dynamics 105
5.1 Setting up the Butler–Volmer style model . . . 105
5.2 Numerical simulations . . . 107
5.2.1 Very slowly varying $E(t)$ . . . 107
5.2.2 Intermediate charging rate . . . 109
5.2.3 Slowly varying $E(t)$ . . . 109
5.2.4 Implications . . . 111
5.3 A deterministic two-compartment model . . . 112
5.3.1 Bifurcation analysis . . . 112
5.3.2 Dynamics . . . 117
5.4 Discussions . . . 120

6 A stochastic multicompartment model 121
6.1 A stochastic two-compartment model . . . 121
6.1.1 Chemical master equation . . . 121
6.1.2 Stationary distribution . . . 124
6.1.3 Numerical simulations . . . 127
6.1.4 A discrete-to-continuum model . . . 128
6.1.5 Discrete limit . . . 135
6.1.6 Continuum limit . . . 137
6.1.7 Dynamic trajectories of the mean concentration . . . 143
6.2 Summary of the two-compartment model . . . 144
6.3 Generalising to a M-compartment model . . . 145
6.3.1 Equilibrium behaviour . . . 145
6.3.2 Dynamics . . . 147
6.3.3 Further discussions . . . 149

7 Investigating the interaction law 151
7.1 A general model for the interaction energy . . . 152
7.2 Finite K-nearest neighbour interaction . . . 154
7.2.1 Numerical simulations . . . 154
7.2.2 General properties . . . 155
7.3 Long-range interaction . . . 159
7.3.1 Numerical simulations . . . 160
7.3.2 A semi-continuous model . . . 164
7.4 Applications: the staging phenomenon of lithium graphite . . . 165
7.4.1 A repeated periodic structure . . . 165

7.4.2 Numerical simulations with deterministic dynamic models . . 168
7.4.3 Numerical simulations with thermal noise 170
7.4.4 Extension: a triple well energy 174
7.5 Summary 177

8 Conclusions **179**
8.1 Summary of results 179
8.2 Discussions and future research 183

A Simulating the one-step process as a random walk **186**

B Simplification of the transition probabilities **187**

C Equilibria of the three-compartment system **189**

D Numeric difficulties in solving the two-compartment Butler–Volmer model **201**

E Approximations of discrete sums **203**

Bibliography **205**

List of Figures

1.1 Energy conversion of an electrochemical system. 2
1.2 A schematic illustration of a lithium ion battery, which is composed of cathode, anode, and electrolyte. 3
1.3 A schematic illustration of the staging of lithium graphite compounds. 5
1.4 Top view of the lattice structure of Li-graphite. 6
1.5 A double well Gibbs free energy $g(c)$ and the associated potential $\mu(c)$ that induces phase-separation. 7
1.6 A schematic illustration of hysteresis of a nanoparticulate LFP cathode. 8
1.7 A charging process described by the shrinking core model. 9
1.8 Phase separation in bulk material and in nano material. 11
1.9 Various voltage paths in the charging/discharging of a many particle system. 12
1.10 Potential of lithium-graphite versus concentration. 13

2.1 Two possible shapes for the double-well Gibbs free energy $g(c)$ given by equation (2.1). 22
2.2 Chemical potential corresponding to a double-well potential. 22
2.3 Bifurcation diagram for equilibria of the Butler–Volmer system (2.9), as functions of the control parameter E, plotted with $\epsilon = 0.25$. . . . 26
2.4 Trajectory of the dynamics of a single-compartment model. 28
2.5 Solution of sub-stage (ic). 30
2.6 Solution of sub-stage (id). 31
2.7 Numerical solution of the initial-value problem (2.48). 34
2.8 Stage (i) comparison between the asymptotic solution and the numerical solution. 36
2.9 Stage (ii) comparison between the asymptotic solution and the numerical solution. 37

2.10 Stage (iii) comparison between the asymptotic solution and the numerical solution. 38
2.11 The scaled transition delay $(\mu_{\text{dyn}} - \mu^*)/\epsilon$ plotted versus ϵ for different values of θ. 39
2.12 Delay of the dynamic transitions under different charging speed. . . . 40

3.1 Illustration of an one-step process. 44
3.2 Plot of $F(c) = g(c) - cE$ as in (3.21), with $\epsilon = 0.25$. 49
3.3 Logarithm of the stationary distribution p_i^{s} plotted versus $c = i\Delta C$ for various values of the applied potential E. 49
3.4 Mean concentration corresponding to the stationary distribution (3.19) plotted versus E 50
3.5 Stationary distribution for different N givey by (3.19). 51
3.6 The concentration evolution viewed as a collection of random walks. . 52
3.7 Simulation of the left inner layer problem (3.41) 58
3.8 $Q(\alpha;\tau)$, the flux from the left inner region to the outer region, plotted as a function of τ 59
3.9 A schematic illustration of the reduced model. 60
3.10 Comparison between the solutions of the full model of the chemical master equation (3.1) and of the reduced model (3.41), (3.49) that only considers the left inner layer and the highest state. 61
3.11 The probability density $p_N(\tau)$ of the highest state plotted versus τ with $\alpha = 2$ and with $\alpha = 0.2$. 62
3.12 Expected concentration $\bar{c}$ plotted versus varying potential E in the discrete limit. 63
3.13 Quasi-equilibrium distribution prescribed by (3.55) with the sum $\sum p_i$ normalised to 1. 64
3.14 Distribution profiles computed by using the continuum approximation and by the solution of the discrete system (3.30). 67
3.15 Comparisons of the distribution mean $\bar{x}$ and amplitude A predicted by the continuum approximation (3.69) and (3.73) and by the discrete system (3.30). 68
3.16 Mean concentration evolution when I_0 is modelled as being proportional to $c^{1/2}(1-c)^{1/2}$, with the distribution in the left-inner layer determined by (3.80). 70

4.1 Numerical simulation of a lithiation process using the gradient flow model (4.8) with $C(t) = C(0) + 10^{-3}t$. 77
4.2 Hysteresis in a complete lithiation/delithiation cycle cycle. 78
4.3 Numerical simulation of a delithiation process using the gradient flow model (4.8) with $C(t) = C(0) - 10^{-3}t$. 79
4.4 Equilibria of the three-compartment system. 86
4.5 Symmetry-preserving bifurcation when the total concentration is algebraically small. 88
4.6 Illustration of the symmetry-preserving bifurcation B_{I} when the total concentration is algebraically small. 89
4.7 Contour plot of σ in the $\alpha - \beta$ plane. 90
4.8 Contour plots for σ and Γ in the $\alpha - \beta$ plane. 91
4.9 Contour plot of σ and Γ. 92
4.10 Contour plots showing the intersections of a fixed σ contour and various Γ contours. 92
4.11 Plot of the critical value Γ verus σ for the saddle-node bifurcation B_{o}, which only occurs when $\sigma < 0.26$. 93
4.12 Critical parameter values for the two bifurcations that break symmetry when the total concentration is algebraically small. 94
4.13 Illustration of the symmetry-preserving bifurcation when total concentration is algebraically small. 95
4.14 Illustration of the symmetry-preserving bifurcation when total concentration is algebraically small. 96
4.15 Illustration of the symmetry-preserving bifurcation when total concentration is algebraically small. 97
4.16 Critical values when C is small. 98
4.17 Four possible bifurcation scenarios when C is algebraically small. . . 99
4.18 Equilibria when C is close to 3. 101
4.19 Two possible approaches to fill up 3 compartments. 102

5.1 In the voltage control model, each compartment can only exchange lithium ions with the electrolyte bath. 106
5.2 Numerical simulation of a slow charging nearest-neighbour interaction Butler–Volmer model. 108

5.3 Total energy and potential versus the total concentration of the nearest-neighbour interaction Butler–Volmer model with three different charging speed. . . . 109
5.4 Numerical simulation of a fast charging nearest-neighbour interaction Butler–Volmer model. . . . 110
5.5 Numerical simulation of a nearest-neighbour interaction Butler–Volmer model with intermediate charging rate. . . . 111
5.6 Bifurcation diagram of the system (5.8) in the $c_1 + c_2$ versus E plane. 113
5.7 Bifurcation I includes a pitchfork bifurcation of (5.18) and a saddle-node bifurcation of (5.19). . . . 115
5.8 Bifurcation II is similar to bifurcation I. . . . 116
5.9 Bifurcations III and IV. . . . 117

6.1 One-step process for a two-compartment system. . . . 123
6.2 Illustration of the equilibrium distribution of a two-compartment model according to (6.16) for three different values of E, with $\sigma = 0.2$. . . . 126
6.3 Mean concentration $\bar{c}_1 + \bar{c}_2$ corresponding to the stationary distribution (6.16) plotted versus E. . . . 127
6.4 Numerical simulations of the two-dimensional chemical master equation compartments (6.5). . . . 129
6.5 A schematic of the 6 regions on the (i, j) plane. . . . 130
6.6 Probability distribution evolutoin of region I by simulating (6.22). . . 132
6.7 Evolution of the joint probability distribution of a two-compartment system in the discrete limit. . . . 137
6.8 Quasi-equilibrium distribution given by (6.40) with the sum $\sum p_i$ normalised to 1. . . . 139
6.9 Numerical solution of the system (6.58) subject to the initial condition (6.58c). . . . 143
6.10 Comparison between the equilibrium and dynamic trajectories of $C_1 + C_2$ of the stochastic model. . . . 144
6.11 The relation between the averaged concentration and the voltage E, associated with the probability distribution of (6.59). We compare the result of a two-, four-, and six-compartment system. . . . 147
6.12 Comparison between possible paths of a deterministic model and a stochastic model. . . . 148

7.1 A full lithiation/delithiation cycle of a 2-nearest neighbour interaction model found by simulating (7.8). 156
7.2 The total energy g_{tot} and the equivalent potential $E(t) = -\lambda(t)$ during the lithiation/delithiation cycle of the 2-nearest neighbour interaction model. 157
7.3 A schematic representation of the change of configuration before and during the filling of compartment-m, which depends on m's remainder mod 3. 157
7.4 The equivalent voltage $E(t) = -\lambda(t)$ by simulating a three-nearest neighbour interaction model and a 15-nearest neighbour interaction model using (7.8). 159
7.5 Numerical simulation of a long-range interaction current control model (7.2), (7.4), (7.8), (7.13) with a decay factor $\omega = 2$. 161
7.6 Numerical simulation of a long-range interaction current-control model (7.2), (7.4), (7.8), (7.13) with a decay factor $\omega = 1$. 162
7.7 Numerical simulation of a long-range interaction current control model (7.2), (7.4), (7.8), (7.13) with a decay factor $\omega = 0.5$. 163
7.8 The total energy versus total concentration of the three simulations presented Figs. 7.5 – 7.7. 163
7.9 The equivalent potential versus total concentration of the three simulations presented Figs. 7.5 - 7.7. 164
7.10 Energy minimizers with periods $R = 2, 3, 4$ by solving the minimisation problem (7.23) with Matlab **fmincon**. 169
7.11 The total energy corresponds to the energy minimizers with periods $R = 2, 3, 4$ of the minimisation problem (7.23), with respect to the total concentration varying from near 0 to near 1. 170
7.12 A full lithiation/delithiation cycle of a 7-nearest neighbour interaction model. 171
7.13 The total energy g_{tot} and the equivalent potential $E(t) = -\lambda(t)$ during the lithiation/delithiation cycle of the 7-nearest neighbour interaction model. 172
7.14 Numerical simulations of the current control model with noise (7.24) with $\mathrm{d}C(t)/\mathrm{d}t = 10^{-3}$. 173
7.15 Numerical simulations of the current control model with noise (7.24) with $C(t)$ being kept constant. 174
7.16 A triple well intra-layer free energy given by (7.26b). 175

7.17 Numerical simulations of a lithiation process, using a triple-well intra-layer energy and a three-nearest neighbour inter-layer energy. 176
7.18 The total energy and the potential versus the total concentration, associated with the simulation presented Figs. 7.17. 177

D.1 Solving the system (D.1) with two different Matlab solvers, **ode15s** and **ode23tb**. 202
D.2 Solving the system (D.2) with two different Matlab solvers, **ode15s** and **ode23tb**. 202

Chapter 1

Introduction

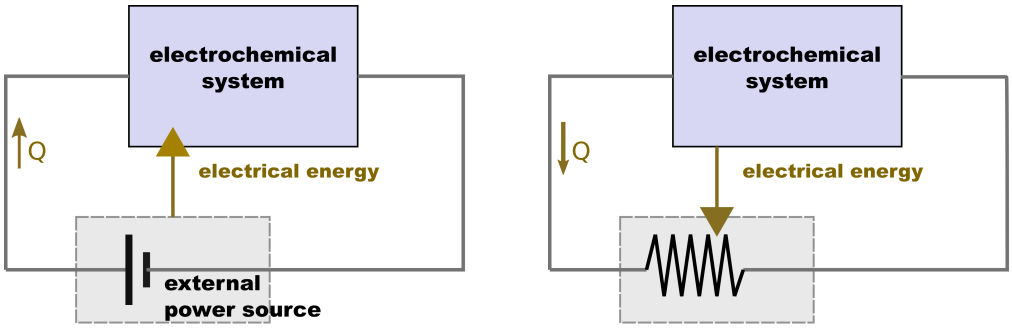
Rechargeable lithium-ion batteries are currently the mainstream battery technology in the fast-growing portable electronics industry. Potentially, lithium-ion batteries are also applicable to electric vehicles and to the next generation of clean energy [25]. Compared to other battery technologies, lithium-ion batteries features high energy density, good design flexibility, better reliability, and longer durability [34]. Research into lithium ion batteries is a fast-growing area, with activity taking place in a variety of areas from the chemical synthesis of new materials to higher level design engineering. These efforts, however, are mainly experimental, and sometimes an understanding of the fundamental science is lacking [34]. Furthermore, there is still a variety of technological barriers remaining to be resolved; a lot of work is being applied to increasing energy storage density, power density, charging/discharging speed, long-term stability, and safety of lithium ion batteries. This means that there are great opportunities for applied mathematicians to build mathematical models of some very basic but not well-understood phenomena arising from lithium ion battery operations, and to thereby make a practical difference to battery manufacture.

1.1 Background

1.1.1 The lithium ion battery

Unlike a primary battery, a rechargeable battery usually adopts layered intercalation materials as its electrode, so that lithium ions can insert into and remove themselves from the electrodes repeatedly without damaging the crystalline structure. This is the key feature that makes the charging/discharging cycles possible, as a result facilitating the conversion between chemical energy and electrical energy. A simple schematic showing the basic operation of this electrochemical system is in Fig. 1.1.

During discharge, the electrochemical system outputs current to the external circuit, converting chemical power to electrical power. During charging, the electrochemical system is connected to an external power source, pushing the chemical reactions in the reverse direction, restoring the chemical energy lost in the discharging process.



(a) Charge. (b) Discharge.

Figure 1.1: Energy conversion of an electrochemical system during charging and discharging. During charging, the external power source supplies energy to the electrochemical system. During discharging, the electrochemical system outputs power to the external circuit. The figure is drawn according to [5].

We illustrate how this energy conversion process is implemented in a lithium ion battery cell in Fig. 1.2. Each cell has three components: cathode, anode, and electrolyte. The cathode and anode are where the chemical reactions take place, and they are immersed in an electrolyte solution where lithium ions can move freely. Between them is a separator that enables ionic transport and stops the electronic flow, forcing electrons to flow through the external circuit [34].

Taking a graphite anode during discharge as an example, during discharging, the following oxidation reaction happens at the anode:

$$\mathrm{LiC_6} \rightarrow \mathrm{Li^+} + \mathrm{C_6} + \mathrm{e^-}. \tag{1.1}$$

Thus lithium ions are extracted from the anode, transported through the electrolyte, and inserted into the cathode. Here, a reduction reaction takes place. Taking lithium iron phosphate as an example material, this takes the form

$$\mathrm{Li^+} + \mathrm{e^-} + \mathrm{FePO_4} \rightarrow \mathrm{LiFePO_4}. \tag{1.2}$$

During charging, the above reactions reverse the direction, so lithium ions stored in the cathode are extracted and move back to the anode material [6].

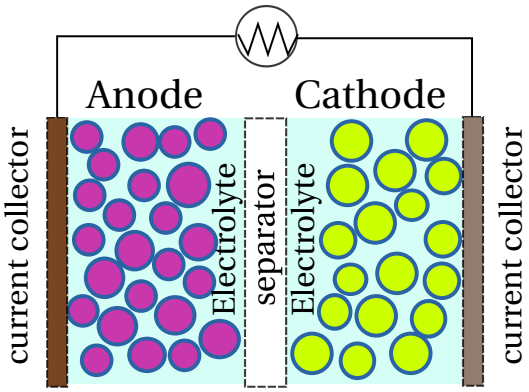


Figure 1.2: A schematic illustration of a lithium ion battery. It is mainly composed of three components: cathode, anode, and electrolyte. The electrodes are usually formed by particles immersed in the electrolyte. Traditionally, the constituent particles are of μm scale, while in some new materials they are of nanoscale.

Despite the apparently simple working mechanism, a complete operation cycle of the lithium ion battery involves the interaction of many complicated processes. Even with great simplification, we need to consider key processes such as transportation of lithium ions in the electrodes, transportation of lithium ions in the electrolyte, and reaction at the electrode surface. Further considerations include the interaction between thermodynamics and the mechanical properties, and the depletion of electrolyte.

As illustrated in Fig. 1.2, both the cathode and the anode are often porous, composed of a large number of dependent particles, all in contact with the electrolyte, and all in electrical contact with the current collector via a network of conducting material. Traditionally, the particles forming the porous electrode are relatively large (on the order of μm [17]), and we call this type of material "bulk material". With the progress of new techniques in nano technology, much smaller particles are possible and nano materials are becoming popular in the fabrication of electrodes. This has the potential to introduce both simplifications and complexities to our understanding of material performance. For instance, the size of the particles could have an impact on the relation between the output voltage V and the state of charge of the material. This relation is an important property of the electrode, as it directly affects the performance of the battery as a power source. We will refer to this relation as the C-V curve in later discussions.

1.1.2 A short review of the electrode materials

As mentioned above, a primary feature of the electrode materials, both cathode and anode, is their crystalline microstructure, which facilitates both the repeated insertion and extraction of lithium ions without destroying the electrode lattices.

1.1.2.1 Cathode materials

A variety of lithium compounds have been used as the cathode material, including lithium cobalt oxide ($LiCoO_2$), lithium manganese oxide ($LiMnO_2$), and lithium iron phosphate (LFP). At the microscopic level, all of these lithium compounds comprise a crystalline structure, in order to facilitate the insertion and the extraction of lithium ions. At the macroscopic level, however, their properties can be quite different. For instance, $LiCoO_2$ is an isotropic material, while LFP is a highly anisotropic material.

On the other hand, for the same material, its macroscopic properties can vary depending on the scale of the material. A good illustrative example of this is LFP. Although LFP is currently one of the most popular material, for a long time its wide application had been hindered by the slow diffusion rate of lithium in LFP and the low electrical conductivity of LFP [33]. It was later found experimentally that, to overcome this problem and achieve ultrafast charging rate, LFP cathodes should be composed of a large number of carbon-coated nanoparticles, which helps to shorten the diffusion length and increase its conductivity [18, 25, 15]. This modern laboratory technique has proved extremely useful.

When LFP particles are nanosized, the dominant reaction mechanisms and rate-limiting steps are very different from what they would be in an electrode composed of the same material, but with fewer, larger particles. For example, if every particle is exceptionally small, then the time scale for lithium diffusion within a particle is much shorter than the time scale for charging/discharging, and the concentration of lithium within any particle can therefore be treated as being approximately uniform [14].

Take LFP as an example. Given the diffusion coefficients are $10^{-12}\text{cm}^2\text{s}^{-1}$ [14], the diffusional relaxation time of a single particle of 500nm diameter is smaller than a second, indeed much smaller than the charging/discharging time, which is normally on the scale of hours [12]. This is very different from traditional lithium-ion cathode materials, where the diffusion of lithium through the particles is a critical rate-limiting step. Similarly, the large surface-area-to-volume ratio of a nanoparticle means that surface reactions may dominate bulk reactions and transport within each particle [27].

1.1.2.2 Anode materials

For anode, the most common material is carbon graphite. Graphite has a well-known layered structure of graphene sheets, and when lithium ions intercalate into and out of graphite, this layered structure leads to a phenomenon called staging: the intercalated lithium ions form a periodic structure of lithium layers sitting inbetween the graphite sheets, without destroying the graphite lattice [26]. This in turn has an effect on capacity-voltage curves.

In a typical partially-charged lithium graphite, the number, n, of graphite layers between two intercalated lithium layers is fixed, and it cannot be an arbitrary number: experiments find that n is typically of 1, 2, 3, 4, and 8, and the resulting compounds is called stage 1, 2, 3, 4, and 8 compounds, as illustrated in Fig. 1.3.

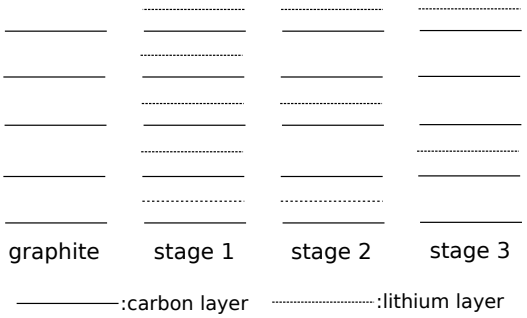
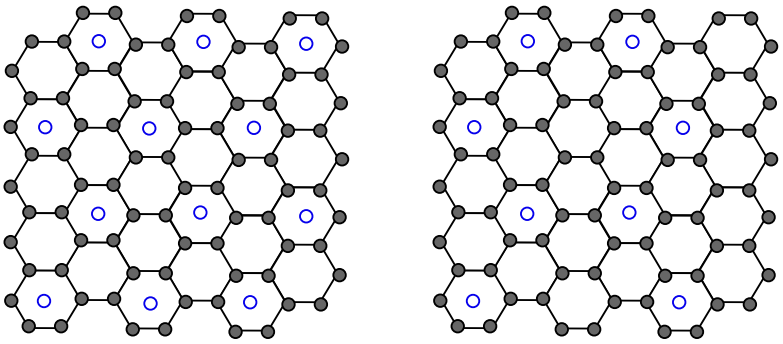


Figure 1.3: A schematic illustration of the staging of lithium graphite compounds. From left to right, we show in sequence the graphite, the stage 1, stage 2, and stage 3 lithium graphite.

This staging phenomenon is thought to occur irrespective of the in-plane ordering of lithium atoms, which can take three different forms. When lithium concentration is small, the in-plane ordering can be random. Then, as lithium concentration increases, two regularly ordered structure can occur: a close-packed in-plane ordering, shown in Fig. 1.4(a), and a hexagonally packed ordering, shown in Fig. 1.4(b) [31]. Among the three orderings, the close-packed in-plane ordering is the most common, and if we do not specify otherwise, we assume this as the default in-plane ordering.

In addition to lithium graphite, new anode structures using nano technology are being widely investigated, such as silicon nanowires and carbon nanotubes. These nanomaterials have the potential of holding several times more charge than the traditional graphite anodes and have faster charging/discharging rate, and making them strong candidates for the future generation batteries [2, 8]. Some of the nano-structured anodes, for instance, silicon nanowires, are already in commercial pro-



(a) Top view of close-packed in-plane ordering.

(b) Top view of hexagonally packed in-plane ordering.

Figure 1.4: Top view of the lattice structure of Li-graphite. The figure is drawn according to [29].

duction, but compared to lithium graphite, they are vulnerable to the crystalline destruction, as silicon swells with the repeated insertion/desertion of lithium ions [2].

1.1.3 A short review of phase-separation

In the previous section, we showed that lithium graphite undergoes a series of orderly changes in its lithiation/delithiation. This is associated with the transition between multiple phases.

Similar phenomena happen in a variety of lithium compounds. Usually, the electrode material tends to phase separate into a Li-rich region and a Li-poor region, which is the phenomenon that directly relates to the electric properties of the material – the flat C-V curve, namely that the output voltage stays almost constant as the lithium concentration varies. Therefore, phase separation has long been the subject of mathematical modelling.

As a common physical process, phase-separation often happens in a system that has multiple local minima in its Gibbs free energy. Consider a simple system that has a symmetric free energy with two local minima, as shown in Fig. 1.5. We denote the two minima as c_α and c_β. If the average concentration c is between the two minima, $c \in [c_\alpha, c_\beta]$, in order to minimise the Gibbs free energy, the system tends to separate spatially into two phases, a low concentration phase α, and a high concentration phase β. Meanwhile, in the region between the two inflection points where $g''(c) < 0$ and $g(c)$ loses convexity, any composition fluctuations would lead to an increase in energy, therefore, the phase-separation is spontaneous, and the two phases can coexist in a stable way [5].

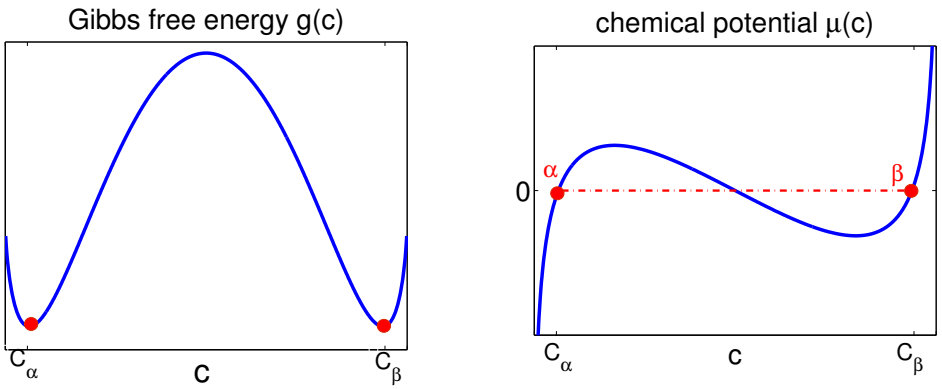


Figure 1.5: A double well Gibbs free energy $g(c)$ and the associated potential $\mu(c)$ that induces phase-separation. α and β denote the two phases that correspond to the local minima of the free energy. In equilibrium, the phase separating system exhibits the red dash-dot curve in the $\mu - c$ plane, which is known as the Maxwell line.

The Gibbs free energy $g(c)$ also specifies the chemical potential $\mu(c) = \mathrm{d}g(c)/\mathrm{d}c$, as plotted in the right panel of Fig. 1.5. The two local minima of $g(c)$ correspond to the zeros of $\mu(c)$ where $\mu'(c)$ is positive, and by connecting these two points on the μ versus c plot, we obtain a red dashed line known as the Maxwell line [30]. As the total concentration varies, the proportion of α-phase and β-phase changes, and the μ-c relation follows the Maxwell line.

It is further found that phase separation also depends on size of the particle, and the above situation discussed above only happens in a particle that is large enough. This is because when two different phases coexist in a single particle, an interface forms and therefore causes additional interfacial energy [12]. For small enough particles, such interfacial energy makes the coexisting phases unstable, and hence each particle can only accommodate a single phase [11, 35]. As a result, individual particles tend to remain single-phased: some particles stay in the Li-rich phase and some particles stay in the Li-poor phase, with the overall effect that the averaged concentration is somewhere in between.

Another phenomenon that accompanies phase-separation is associated with hysteresis. For instance, as illustrated in Fig. 1.6, the voltage curves associated with the charging and discharging differ by a small amount. Even as the charging current decreases to zero, the difference does not disappear [14]. It is also found that, if one slowly charges/discharges a nanoparticulate electrode of LFP but keeps its final concentration equal to its initial concentration, the final output voltage does not equal its initial voltage, suggesting that the final state differs from the initial state. Experimentally, it has been found that this hysteresis of nano particulate electrodes is

present even in the zero current limit.

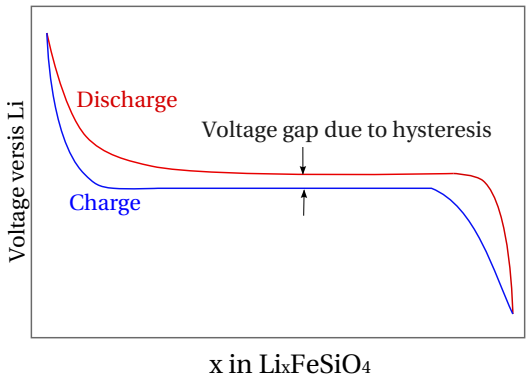


Figure 1.6: A schematic illustration of hysteresis of a nanoparticulate LFP cathode.

In short, a desirable feature of the electrode material is a flat voltage curve that does not change with respect to concentration, which enables the battery to maintain a stable voltage while outputting power to the external circuit. Phase-separation is the essential phenomenon that determines such property. It depends on the material, but can also depend on the size of particles that constitute the material. Being able to model the phase-separation is important in obtaining the right C-V curve.

1.2 Phase-separation in the cathode materials

In the cathode materials that we consider, $LiCoO_2$ and LFP, the output C-V curves are both flat. As discussed above, this indicates a two phase system. In this section, we review some models that have been proposed for explaining the phase separation of the two phase systems.

1.2.1 Two-phase models for bulk materials

In bulk material, each single particle separates into a lithiated region and an unlithiated region, with interfaces forming between different phases [27]; and for this kind of material, the focus of modelling is on the interfaces. Two popular models have been proposed for this purpose: the shrinking core model proposed by by Padhi et al. [28], and the phase-field model adopted by Bazant's research group [4].

Shrinking core model In the shrinking core model, the basic assumption on the two coexisting phases is that one phase constitutes the core region, and the second phase forms the shell that surrounds the core. The model then describes the moving

boundary between the two phases, assuming it is driven by chemical reactions at the surfaces.

A schematic for a charging process of the model is plotted in Fig. 1.7. In the charging process, lithium ions are extracted from the electrode. Initially, the extraction is uniform across the particle, until the concentration in lithium reaches a critical value. At this critical value, phase separation occurs, leaving the core material remaining Li-rich (denoted as $Li_{1-x}FePO_4$), and meanwhile creating a shell of a Li-poor phase (denoted as Li_yFePO_4, x and y are small numbers but are not necessarily equal) surrounding the core. With more and more lithium ions extracted, this two-phase configuration remains, with the boundary moving towards the centre. At the point when the boundary moves to the centre, the Li-rich phase vanishes, and the entire particle is composed of a single Li-poor phase. As the lithium concentration decreases further, the concentration of Li diminishes uniformly across the particle, and the particle turns into $FePO_4$ when fully charged. The process is similar for the discharging cycle.

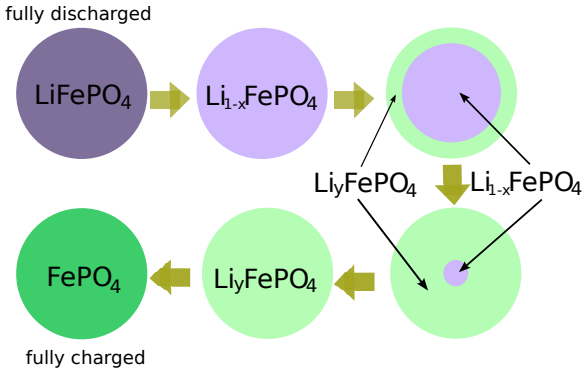


Figure 1.7: A charging process described by the shrinking core model. This figure is drawn according to [33].

Phase-field model In the phase-field model, no prior assumptions are made on the boundary of the two phases. Instead, the co-existence of two phases are the result of a specific functional for the Gibbs free energy $\mathcal{F}$. The model adopts the Cahn–Hilliard equation for $\mathcal{F}$:

$$\mathcal{F} = \iiint_V \left[\bar{f}(c) + \frac{1}{2} (\nabla c)^T K (\nabla c) \right] dV, \tag{1.3a}$$

$$\bar{f}(c) = ac(1-c) + \rho k_B T \left(c \log(c) + (1-c) \log(1-c) \right), \tag{1.3b}$$

where c is the normalized concentration, ∇c is the concentration gradient, and K is a symmetric, positive definite tensor that represents the energy penalties for maintaining concentration gradients. The homogeneous free energy density, $\bar{f}(c)$, adopts

a double-well potential (1.3b), where a is the average energy density of the interaction between Li ions, ρ is the number of intercalation sites per unit volume, k_{B} is Boltzmann's constant, and T is the absolute temperature.

Now, the $\bar{f}(c)$ term in (1.3a) represents the homogeneous free energy that is independent of the concentration gradient, and the second term models the energy that is due to concentration gradient. In this model, phase-separation happens as a result of the double-well energy for the homogeneous free energy.

With this model, anisotropic diffusion can be modelled, and the ionic flux j follows from the chemical potential μ by

$$\mu = \frac{\delta \mathcal{F}}{\delta c}, \tag{1.4}$$

$$j = -c\mathbf{B}\nabla\mu, \tag{1.5}$$

where $\mathbf{B}$ is the mobility tensor.

The shrinking-core model is essentially an isotropic model, and the phase-field model does not have this constraint. Therefore, in describing the transport of lithium ion in a solid electrode, the shrinking-core model can be selected for isotropic diffusivity, while the phase-field model is capable of modelling both isotropic and anisotropic transport. The two cases are summarised in Fig. 1.8, scenario (1).

1.2.2 Two-phase models for nano materials

On the other hand, as the particle sizes shrink to nano scale, phase separation occurs at the particle level, unlike bulk electrode materials where phase separation happens inside particles [14, 27]. Therefore, a different approach of modelling is needed.

For small enough particles, Dreyer et al. proposed that each individual particle contains a uniform concentration of lithium, but that the collection of nanoparticles separates into a high-lithium group and a low-lithium group [14]. Instead of all the particles filling or emptying at the same rate, individual particles rapidly go from being empty to being full (or *vice versa*), while the overall dynamics of the ensemble of particles in the electrode appears as a smooth change in the concentration of lithium [12].

One theoretical prediction of this particle-by-particle filling mechanism is that it supports multiple equilibria, with the number of equilibrium branches increasing as the number of particles going up, under a constraint that the total amount of lithium of all particles is fixed [13]. This is then used to explain the hysteresis between the

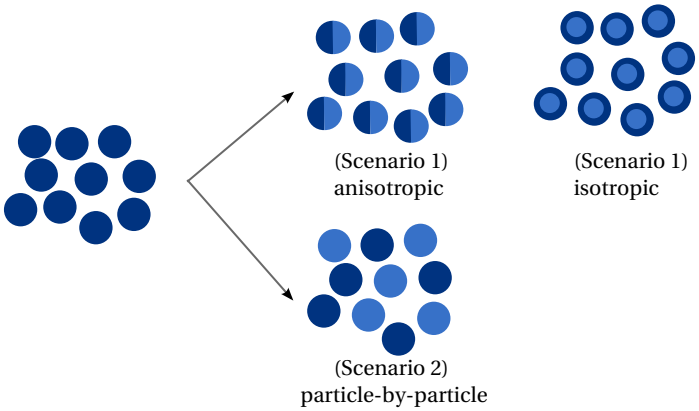
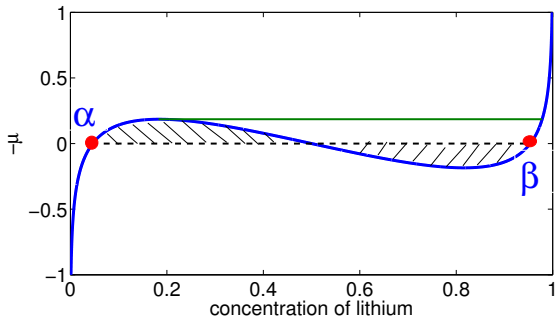


Figure 1.8: In bulk material, each particle phase separates into a Li-rich region and a Li-poor region, as in scenario (1). Depending on the diffusion of lithium inside the particle, this can be further divided into an anisotropic case where the locations of the phase boundaries would need to be found using the phase-field model, and an isotropic case where the shrinking core model can be used. For nanosized materials, particle-by-particle filling is proposed [14], as in scenario (2).

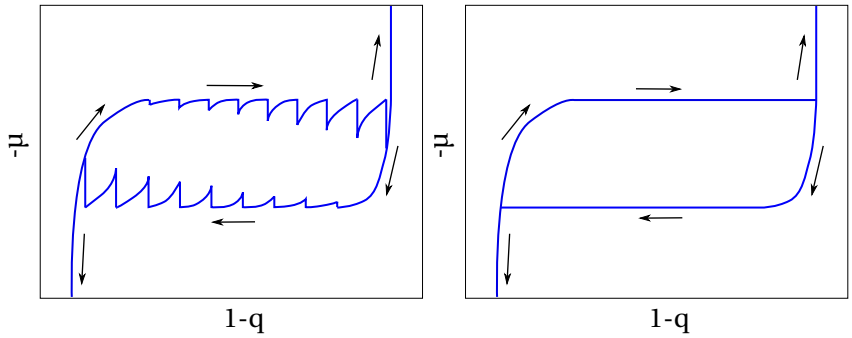
charging and discharging of nanoparticle LFP electrodes, as in charging/discharging the ensemble follows different equilibrium paths [14].

It is noteworthy that this particle-by-particle phase separation and the hysteresis is a special case within the many scenarios that an ensemble of particles can exhibit, and a full list of possible paths such an ensemble of particles can exhibit is summarised in [12]. As noted by that paper, two factors determines the behaviour: the relaxation time of the ensemble, and statistical entropy. For the particle-by-particle phase separation and the resulting hysteresis path to occur, two conditions are essential: i) the relaxation time of the ensemble must be much smaller than the time of charging/discharging; ii) the statistical entropy must be significant. If either of these two conditions is broken, the ensemble would behave differently. In fact, it is found by Li et al. that this particle-by-particle interaction only happens in slow loading [24]. When the charging rate is sufficiently high, the ensemble of nanoparticles switches to simultaneous charging, and an ensemble of nanoparticulate LFP electrodes all filling at the same rate has been observed in [22].

This phase-separation phenomenon and which path is takes is important since it affects the output voltage curve. Different charging path exhibits different voltage curves. As summarised by Dreyer et al. in [14], for the simultaneous charging, the equilibrium potential of the system follows the green line in Fig. 1.9(a). Meanwhile, if, instead, the relaxation time of the ensemble is much smaller than the charging/discharging time, then the ensemble proceeds according to the Maxwell line, that is, the



(a) The equilibrium potential of a single particle is the black dashed line, and the equilibrium potential of a many-particle system is the green solid line.



(b) When the number of particles is finite, the equilibrium voltage of a many-particle system is jagged as plotted in the left panel. When the number of particles is infinite, the equilibrium voltage curve is smooth, as plotted in the right panel.

Figure 1.9: Various voltage paths in the charging/discharging of a many particle system. All three figures are drawn according to [14].

same black line as the individual particle equilibrium potential.

Therefore, although the modelling of nanoparticles can be simplified in that each nanoparticle can be regarded as homogeneous, the phase-separation at the many-particle level raises new complexities.

1.3 Phase-separation in lithium graphite

Unlike the cathode materials, whose C-V curves are mostly flat lines, lithium graphite has a staircase-like C-V curve, as plotted in Fig. 1.10. The multiple steps in the C-V curve indicate multiple phase changes: when fully lithiated graphite LiC_6 is oxidised to natural graphite, it undergoes a series of phase changes, and the plot suggests that such transitions happen at $x = 0.17$, 0.33, and 0.5. Meanwhile, a small hysteresis exists between lithiation and delithiation.

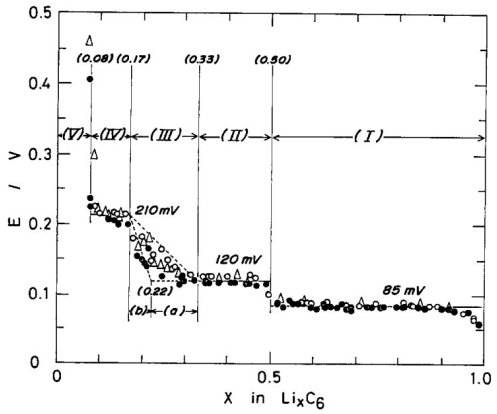


Figure 1.10: Potential of lithium-graphite versus its concentration. Experimental data below $x = 0.08$ is lacking. Open circles, closed circles, and triangles in the figure indicate open-circuit voltages measured with different experiment techniques (figure reproduced from [26]).

Experimentally, it has been established that the phase changes in lithium graphite are connected to the staging phenomenon and the different in-plane orderings discussed in Section 1.1.2.2. In the oxidation of lithiated graphite to natural graphite, the staging sequence is stage 1, stage 2, stage 2 with hexagonal in-plane ordering, stage 3, and stage 4 [31]. However, such sequence can be affected by experimental conditions, and a variety of different staging sequences have been reported. For instance, in Table 1.1, we compare the results from two experiments and notice a few discrepancies: in the low concentration regime, [31] reported a dilute stage 1, but [26] indicated a higher stage than stage 8; meanwhile, in [31], no stage 3 or reduced stage 2 compounds were reported. Although the staging phenomenon was observed as early as in the 1980s, the transition mechanisms behind it remains unclear [21].

Because of these difficulties, in the modelling of lithium graphite as an anode material, studies tend to ignore higher stages and focus on the intermediate concentration regime, namely the relatively simple stage 1 and stage 2 [16].

1.4 Motivation

A variety of phase-separation patterns introduced in Sections 1.2 and 1.3 feature homogeneous concentration of lithium in each constituent compartment. First, in the nano-particulate LFP, because the time-scale of lithium diffusion will typically be much smaller than the time-scale of charging and discharging, the concentration of lithium within a nanoparticle can often be treated as being spatially uniform. On the

x	compounds found in [26]	x	compounds found in [31]
$x < 0.08$	higher stage than stage 8	$x < 0.05$	dilute stage 1
$[0.08, 0.17]$	stage 4 and stage 8	$[0.05, 0.2]$	dilute stage 1 and stage 4
$[0.17, 0.22]$	stage 3 and stage 4	$[0.2, 0.5]$	stage 4 and stage 2
$[0.22, 0.33]$	reduced stage 2 and stage 3	$[0.5, 1]$	stage 2 and stage 1
$[0.33, 0.5]$	reduced stage 2 and stage 2	–	–
$[0.5, 1]$	stage 1 and stage 2	–	–

Table 1.1: Staging of lithium graphite with respect to the concentration, summarised from [26] and [31]. The reduced stage 2 refers to hexagonally packed ordering, while the dilute stage 1 refers to random in-plane ordering. Without specifying otherwise, we assume close-packed in-plane ordering is the default in-plane ordering.

other hand, lithium graphite can be thought of as a stack of intercalated lithium sheets between graphite sheets, and in each lithium sheet the concentration of lithium can be approximated as homogeneous. Therefore, we treat a single nanoparticle or a lithium graphite layer as the basic compartment that constitutes the electrode material.

In each case, the spatially uniform concentration simplifies the mathematical models for lithiation and delithiation of a single compartment, and leads to phase-separation patterns at the many-compartment level due to the coupling between compartments. We are hence motivated to develop mathematical models for such systems, which can be decomposed into many basic compartments, with the concentration of lithium in each basic compartment being spatially homogeneous. We then aim to examine the phase-separation pattern, which occurs as a result of the interactions between the compartments. This model is developed as an abstraction of both lithium graphite (an anode material) and nanoparticulate lithium iron phosphate (LFP) (a cathode material), but it can in principle be extended to other materials as long as such material can be decomposed into interacting compartments and each compartment can be assumed to be homogeneous.

If the compartments that constitute the electrode are nanosized, bulk processes, such as phase separation within a compartment, essentially play no role in the lithiation dynamics, while the change in lithium concentration of each compartment is purely controlled by surface reactions. Therefore, it is essential for the model to capture the effect of various surface reaction mechanisms, and in this thesis, we mainly discuss two kinds of relations between the change of lithium concentration

in a compartment and the voltage applied to the compartment: a linear relation and a nonlinear Butler–Volmer law.

Another issue which arises due to the small size of each compartment is the limited number of lithium ions it can host. When a compartment hosts just a few tens of thousands of lithium atoms, it is possible that a continuum concentration will not be an appropriate way of representing the amount of intercalated lithium in any particle. Moreover, thermal fluctuations in the amount of intercalated lithium may have a significant effect on the lithiation dynamics. Therefore, it is necessary to devise stochastic models that consider the effect of thermal fluctuations.

Meanwhile, our focus is on the phase separation at the many-compartment level. Generally, phase separation is modelled by a double well Gibbs free energy. If these compartments are completely decoupled, phase separation can still occur as some compartments are in the Li-rich phase, while other compartments are in the Li-poor phase, but which compartments are near full and which are near empty occurs at random. As a result, there does not exist a clear pattern of phase separation, although the system as a whole may obey some statistical law. In a real electrode material, each compartment is strongly coupled to its neighbours, and this work considers such coupling by incorporating an interaction potential into the free energy. In this case, the double well Gibbs free energy induces phase separation, and different interaction laws lead to different patterns of phase-separation. This is similar to the phase-field model, where the gradient penalty term determines the phase front in a phase-separating bulk material.

Then the interaction energy can be combined with the dynamic models, both deterministic and stochastic, to obtain a phase separation profile and the associated C-V curve, as well as possible hysteresis. By analysing the resulting equilibria and dynamics in detail, we hope to identify how the underlying reactions fundamentally determine the phase-separation at the system level. In particular, we are interested in an orderly phase transition, such as the multiple phase-transition of lithium graphite.

1.5 Overview

The thesis is organised as follows.

We begin by considering the lithiation/delithiation process of a single compartment. As discussed, two issues are important when considering a single compartment: the surface reaction, and the impact of discreteness and thermal fluctuations. We address the first issue by considering a deterministic model using the Butler–Volmer

equation, and address the second issue by presenting a stochastic model based on the chemical master equations.

In Chapter 2, we consider a single compartment where the lithium concentration is treated as a continuum variable, which evolves deterministically according to the Butler–Volmer equation. Two fundamental factors are incorporated into the model: first, a double-well energy same the as (1.3b) is adopted to model the phase-separation process; second, the dynamics is described by the Butler–Volmer equation, which is a fundamental result from electrochemistry, and connects the current (in this context, the rate of change of the lithium concentration in the single compartment) with the overpotential (the difference between the applied potential and the chemical potential of the compartment), through a nonlinear relation. This model enables us to analyse both equilibrium and dynamic properties of a single compartment, when the control variable is the applied potential.

We first analyse the equilibrium using perturbation methods, and find that the compartment suddenly changes phase between being near-empty or near-full when a critical voltage is reached. The critical voltage, however, depends on the direction of the jump, thus suggesting hysteresis. We also study a canonical lithiation process assuming a time varying voltage, using both asymptotic and numerical methods. We find that the dynamic trajectory is similar to its equilibrium path, except that in the dynamics the jump from near-empty to near-full is delayed by a small amount. The delithiation process is mathematically equivalent, and the hysteresis between lithiation and delithiation remains. Although apparently a simple differential equation model, we find that the logarithmic terms in the double-well potential and the exponential terms in the Butler–Volmer equation lead to subtle and complicated dynamics. This confirms our previous suspicion, that a small amount of stochastic noise added to the deterministic model might alter the dynamics completely.

Therefore, in Chapter 3, we explore the impact of thermal noise with a discrete, probabilistic model of the lithium concentration in a single compartment based on the chemical master equation. This model is set-up in a way to retain the Butler–Volmer dynamics in its deterministic limit, but we find that it may behave very differently from those predicted by the deterministic model with a continuum concentration variable. A noticeable difference is in the equilibrium behaviour: in the stochastic model, hysteresis is wiped out, and the sudden phase change between near-empty and near-full occurs at a fixed voltage $E = 0$, regardless of the direction of the phase-change. Meanwhile, the hysteresis remains in a dynamic process, but the critical voltages for

the phase-change may deviate significantly from the deterministic model. By developing the chemical master equation into a hybrid discrete-to-continuum model, we find that the effects of discreteness and thermal noise can be quantified by an important dimensionless factor, α, which describes the effect of the discreteness: $\alpha \ll \mathcal{O}(1)$ represents the continuum limit, where the compartment hosts a large number of lithium ions; $\alpha \gg \mathcal{O}(1)$ represents the discrete limit, where the limited number of lithium ions means that the two local minima of the double well Gibbs free energy are not felt, the dynamic behaviour is governed by discrete effects, and hence the critical voltages deviate greatly from the deterministic model.

Having analysed the discrete model, we then consider a system of interacting compartments, first assuming that interactions exist only between adjacent compartments, and modelling the Gibbs free energy for the system as a discrete sum of intra-compartment energy and inter-compartment energy between adjacent compartments. We investigate the nearest neighbour interaction model under three different dynamic laws: a gradient flow model in Chapter 4, a Butler–Volmer model in Chapter 5, and a stochastic model in Chapter 6.

A gradient flow model assumes a linear relation between the applied voltage and the rate of change in the lithium concentration of a compartment, and, as will be shown, it is a linearisation of the Butler–Volmer model. In Chapter 4, we begin by examining the linear dynamics, assuming that the total concentration of lithium of the system is known over time. First, we perform some numerical experiments and show a basic phase-separation pattern: the nearest-neighbour interaction leads to a filling sequence of every other compartment when the total concentration is not near empty or full; in contrast, when the total concentration is near empty or full, all compartments are filled at the same rate. Consequently, this leads to a two-stage lithiation/delithiation process.

The numerical experiments are conducted using a slow charging rate, so that presumably the observed pattern is close to the equilibrium behaviour. We then reduce the system to 3 interacting compartments, and conduct asymptotic analysis to find equilibria of the system as well as identifying the bifurcations that connect them. The asymptotic analysis supports the observation of a two-stage process at intermediate concentration, as well as explaining the uniform concentration of all compartments when the system is near empty or near full. Meanwhile, the subtlety of the asymptotic analysis is an indication of the complication of this deterministic system.

In Chapter 5, we move on to the nonlinear dynamics and consider a modified Butler–Volmer equation, assuming voltage control. First, by reducing the system to two interacting compartments and identifying its bifurcation structure using asymptotic analysis, we find that, compared to the current control problem, the voltage control problem supports even more equilibria, therefore leading to extremely subtle equilibrium behaviour. In addition, the nonlinear dynamics of the Butler–Volmer model adds further complications to the dynamics: in numerical experiments, we find that the rate at which the voltage varies can have a significant impact on the charging profile: slow charging leads to compartment-to-compartment filling, while a fast charging leads to simultaneous filling of all compartments. We try and understand this by examining the Butler–Volmer dynamics of a two-compartment model. Preliminary investigations indicate that the dynamics depends parametrically on the initial conditions, and this dependence is so sensitive that the solution structures cannot even be captured by the numerics, as a result of numerical rounding errors. Therefore, once again we need to examine how the solutions would be altered by thermal noise.

In Chapter 6, we carry the framework that we developed for a stochastic single-compartment model in Chapter 3 to investigate the effects of thermal noise for a two-compartment system. We find that if the system progresses in quasi-equilibrium, the situation is similar to Chapter 3, in that hysteresis is wiped out. On the other hand, in the dynamic transition under time varying E, the situation is considerably simplified compared with the deterministic model: thermal noise always selects an asymmetric growth path. In the lithiation process, one compartment is filled first and then the other compartment; the two compartments never fill at the same rate. Hence, when generalising to a multicompartment system, we propose that a non-uniform growth is preferred over a uniform growth in every charging process.

In short, in Chapters 4–6, we examine different lithiation profiles of a nearest-neighbour interacting system, where a two-phase process is evident. In order to describe the multi-phase transitions, in Chapter 7, we examine interactions over longer distances. First, we consider when a compartment may only interact with nearby compartments, in which case, the staging phenomenon is very similar to the nearest neighbour models, but is associated with multiple stages instead of just 2. We show that by considering a 7-nearest neighbour interaction model, it is possible to predict a 8-4-3-2-1 phase-change as observed in lithium graphite, although the direct transition into stage 3 from stage 2 and stage 4 compounds can be relatively difficult. Generally, a K-nearest neighbour interaction model leads to a C-V curve with K steps, and as

K increases, the C-V curve is smoothed. This motivates us to consider a long-range model, where we assume the inter-compartment interaction can exist between any two compartments. Preliminary investigations suggest that, if the interaction strength is properly scaled with respect to distance, the discrete sum of total energy may be turned into a semi-continuous model.

Finally, in Chapter 8, we conclude the thesis and discuss possible avenues for future research.

Chapter 2

A deterministic model for a single compartment

In Section 1.4, we introduced the subject that this thesis aims to model: an electrode system which is composed of many interacting compartments, with the lithium concentration of each compartment being spatially uniform. Examples of such systems include an ensemble of LFP nanoparticles as the cathode material, or lithium graphite as the anode material. In these two examples, the basic compartment can be thought of as a single LFP nanoparticle, or an intercalated lithium sheet. In later chapters, we will develop multicompartment models where all compartments are assumed to be identical and obey the same laws. To understand these models well, we need a detailed understanding of a single compartment in the first place.

In this chapter, we introduce a deterministic model for a single compartment. This will form the basis for our later multicompartment models. As discussed in Section 1.4, for a nanoparticle with homogeneous concentration, surface reaction plays a dominant role in lithiating/delithiating the nanoparticle. It is therefore essential for our model to investigate how the control variable, in this case the external voltage, governs the change of the lithium concentration in the compartment.

We begin by introducing the Gibbs energy for each compartment, which relates the concentration to the chemical potential. We then use the Butler–Volmer equation to model the rate of change of lithium concentration in the compartment, assuming that each compartment is controlled by an external potential. This is the simplest model for a single compartment that also captures its essential thermodynamic properties. By analysing the Butler–Volmer equation coupled to a non-monotonic potential associated with the double well Gibbs energy, we are able to examine how the C-V curve is affected by the charging speed. In section 2.2 we conduct a bifurcation analysis to identify the equilibrium/quasi-equilibrium behaviour, which is intrinsic to the

double-well Gibbs free energy. In section 2.3 we consider a generic dynamic problem when the external voltage varies at a time scale that is inherent to physical properties of each compartment, which enables us to identify the effect of the nonlinear relation between the applied potential and the change of lithium concentration of each compartment.

All analysis in this chapter assumes voltage as the control variable. We do not consider current control because in that case the concentration is known over time, and the chemical potential simply follows the logarithmic law as a result of the assumption of homogeneous concentration. A current-control problem for a single compartment is hence trivial. However, when we consider a collection of many compartments, the current-control problem would be more complicated because we need to understand how ions are distributed given the total concentration constraint. This will be discussed in Chapter 4.

2.1 Model Formulation

2.1.1 A double-well Gibbs energy

First, we introduce a double-well model for the Gibbs free energy that is widely used for phase-separating materials [27, 12]. A single compartment with normalised concentration $c \in (0, 1)$ is assumed to have a free energy given by

$$g(c) = \Omega c(1-c) + k_{\mathrm{B}}T\big[c\log(c) + (1-c)\log(1-c)\big], \tag{2.1}$$

where Ω is the enthalpy of mixing, k_{B} is Boltzmann's constant and T is the absolute temperature. In this Gibbs free energy, the first term is the enthalpy term, which promotes separation as it is maximised when $c = 1/2$. The second term is the constitutional entropy term which promotes mixing.

The shape of the Gibbs free energy curve, $g(c)$, hence depends on the relative importance of entropy and enthalpy to the total energy. We define the dimensionless ratio of the characteristic thermal energy versus enthalpy by

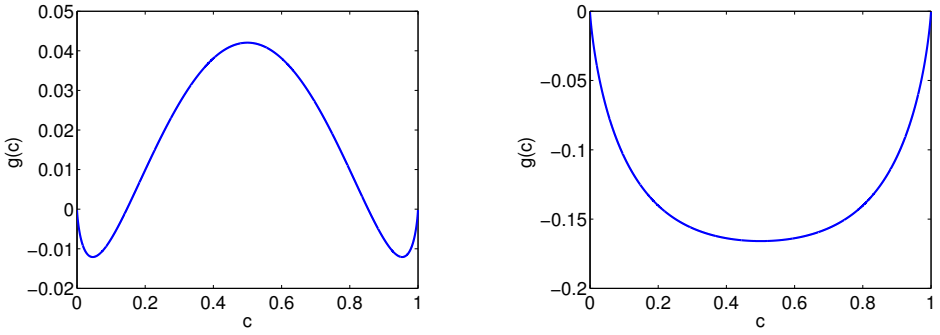
$$\epsilon = \frac{k_{\mathrm{B}}T}{\Omega}. \tag{2.2}$$

At high temperature, when ϵ is large, the entropic contribution dominates, promoting better mixing. At low temperature, when ϵ is small, entropy is relatively important, mixing is suppressed.

As long as $\epsilon < 0.5$, or equivalently when T is below a critical temperature $1/(2\Omega k_{\mathrm{B}})$, the Gibbs free energy $g(c)$ represents a double-well potential. As shown

in Fig. 2.1(a), the energy minima of this double-well potential are not exactly at the empty/full states. Instead, the minima are away from the boundaries by an amount which is exponentially small in ϵ.

When $\epsilon > 0.5$ the double-well structure disappears, as shown in Fig. 2.1(b). In this case phase separation does not occur; therefore we assume henceforth that $\epsilon < 0.5$.



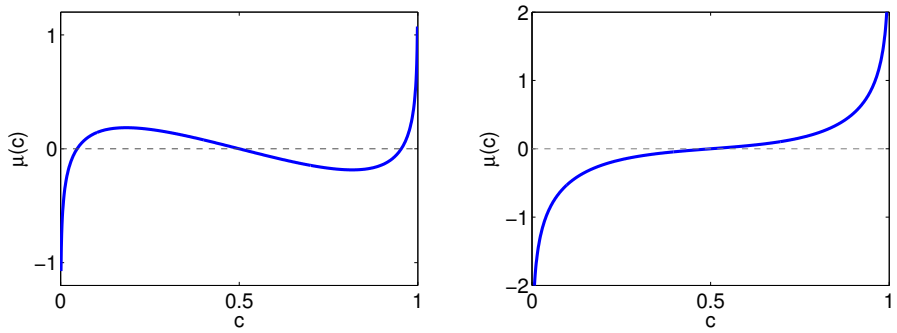
(a) $\epsilon = 0.3$. (b) $\epsilon = 0.6$.

Figure 2.1: Two possible shapes for the double-well Gibbs free energy $g(c)$ given by equation (2.1); $g(c)$ is nondimensionalised by Ω and $\epsilon = k_{\mathrm{B}}T/\Omega$. The function $g(c)$ will have a double-well shape when $\epsilon < 0.5$, but not when $\epsilon > 0.5$.

The associated chemical potential for this free energy is

$$\mu(c) = \frac{\mathrm{d}g}{\mathrm{d}c} = \Omega(1-2c) + k_{\mathrm{B}}T \log\left(\frac{c}{1-c}\right). \tag{2.3}$$

Provided again that $\epsilon < 0.5$, this chemical potential is "N-shaped", as shown in Fig. 2.2(a), indicating that three equilibrium concentrations of lithium are possible for certain values of the chemical potential. In contrast, $\mu(c)$ is monotonic when $\epsilon > 0.5$, as shown in Fig. 2.2(b).



(a) $\epsilon = 0.3$. (b) $\epsilon = 0.6$.

Figure 2.2: Chemical potential corresponding to equation (2.3); $\mu(c)$ is nondimensionalised by Ω, and $\epsilon = k_{\mathrm{B}}T/\Omega$.

2.1.2 Butler–Volmer equation

We now develop a deterministic model of the lithiation of a single compartment based on the Butler–Volmer equation. In this model (and indeed throughout this thesis), we assume that lithium ions are abundant in the electrolyte, that there are no limitations based on the rate of reaction at the reference electrode or auxiliary electrode, and that there is no competition with reactions at other compartments in the working electrode. Thus, we concentrate on the simplified problem where the applied electric potential at a compartment is specified, and we observe the changing lithium content of the single compartment in response to this potential. Possible extensions of the present model, such as coupling together many compartments into a single electrode, will be discussed in Chapters 4 and 5.

We take a nanoparticle LFP cathode as an example and consider a half-cell battery that is composed of a nanoparticle LFP cathode, a metallic lithium anode, and an electrolyte. The electrochemical reaction under consideration is

$$\mathrm{Li}^+ + \mathrm{e}^- + \mathrm{FePO}_4 \rightleftharpoons \mathrm{LiFePO}_4. \tag{2.4}$$

In the forward reaction, lithium ions in the electrolyte recombine with electrons at the cathode-electrolyte interface, and the concentration of lithium in the cathode increases. In the reverse reaction, lithium atoms stored in the nanoparticle cathode are extracted, and the concentration of lithium in the cathode decrease. The Butler–Volmer equation [7] accounts for the net rate of the two reactions and relates the current density, I, to the overpotential, η, by

$$I = I_0 \left[\exp\left(\frac{ae}{k_\mathrm{B}T} \eta \right) - \exp\left(-\frac{(1-a)e}{k_\mathrm{B}T} \eta \right) \right], \tag{2.5}$$

where a is the charge transfer coefficient with $0 < a < 1$, e is the charge on an electron, and I_0 is the exchange current density. Following convention [7], we will assume that charge transfer is symmetric, so that $a = \frac{1}{2}$. Moreover, we will treat I_0 as a constant; in some cases, I_0 can be a function of the ion concentration, and the effect of including this into our model is discussed in Section 2.4.1.

The overpotential η is defined as the difference between the electrode potential and a constant equilibrium potential. When $\eta = 0$, the forward and reverse reactions cancel so that the net current density, I, is zero. In the half-cell setting of this chapter, the overpotential will depend on the difference between the applied potential over the nanoparticle interface, $E(t)$, and the chemical potential of the nanoparticle, $\mu(c)$.

Specifically, we follow [27] to obtain

$$\eta(t) = E(t) - \frac{\mu\big[c(t)\big]}{e}. \tag{2.6}$$

The current density, I, is in turn related to the flux of lithium in or out of the compartment. Specifically, we find that

$$I = \pm\frac{e\rho V}{S}\,\frac{\mathrm{d}c}{\mathrm{d}t}, \tag{2.7}$$

where ρ is the lattice density (the number of potential sites for intercalated lithium per unit volume), V is volume of the compartment, S is the surface area, and e is the charge on an electron as above. The positive sign should be taken in the case of a cathode material (where positive current density corresponds to flux of lithium into the cathode material), while the negative sign should be taken in the case of an anode material.

We note that $g(c)$ is a symmetric function of c in that $g(c) = g(1-c)$, and that picking $a = \frac{1}{2}$ means that $I(-\eta) = -I(\eta)$. These symmetries mean that lithiation and delithiation are mathematically equivalent, and similarly that cathode material and anode material are mathematically equivalent. Thus, without loss of generality, we will concentrate on the lithiation of a cathode material.

We nondimensionalise the equations above using the intrinsic time-scale

$$t_{\mathrm{int}} = \frac{eV\rho}{SI_0}, \tag{2.8}$$

which corresponds to the time required to deplete a fully-lithiated compartment at constant current density I_0. Additionally, we rescale energy with respect to Ω, and potential with respect to Ω/e. This leads to the dimensionless Butler–Volmer model:

$$\frac{\mathrm{d}c}{\mathrm{d}t} = \sinh\left(\frac{E(t) - \mu\big[c(t)\big]}{2\epsilon}\right), \tag{2.9a}$$

$$\mu(c) = 1 - 2c + \epsilon\log\left(\frac{c}{1-c}\right). \tag{2.9b}$$

The parameter

$$\epsilon = k_{\mathrm{B}}T/\Omega \tag{2.10}$$

represents the relative importance of entropy and enthalpy, and it controls the shape of the function $\mu(c)$. Typically we expect ϵ to be small, so that at a stable equilibrium the compartment is either nearly empty of lithium ($c \approx 0$) or nearly full of lithium ($c \approx 1$). We will carry out asymptotic analysis in the limit $\epsilon \to 0$.

2.2 Equilibrium

When E varies slowly enough, the compartment has enough time to exchange lithium ions freely with electrolyte until its concentration satisfies $\mu(c) = E$, so that forward and reverse reactions balance. As a result the system is always in quasi-steady-state, and the lithium concentration simply follows the equilibria of the system (2.9). Depending on the value of E, the system can have either one stable equilibrium (when $E > \mu^*$ or $E < \mu^{**}$), or one unstable and two stable equilibria (when $\mu^{**} < E < \mu^*$), where μ^* and μ^{**} are bifurcation values of E, which depend on ϵ. Fig. 2.3 shows the three equilibrium branches (labelled s_{I}, s_{II} and s_{III}), illustrating the bifurcation potentials μ^* and μ^{**}, which will be near 1 and -1 respectively.

It is clear that this system exhibits hysteresis. If we start from the lower stable branch s_{I} and increase E, the lithium concentration will jump to the upper stable branch s_{III} at the turning point A in Fig. 2.3, when $E = \mu^*$. Similarly, if we start from the higher stable branch s_{III} and decrease E, the lithium concentration switches from the upper branch s_{III} to the lower branch s_{I} at the turning point B in Fig. 2.3, when $E = \mu^{**}$.

We can obtain expressions for the turning points and equilibrium branches by standard asymptotic analysis. Away from the two turning points A (c^*, μ^*) and B (c^{**}, μ^{**}), the three equilibrium branches are given by

$$s_{\mathrm{I}} \sim e^{-(E-1)/\epsilon}, \qquad s_{\mathrm{II}} \sim (1-E)/2, \qquad s_{\mathrm{III}} \sim e^{-(E+1)/\epsilon}, \tag{2.11}$$

obtained by solving (2.9) by a regular asymptotic expansion. To find the local behaviour around A, we expand by

$$E = 1 - \epsilon \log \frac{1}{\epsilon} + \epsilon \bar{E} + \mathcal{O}(\epsilon^2), \qquad c = \epsilon \bar{c} + \mathcal{O}(\epsilon^2), \tag{2.12}$$

where $\bar{E}$ and $\bar{c}$ are the local variables near the turning point A. We obtain an implicit relation between $\bar{E}$ and $\bar{c}$ by finding the leading order solution to $E = \mu(c)$, namely

$$\bar{E} = -2\bar{c} + \log \bar{c} + \mathcal{O}(\epsilon). \tag{2.13}$$

This is plotted in the right panel of Fig 2.3, and we see that there are two solutions when $\bar{E} \leq -1 - \log 2$

$$\bar{c}_I = -\frac{1}{2} W(0, -2\bar{E}), \qquad \text{stable} \tag{2.14a}$$

$$\bar{c}_{II} = -\frac{1}{2} W(1, -2\bar{E}), \qquad \text{unstable} \tag{2.14b}$$

where $W(i,\cdot)$ denotes the ith branch of the Lambert-W function ($z = W(i,z)e^{W(i,z)}$). This associates the turning point A (with corrections of order ϵ^2)

$$(c^*, \mu^*) \sim \left(\frac{\epsilon}{2}, 1 - \epsilon - \epsilon \log \frac{2}{\epsilon}\right) \tag{2.15}$$

with a saddle-node bifurcation. Similar analysis indicates a saddle-node bifurcation at B (with corrections of order ϵ^2),

$$(c^{**}, \mu^{**}) \sim \left(1 - \frac{\epsilon}{2}, -1 + \epsilon - \epsilon \log \frac{1}{2\epsilon}\right). \tag{2.16}$$

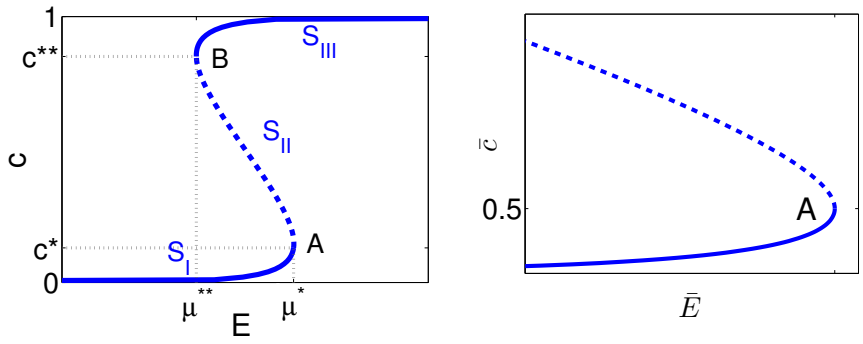


Figure 2.3: Bifurcation diagram for equilibria of the Butler–Volmer system (2.9), as functions of the control parameter E, plotted with $\epsilon = 0.25$. The three equilibrium branches (s_{I}, s_{II} and s_{III}) are connected by saddle-node bifurcations at the critical points A and B. On rescaling c and E as given by (2.13), we obtain the implicit expression for the local behaviour around the critical point A described by (2.14).

2.3 Dynamics

When the applied potential $E(t)$ varies on a time scale similar to or smaller than the intrinsic time t_{int}, we need to solve a dynamic problem to understand the out-of-equilibrium behaviour. As noted above, the problem (2.9) is invariant under the transformation $c \mapsto 1 - c$ and $E \mapsto -E$, and so no generality is lost in considering only an increasing E. Specifically, we consider a linearly increasing $E(t)$ and set

$$E(t) = 1 + \kappa t, \tag{2.17}$$

so that the constant κ controls how fast the applied potential increases relative to the intrinsic timescale t_{int}, while we expect the transition from the low branch to the high branch to occur in the vicinity of $t = 0$. When considering a lithiation process,

we assume that the initial voltage is well below the critical voltage, i.e. that initially t is a negative value.

In this section we focus on the specific case $\kappa = 1$; it will be shown that varying κ does not alter the qualitative dynamics of the problem provided $\kappa = \mathcal{O}(1)$. Moreover, $\kappa = \mathcal{O}(1)$ is also a realistic assumption since using values for lithium iron phosphate of $I_0 = 1.75 \times 10^{-2}$ Am^{-2} [32] and $\rho = 1.26 \times 10^{28}$ m^{-3} [27], we find t_{int} to be around 17 hours, which is comparable to a typical charging time [12].

The main result from the analysis that follows is that when $E(t)$ increases linearly with $\kappa = 1$, the dynamic transition voltage μ_{dyn} is $\mathcal{O}(\epsilon)$ larger than the static transition voltage μ^*. Thus, the system jumps from near-empty to near-full at a voltage higher than the corresponding open circuit voltage. Moreover, the dynamic transition potential does not depend on the initial state, suggesting that the process is memoryless except for the above-mentioned charging/discharging hysteresis.

2.3.1 A matched asymptotic solution

We let $E(t) = t + 1$ and solve the initial value problem

$$\frac{\mathrm{d}c}{\mathrm{d}t} = \frac{1}{2}\sqrt{\frac{1-c}{c}}\,\exp\left(\frac{t+2c}{2\epsilon}\right) - \frac{1}{2}\sqrt{\frac{c}{1-c}}\,\exp\left(-\frac{t+2c}{2\epsilon}\right), \quad c(-t_0) = c_0, \tag{2.18}$$

in the limit of $\epsilon \to 0$. We assume that $0 < 2c_0 < t_0$ and that t_0, c_0 and $1 - c_0$ are all $\mathcal{O}(1)$ to ensure that the initial position is within the attractor of the lower stable branch.

The step-by-step asymptotic analysis carried out from Sections 2.3.1.1 to 2.3.1.5 reveals four major stages along the solution trajectory: (i) c falls rapidly from its initial position to the lower s_{I} branch; (ii) c stays on s_{I} until E approaches the dynamic critical value μ_{dyn}; (iii) c switches rapidly to the higher branch s_{III}; (iv) c remains on s_{III} as E increases further. This behaviour is illustrated in Fig. 2.4, where C labels the initial point $(c, E) = (c_0, 1 - t_0)$. In plotting the figure we use $\epsilon = 0.25$, so that the transitions are relatively smooth. For smaller values of ϵ, the transitions occur much faster; as we will see in the asymptotic analysis, some transitions happen over exponentially short time scales.

In the asymptotic analysis that follows, we seek leading-order asymptotic approximations of the solution to (2.18) in each of the stages (i) to (iv) described above. We proceed by introducing different scalings for c and t in each of the domains considered (in some cases even splitting the domains into subdomains), and using matched asymptotics to connect the different regions.

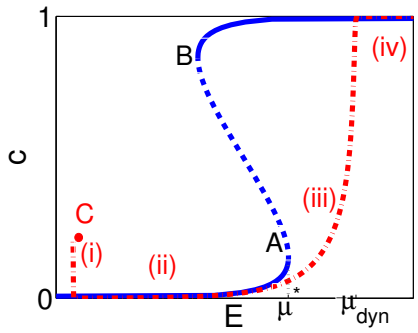


Figure 2.4: The red curve illustrates the dynamics of the initial-value problem (2.18) with $\epsilon = 0.25$, $c_0 = 0.2$, and $t_0 = -3$, while the blue curve shows the equilibria of the system with static E. As described in the asymptotic analysis, the solution trajectory can be divided into four stages: two fast transition stages (i), (iii) and two slow stages (ii), (iv). Comparison with the equilibrium plot in blue suggests a delay when $E(t)$ passes the saddle-node bifurcation at μ^* at a rate of $\mathrm{d}E/\mathrm{d}t = 1$. For smaller values of ϵ, the transitions occur much faster.

2.3.1.1 Initial transition to lower branch (i)

We assume that the initial lithium concentration, c_0, is order 1 in size. Because the initial voltage, E is well below μ^*, we expect the lithium concentration to decrease rapidly to the lower stable branch s_{I} in the earliest stage of the lithiation dynamics. We will show this stage is exponentially fast and can be divided into four sub-stages, (ia), (ib), (ic), and (id).

Initial transition (ia) In a tiny neighbourhood around the initial time $-t_0$, c decreases but is still $\mathcal{O}(1)$. Therefore, $(-t_0 + 2c)/\epsilon < (-t_0 + 2c_0)/\epsilon$ will be large and negative, and hence the positive term on the right-hand side of (2.18) is exponentially small, while the negative term is exponentially large. This means that the leading-order dynamics will be given by

$$\frac{\mathrm{d}c}{\mathrm{d}t} = -\frac{1}{2}\left(\frac{c}{1-c}\right)^{1/2} \exp\left[\frac{t_0 - 2c + \mathcal{O}(\tilde{t}_0)}{2\epsilon}\right] + \text{e.s.t}, \tag{2.19}$$

where $\tilde{t}_0$ is the width of this exponentially tiny neighbourhood and e.s.t means exponentially small term. Balance of leading terms indicates

$$\tilde{t}_0 = 2\epsilon(1-c_0)^{1/2} c_0^{-1/2} e^{\frac{-t_0+2c_0}{2\epsilon}}. \tag{2.20}$$

Meanwhile, preliminary analysis suggests that due to the exponentially large term in (2.19), a nonlinear scaling is needed in the time variable t. To work out the

appropriate nonlinear scaling, we first present a tentative scaling, assuming a linear scaling in t.

Tentative scaling We first pose a tentative scaling of

$$c = c_0 + \epsilon \bar{c}_a, \qquad t = -t_0 + \tilde{t}_0 \bar{t}_a, \tag{2.21}$$

where $\bar{t}_a$ is the local time variable. This gives the leading order equation

$$\frac{\mathrm{d}\bar{c}_a}{\mathrm{d}\bar{t}_a} = -e^{-\bar{c}_a}. \tag{2.22}$$

Solving this subject to $\bar{c}_a = 0$ when $\bar{t}_a = 0$ gives

$$\bar{c}_a = -\log(1 - \bar{t}_a), \tag{2.23}$$

which predicts finite time blow up as $\bar{t}_a \uparrow 1$.

Updated scaling Equation (2.23) implies that $\bar{c}_a$ explodes as $\bar{t}_a \uparrow 1$, or $t \uparrow -t_0 + \tilde{t}_0$. The way $\bar{c}_a$ blows up motivates us to keep $c \sim \mathcal{O}(1)$, but introduce a new scaling in t :

$$t = -t_0 + \tilde{t}_0(1 - e^{-t_a/\epsilon}), \qquad t_a \geq 0, \tag{2.24}$$

where t_a is the local time variable. With the new scaling, the leading order dynamics becomes

$$\frac{\mathrm{d}c}{\mathrm{d}t_a} = -\frac{1}{2}\left(\frac{1-c_0}{c_0}\right)^{1/2}\left(\frac{c}{1-c}\right)^{1/2} \exp\left[\frac{c_0 - c - t_a + \mathcal{O}(\tilde{t}_0)}{\epsilon}\right] + \text{e.s.t}, \tag{2.25}$$

so the leading order solution is

$$c = c_0 - t_a + \mathcal{O}(\epsilon). \tag{2.26}$$

Therefore c goes down linearly with t_a provided $t_a < c_0$.

When $t_a \to c_0$, namely $t \to -t_0 + \tilde{t}_0(1 - e^{-c_0/\epsilon})$, we see that c approaches zero, and we need to rescale the problem. To find the scaling of the next stage, we expand (2.26) to the next order by

$$c = c_0 - t_a + \epsilon \hat{c}_a + \mathcal{O}(\epsilon^2), \tag{2.27}$$

and substitute (2.27) into (2.19) to get

$$c = c_0 - t_a + \epsilon\left(\frac{c_0}{1-c_0}\right)^{1/2}\left(\frac{1-c_0+t_a}{c_0-t_a}\right)^{1/2} + \mathcal{O}(\epsilon^2), \tag{2.28}$$

which suggests that the leading order expansion breaks down when $c_0 - t_a \sim \mathcal{O}(\epsilon^{2/3})$.

Initial transition (ib) The new balance when solution (2.26) breaks down suggests us to rescale the problem by

$$c = \epsilon^{2/3} c_b, \qquad t = -t_0 + \tilde{t}_0 - 2(1-c_0)^{1/2} c_0^{-1/2} \epsilon^{2/3} e^{-t_0/2\epsilon} e^{t_b/\epsilon^{1/3}}, \tag{2.29}$$

where t_b is the local time variable, to get the leading order equation

$$\frac{\mathrm{d}c_b}{\mathrm{d}t_b} = \sqrt{c_b} \exp\left[\frac{t_b - c_b + \text{e.s.t}}{\epsilon^{1/3}}\right] + \text{e.s.t.} \tag{2.30}$$

and the asymptotic solution

$$c_b = t_b + \frac{\epsilon^{1/3}}{2}\left(\log t_b + \log\frac{1-c_0}{c_0}\right) + \mathcal{O}(\epsilon^{2/3}). \tag{2.31}$$

In this stage, as t increases, t_b decreases. It can be shown that (2.31) agrees with the stage (ia) solution to the leading order as $t_b \to \infty$, and it breaks down as $t_b \to 0$.

Initial transition (ic) As $t_b \to 0$, we rescale the problem by

$$c = \epsilon c_c, \qquad t = -t_0 + \tilde{t}_0 + 2\epsilon^{1/2} e^{-t_0/2\epsilon} t_c, \tag{2.32}$$

where t_c is the local time variable. The leading order dynamics is

$$\frac{\mathrm{d}c_c}{\mathrm{d}t_c} \sim -\sqrt{c_c} \exp\left(-c_c\right), \tag{2.33}$$

which is integrated to give

$$e^{c_c} D_+(\sqrt{c_c}) \sim -\frac{t_c - t_c^0}{2}, \tag{2.34}$$

where $D_+(x) = e^{-x^2}\int_0^x e^{t^2}\mathrm{d}t$ is the Dawson function and t_c^0 is the integration constant. To determine t_c^0, we substitute $c_b = \epsilon^{1/3} c_c$ and $t_b = -\epsilon^{1/3}\log(-t_c) + \frac{1}{2}\epsilon^{1/3}\log\epsilon^{1/3}$ into (2.34), exploit the asymptotics of the Dawson integral that $D_+(x) \approx 1/(2x)$ when x is large, and match with the stage (ib) solution (2.31) to get

$$t_c^0 = 0. \tag{2.35}$$

We plot the solution in Fig. 2.5 to show how c_c decays to 0 as t_c approaches 0.

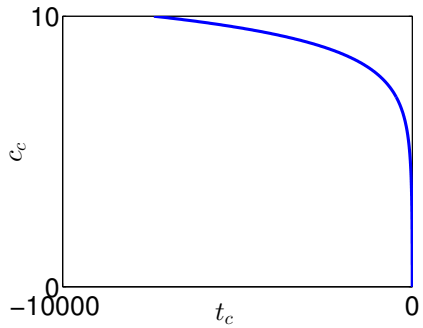


Figure 2.5: Plot of the sub-stage (ic) solution (2.34) with $t_c^0 = 0$.

When $c_c \to 0$, $D_+(\sqrt{c_c}) \approx \sqrt{c_c}$, therefore we find the asymptotics for c_c approaching 0 as

$$c_c \sim \frac{t_c^2}{4}, \qquad t_c \to 0. \tag{2.36}$$

When c_c shrinks further, the positive term in the full dynamics equation (2.18) becomes non-negligible, and we need to rescale the problem to reflect the contribution of the positive term.

Initial transition (id) When both positive term and negative term of the dynamics are of similar size, we choose

$$c = e^{-t_0/\epsilon} c_d, \qquad t = -t_0 + \tilde{t}_0 + e^{-t_0/\epsilon} t_d, \tag{2.37}$$

where t_d is the local time variable, to get the leading order equation

$$\frac{\mathrm{d}c_d}{\mathrm{d}t_d} \sim \frac{1}{2\sqrt{c_d}} - \frac{1}{2}\sqrt{c_d}. \tag{2.38}$$

The solution can be written as

$$\log[(1+\sqrt{c_d})/(1-\sqrt{c_d})] - 2\sqrt{c_d} \sim \frac{1}{2}(t_d + t_d^0), \tag{2.39}$$

and the integration constant can be found to be $t_d^0 = 0$ by matching with (2.36) when $c_d \to \infty$. We plot the solution in the right panel of Fig. 2.6 and see that c_d decays to 1 as t_d increases.

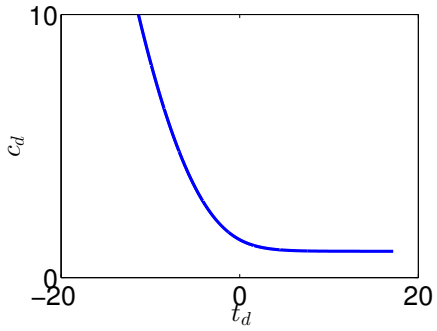


Figure 2.6: Plot of the sub-stage (id) solution (2.39) with $t_d^0 = 0$.

When $c = O\left(\mathrm{e}^{-t_0/\epsilon}\right)$, the positive term in (2.18) becomes important, and prevents c from reaching zero. Instead, we find that the solution rapidly attains a quasi-equilibrium, where the positive and negative terms in (2.18) balance, over a timescale where $t = -t_0 + \tilde{t}_0 + O\left(\mathrm{e}^{-t_0/\epsilon}\right)$. In summary, regardless of the initial conditions, c undergoes an extremely rapid transition (over an exponentially small timescale) and joins the slow-varying stable branch s_{I}.

2.3.1.2 Lower stable branch solution (ii)

Now c is exponentially small and, up to exponentially small correction terms, (2.18) becomes

$$\frac{\mathrm{d}c}{\mathrm{d}t} \sim \frac{\mathrm{e}^{t/2\epsilon}}{2\sqrt{c}} - \frac{\sqrt{c}\,\mathrm{e}^{-t/2\epsilon}}{2}. \tag{2.40}$$

The leading order solution to this equation is

$$c \sim \mathrm{e}^{t/\epsilon} \qquad (t < 0). \tag{2.41}$$

To find higher corrections, we introduce the expansion

$$c \sim \mathrm{e}^{t/\epsilon}\left(1 + \tilde{c}_1(t) + \tilde{c}_2(t) + \tilde{c}_3(t) + \cdots\right) \tag{2.42}$$

where $1 \gg \tilde{c}_1(t) \gg \tilde{c}_2(t) \ldots$. Substituting

$$\sqrt{c} \sim \mathrm{e}^{t/(2\epsilon)}\left(1 + \frac{1}{2}\tilde{c}_1(t) + \frac{1}{2}\tilde{c}_2(t) + \cdots\right), \tag{2.43a}$$

$$\frac{1}{\sqrt{c}} \sim \mathrm{e}^{-t/(2\epsilon)}\left(1 - \frac{1}{2}\tilde{c}_1(t) - \frac{1}{2}\tilde{c}_2(t) - \cdots\right), \tag{2.43b}$$

into (2.40),

$$\frac{\mathrm{d}}{\mathrm{d}t}\left(\mathrm{e}^{t/\epsilon}\right) + \frac{\mathrm{d}}{\mathrm{d}t}\left(\mathrm{e}^{t/\epsilon}\tilde{c}_1(t)\right) + \frac{\mathrm{d}}{\mathrm{d}t}\left(\mathrm{e}^{t/\epsilon}\tilde{c}_2(t)\right) + \cdots = -\frac{1}{2}\left(\tilde{c}_1(t) + \tilde{c}_2(t) + \tilde{c}_3(t) + \cdots\right). \tag{2.44}$$

Matching at each order gives

$$\tilde{c}_1(t) = -\frac{2}{\epsilon}\mathrm{e}^{t/\epsilon}, \quad \tilde{c}_2(t) = \frac{8}{\epsilon^2}\mathrm{e}^{2t/\epsilon}, \quad \cdots \tag{2.45}$$

i.e.

$$c \sim \mathrm{e}^{t/\epsilon} - \frac{2}{\epsilon}\mathrm{e}^{2t/\epsilon} + \frac{8}{\epsilon^2}\mathrm{e}^{3t/\epsilon} + O\left(\mathrm{e}^{4t/\epsilon}\right) \qquad (t < 0). \tag{2.46}$$

Equation (2.46) predicts slow evolution along the lower stable branch s_{I}. Note that the solution has ceased to depend on the values of t_0 and c_0, and so the initial conditions will have no effect (to leading order) on the solution in stages (iii) and (iv).

The second term in (2.46) will be small compared to the first term while $\mathrm{e}^{t/\epsilon} \ll \epsilon$, meaning that (2.46) can only be a valid asymptotic expansion while this condition holds. Once $\mathrm{e}^{t/\epsilon}$ and ϵ are the same order, we will need to introduce a new rescaling and apply the method of matched asymptotics.

Thus, we find that the next stage occurs when $t = -\epsilon\log\big(1/\epsilon\big) + \mathcal{O}(\epsilon)$, and hence the two terms in (2.46) are balanced. This is consistent with our expectations based on the equilibrium analysis in Section 2.2, where a jump in concentration at $t = -\epsilon\log\big(2/\epsilon\big) - \epsilon$ is predicted from equation (2.15).

2.3.1.3 Jump stage (iii)

As t approaches $\mathcal{O}(\epsilon)$, the positive term begins to outweigh the negative term, so that c jumps from the lower stable branch to the higher stable branch. This jump process is analogous to transition (i), and we divide it into sub-stages (iiia), (iiib), (iiic), and (iiid).

Jump solution (iiia) To show how c exits the lower branch, we perform the scalings

$$c = \epsilon x, \qquad t = -\epsilon \log\bigl(1/\epsilon\bigr) + \epsilon\tau. \tag{2.47}$$

The leading-order dynamics in this regime is governed by the canonical equation

$$\frac{\mathrm{d}x}{\mathrm{d}\tau} = \frac{1}{2\sqrt{x}}\,\mathrm{e}^{\tau/2+x} - \frac{\sqrt{x}}{2}\,\mathrm{e}^{-\tau/2-x} = \sinh\left(\frac{\tau}{2} + x - \frac{1}{2}\log(x)\right), \tag{2.48a}$$

subject to the matching condition

$$x(\tau) \sim \mathrm{e}^{\tau} - 2\mathrm{e}^{2\tau} + \cdots \quad \text{as } \tau \to -\infty, \tag{2.48b}$$

obtained from (2.46). Equation (2.48a) needs to be solved numerically once and for all.

The numerical solution $x(\tau)$ of the initial value problem (2.48) is plotted in Fig. 2.7. The solution blows up at a finite value of $\tau = \tau^*$, where the local behaviour is

$$2\sqrt{x(\tau)}\,\mathrm{e}^{-x(\tau)} \sim \mathrm{e}^{\tau^*/2}\,(\tau^* - \tau) \quad \text{as } \tau \to \tau^*. \tag{2.49}$$

The dashed curve in Fig. 2.7 demonstrates that this approximation indeed describes the behaviour near $\tau = \tau^*$, and by fitting we find that $\tau^* \approx 0.81498$.

Jump solution (iiib) The local blow-up asymptotics (2.49) implies that $c = \mathcal{O}(1)$ in the next phase, where we rescale t according to

$$t = -\epsilon \log\bigl(1/\epsilon\bigr) + \epsilon\tau^* - 2\sqrt{\epsilon}\,\mathrm{e}^{-\tau^*/2}\mathrm{e}^{-\hat{\tau}/\epsilon}, \tag{2.50}$$

where the local time variable $\hat{\tau} = \mathcal{O}(1)$. Now the positive term in (2.18) dominates, giving the leading order dynamics

$$\frac{\mathrm{d}c}{\mathrm{d}\hat{\tau}} = \sqrt{\frac{1-c}{c}}\,\exp\left(\frac{c-\hat{\tau}}{\epsilon}\right) \tag{2.51}$$

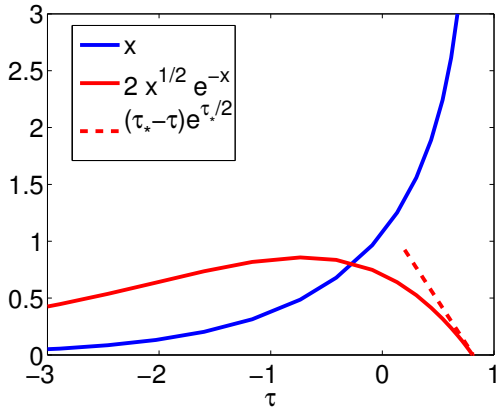


Figure 2.7: Numerical solution of the initial-value problem (2.48). The three curves show the scaled concentration $x(\tau)$, the function $2\sqrt{x(\tau)}\,\mathrm{e}^{-x(\tau)}$ and the linear fit (2.49).

up to exponentially small corrections. The solution of (2.51) that matches with (2.49) as $c \to 0$ is

$$c = \hat{\tau} + \frac{\epsilon}{2} \log\left(\frac{\hat{\tau}}{1-\hat{\tau}}\right) + \mathcal{O}(\epsilon^2). \tag{2.52}$$

The approximation (2.52) breaks down as $\hat{\tau} \to 1$, implying that c increases from $\mathcal{O}(\epsilon)$ to $1 - \mathcal{O}(\epsilon)$ exponentially rapidly as t approaches $-\epsilon \log\big(1/\epsilon\big) + \epsilon\tau^*$.

Jump solution (iiic) The remaining stages of c joining the upper stable branch are similar to when it approaches the lower stable branch in stage (ic) and (id). Here we only present the main results and leave out any details.

In (iiic), we rescale with

$$c = 1 - \epsilon y_c, \qquad t = -\epsilon \log\frac{1}{\epsilon} + \epsilon\tau^* + 2e^{-\tau^*/2} e^{-\frac{1}{\epsilon}} \tau_c, \tag{2.53}$$

where τ_c is the local time variable, to get the leading order solution

$$e^{y_c} D_+(\sqrt{y_c}) \sim -\frac{\tau_c}{2}. \tag{2.54}$$

Therefore y_c decreases exactly in the same way as c_c in stage (ic). We can refer to the left panel of Fig. 2.5 to understand how $1 - c$ decreases from $\mathcal{O}(\epsilon)$ to $o(\epsilon)$.

Jump solution (iiid) Similar to stage (id), we scale with

$$c = 1 - \frac{1}{\epsilon} e^{-2/\epsilon} e^{-\tau^*} y_d, \qquad t = -\epsilon \log\frac{1}{\epsilon} + \epsilon\tau^* + \frac{1}{\epsilon} e^{-\tau^*} e^{-\frac{2}{\epsilon}} \tau_d, \tag{2.55}$$

where τ_d is the local time variable, to get

$$\log[(1+\sqrt{y_d})/(1-\sqrt{y_d})] - 2\sqrt{y_d} \sim \frac{\tau_d}{2}. \tag{2.56}$$

Again this is identical to the stage (id) solution (2.39) and predicts how y_d decays to 1 as $\tau_d \to +\infty$, and c joins the upper stable branch s_{III}.

Combing stages (iiia) to (iiid), we see that c jumps c_I to s_{III} exponentially quickly around $t \sim -\epsilon \log \frac{1}{\epsilon} + \epsilon\tau^*$.

2.3.1.4 Upper stable branch solution (iv)

Now c stays on the upper stable branch s_{III} as E increases further. A similar procedure to Section 2.3.1.2 finds its asymptotic behaviour as

$$c = 1 - e^{-(t+2)/\epsilon} + \frac{2}{\epsilon}e^{-2(t+2)/\epsilon} + \frac{8}{\epsilon^2}e^{-3(t+2)/\epsilon} + \mathcal{O}(e^{-4(t+2)/\epsilon}). \tag{2.57}$$

2.3.1.5 Summary

Putting the various stages together, we have a complete leading-order description of the solution to the initial value problem (2.18). It reveals that an effectively instantaneous transition happens as E passes through a critical value

$$\mu_{\mathrm{dyn}} = 1 + \epsilon\tau^* - \epsilon \log\bigl(1/\epsilon\bigr). \tag{2.58}$$

Comparing this with the expression (2.15) for the equilibrium turning point μ^*, we see that dynamics delays the bifurcation by a distance

$$\mu_{\mathrm{dyn}} - \mu^* = \epsilon(1 + \log 2 + \tau^*) \approx 2.51\epsilon. \tag{2.59}$$

This delay is universal and applies to any initial condition that is within the attractor of the lower stable branch.

The canonical equation (2.48a) describes the key stage in the transition where the solution departs from the lower stable branch. A "once and for all" numerical calculation determines the local blow-up time τ^*, which is the only information that feeds into the global solution.

2.3.2 Consolidation by numerics

In Section 2.3, we analysed the matched asymptotic solution to the initial value problem (2.18). Now we consolidate it by a stage-to-stage comparison with the numerical solution. To compute the numerical solution in each stage, we use the asymptotic

solution from the end of the previous stage as the initial condition and solve the full equation (2.18) with Matlab **ODE23s**.

Figure 2.8 examines the four sub-stages of the initial transition stage (i), where c joins the stable manifold s_{I} from its initial position. The two solutions are in good agreement. First, the asymptotics correctly predicts the transition timescale. In numerics, c goes down to near zero at around $t + t_0 = 1.24 \times 10^{-4}$, which is very close to the asymptotic prediction $\tilde{t}_0 = 1.17 \times 10^{-4}$. Second, the asymptotics also works well in sub-stages (ia), (ic), and (id), although the two solutions are displaced by a small amount. This is due to the initial value we choose in each substage when computing the numerical results. Since $\epsilon = 0.05$ is not infinitesimal, the stages do not necessarily match exactly, and if we impose the same initial condition for the numerical problem as the asymptotic solution, the two solutions match very well in each sub-stage.

On the other hand, the discrepancy is most obvious in stage (ib) and in the end of stage (ia). This can be explained by the relatively large value of $\epsilon^{2/3}$, which is 0.14 in this example.

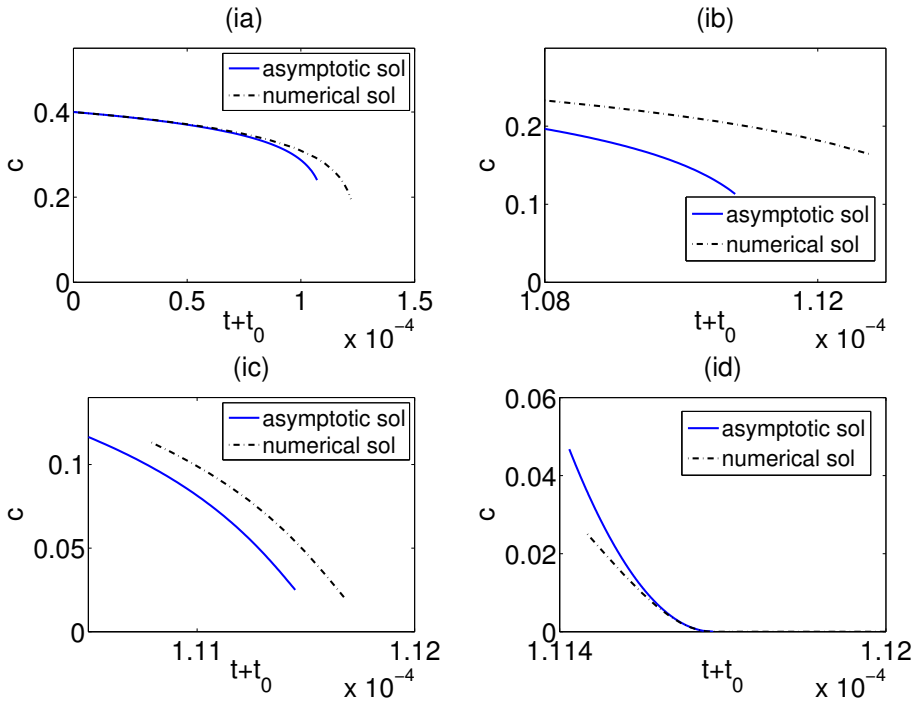


Figure 2.8: Comparison between the asymptotic solution and the numerical solution of the four sub-stages (ia-ib) analysed in Section 2.3.1.1. In both the numerics and the asymptotics we use $\epsilon = 0.05$, $t_0 = 1.5$ and $c_0 = 0.4$.

Figure 2.9 illustrates the stage (ii) comparison when c is on the slow varying

branch. Both the left and right panels plot the evolution of $c(t)$, but the right panel uses a log-scale. As can be seen, the two solutions agree well until $t \sim \mathcal{O}(\epsilon)$.

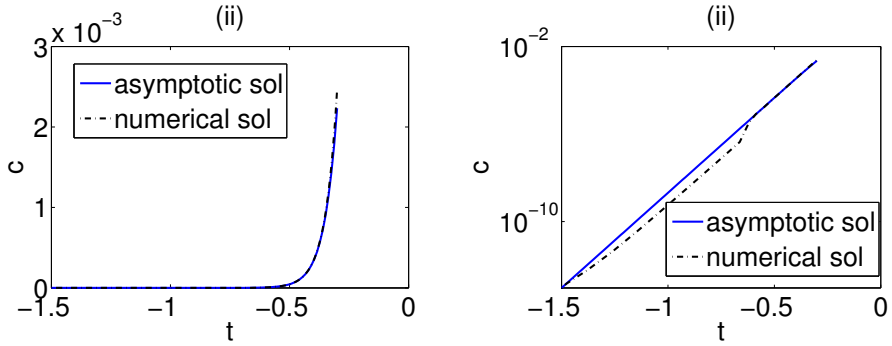


Figure 2.9: Comparison between the asymptotic solution and the numerical solution in stage (ii), which is analysed in Section 2.3.1.2. Parameter values are $\epsilon = 0.05$, $t_0 = 1.5$ and $c_0 = 0.4$.

Figure 2.10 shows a comparison of the jump stage (iii), when c jumps from near-0 to near-1. In the upper left panel is the jump solution (iiia). Because we do not have an analytical solution to this stage, what we compare is numerics of the scaled problem (2.48a) against that of the full problem (2.18). A major difference is that in the scaled problem we do not include the $\epsilon \log(1-c)$ term, so the scaled solution grows unboundedly.

Stage (iiib-iiid) can be explained similarly to (ib-id) and we see that in this region the asymptotic solution works well. The only difference is that in (iiib) the initial condition of the numerics is set to be the same as the asymptotics, as there is no asymptotic solution available from (iiia).

In general we find good agreement in the comparison, in spite of the relative largeness of ϵ (and $\epsilon^{1/3}$). Even with the initial discrepancy in each stage, the two solutions always converge in the end of each stage, thus consolidating our matched asymptotic analysis.

2.4 Discussions

2.4.1 Non-constant exchange current

In this section we discuss the effects of relaxing the assumptions of constant exchange current. The analysis is identical to previous sections, so we do not repeat the details here and just present the main results.

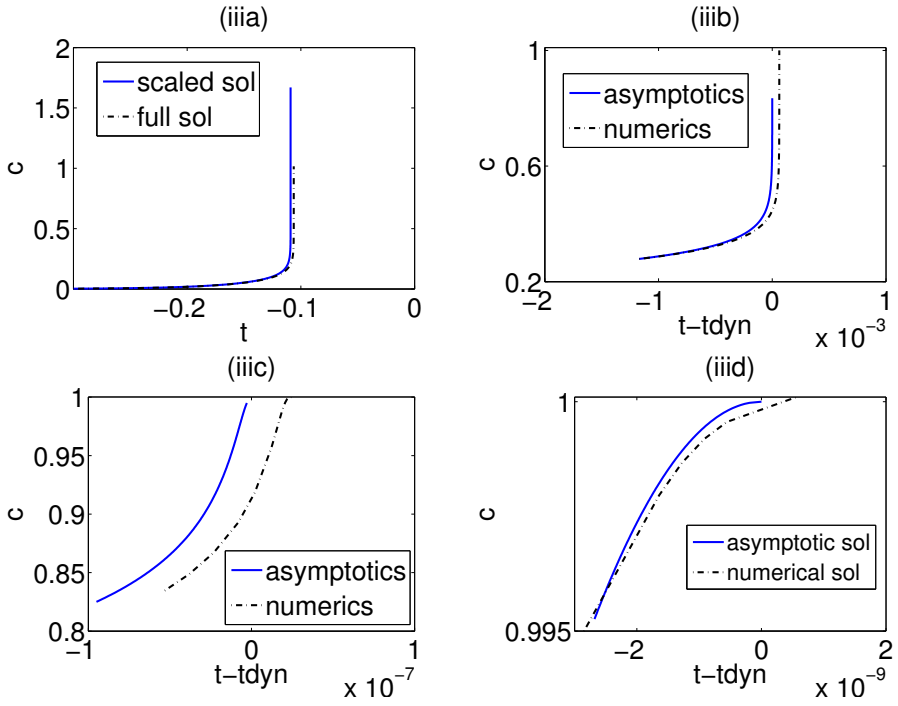


Figure 2.10: Comparison between the asymptotic solution and the numerical solution of the substages (iiia-iiid) in Section 2.3.1.3. Parameter values are $\epsilon = 0.05$, $t_0 = 1.5$ and $c_0 = 0.4$, and $t_{dyn} = -\epsilon \log \frac{1}{\epsilon} + \epsilon\tau^*$.

As an example consider a simple but widely used model (after appropriate scaling) of $I_0(c) = c^{1/2}(1-c)^{1/2}$ [7]. The dimensionless deterministic model (2.9) becomes

$$\begin{aligned}\frac{\mathrm{d}c}{\mathrm{d}t} &= I_0(c)\sinh\left(\frac{E-\mu(c)}{2\epsilon}\right)\\ &= \frac{1}{2}(1-c)\exp\left(\frac{E-1+2c}{2\epsilon}\right) - \frac{1}{2}c\exp\left(-\frac{E-1+2c}{2\epsilon}\right).\end{aligned} \tag{2.60}$$

The equilibria are the same as in Section 2.2, and we still expect the out-of-equilibrium dynamics to experience slow evolution along the stable branches and exponentially fast transitions between them as in Section 2.3.

The major difference from the constant I_0 model occurs in the jump regime in which $E-1 = \mathcal{O}(\epsilon)$ and $c = \mathcal{O}(\epsilon)$. In this regime the positive term on the right-hand side of (2.60) dominates the negative term, so the local jump dynamics is analytically solvable, unlike Section 2.3.1.3, where a numerical solution was required. It can be shown that in this case the jump happens when $t = o(\epsilon)$.

More generally, suppose that $I_0 \propto c^{\theta}(1-c)^{1-\theta}$. Simple calculations reveal that we need $\theta \geq 1/2$ to have the positive flux dominate in the jump regime as above. If we further specify $1/2 \leq \theta \leq 3/2$, then the delay in the dynamic transition time can be

expressed as

$$\frac{\mu_{\text{dyn}} - \mu^*}{\epsilon} = -2\theta \log \epsilon + 1 + 2\log\big(\Gamma(3/2 - \theta)\big) + \log 2, \tag{2.61}$$

where Γ is the Gamma function. This should be compared with the constant-I_0 prediction (2.59).

We plot the prediction (2.61) of the delay versus numerical results under different values of θ in Fig. 2.11. The asymptotics agree well with the numerics for $\epsilon \lesssim 0.1$ and do not deviate much for larger values of ϵ. In general, a larger value of θ induces a longer delay, as expected physically since increasing θ decreases the forward current around $E \approx 1$ and therefore postpones the transition.

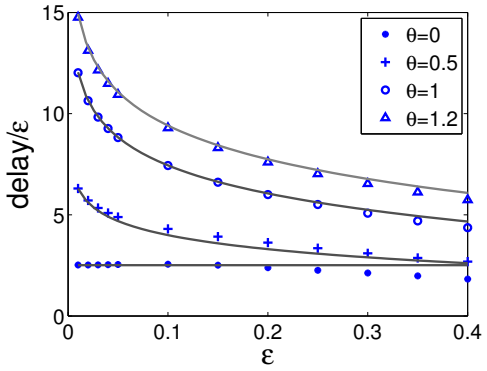


Figure 2.11: The scaled transition delay $(\mu_{\text{dyn}} - \mu^*)/\epsilon$ plotted versus ϵ for different values of θ. The gray curves show the prediction (2.61) of the asymptotic analysis. The blue markers show values obtained by solving the corresponding initial-value problem numerically, where the transition time is identified as the time when c reaches $1/2$.

2.4.2 The effect of charging speed

In Section 2.3, we studied the dynamics of lithiation of a single-compartment, and considered the specific charging rate where $E = 1 + \kappa t$ and $\kappa = 1$ as a canonical example. In real-life charging/discharging, κ is generally of order $\mathcal{O}(1)$, and here we show that varying κ does not alter the qualitative dynamics of the problem provided $\kappa = \mathcal{O}(1)$.

Given $E = 1 + \kappa t$, the governing ODE (2.9) becomes

$$\frac{\mathrm{d}c}{\mathrm{d}t} = \frac{1}{2}\sqrt{\frac{1-c}{c}}\exp\left(\frac{\kappa t + 2c}{2\epsilon}\right) - \frac{1}{2}\sqrt{\frac{c}{1-c}}\exp\left(-\frac{\kappa t + 2c}{2\epsilon}\right). \tag{2.62}$$

As in the $\kappa = 1$ case, the essential stage in the transition occurs around $E = 1 + \mathcal{O}(\epsilon)$ and $c = \mathcal{O}(\epsilon)$. Before and after this stage, c follows the slow-varying stable branches. In the critical region, we rescale the problem by

$$t = \frac{1}{\kappa}\left(\epsilon \log \epsilon + \epsilon\tau'\right), \qquad c = \epsilon x,$$

which gives the leading order dynamics

$$\kappa \frac{\mathrm{d}x}{\mathrm{d}\tau'} \sim \left(\frac{1}{2\sqrt{x}} e^{\tau'/2+x} - \frac{\sqrt{x}}{2} e^{-\tau'/2-x}\right). \tag{2.63}$$

This is similar to (2.48a) except for a multiplying factor κ on the left-hand side. The blow-up time is a numerically determined function of κ, which we denote as $\tau^*(\kappa)$.

We show the solution trajectories for various κ in Fig. 2.12. Clearly, $\tau^*(\kappa)$ is a monotonically increasing function of κ. As κ increases, the blow-up time is further delayed compared to the equilibrium transition point.

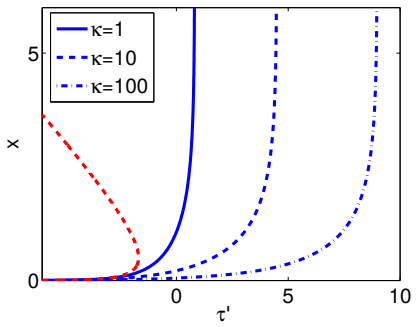


Figure 2.12: Blue curves plot the dynamic trajectories under various fast charging rates by numerically solving (2.63) with Matlab **ODE23tb**, assuming initially $\tau_0 = -10$ and c_0 makes the right-hand side of (2.63) zero. The red dashed curve plots the nullcline of equation (2.63).

In terms of potential, the dynamic transition happens at a numerically determined function $\mu_{\mathrm{dyn}}(\kappa)$ that satisfies

$$\mu_{\mathrm{dyn}}(\kappa) - \mu^* = \epsilon\left(1 + \log 2 + \tau^*(\kappa)\right). \tag{2.64}$$

Therefore, as long as $\kappa = \mathcal{O}(1)$, we expect the dynamic transition voltage $\mu_{\mathrm{dyn}}(\kappa)$ to remain $\mathcal{O}(\epsilon)$ larger than the static transition voltage μ^*. The monotonic increasing $\tau^*(\kappa)$ indicates that at very high charging rate, the dynamic transition might happen at a significantly larger voltage than μ^*. Meanwhile, we expect the dynamic transition voltage $\mu_{\mathrm{dyn}}(\kappa)$ to approach the static transition voltage μ^* in the slow charging limit of $\kappa \downarrow 0$.

2.4.3 The nonlinear rescaling

In finding the asymptotic solutions for the lithiation process in Section 2.3, we introduced nonlinear scalings in the t variable in stages (ia), (ib) and (iiib). In the three stages, the concentration c equals $\mathcal{O}(1)$, $\mathcal{O}(\epsilon^{2/3})$, and $\mathcal{O}(1)$ respectively, and is not close to 0 or 1. In contrast, we used linear scalings in t in all other stages, where c is either near 0 or 1. This is in line with the exponential term in the Butler–Volmer equation: when c is away from 0 or 1 by an amount larger than $\mathcal{O}(\epsilon)$, $\mu(c)$ is approximately linear in c, and in turn $\mathrm{d}c/\mathrm{d}t$ is proportional to $e^{\pm c/\epsilon}$, hence leading to the nonlinear scaling in time.

The nonlinear scaling is an example of the delicacy introduced by the highly nonlinear surface reaction rate.

2.5 Summary

In this chapter and the next chapter, we develop mathematical models for the lithiation/delithiation process of a single compartment. This model features a homogeneous lithium concentration of the compartment, with the dynamics of the concentration governed by the Butler–Volmer equation. This enables us to identify the effect of the nonlinear relation between the control voltage and the change in the lithium concentration.

We take the approach of representing the lithium concentration in a single compartment by a continuum variable that behaves as a deterministic function of time. In the physically relevant limit where $\epsilon = k_{\mathrm{B}}T/\Omega \ll 1$ (and so it is energetically very favourable for the compartment to be either empty or full), the governing ODE is stiff, and its solutions exhibit slow quasi-equilibrium dynamics with fast transitions between equilibria.

We analyse the dynamics of this model using perturbation methods, and show that the lithiation/delithiation process causes the compartment to jump from being near-empty to near-full very abruptly. From our equilibrium analysis, we see that there is a bifurcation associated with a critical voltage where the near-empty steady state will cease to exist. Similarly, the dynamic model reveals a critical voltage where the compartment will suddenly jump from being near-empty to being near-full as the voltage is increased. These two critical voltages are similar, but the critical voltage associated with the dynamic model occurs slightly later than the bifurcation value revealed using a static analysis.

To determine whether this solution structure is robust to discrete effects and thermal fluctuations, we will consider a stochastic model for the probability distribution of the concentration of lithium in a single compartment in the next chapter.

Chapter 3

A stochastic model for a single compartment

There are several issues arising from the deterministic model analysed in Chapter 2. First, it is known that thermal fluctuations in chemical reactions often cannot be ignored [20], but such effects are assumed to be negligible in (2.18). The validity of this assumption should depend on the number of lithium ions each compartment can host, as well as the temperature. When the number of lithium ions is relatively small, thermal fluctuations involving the addition or removal of a small number of lithium ions could have a significant impact. This indicates a second important problem to consider, namely the discreteness of the system. It remains unclear whether it is reasonable to describe the concentration using the continuous function $c(t)$, or whether there is a size limit below which we should switch from a continuum model to a discrete model.

To address both of these issues, we now develop a stochastic model under the framework of the chemical master equation. We treat the concentration $c(t)$ as a random variable in a state space; then randomness is described by its probability distribution, while the discreteness is reflected in the number of available states.

The analysis of the deterministic model carried out in Section 2.3 revealed the subtle asymptotic behaviour of the delayed transition between the two equilibria. Our aim now is to determine how these dynamics change in the presence of thermal noise and discreteness. We may expect both effects to have a profound influence on the asymptotic structure identified in Section 2.3 (involving, as it does, transitions that happen over exponentially small timescales or involving exponentially small concentrations), and possibly to destroy the asymptotic structure completely.

3.1 Model formulation

3.1.1 Chemical master equation

A natural state space to consider consists of the discrete concentration

$$c \in \{i\Delta C : i = 1, \ldots, N\}, \quad \Delta C = 1/(N+1)$$

to ensure that the completely empty and completely full states are never reached. Thus N represents the number of available states, or equivalently the total number of lithium ions that each compartment can accommodate. Smaller N means that discreteness is more likely to play a prominent role; we will show that the 'importance' of discreteness is best measured by the product $(N+1)\epsilon$.

The dynamics of lithiation is modelled by a standard one-step process [20], which assumes that i) the random variable $c(t)$ is only allowed to switch between adjacent states; ii) in small enough time Δt, it only jumps once, and the probability that it jumps more than once is $\mathcal{O}(\Delta t^2)$ [20]. We illustrate this in Fig. 3.1.

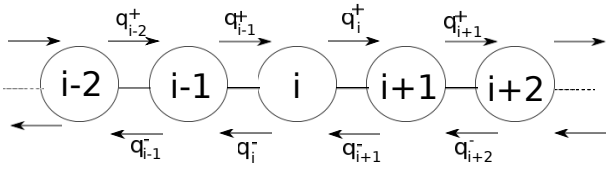


Figure 3.1: Illustration of an one-step process and the transition probabilities. Values inside the circles denote the states of the system, arrows denote the jumps that are allowed between the states, with transition probabilities labelled accordingly.

Let $p_i(t)$ denote the probability of the system being in state i at time t. The chemical master equation for p_i reads

$$\frac{\mathrm{d}p_i}{\mathrm{d}t} = q^+_{i-1}p_{i-1} - q^-_i p_i - q^+_i p_i + q^-_{i+1}p_{i+1}, \quad i = 2, \cdots, N-1 \tag{3.1a}$$

$$\frac{\mathrm{d}p_1}{\mathrm{d}t} = -q^+_1 p_1 + q^-_2 p_2, \tag{3.1b}$$

$$\frac{\mathrm{d}p_N}{\mathrm{d}t} = q^+_{N-1}p_{N-1} - q^-_N p_N, \tag{3.1c}$$

where $q^\pm_i$ denote the positive and negative transition probabilities from state i. Equivalently, (3.1) may be written in matrix form as

$$\frac{\mathrm{d}\mathbf{P}}{\mathrm{d}t} = \mathbb{W}\mathbf{P}, \tag{3.2}$$

where $\mathbf{P} = [p_1, \cdots, p_N]^T$ and the transition matrix $\mathbb{W}$ is tridiagonal:

$$\mathbb{W}_{ij} = \begin{cases} -(q_i^+ + q_i^-) & i = j, \\ q_{i+1}^-, & i - j = -1, \\ q_{i-1}^+, & i - j = 1, \end{cases} \tag{3.3}$$

or

$$\mathbb{W} = \begin{pmatrix} -q_1^+ & q_2^- & 0 & 0 & \cdots & 0 & 0 \\ q_1^+ & -q_2^+ - q_2^- & q_3^- & 0 & \cdots & 0 & 0 \\ 0 & q_2^+ & -q_3^+ - q_3^- & q_4^- & \cdots & 0 & 0 \\ 0 & 0 & \ddots & \ddots & \ddots & \vdots & \vdots \\ \vdots & \vdots & \vdots & \ddots & \ddots & \ddots & \vdots \\ 0 & 0 & \cdots & 0 & q_{N-2}^+ & -q_{N-1}^+ - q_{N-1}^- & q_N^- \\ 0 & 0 & 0 & \cdots & 0 & q_{N-1}^+ & -q_N^- \end{pmatrix}. \tag{3.4}$$

3.1.2 Transition probability

The process specified by equation (3.1) is Markovian, and its behaviour is uniquely determined by the transition matrix $\mathbb{W}$, or equivalently, the transition probabilities q_i^+ and q_i^-. To find appropriate expressions for q_i^+ and q_i^-, we consider the dynamics of the mean concentration and compare it with the deterministic Butler–Volmer model from Section 2.1.2.

The mean concentration

$$\bar{c}(t) = \sum_{i=1}^{N} p_i(t) c_i = \Delta C \sum_{i=1}^{N} i p_i \tag{3.5}$$

satisfies

$$\frac{\mathrm{d}\bar{c}(t)}{\mathrm{d}t} = \Delta C \sum_{i=1}^{N} i \frac{\mathrm{d}p_i(t)}{\mathrm{d}t}. \tag{3.6}$$

Substituting (3.1) into (3.6) and rearranging, we obtain

$$\frac{\mathrm{d}\bar{c}(t)}{\mathrm{d}t} = \Delta C \sum_{i=1}^{N} (q_i^+ - q_i^-) p_i(t). \tag{3.7}$$

In the deterministic limit where all the probability is concentrated in one state, $p_i(t) = \delta_{i,j}$ and $\bar{c}(t) = j\Delta C$, and hence

$$\frac{\mathrm{d}\bar{c}(t)}{\mathrm{d}t} = \Delta C (q_j^+ - q_j^-) = \Delta C (q^+(\bar{c}) - q^-(\bar{c})). \tag{3.8}$$

By comparison with the Butler–Volmer dynamics

$$\frac{\mathrm{d}\bar{c}(t)}{\mathrm{d}t} = \frac{1}{2}\exp\left[\frac{E-\mu(\bar{c})}{2\epsilon}\right] - \frac{1}{2}\exp\left[\frac{-E+\mu(\bar{c})}{2\epsilon}\right], \tag{3.9}$$

we choose

$$q_i^+ = \frac{1}{2\Delta C}\exp\left[\frac{1}{2\epsilon}\left(E - \frac{g_{i+1}-g_i}{\Delta C}\right)\right], \quad i = 1, \cdots, N-1 \tag{3.10a}$$

$$q_i^- = \frac{1}{2\Delta C}\exp\left[\frac{1}{2\epsilon}\left(-E + \frac{g_i-g_{i-1}}{\Delta C}\right)\right], \quad i = 2, \cdots, N \tag{3.10b}$$

where $g_i = g(c_i)$ is the chemical free energy associated with state i. (3.10) indicates that, for each i, $q_i^{\pm}$ depends on the associated change in energy when varying c_i by an amount of $\pm\Delta C$.

3.1.3 The Langevin equation

It is straightforward to find the Langevin equation from the chemical master equation. We can view the process as a one-dimensional asymmetric random walk on the state space with step size ΔC and time step Δt. If the random walk is in state i at time t_j, the mean and variance of the displacement after the next jump are

$$\mathrm{E}[C(t_j+\Delta t) - C(t_j)|C(t_j) = c_i] = \Delta C\left(\bar{P}_i^+ - \bar{P}_i^-\right), \tag{3.11}$$

$$\mathrm{Var}[C(t_j+\Delta t) - C(t_j)|C(t_j) = c_i] = \Delta C^2\left(\bar{P}_i^+ + \bar{P}_i^-\right), \tag{3.12}$$

where $\bar{P}_i^+$ and $\bar{P}_i^-$ are respectively the probabilities for a +1 jump and a -1 jump in time Δt. They are specified by the one-step process

$$\bar{P}_i^+ = q_i^+\Delta t + \mathcal{O}(\Delta t^2) \sim \frac{1}{2\Delta C}\exp\left[\frac{1}{2\epsilon}\left(E - \frac{g_{i+1}-g_i}{\Delta C}\right)\right]\Delta t, \tag{3.13a}$$

$$\bar{P}_i^- = q_i^-\Delta t + \mathcal{O}(\Delta t^2) \sim \frac{1}{2\Delta C}\exp\left[\frac{1}{2\epsilon}\left(-E + \frac{g_i-g_{i-1}}{\Delta C}\right)\right]\Delta t. \tag{3.13b}$$

Substitution into the mean and the variance (3.11) and (3.12) gives the Langevin equation

$$\begin{aligned}\Delta C(t_j) = &\frac{1}{2}\left(\exp\left[\frac{1}{2\epsilon}\left(E - \frac{g_{i+1}-g_i}{\Delta C}\right)\right] - \exp\left[\frac{1}{2\epsilon}\left(-E + \frac{g_i-g_{i-1}}{\Delta C}\right)\right]\right)\Delta t \\ &+\sqrt{\frac{\Delta C}{2}}\left\{\exp\left[\frac{1}{2\epsilon}\left(E - \frac{g_{i+1}-g_i}{\Delta C}\right)\right] + \exp\left[\frac{1}{2\epsilon}\left(-E + \frac{g_i-g_{i-1}}{\Delta C}\right)\right]\right\}^{1/2}\Delta L(t_j),\end{aligned} \tag{3.14}$$

where $\Delta C(t_j) = C(t_j + \Delta t) - C(t_j)$, and the fluctuating force $\Delta L(t)$ is a Brownian motion that satisfies $\mathrm{E}[\Delta L(t)] = 0$ and $\mathrm{Var}[\Delta L(t)] = \Delta t$ [20].

Therefore in the Langevin equation (3.14), the first term is the discrete version of the Butler–Volmer equation, and the second term gives an explicit formulae for random noise. Clearly the magnitude of the randomness is a function of which state the system is in, and is proportional to square root of ΔC.

The continuum limit of (3.14) is

$$dC_t = \sinh\left[\frac{1}{2\epsilon}\left(E - g'(C_t)\right)\right]dt + \sqrt{\frac{\Delta C}{2}}\left\{\cosh\left[\frac{1}{2\epsilon}\left(E - g'(C_t)\right)\right]\right\}^{1/2} dW_t, \quad (3.15)$$

which can be turned into a Fokker-Planck equation for the probability density $p(c,t)$ using the Feynman-Kac formula

$$\frac{\partial p}{\partial t} = -\frac{\partial}{\partial c}\left[\sinh\left(\frac{E - g'(c)}{2\epsilon}\right)p\right] + \frac{\Delta C}{2}\frac{\partial^2}{\partial c^2}\left[\cosh\left(\frac{E - g'(c)}{2\epsilon}\right)p\right]. \quad (3.16)$$

However, we will show in the next section that this form of the Fokker-Planck equation is valid when $\Delta C \ll \epsilon$. More importantly, it does not apply to boundary states that are close to full or empty, because a continuum limit of $(g_i - g_{i-1})/\Delta C$ does not exist near the boundaries due to stiffness of the double-well energy.

3.2 Stationary behaviour

In this section, we study the equilibrium distributions of the stochastic model developed in Section 3.1.1. First we will examine the stationary distribution according to the chemical master equation. Then we will simulate random walks using a constant value of E to show how the stationary distribution is approached in cases where that the initial distribution is not in equilibrium. The purpose of this analysis is to show that the equilibrium behaviour of the stochastic model can deviate greatly from the deterministic model, mainly because of the double well potential.

3.2.1 Equilibrium distribution

First, we examine the equilibrium distribution under a constant voltage E. Let p_i^{s} denote the probability for the system to be in state i in steady state. Since p_i^{s} stays constant, equation (3.1) reads

$$q_{i-1}^{+}p_{i-1}^{\mathrm{s}} - q_i^{-}p_i^{\mathrm{s}} = q_i^{+}p_i^{\mathrm{s}} - q_{i+1}^{-}p_{i+1}^{\mathrm{s}} = J, \quad (3.17)$$

where J is a constant. The no-flux boundary condition requires $J = 0$, and hence

$$p_i^{\mathrm{s}} = \frac{q_{i-1}^{+}}{q_i^{-}} p_{i-1}^{\mathrm{s}} = \exp\left[\frac{1}{\epsilon}\left(E - \frac{g_i - g_{i-1}}{\Delta C}\right)\right] p_{i-1}^{\mathrm{s}}, \qquad i = 2, \cdots, N. \tag{3.18}$$

By iteration,

$$p_i^{\mathrm{s}} = \exp\left[\frac{1}{\epsilon}\left((i-1)E - \frac{g_i - g_1}{\Delta C}\right)\right] p_1^{\mathrm{s}}, \tag{3.19}$$

where p_1^{s} is fixed by normalizing with $\sum_{i=1}^{N} p_i^{\mathrm{s}} = 1$.

Consequently, the stationary distribution can be viewed as a Boltzmann distribution, $p_i^{\mathrm{s}} \propto e^{-F_i/(k_B T)}$, where F_i is the energy of state i. To fit (3.19) into the Boltzmann expression, we rewrite it with $\epsilon = k_B T/\Omega$ and $c_i = i\Delta C$ to get

$$p_i^{\mathrm{s}} \propto \exp\left[-\frac{1}{k_B T}\left(\frac{\Omega}{\Delta C}(g_i - E c_i)\right)\right], \tag{3.20}$$

so that the dimensional energy of state i given constant potential E is

$$F_i = \frac{\Omega}{\Delta C}(g_i - c_i E). \tag{3.21}$$

Equation (3.21) simply states that the energy of any given state is the sum of its chemical energy g_i and the electrostatic energy $-c_i E$. Here a negative sign in $-c_i E$ is expected, since a positive E drives lithium ions from the electrolyte intercalating into the electrode and therefore corresponds to a lower energy in the electrode.

The exponential in the Boltzmann distribution means we are most interested in locating the energy minimum under different values of E. Since the state energy (3.21) is simply a double well energy plus a linearly increasing/decreasing term, it is clear that when E is near zero, the linear component is small so that the double well structure is retained and $f(c)$ still has two local minima. With nonzero E the symmetry is broken. This is illustrated in Fig. 3.2, where we show the dimensionless state energy $F(c) = g(c) - cE$, under $E = -0.1$, 0, and 0.1. In terms of probability distribution, this leads to a bimodal distribution. On the other hand, when E is far away from zero, the linear component in (3.21) dominates and hence $F(c)$ is monotonically increasing/decreasing, except for a very small region near the boundaries. In this case, the distribution is unimodal, and the concentration is a spike near the boundary states.

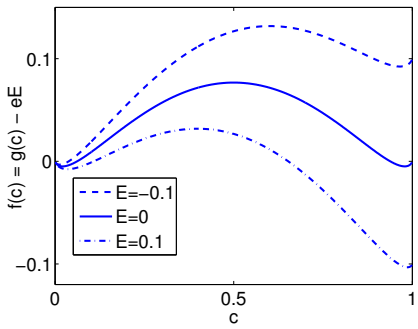
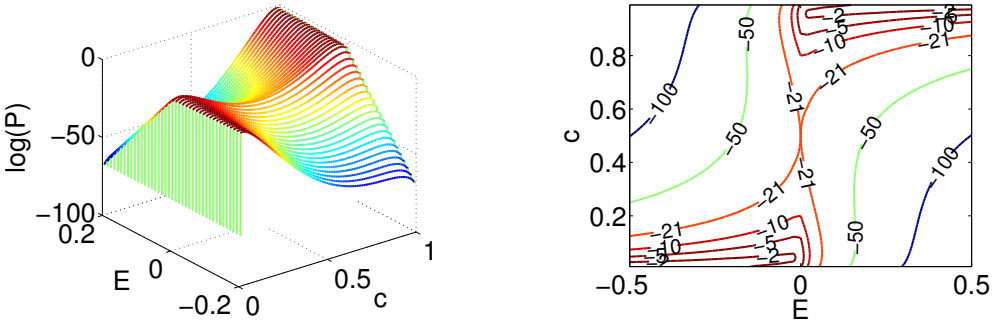


Figure 3.2: Plot of $F(c) = g(c) - cE$ as in (3.21), with $\epsilon = 0.25$.

The stationary distribution p_i^s is plotted versus $c = i\Delta C$ and E in Fig. 3.5. If E is far from 0, the distribution is strongly localised, so that the behaviour of the stochastic model appears close to deterministic. In contrast, when E is near 0, the distribution becomes bimodal, so the system is likely to be in high concentration states or low concentration states, while the average concentration takes an intermediate value. Such bimodal behaviour clearly cannot be captured by a deterministic model.



(a) Each curve plots $\log p_i^s$ for a specific value of E.

(b) Contours of $\log p_i^s$ with respect to E and c.

Figure 3.3: Logarithm of the stationary distribution p_i^s plotted versus $c = i\Delta C$ for various values of the applied potential E, with $\epsilon = 0.25$ and $N = 100$.

We show the mean concentration at equilibrium as a function of E in Fig. 3.4. In sharp contrast to the deterministic model, the mean concentration of the stationary distribution does not exhibit any hysteresis but instead transitions directly from $c \approx 0$ to $c \approx 1$ at $E \approx 0$, following the Maxwell line for phase separation [23]. The same path is found in [14] for an ensemble of nano-particulate LFP given the relaxation time of the ensemble is much smaller than the charging/discharging time, as plotted in the black dashed line in Fig. 1.9. There is only one steady state for any given E, and hence there is no hysteresis. This shows that the global equilibrium of an ensemble

of non-interacting compartments, each with the same equilibrium distribution, is quite different from that for a single compartment, and indicates that discrete and stochastic effects may indeed have a profound influence on the system.

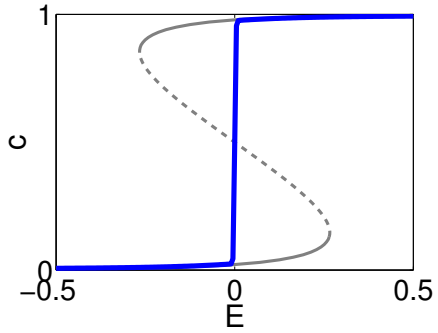
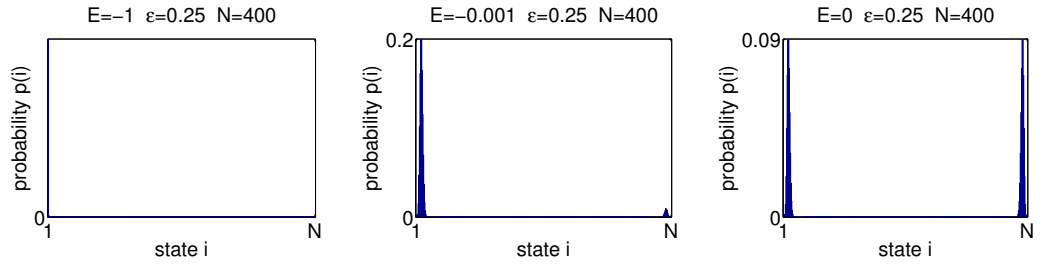


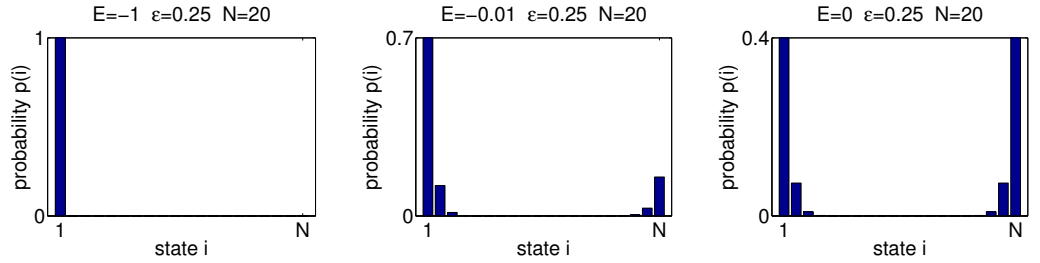
Figure 3.4: Mean concentration corresponding to the stationary distribution (3.19) plotted versus E, with $\epsilon = 0.25$ and $N = 100$. The equilibrium curve for the corresponding deterministic model, with the same parameter as Fig. 2.3, is plotted in grey.

In Fig. 3.3, we showed $\log p^{\mathrm{s}}$ as a function of the continuum variable c, but it is important to note that there may be discrepancies between this and the true log probabilities. In the continuum limit, $F(c)$ is always nonmonotonic near its local minima, although width of the local minima can be exponentially thin. This makes the discreteness of the system important, because if ΔC is big enough, the local well structure will not be captured by the state space, thereby changing the nonmonotonic structure into monotonic.

To further illustrate this, we compare the stationary distribution for two different values of N, $N = 400$ and $N = 20$, in Fig. 3.5. From left to right, we show $E = -1$, $E = -10^{-3}$ (-10^{-2} in (b)), and $E = 0$ respectively. As E increases, the distribution evolves from a degenerate Delta distribution to an asymmetric bimodal distribution, then to a symmetric bimodal distribution. Comparing the two cases, we see that when the distributions are bimodal, as in the middle panels and right-most panels, the distributions around each mode with $N = 400$ are two-sided, while the distributions around each mode with $N = 20$ are one-sided. This implies that the energy is nonmonotonic in the first case, but is monotonic in the latter case. Since the continuum model will never yield monotonic energy, the effect of discreteness is essential when N is relatively small.



(a) $N = 400$. In the leftmost panel the concentration is nearly a delta distribution at $i = 1$.



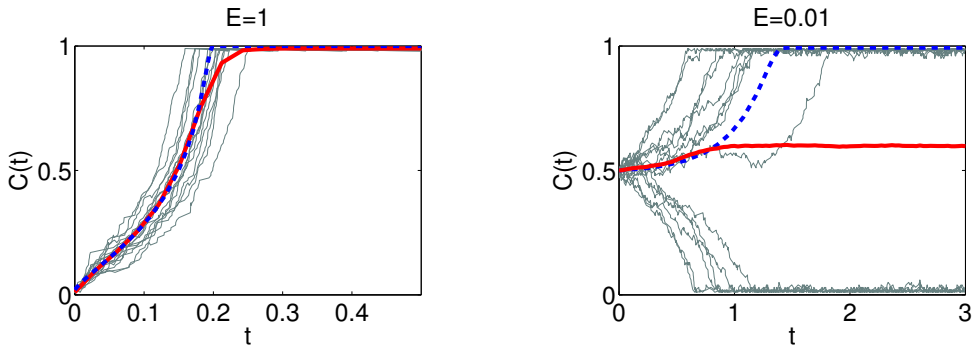
(b) $N = 20$

Figure 3.5: Stationary distribution for $N = 400$ and $N = 20$ given by (3.19). In the plot we use the same $\epsilon = 0.25$ as in Fig. 3.4.

3.2.2 Random walk simulations under constant E

Deviation of the equilibrium behaviour of a stochastic model from its deterministic behaviour can also be illustrated by simulating a collection of random walks, each of which is sampled from a compound Poisson process whose jump probabilities are specified by (3.10), with E held constant (as described in Appendix A). Each random walk represents the concentration in an individual compartment in an ensemble of non-interacting compartments.

Some results of this approach are summarized in Fig. 3.6. In the left panel we see that, when E is far from 0 and the equilibrium distribution is unimodal, the averaged concentration agrees well with the deterministic dynamics. In contrast, in the right panel we show some random walks under a slightly asymmetric bimodal distribution where E is close to 0. In this case some trajectories end up in the highest-lithium state, while others end up in the lowest-lithium state, and the final equilibrium concentration is close to a half. In contrast, the equivalent deterministic model would predict the equilibrium concentration from these initial conditions to be nearly full.



(a) $E = 1$. The starting state is the ground state $i = 1$.

(b) $E = 0.01$. The starting state is the middle state $i = 100$.

Figure 3.6: The concentration evolution viewed as a collection of random walks, with $N = 200$ and $\epsilon = 0.2$. Paths of 15 random walks are shown as grey curves; the averaged concentration over 200 simulations is plotted as a red solid curve; and the deterministic solution is plotted as a blue dashed curve.

3.3 A discrete-to-continuum model

The chemical master equation (3.1) and the Langevin equation (3.14) can be used to find the stationary distribution when E is constant, or to simulate random walks and understand their statistical properties. However, to study the out-of-equilibrium dynamics under a time-varying E, it is useful for us to reformulate the chemical master equation (3.1), in a form that is amenable to asymptotic analysis.

We now derive an approximation to the master equation (3.1) which exploits *both* the smallness of ϵ *and* the assumed largeness of N. We find that a distinguished limit occurs when $N = \mathcal{O}(1/\epsilon)$, and we therefore define a parameter

$$\alpha = \frac{\Delta C}{\epsilon} = \frac{1}{(N+1)\epsilon}. \tag{3.22}$$

As we will see, α can be thought of as representing the importance of discreteness; when $\alpha \to 0$, the model behaves mostly as a continuum, while if $\alpha \to \infty$, discrete effects are very important. These limiting cases will be dealt with in more detail in Section 3.4.2 and Section 3.4.3, but for now we consider the case where $\alpha = \mathcal{O}(1)$ and we take the distinguished limit as $\epsilon \to 0$ and $N \to \infty$.

As usual, the limit $N \to \infty$ results in a Fokker–Planck (F-P) type partial differential equation for a smooth function $p(c, t)$ which approximates the discrete distribution function $p_i(t)$. However, this continuum approximation breaks down in neighbourhoods of $c = 0$ and $c = 1$. We therefore end up with a hybrid discrete-continuum model, which looks like a continuous F-P equation for intermediate states, and a discrete system of master equations for boundary states.

Below we analyse in turn a discrete 'left inner layer' near $i = 1$; a continuous 'outer region' where c and $(1-c)$ are $\mathcal{O}(1)$; and a discrete 'right inner layer' where i is close to N. By matching the three regions together, we obtain a complete description of the dynamic process.

Note that, unlike the continuum problem where we were matching different domains in *time*, we are here concerned with matching between different regimes based on values of c.

3.3.1 Outer layer - the continuum limit

First, we find the Fokker-Planck equation and identify the region where it is valid. Defining variables in the continuum set-up as

$$c = c_i = i\Delta C, \qquad p(c,t) = p_i(t), \qquad q^{\pm}(c,t) = q_i^{\pm}(t) \tag{3.23}$$

and rewriting the master equation (3.1) as

$$\frac{\mathrm{d}p_i}{\mathrm{d}t} = \left[-q_j^{+}p_j + q_{j+1}^{-}p_{j+1}\right]_{j=i-1}^{j=i}, \tag{3.24}$$

we can Taylor expand the right-hand side of (3.24) to get

$$\frac{\partial p}{\partial t} \sim \frac{\partial}{\partial c}\left(q^{-}p - q^{+}p\right)\Delta C + \frac{1}{2}\frac{\partial^2}{\partial c^2}\left(q^{-}p + q^{+}p\right)\Delta C^2 + \cdots. \tag{3.25}$$

This is the Fokker-Planck type PDE that we seek.

Taylor expansions for $q^{\pm}(c,t)$ are

$$\begin{aligned} q^{+}(c,t) &\sim \frac{1}{2\Delta C}\exp\left[\frac{1}{2\epsilon}\left(E - \frac{g'(c)\Delta C + \frac{1}{2}g''(c)\Delta C^2 + \cdots}{\Delta C}\right)\right] \\ &\sim \frac{e^{\alpha/2}}{2\Delta C}\sqrt{\frac{1-c}{c}}\exp\left[\frac{E-1+2c}{2\epsilon}\right]\exp\left[-\frac{1}{4}\left(\frac{\Delta C}{c} + \frac{\Delta C}{1-c}\right) + \mathcal{O}(\Delta C^2)\right] \end{aligned} \tag{3.26}$$

and

$$q^{-}(c,t) \sim \frac{e^{\alpha/2}}{2\Delta C}\sqrt{\frac{c}{1-c}}\exp\left[-\frac{E-1+2c}{2\epsilon}\right]\exp\left[-\frac{1}{4}\left(\frac{\Delta C}{c} + \frac{\Delta C}{1-c}\right) + \mathcal{O}(\Delta C^2)\right], \tag{3.27}$$

therefore, due to the stiffness of the logarithmic potential at the boundaries, the leading order expansions

$$q^{\pm}(c,t) \sim \frac{e^{\alpha/2}}{2\Delta C}\exp\left[\pm\frac{E-1+2c-\epsilon\log(c/(1-c))}{2\epsilon}\right] \tag{3.28}$$

do not hold in near-empty or near-full states, where $c \sim \mathcal{O}(\Delta C)$ or $1 - c \sim \mathcal{O}(\Delta C)$. Hence, the Fokker-Planck equation is

$$\frac{\partial p}{\partial t} = -e^{\alpha/2}\frac{\partial}{\partial c}\left[\sinh\left(\frac{E-\mu(c)}{2\epsilon}\right)p\right] + \frac{\Delta C e^{\alpha/2}}{2}\frac{\partial^2}{\partial c^2}\left[\cosh\left(\frac{E-\mu(c)}{2\epsilon}\right)p\right], \quad (3.29)$$

and it only applies to the outer region where $c \gg \Delta C$ and $1 - c \gg \Delta C$.

Comparing (3.29) with (3.16), we see that when deriving the Fokker-Planck equation from the Langevin equation, we have missed a factor of the $e^{\alpha/2}$, i.e. we have implicitly assumed $\alpha \ll 1$, or $\Delta C \ll \epsilon$.

3.3.2 Boundary layers - a simplified discrete model

The regions where $c \sim \mathcal{O}(\Delta C)$ and $1 - c \sim \mathcal{O}(\Delta C)$ constitute two boundary layers that cannot be explored under a continuum framework. We consider a left inner layer composed of states 1 to K, and a right inner symmetric to the left inner layer, composed of states $N - 1 + K$ to N. We assume size of the boundary layers satisfies $1 \ll K \ll N$.

Left inner layer Defining a column vector $\mathbf{P}^{\mathrm{L}} = [p_1, p_2, \cdots, p_K]'$, where $'$ denotes the transpose, the left inner problem is rewritten as

$$\frac{\mathrm{d}\mathbf{P}^{\mathrm{L}}}{\mathrm{d}t} = \mathbb{W}_{\mathbb{L}}\mathbf{P}^{\mathrm{L}}, \quad (3.30)$$

where the probability transition matrix $\mathbb{W}_{\mathbb{L}}$ is the $K \times K$ upper-left block of the full transition matrix $\mathbb{W}$ defined by (3.3). The overall probability of this layer is not conserved, since summing up the rows of (3.30) gives

$$\sum_{i=1}^{K}\frac{\mathrm{d}p_i}{\mathrm{d}t} = -q_K^+ p_K, \quad (3.31)$$

implying that the left inner layer loses probability mass at a rate of $-q_K^+ p_K$.

The transition probabilities q_i^+ and q_i^- in this region can be simplified to

$$q_i^+ \sim \epsilon^{-3/2}\exp\left(\frac{E-1}{2\epsilon}\right)f_i^+(\alpha), \qquad q_i^- \sim \epsilon^{-1/2}\exp\left(-\frac{E-1}{2\epsilon}\right)f_i^-(\alpha), \quad (3.32)$$

as described in Appendix B.1, where $f_i^{\pm}(\alpha)$ are defined as

$$f_i^+(\alpha) = \frac{1}{2\alpha^{3/2}}\exp\left(\frac{1+\alpha(2i+1)+i\log(i)-(i+1)\log(i+1)}{2}\right), \qquad i \geq 1, \quad (3.33a)$$

$$f_i^-(\alpha) = \frac{1}{2\alpha^{1/2}}\exp\left(\frac{-1-\alpha(2i-1)+i\log(i)-(i-1)\log(i-1)}{2}\right), \qquad i \geq 2. \quad (3.33b)$$

Here we assume that $f_0^+ = f_1^- = 0$ to ensure that there is no flux into or out of the disallowed state $i = 0$. By writing the transition probabilities in the form of (3.32), we separate the effects of E and ϵ into the prefactor – all the dependence on i and α is expressed in the function $f_i^{\pm}(\alpha)$.

Therefore, the master equation reads

$$\begin{aligned}\frac{\mathrm{d}p_i}{\mathrm{d}t} &= \epsilon^{-3/2}\exp\left(\frac{E-1}{2\epsilon}\right)(f_{i-1}^+ p_{i-1} - f_i^+ p_i) \\ &\quad + \epsilon^{-1/2}\exp\left(-\frac{E-1}{2\epsilon}\right)(f_{i+1}^- p_{i+1} - f_i^- p_i), \quad i \ll N\end{aligned} \tag{3.34}$$

and the transition matrix $\mathbb{W}_{\mathrm{L}}$ can be decomposed into two components: a forward term that drives the probability density to higher states and a backward term which drives the probability density towards lower states:

$$\mathbb{W}_{\mathbb{L}} = \epsilon^{-3/2}\exp\left(\frac{E-1}{2\epsilon}\right)F^+(\alpha) + \epsilon^{-1/2}\exp\left(-\frac{E-1}{2\epsilon}\right)F^-(\alpha), \tag{3.35}$$

where $F^+(\alpha)$ and $F^-(\alpha)$ are two constant tridiagonal matrices given by

$$F_{ij}^+ = \begin{cases} -f_i^+(\alpha) & i = j, \\ f_{i-1}^+(\alpha) & i = j+1, \\ 0 & \text{otherwise}, \end{cases} \qquad F_{ij}^- = \begin{cases} -f_i^-(\alpha) & i = j, \\ f_{i+1}^-(\alpha) & i = j-1, \\ 0 & \text{otherwise}. \end{cases} \tag{3.36}$$

Clearly $E \sim 1$ is the critical region where the forward term balances with the backward term. When E is well below this value, the backward term is much larger than the forward term, driving the probability to the lowest state, so that the distribution resembles a Delta distribution. When E is above this value, the forward term dominates, the probability mass moves to higher states, and the total probability mass of the left inner layer decreases.

Right inner layer By symmetry of $g_i = g_{N+1-i}$, it can be shown that the right inner layer dynamics satisfies very similar equation to the left inner layer, namely

$$\begin{aligned}\frac{\mathrm{d}p_i}{\mathrm{d}t} &= \epsilon^{-1/2}\exp\left(\frac{E+1}{2\epsilon}\right)(f_{j-1}^- p_{i-1} - f_j^- p_i) \\ &\quad + \epsilon^{-3/2}\exp\left(-\frac{E+1}{2\epsilon}\right)(f_{j+1}^+ p_{i+1} - f_j^+ p_i), \quad j = N+1-i \ll N.\end{aligned} \tag{3.37}$$

Now, define $\mathbf{P}^{\mathrm{R}} = [p_N, p_{N-1}, \cdots, p_{N+1-K}]'$, so that in matrix form

$$\frac{\mathrm{d}\mathbf{P}^{\mathrm{R}}}{\mathrm{d}t} = \mathbb{W}_{\mathbb{R}}\mathbf{P}^{\mathrm{R}}, \tag{3.38}$$

where the transition matrix for the right inner layer is

$$\mathbb{W}_{\mathbb{R}} = \epsilon^{-3/2} \exp\left(-\frac{E+1}{2\epsilon}\right) F^{+}(\alpha) + \epsilon^{-1/2} \exp\left(\frac{E+1}{2\epsilon}\right) F^{-}(\alpha). \tag{3.39}$$

For all details of the derivation, see Appendix B.2.

Now, in the right inner layer dynamics (3.38) and (3.39), the qualitative structure is the same as the left inner layer dynamics (3.30) and (3.35); here $E = -1$ is the critical value.

So far, we have derived three approximate models for the different regimes that are all based on the chemical master equation. It is composed of a Fokker-Planck type equation (3.29) for the outer layer, and two ODE systems (3.30) (3.38) for the boundary layers. The outer layer needs to match with the boundary layers when $K \to \infty$ and $c \to 0$ or $c \to 1$.

3.4 Dynamics

As illustrated above, the equilibrium behaviours of the deterministic and stochastic models may be qualitatively different, particularly when E is close to zero and the equilibrium distribution of the stochastic model is bimodal. Thermal noise therefore plays an important role when the external voltage is constantly near zero. However, we now wish to determine whether it is equally important in dynamic situations where E varies with time.

We therefore study the dynamics of the stochastic model using the discrete-to-continuum model developed in Section 3.3, again assuming that the applied potential takes the form

$$E(t) = t$$

on the domain $t > -t_0$. Referring to Section 2.3, this implies a charge rate in the unit of 17 hours. Assuming that $t_0 > 1$ so that $E(-t_0) < -1$ initially, the negative transition probabilities q_i^- are exponentially larger than the positive transition probabilities q_i^+ for all i. Therefore, regardless of the initial conditions, the system rapidly relaxes to a delta distribution at the lowest-lithium state, $i = 1$, in an analogous manner to stage (i) of the deterministic dynamics analysed in Section 2.3.1.1.

The delta distribution remains until $t \to 0$ and $E(t) \to 1$, so that q_i^+ and q_i^- start to balance when i is small. It can be seen from equation (3.35) that q_i^+ and q_i^- are of the same order of $i \ll N$ when $E(t) \sim 1 - \epsilon \log\big(1/\epsilon\big)$. The transition where the

distribution spreads away from $i = 1$ and eventually concentrates at $i = N$ occurs in a local regime where

$$t = 1 - \epsilon \log\big(1/\epsilon\big) + \epsilon\tau \tag{3.40}$$

and $\tau = \mathcal{O}(1)$ in the transition. This coincides with the scaling (2.47) for the jump region (iii) in the deterministic model.

3.4.1 Distinguished limit: $\alpha = \mathcal{O}(1)$

First, we study the dynamics when $\alpha = \mathcal{O}(1)$, so that the small parameter for the double-well potential ϵ and the spacing between states ΔC are of similar magnitudes.

3.4.1.1 Dynamics in the left inner layer

The left inner layer master equation (3.30) reduces to

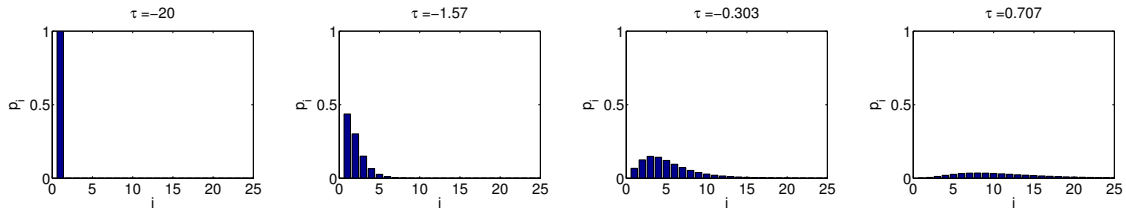
$$\frac{\mathrm{d}\mathbf{P}^{\mathrm{L}}}{\mathrm{d}\tau} = e^{\tau/2} F^{+}(\alpha)\mathbf{P}^{\mathrm{L}} + e^{-\tau/2} F^{-}(\alpha)\mathbf{P}^{\mathrm{L}}, \tag{3.41}$$

When τ is large and negative, the negative flux term dominates and drives the system towards a delta distribution at $i = 1$. As τ passes through zero, the positive and negative fluxes balance and the distribution begins to spread away from $i = 1$. As τ increases further, the probability is driven towards even higher states, and the total probability mass remaining in the left inner layer decreases towards zero.

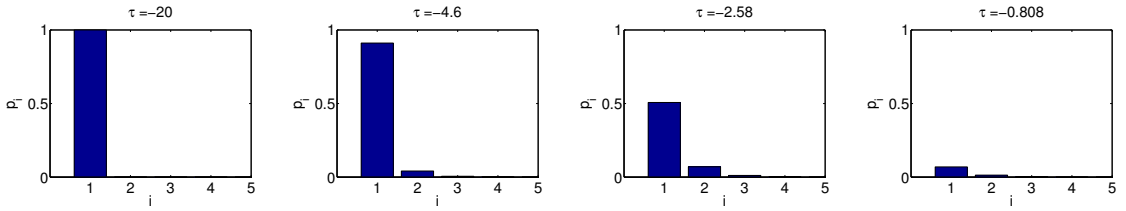
The flux *into* the left inner layer from the outer region is negligible throughout, because the product $F^{-}_{iK} p_K$ is always exponentially small when $K \gg 1$. Therefore, the inner layer problem (3.41) may be simulated independently of the outer problem, subject to the initial condition

$$p_i \to \delta_{1i}, \quad \text{as } \tau \to -\infty. \tag{3.42}$$

We find that solutions generically exhibit one of two distinctive patterns. At small values of α, the initial delta distribution spreads out and travels towards higher states as a wave, as shown in Fig. 3.7(a) (with $\alpha = 0.02$). In contrast, for larger values of α, the distribution remains highly localised at $i = 1$ for all τ, as shown in Fig. 3.7(b) (with $\alpha = 2$). This qualitative change in behaviour will be explored further in Section 3.4.2 and Section 3.4.3 by examining the asymptotic limits where $\alpha \ll 1$ and $\alpha \gg 1$. In either case, the overall probability of the left inner layer eventually decreases as a result of the flux into the outer layer.



(a) $\alpha = 0.2$ and $K = 25$.



(b) $\alpha = 2$ and $K = 5$.

Figure 3.7: Simulation of the left inner layer problem (3.41) .

Limiting behaviour as $i \to \infty$ To obtain the solution in the outer region which matches the behaviour of the inner layer, we require the limiting behaviour of $p_i(\tau)$ from the inner layer model as $i \to \infty$. For large i, the positive flux term in (3.41) dominates, and hence we find that

$$e^{\tau/2} p_i(\tau) f_i^+(\alpha) \to Q(\alpha; \tau) \quad \text{as } i \to \infty. \tag{3.43}$$

Here the function Q, which measures the net probability flux out of the inner layer, is independent of i, and is determined in principle by numerical solution of the discrete inner problem (3.41)–(3.42).

We plot $Q(\alpha; \tau)$ versus τ in Fig. 3.8 for the cases $\alpha = 0.2$ and $\alpha = 2$, corresponding to the distributions plotted in Figs. 3.7(a) and 3.7(b) respectively. Generically Q increases to a maximum and then decreases again as a function of τ, as the distribution function initially concentrated at $i = 1$ spreads and propagates out of the inner layer. For the smaller value of α, the peak in Q is both higher and narrower, and the time taken for the probability mass to leave the inner region completely is longer. This is explained by the fact that the larger α is, the fewer states are involved in the transition, so that the probability mass passes through this region more quickly. Each graph has unit area, by net conservation of probability.

3.4.1.2 Outer problem

In the outer region where $iN = O(1)$, the probability distribution is approximated by a continuous function $p_i(\tau) \sim p(c, \tau)$, where $c = i\Delta C \in (0, 1)$. Under the scaling

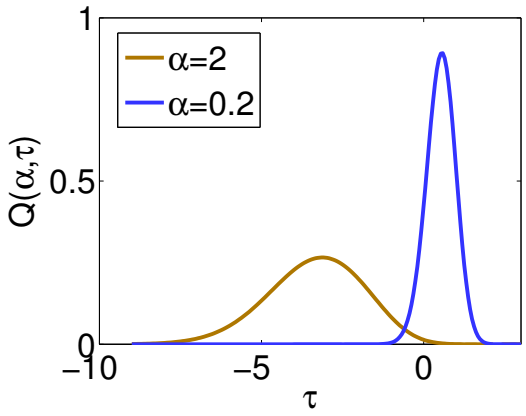


Figure 3.8: $Q(\alpha;\tau)$, the flux from the left inner region to the outer region, plotted as a function of τ with $\alpha = 2$ and $\alpha = 0.2$. The results are obtained by solving chemical master equation for the left inner layer (3.41) numerically.

(3.40), the leading-order transition probabilities in the outer layer are given by

$$q_i^+ \sim q^+(c,\tau) = \frac{\mathrm{e}^{(\alpha+\tau)/2}}{2\alpha\epsilon^{1/2}}\sqrt{\frac{1-c}{c}}\,\mathrm{e}^{c/\epsilon}, \tag{3.44a}$$

$$q_i^- \sim q^-(c,\tau) = \frac{\mathrm{e}^{(\alpha-\tau)/2}}{2\alpha\epsilon^{3/2}}\sqrt{\frac{c}{1-c}}\,\mathrm{e}^{-c/\epsilon}. \tag{3.44b}$$

Hence the positive term q^+ dominates q^-, and the F-P equation reduces to

$$\frac{\partial p}{\partial \tau} \sim -\frac{\epsilon^{1/2}\mathrm{e}^{(\alpha+\tau)/2}}{2\alpha}\frac{\partial}{\partial c}\left(\mathrm{e}^{c/\epsilon}p\sqrt{\frac{1-c}{c}}\right). \tag{3.45}$$

Since the right-hand side is exponentially large, the outer problem is quasi-steady, and to lowest order the bracketed term is a function of τ alone. The scaling for $p(c,\tau)$ can then be determined by matching with the left inner layer using the matching condition (3.43). Hence, we obtain the leading-order outer solution

$$p(c,\tau) = 2\alpha Q(\alpha;\tau)\mathrm{e}^{-(\alpha+\tau)/2}\,\epsilon^{1/2}\mathrm{e}^{-c/\epsilon}\sqrt{\frac{c}{1-c}}. \tag{3.46}$$

Note the presence of the $e^{-c/\epsilon}$ term, which indicates that the probability for the system to be in an intermediate state, with $1 \ll i \ll N$, is always exponentially small.

3.4.1.3 Right inner layer - quasi-equilibrium except for state N

In the right inner layer, we set $i = N + 1 - j$, where $j = O(1)$, and find that the leading-order transition probabilities are given by

$$q^+_{N+1-j} \sim \mathrm{e}^{1/\epsilon}\mathrm{e}^{\tau/2}f_j^-(\alpha), \qquad q^-_{N+1-j} \sim \epsilon^{-2}\mathrm{e}^{-1/\epsilon}\mathrm{e}^{-\tau/2}f_j^+(\alpha), \tag{3.47}$$

where the functions $f^{\pm}(\alpha)$ are still defined by equation (3.33). Since q^{+}_{N+1-j} is exponentially large, the right inner layer is also quasi-steady to leading order, with $q^{+}_{N+1-j}p_{N+1-j}$ independent of j and

$$q^{+}_{N-1}p_{N-1} = q^{+}_{N-2}p_{N-2} = q^{+}_{N-3}p_{N-3} = \cdots = \frac{\mathrm{d}p_N}{\mathrm{d}\tau}. \tag{3.48}$$

On the other hand, matching with the outer solution (3.46) gives $q^{+}_{N+1-j}p_{N+1-j} \to Q$ as $j \to \infty$ and hence

$$\frac{\mathrm{d}p_N}{\mathrm{d}\tau} = Q(\alpha;\tau). \tag{3.49}$$

3.4.1.4 A reduced model

Combining the three regions together gives us the full profile of the probability distribution evolution in the transition region, as sketched in Fig. 3.9. The probability flux out of the inner layer is effectively transferred directly to the highest state $i = N$, with the probabilities of all intermediate states remaining exponentially small throughout.

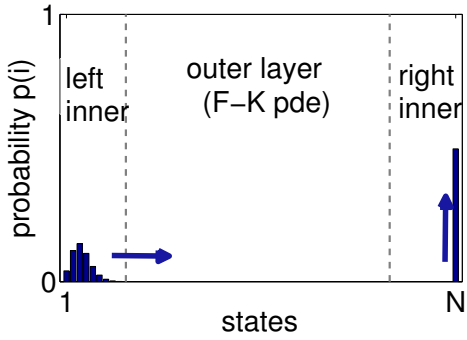
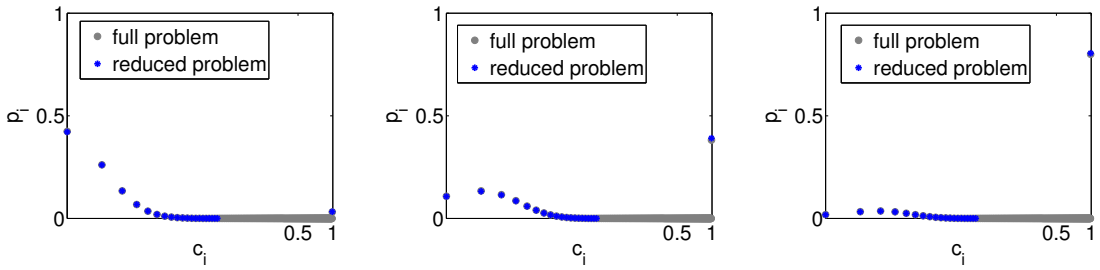
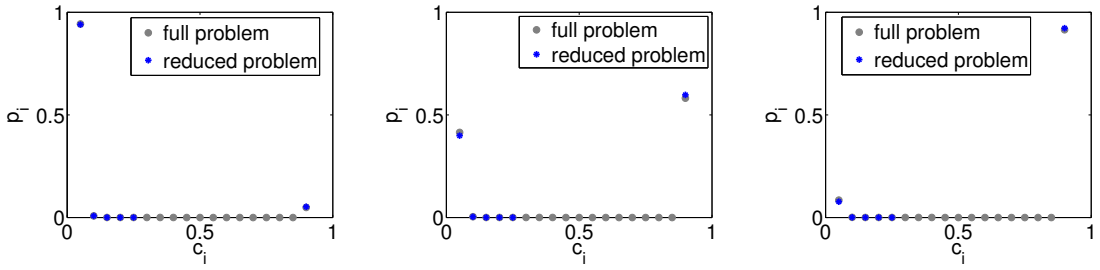


Figure 3.9: A schematic illustration of the reduced model. In the transition region, changes of the probability distribution profile only happen in the left inner layer and the highest state. All other states are in quasi-equilibrium.

To confirm this we compare solutions of a reduced model with solutions of a full model in Fig. 3.10. In the simulations we use the same parameters as the inner layer simulations of Fig. 3.7(a) and 3.7(b), and compare the solutions by solving the chemical master equation (3.1) and by solving the left inner layer equation (3.41). The distribution is initially set as a Delta distribution at $\tau = -20$, and, from left to right, we show its evolution as τ increases. The two solutions agree well, and in both simulations, only the inner layer states plus the highest state are significant in terms of probability.



(a) $N = 200$ and $\epsilon = 0.01$, $\alpha = 0.2$. Left inner layer of the reduced model is truncated at $K = 20$. Here we show the c-axis with logarithmic scale to magnify the left inner layer.



(b) $N = 20$ and $\epsilon = 0.01$, $\alpha = 2$. Left inner layer of the reduced model is truncated at $K = 5$.

Figure 3.10: Comparison between the solutions of the full model of the chemical master equation (3.1) and of the reduced model (3.41), (3.49) that only considers the left inner layer and the highest state.

The resulting predictions for the probability density $p_N(\tau)$ of the highest state are plotted in Fig. 3.11 for the same values $\alpha = 2$ and $\alpha = 0.2$ as above. We see that the dynamics of the full master equation system (3.1) is captured extremely well by the approximate equation (3.49).

We have shown that the transition of probability mass from the lowest-lithium state $i = 1$ to the highest-lithium state $i = N$ is described by the solution of the canonical discrete system (3.41)–(3.42) in the left inner region. In general this problem must be solved numerically for each value of $\alpha = ((N+1)\epsilon)^{-1}$ to determine the flux of probability out of the inner region and thence into the highest-lithium state, $i = N$. However, we will next show how the problem may be simplified when α is either very small or very large. The analysis enables us to explain the qualitative behaviour observed in the numerical solutions shown in Fig. 3.7 and also shows how the effects of both randomness and discreteness in this problem are captured by the single parameter α.

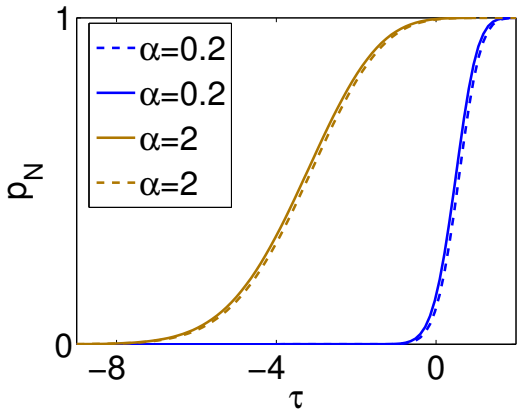


Figure 3.11: The probability density $p_N(\tau)$ of the highest state plotted versus τ with $\alpha = 2$ and with $\alpha = 0.2$. The solid curves show the solution of the approximate equation (3.49), and the dashed curves show the results of solving the full master equation (3.1).

3.4.2 Discrete limit: $\alpha \gg 1$

If the number N of available states is relatively small compared with $1/\epsilon$, then discreteness of the system governs the dynamics. In this case $\alpha \gg 1$ and it follows that $f_i^+ \gg f_{i+1}^+$ and $f_i^+ \gg f_i^-$ for any i in the left inner layer. Hence it follows that $p_i(\tau) \ll p_1(\tau)$ for all $i \geq 1$ in the inner layer and, to lowest order, the system is always either in the lowest-lithium state or the highest-lithium state. Hence we obtain the leading-order solution

$$p_1 = \exp\left(-2f_1^+ \mathrm{e}^{\tau/2}\right), \qquad p_N = 1 - \exp\left(-2f_1^+ \mathrm{e}^{\tau/2}\right), \tag{3.50}$$

and $p_i \sim 0$ for $1 < i < N$, where

$$f_1^+ = \frac{\mathrm{e}^{(3\alpha+1)/2}}{4\alpha^{3/2}}. \tag{3.51}$$

We observe that the dynamic transition of p_1 from 1 to 0 (while p_N does the reverse) occurs in a neighbourhood of $\tau \sim -3\alpha$. In terms of the potential E, this corresponds to $E \sim 1 - 3\Delta C$, which is lower than both the equilibrium turning point μ^* and the dynamic transition potential μ_{dyn} predicted by the deterministic model in Section 2.3. Therefore, when discreteness dominates, with high probability the system always exists in either the $i = 1$ state or the $i = N$ state, and its jump from empty to full occurs earlier than predicted by the deterministic model.

The expected concentration in this limit is approximated by

$$\bar{c} = \frac{1}{N+1}\sum_{i=1}^{N} i p_i(\tau) \sim (1 - \Delta C) + (2\Delta C - 1)\exp\left(-\frac{\mathrm{e}^{(3\alpha+1+\tau)/2}}{2\alpha^{3/2}}\right). \tag{3.52}$$

In Fig. 3.12, we compare the approximation (3.52) with the mean concentration obtained by solving the chemical master equation (3.1) for a case where $\alpha = 5$. We observe good agreement between the two, and the prediction that the jump occurs in the neighbourhood of $E \sim 1 - 3\Delta C$ is also accurate.

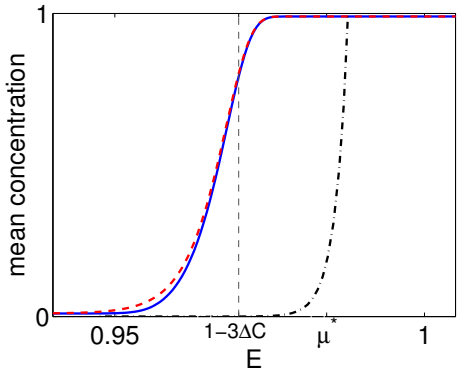


Figure 3.12: Expected concentration $\bar{c}$ plotted versus varying potential E. The blue solid line plots the analytical approximation (3.52) with $\alpha = 5$; the red dashed line plots the numerical simulation of the full problem (3.41) with $\epsilon = 0.002$ and $N = 99$; the black dash-dot line plots the solution trajectory of a deterministic model with $\epsilon = 0.002$, $c_0 = \exp(-20)$, and $E_0 = 1 + \epsilon \log \epsilon - 20\epsilon$. The equilibrium turning point μ^* predicted by the deterministic model is also marked.

3.4.3 Continuum limit: $\alpha \ll 1$

At the opposite extreme where $\alpha \ll 1$, the number of available states is sufficiently large compared with $1/\epsilon$ for even the 'left inner' problem to be treated using a continuum model. We believe this is the relevant model for nano-particle LFP cathode that are used in real life. Assuming density of delithiated LFP is 8.4×10^{28} particle/m^3 [14], a particle with 10nm diameter can host approximately 8×10^4 ions. In reality, LFP particles typically varies from 40nm to 100nm, which are safely in the continuum regime.

In this limit, the discrete chemical master equation is replaced by a continuum Fokker-Planck PDE in a two-stage process. In the beginning stage, the distribution is confined to a very thin region near the ground state, and discreteness is important until the Delta distribution develops into a Gaussian distribution. After formation of the Gaussian distribution, the effect of discreteness can be neglected, and the Gaussian distribution evolves according to a Fokker-Planck PDE.

3.4.3.1 Stage one: the discrete law

As $\alpha \to 0$, the master equation (3.41) reduces to

$$\alpha \frac{\mathrm{d}p_i}{\mathrm{d}\tau'} = \mathrm{e}^{\tau'/2}\left(\tilde{f}_{i-1}^{+} p_{i-1} - \tilde{f}_i^{+} p_i\right) + \mathrm{e}^{-\tau'/2}\left(\tilde{f}_{i+1}^{-} p_{i+1} - \tilde{f}_i^{-} p_i\right), \tag{3.53}$$

where $\tau' = \tau - \log\alpha$ and the coefficients

$$\tilde{f}_i^{+} = \frac{1}{2}\exp\left(\frac{1 + i\log(i) - (i+1)\log(i+1)}{2}\right), \qquad i \geq 1, \tag{3.54a}$$

$$\tilde{f}_i^{-} = \frac{1}{2}\exp\left(\frac{-1 + i\log(i) - (i-1)\log(i-1)}{2}\right), \qquad i \geq 2 \tag{3.54b}$$

no longer depend on α.

To leading order the system is in quasi-equilibrium, and its distribution is given by

$$p_i(\tau') \propto \mathrm{e}^{(i-1)\tau'}\mathrm{e}^{i-1-i\log i}, \tag{3.55}$$

up to a normalization factor. This distribution is plotted in Fig. 3.13 to reveal how it gradually changes from a delta distribution to a Gaussian as τ' increases.

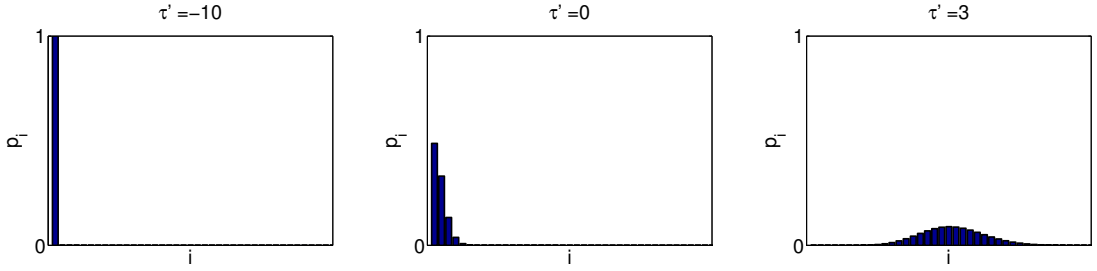


Figure 3.13: Quasi-equilibrium distribution prescribed by (3.55) with the sum $\sum p_i$ normalised to 1.

To approximate the Gaussian distribution for large τ', we note that p_i attains its maximum at $i = e^{\tau'}$, and expand around this maximum with

$$i = e^{\tau'} + e^{\tau'/2}s, \tag{3.56}$$

where s is small. Then

$$i\log i = \left(e^{\tau'} + e^{\tau'/2}s\right)\log\left(e^{\tau'} + e^{\tau'/2}s\right) \approx \tau' e^{\tau'} + e^{\tau'/2}s + e^{\tau'/2}\tau' s + s^2/2 \tag{3.57}$$

and

$$i(\tau' + 1) - i\log i \approx e^{\tau'} - s^2/2. \tag{3.58}$$

Substituting into (3.55) then gives

$$p(s) = p_i(\tau') \propto e^{-(\tau'+1)} e^{i(\tau'+1) - i\log i} \approx e^{-(\tau'+1)+e^{\tau'}} e^{-s^2/2} \tag{3.59}$$

up to a normalisation factor. Using the normalisation requirement that $\sum p_i = 1$, or equivalently $e^{\tau'/2}\int_{-\infty}^{\infty} p(s)\mathrm{d}s = 1$, we find

$$p(s) \sim \frac{1}{\sqrt{2\pi}} e^{-\frac{\tau'}{2}} e^{-\frac{1}{2}s^2}, \tag{3.60}$$

which can be rewritten in terms of τ by

$$p(\xi,\tau) \sim \frac{\sqrt{\alpha}}{\sqrt{2\pi}} e^{-\frac{\tau}{2}} e^{-\frac{1}{2}e^{-\tau}\xi^2}, \qquad \text{where } \xi = \frac{i\alpha - e^{\tau}}{\sqrt{\alpha}}. \tag{3.61}$$

3.4.3.2 Stage two: Gaussian approximation

Now, in the leading-order equations (3.53)–(3.54), we have neglected terms of order αi. Hence the approximate solution (3.55) ceases to be valid for large values of τ' when the tail of the distribution has spread as far as $i = O(1/\alpha)$. In this later stage of the evolution, we define $x = i\alpha$ and $p(x,\tau) = p_i(\tau)$, and find that the approximately continuous distribution is now described by the partial differential equation

$$\frac{\partial p}{\partial \tau} = -\frac{\partial}{\partial x}\big(p\sinh(\tau/2 + x - \log x/2)\big) + \frac{\alpha}{2}\frac{\partial^2}{\partial x^2}\big(p\sinh(\tau/2 + x - \log x/2)\big). \tag{3.62}$$

We assume that the solution distribution is centred at $\bar{x}(\tau)$, and define the local distribution function similar to (3.61) as

$$\sqrt{\alpha}\Phi(\xi,\tau) = p(x,\tau), \qquad \text{where } x = \bar{x}(\tau) + \sqrt{\alpha}\xi. \tag{3.63}$$

We are then able to find a macroscopic law for the mean concentration $\bar{x}(\tau)$, and a linear noise approximation for $\Phi(\xi,\tau)$.

First, we use the chain rule for the change for variables from (x,τ) to (ξ,τ) to obtain

$$\begin{cases} \dfrac{\partial}{\partial x} &= \dfrac{1}{\sqrt{\alpha}}\dfrac{\partial}{\partial \xi}, \\ \dfrac{\partial}{\partial \tau} &= -\dfrac{1}{\sqrt{\alpha}}\dfrac{\mathrm{d}\bar{x}(\tau)}{\mathrm{d}\tau}\dfrac{\partial}{\partial \xi} + \dfrac{\partial}{\partial \tau}, \end{cases} \tag{3.64}$$

so that the left-hand side of (3.62) becomes

$$\frac{\partial p}{\partial \tau} = -\frac{\mathrm{d}\bar{x}}{\mathrm{d}\tau}\frac{\partial \Phi}{\partial \xi} + \sqrt{\alpha}\frac{\partial \Phi}{\partial \tau}. \tag{3.65}$$

Meanwhile, we expand the right-hand side of (3.62) using $x = \bar{x}(\tau) + \sqrt{\alpha}\xi$ to get

$$\frac{\partial}{\partial x}[\sinh(\tau/2 + x - \log x/2)p(x,\tau)] \sim \sinh(\tau/2 + \bar{x} - \log \bar{x}/2)\frac{\partial \Phi}{\partial \xi} + \sqrt{\alpha}\cosh(\tau/2 + \bar{x} - \log \bar{x}/2)\left(1 - \frac{1}{2\bar{x}}\right)\frac{\partial}{\partial \xi}(\xi\Phi) + \mathcal{O}(\alpha) \tag{3.66}$$

and

$$\frac{\alpha}{2}\frac{\partial^2}{\partial x^2}[\cosh(\tau/2 + x - \log x/2)p(x,\tau)] \sim \frac{\sqrt{\alpha}}{2}\cosh(\tau/2 + \bar{x} - \log \bar{x}/2)\frac{\partial^2 \Phi}{\partial \xi^2} + \mathcal{O}(\alpha). \tag{3.67}$$

Substituting into the F-P equation (3.62) gives

$$\begin{aligned}
&\sqrt{\alpha}\frac{\partial \Phi}{\partial \tau} - \frac{\mathrm{d}\bar{x}}{\mathrm{d}\tau}\frac{\partial \Phi}{\partial \xi} \\
&\sim -\sinh(\tau/2 + \bar{x} - \log \bar{x}/2)\frac{\partial \Phi}{\partial \xi} - \sqrt{\alpha}\cosh(\tau/2 + \bar{x} - \log \bar{x}/2)\left(1 - \frac{1}{2\bar{x}}\right)\frac{\partial}{\partial \xi}(\xi\Phi) \\
&\quad + \frac{\sqrt{\alpha}}{2}\cosh(\tau/2 + \bar{x} - \log \bar{x}/2)\frac{\partial^2 \Phi}{\partial \xi^2} + \mathcal{O}(\alpha).
\end{aligned} \tag{3.68}$$

Matching at $\mathcal{O}(1)$ and $\mathcal{O}(\sqrt{\alpha})$ gives

$$\frac{\mathrm{d}\bar{x}}{\mathrm{d}\tau} = \sinh\left(\frac{\tau}{2} + \bar{x} - \frac{1}{2}\log \bar{x}\right), \tag{3.69}$$

$$\frac{\partial \Phi}{\partial \tau} = \cosh(\tau/2 + \bar{x} - \log \bar{x}/2)\left(\frac{1}{2}\frac{\partial^2 \Phi}{\partial \xi^2} - \left(1 - \frac{1}{2\bar{x}}\right)\frac{\partial}{\partial \xi}(\xi\Phi)\right). \tag{3.70}$$

Equation (3.70) admits solutions of a Gaussian form

$$\Phi(\xi,\tau) = A(\tau)\exp(-\pi A(\tau)^2\xi^2), \tag{3.71}$$

and we substitute the Gaussian ansatz into (3.70) to get

$$\frac{\mathrm{d}A}{\mathrm{d}\tau} = \frac{1}{2}\left(-1 + \frac{1}{2\bar{x}} - \pi A^2\right)A\cosh\left(\frac{\tau}{2} + \bar{x} - \frac{1}{2}\log \bar{x}\right). \tag{3.72}$$

The distribution is then fully determined by its mean (mode) $\bar{x}(\tau)$ and amplitude $A(\tau)$. The initial condition is found by matching with (3.61):

$$\bar{x}(\tau) \sim e^{\tau}, \qquad A(\tau) \sim \frac{1}{\sqrt{2\pi}}e^{-\tau/2}, \qquad \text{as } \tau \to -\infty. \tag{3.73}$$

Thus, the discrete initial dynamics selects a specific trajectory for the ODE system (3.69) and (3.72).

Now we see that the mean concentration $\bar{x}(\tau)$ follows the same initial-value problem (2.48) as predicted by the deterministic model for the transition from the lower to the upper equilibrium branch, as described in Section 2.3.1.3. From the analysis there we know that $\bar{x}(\tau)$ tends to infinity as $\tau \to \tau^* \approx 0.81498$; at the same time $A(\tau)$ approaches zero, with

$$A \sim \text{const}\,\sqrt{\tau - \tau^*}. \tag{3.74}$$

Therefore, as $\tau \to \tau^*$, the probability mass flows completely out of the left inner region and accumulates effectively instantaneously at the highest state $i = N$, as described in Section 3.4.1.3.

To check the conclusions of this section, we solve (3.69) and (3.72) numerically subject to (3.73), and compare with the results of solving the chemical master equation (3.30) directly. In Fig. 3.14, we compare the probability distribution functions obtained using the two different methods. In the left two panels of Fig. 3.15, we compare the mean $\bar{x}(\tau)$ and amplitude $A(\tau)$. Finally, in the rightmost panel of Fig. 3.15 we compare the solutions of the continuum models with the average over 200 random walks simulated using the jump probabilities (3.10). The agreement is in all cases excellent, at least until the predicted mean concentration $\bar{x}$ blows up.

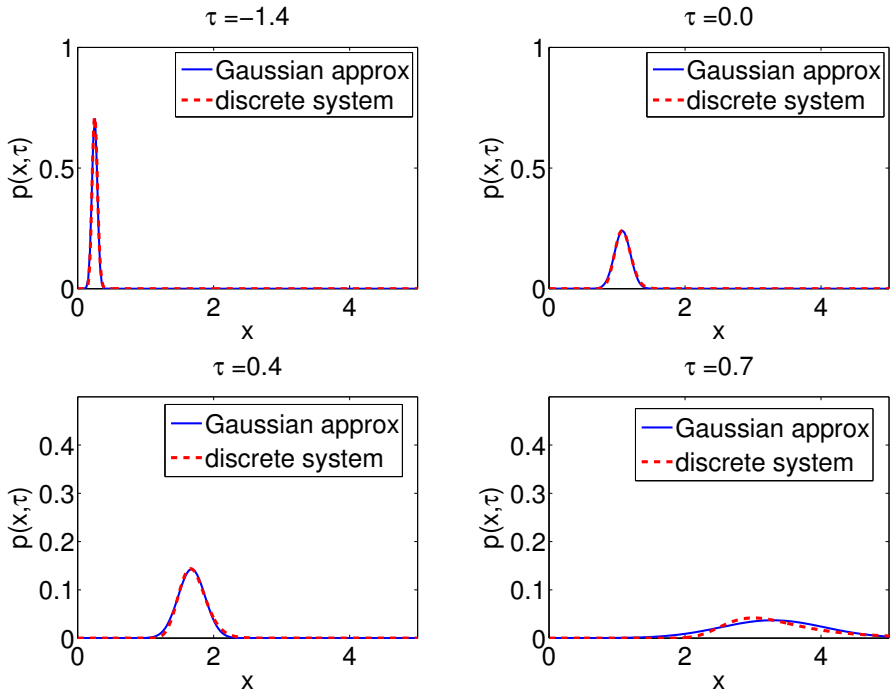


Figure 3.14: Distribution profiles computed by using the continuum approximation and by the solution of the discrete system (3.30). The continuum approximation is solved on the domain $x \in (0, 5]$ with $\alpha = 5 \times 10^{-3}$. The size of the discrete system is $K = 10^3$.

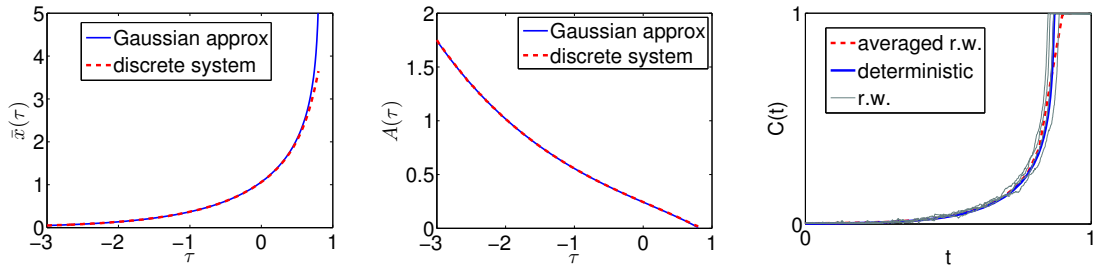


Figure 3.15: The left two panels show comparisons of the distribution mean $\bar{x}$ and amplitude A predicted by the continuum approximation (3.69) and (3.73) and by the discrete system (3.30), with the same parameter values as in Fig. 3.14. The right panel plots the average concentration $\bar{c}(t)$ predicted by the continuum model as well as by averaging over many random walks; here the parameter values are $\epsilon = 0.025$ and $N = 399$, so that $\alpha = 0.1$.

3.4.4 Conclusion of the dynamics

In conclusion, the stochastic dynamics essentially depends on the total number of states N available in a compartment, relative to $1/\epsilon$. When N is small so that discreteness is essential, the stochastic dynamics are driven solely by the transition between the ground state and the highest state. In this case, the behaviour of the model is not well captured by the deterministic model: in particular, the jump from empty to full occurs significantly earlier than either the static μ^* or the dynamic $\mu_{\rm dyn}$ transition points predicted by the deterministic model.

In contrast, when N is large and the discreteness can be ignored, the averaged concentration follows the same law as for the deterministic model. In this case, random effects play a significant role only during a very short period. The distribution function briefly spreads out while the probability mass transfers from the ground state to higher states; thereafter it rapidly accumulates at the highest state $i = N$ and the behaviour again becomes deterministic.

3.5 Discussions

3.5.1 Non-constant exchange current

In Section 2.4.1, we considered the effects of non-constant exchange current density on the deterministic dynamics. In this section, we continue to analyse the effects of non-constant exchange current density on the discrete stochastic system.

As a typical example, let us consider $I_0 = c^{1/2}(1-c)^{1/2}$. In order for the stochastic model to agree with the deterministic model, we modify the transition probabilities to

$$q_i^+ = \frac{1}{2\Delta C} c_i^{1/2}(1-c_i)^{1/2} \exp\left[\frac{1}{2\epsilon}\left(E - \frac{g_{i+1}-g_i}{\Delta C}\right)\right], \quad i = 1, \cdots, N-1 \tag{3.75a}$$

$$q_i^- = \frac{1}{2\Delta C} c_i^{1/2}(1-c_i)^{1/2} \exp\left[\frac{1}{2\epsilon}\left(-E + \frac{g_i-g_{i-1}}{\Delta C}\right)\right], \quad i = 2, \cdots, N. \tag{3.75b}$$

The discrete-continuum model is still valid, and the division of the full problem into two boundary layers and an outer layer remains unchanged. In addition, the dynamic process is similar, with the left inner layer governing the dynamics of the lithiation process. In the left inner layer, (3.75) reduces to

$$q_i^+ \sim \frac{1}{\epsilon} \exp\left(\frac{E-1}{2\epsilon}\right)(i\alpha)^{1/2} f_i^+(\alpha), \quad q_i^- \sim \exp\left(-\frac{E-1}{2\epsilon}\right)(i\alpha)^{1/2} f_i^-(\alpha), \quad i \ll N \tag{3.76}$$

with $f_i^{\pm}(\alpha)$ still defined in (3.33).

Again, the critical transition region is around $E \sim 1 + \mathcal{O}(\epsilon)$. We rescale with

$$E = 1 + t, \qquad t = \epsilon t' \tag{3.77}$$

and find that the dynamics are dominated by the positive flux term:

$$\frac{\mathrm{d}\mathbf{P}^{\mathrm{L}}}{\mathrm{d}t'} = e^{t'/2}\bar{F}^+(\alpha)\mathbf{P}^{\mathrm{L}} + \mathcal{O}(\epsilon), \tag{3.78}$$

$$p_i(t') \to \delta_{1i}, \qquad \text{as } t' \to -\infty. \tag{3.79}$$

Here the $\bar{F}^+(\alpha)$ has the same structure as $F^+(\alpha)$ defined by (3.36), but the elements are related by $\bar{f}_i^+ = (\alpha i)^{1/2} f_i^+$.

Again the problem in the transition regime is simplified, and there is a full analytical solution, namely

$$\begin{aligned}
p_1 &= \mathrm{e}^{-2\bar{f}_1^+ \mathrm{e}^{t'/2}}, \\
p_2 &= \frac{\bar{f}_1^+}{\bar{f}_2^+ - \bar{f}_1^+}\left(\mathrm{e}^{-2\bar{f}_1^+ \mathrm{e}^{t'/2}} - \mathrm{e}^{-2\bar{f}_2^+ \mathrm{e}^{t'/2}}\right), \\
&\vdots \\
p_K &= \sum_{i=1}^{K} \frac{\prod_{j=1}^{K-1} \bar{f}_j^+}{\prod_{j=1, j\neq i}^{K}\left(\bar{f}_j^+ - \bar{f}_i^+\right)} \mathrm{e}^{-2\bar{f}_i^+ \mathrm{e}^{t'/2}}.
\end{aligned} \tag{3.80}$$

Now all the physical quantities of interest are fully determined regardless of the value of α. We plot the evolution of the mean concentration under three values of α in Fig. 3.16. As in the constant-I_0 case, we observe that the greater the value of α, the earlier the stochastic jump starts than the deterministic prediction.

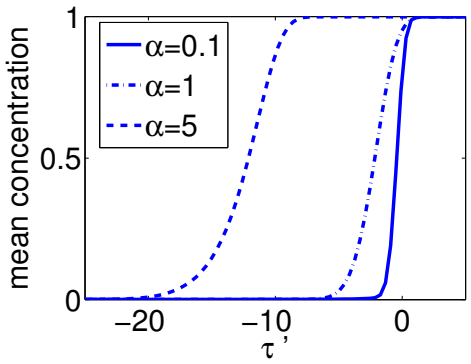


Figure 3.16: Mean concentration evolution when I_0 is modelled as being proportional to $c^{1/2}(1-c)^{1/2}$, with the distribution in the left-inner layer determined by (3.80).

3.5.2 The effect of charging speed

Now we continue the discussion of Section 2.4.2 on the effect of charging speed. Again we will show that the dynamics of the stochastic model does not change qualitatively provided the charging rate satisfies $E(t) = 1 + \kappa t$ and $\kappa = \mathcal{O}(1)$.

In the critical transition near $E \sim 1 + \epsilon \log \epsilon$, the dynamic problem can be rescaled by

$$t = \frac{1}{\kappa} \left(\epsilon \log \epsilon + \epsilon \tau' \right), \tag{3.81}$$

which gives the governing equation for the left inner problem,

$$\kappa \frac{\mathrm{d}\mathbf{P}^{\mathrm{L}}}{\mathrm{d}\tau'} = \left(e^{\tau'/2} F^{+}(\alpha) + e^{-\tau'/2} F^{-}(\alpha) \right) \mathbf{P}^{\mathrm{L}}, \tag{3.82}$$

subject to a Delta distribution when $\tau \to -\infty$. As in the canonical problem where $\kappa = 1$, the solution to (3.82) needs to be determined numerically for each value of κ.

The resulting evolution of the probability distribution is qualitatively similar to what we identified in the case $\kappa = 1$: the probability distribution first spreads out into higher states of the left inner layer, it then leaves the left inner layer, and finally all the probability mass accumulates at the highest state.

Generally, we find that a large κ is associated with the probability distribution passing through the left inner layer quickly, thereby involving fewer states in the transition, and making the system behave as if the effect of discreteness is prominent.

On the other hand, for the dynamic probability distribution to resemble the stationary distribution, we find that the charging rate κ has to be exponentially small, requiring significant changes in the asymptotic analysis. Such exponentially slow charging is unlikely to be of interest in real-life.

3.6 Summary

To determine whether the solution structure of the deterministic Butler–Volmer model for a single compartment, as found in Chapter 2, is robust to discrete effects and thermal fluctuations, in this chapter we consider a stochastic model for the probability distribution of the concentration of lithium in a single compartment, assuming that the concentration can vary over a discrete state space of size N. We start with the chemical master equation, and choose appropriate transition probability in order to have the chemical master equation to mimic the Butler–Volmer equation in its deterministic limit. Again we exploit the assumed smallness of ϵ to reformulate it as a continuous Fokker–Planck PDE coupled to two discrete inner layers. As a compartment is lithiated, we find that the probability distribution of lithium concentration evolves from a Delta distribution at the lowest-lithium state to a Delta distribution at the highest-lithium state, and that the probability mass is always strongly localized around the lowest-lithium and highest-lithium states. The probability of all intermediate states remains small throughout the transition, and this happens regardless of the number of available states, N, provided it is sufficiently large.

The detailed shape of the probability distribution during the transition is found to depend on a single parameter $\alpha = \big((N+1)\epsilon\big)^{-1}$, which measures the importance of discreteness. In the limit $\alpha \ll 1$, the probability density is approximately a continuous Gaussian: the macroscopic law for the expected concentration is essentially identical to the deterministic model dynamics, and the thermal noise is described by an extra diffusion term of order $\alpha^{1/2}$. In the opposite limit $\alpha \gg 1$, the probability distribution is essentially degenerate: the probability mass leaks directly from the lowest-lithium state to the highest-lithium state, and consequently the rate and timing of the transition is determined by the spacing between available states rather than the depth of the double well potential.

When our model is applied to a battery particle where stochastic effects may be important, it should first be determined whether to adopt a discrete or continuum model. Generally, a typical LFP nano-particle with diameter of 50–1000 nm can accommodate enough lithium atoms to be in the continuum regime.

Nevertheless, although the stochastic model in the continuum limit predicts the same dynamic transition potential as the deterministic model, it has very different implications when considered more broadly.

Most notably, the equilibrium behaviour of the stochastic model is very different from the equilibrium behaviour of the deterministic model, indicating that significant

differences might be seen if lithiation is performed more slowly. As a clear demonstration of this difference, we note that Fig. 3.4 shows that equilibrium analysis of the deterministic model predicts hysteresis, while the continuum stochastic model does not. Moreover, since the stochastic model predicts a bimodal probability distribution for lithium concentration (especially in the vicinity of $E = 0$), we can anticipate that an ensemble of compartments may behave very differently from a single compartment, since some compartments in the ensemble can be in a low lithium state while others are simultaneously in a high lithium state but with an similar energy.

Although developed as a stochastic model for a single compartment, the stochastic property means it could be used to predict the average behaviour of an ensemble of completely decoupled compartments. In a real cathode material, however, each compartment is strongly coupled to its neighbours. In principle, this complication could be introduced to either the stochastic model or the deterministic model by incorporating an interaction potential into the free energy (2.1). In the deterministic setting, one ends up with a coupled system of Butler–Volmer type ODEs similar to (2.9). This would lead to a system where the resulting bifurcation structure and dynamic behaviour are much more complicated and delicate than the one-compartment case considered in Chapter 2. These cases will be considered in Chapters 5 and 6.

Chapter 4

A deterministic multicompartment model with linear dynamics

We now move on to build models for multiple interacting compartments. In Chapters 4, 5 and 6, we will present in sequence a deterministic multicompartment model with linear dynamics, a deterministic multicompartment model with nonlinear dynamics, and a stochastic multicompartment model. The multicompartment model can be used to describe a variety of different electrochemical systems. One example where the interacting multicompartment system might be useful is lithium graphite. As in Section 1.3, in lithium graphite, ions sit between the graphene sheets, which act as walls that are impermeable to lithium transport, hence it can be viewed as a one-dimensional multilayer system with each layer being treated as a compartment.

Modelling the intercalation process of lithium graphite includes choosing a suitable energy function for the system as well as a dynamic law. In this chapter and the next chapter, we will adopt an energy model that is based on the logarithmic double well energy introduced in Chapter 2, but which includes an extra term associated with the interaction between neighbouring compartments. To model the dynamics of the system, we will present a gradient flow model which is convenient to describe current control, and a Butler–Volmer model which is convenient for voltage control. Essentially, the gradient flow model imposes a linear relation between the potential and the change in lithium concentration, and a Butler–Volmer model imposes a nonlinear relation between the potential and the change in lithium concentration.

Even with the simplified nearest-neighbour interaction model, we are able to partially explain the clear trend of two stages in the lithium graphite intercalation as previously discussed in Fig. 1.10. In Chapter 7, we will expand the model to a more general case where interaction between non-neighbouring compartments is included,

with the aim of capturing more details of the stepped C-V curve described in Section 1.3.

4.1 Model formulation

4.1.1 A free energy model

We start by looking at lithium graphite as an M-compartment structure. Each compartment has a normalised lithium concentration of c_i $(i = 1, 2, \cdots, M,\ 0 < c_i < 1)$; altogether they sum up to an average concentration of $\bar{c} = \sum_{i=1}^{M} c_i/M$. The total energy is formulated as

$$g_{\text{tot}} = \sum_{i=1}^{M} g(c_i) + \sum_{i=1}^{M-1} h(c_i, c_{i+1}). \tag{4.1}$$

Here the first term $\sum_{i=1}^{M} g(c_i)$ accounts for energy of individual compartments, and we adopt the double well energy

$$g(c) = c(1-c) + \epsilon(c\log(c) + (1-c)\log(1-c))$$

as introduced in Section 2.1.1.

The second term in (4.1) represents an interaction energy between neighbouring compartments: this reflects the fact that neighbouring compartments share a graphene sheet, and the change associated with the lithium ions means that it is unfavourable for both to be full at the same time. The function $h(c_i, c_{i+1})$ should therefore be a symmetric function in its two arguments, and monotone increasing in each argument. For simplicity, we take

$$h(c_i, c_{i+1}) = \sigma c_i c_{i+1}, \tag{4.2}$$

where σ is a constant that represents relative strength of intra-compartment energy and inter-compartment energy. To be consistent with the nondimensionlisation of a single compartment (2.1), σ is obtained by scaling with Ω, enthalpy of mixing per site. Note that in this thesis we always regard ϵ to be small and use $\epsilon \ll 1$ to perform asymptotic analysis. However we do not make the same assumption on σ, and σ is regarded as $\mathcal{O}(1)$.

4.1.2 Gradient flow model

To begin with, we suppose that the system attempts to minimize the total energy while the total amount of lithium $C(t)$ is an imposed function of time:

$$C(t) = \sum_{i=1}^{M} c_i(t) = M\bar{c}(t). \tag{4.3}$$

This is equivalent to specifying the current that flows into/out of the system. We therefore introduce a Lagrange multiplier $\bar{\lambda}(t)$ to impose the constraint on the total amount of lithium (4.3), and the dynamics of each concentration, $c_i(t)$, is assumed to be given by a gradient flow model,

$$\frac{\mathrm{d}c_i(t)}{\mathrm{d}t} = -L\frac{\partial g_{\mathrm{tot}}(t)}{\partial c_i(t)} - \bar{\lambda}(t), \qquad i = 1, 2, \cdots, M \tag{4.4}$$

where g_{tot} is defined in (4.1), and L is the sensitivity of c_i to energy fluctuations. We will show in Section 5.1 that

$$\frac{1}{L} = 2\epsilon t_{\mathrm{int}}, \tag{4.5}$$

where ϵ is the relative importance of entropy and enthalpy as defined in (2.10), and t_{int} is the intrinsic time to deplete a fully-lithiated compartment at the constant exchange current density, as defined in (2.8). We have calculated t_{int} to be 17 hours for a 50nm LFP nanoparticle, which makes $1/L$ to be around 8 hours if $\epsilon = 0.25$. Rescaling t with respect to $1/L$ gives us a dimensionless model,

$$\frac{\mathrm{d}c_i(t)}{\mathrm{d}t} = -\frac{\partial g_{\mathrm{tot}}(t)}{\partial c_i(t)} - \lambda(t), \qquad i = 1, 2, \cdots, M \tag{4.6}$$

where $\lambda(t) = \bar{\lambda}(t)/L$. Summing equation (4.6) from 1 to M, we find that $\lambda(t)$ is given by

$$\lambda(t) = -\frac{1}{M}\sum_{i=1}^{M}\frac{\mathrm{d}c_i(t)}{\mathrm{d}t} - \frac{1}{M}\sum_{i=1}^{M}\frac{\partial g_{\mathrm{tot}}(t)}{\partial c_i}. \tag{4.7}$$

Substituting (4.7) back into (4.6), we therefore find that

$$\frac{\mathrm{d}c_i(t)}{\mathrm{d}t} = -\left(1 - \frac{1}{M}\right)\frac{\partial g_{\mathrm{tot}}(t)}{\partial c_i(t)} + \frac{1}{M}\sum_{j=1, j\neq i}^{M}\frac{\partial g_{\mathrm{tot}}}{\partial c_j} + \frac{1}{M}\frac{\mathrm{d}C(t)}{\mathrm{d}t}. \tag{4.8}$$

This is the system of equations that we will concentrate on in this chapter.

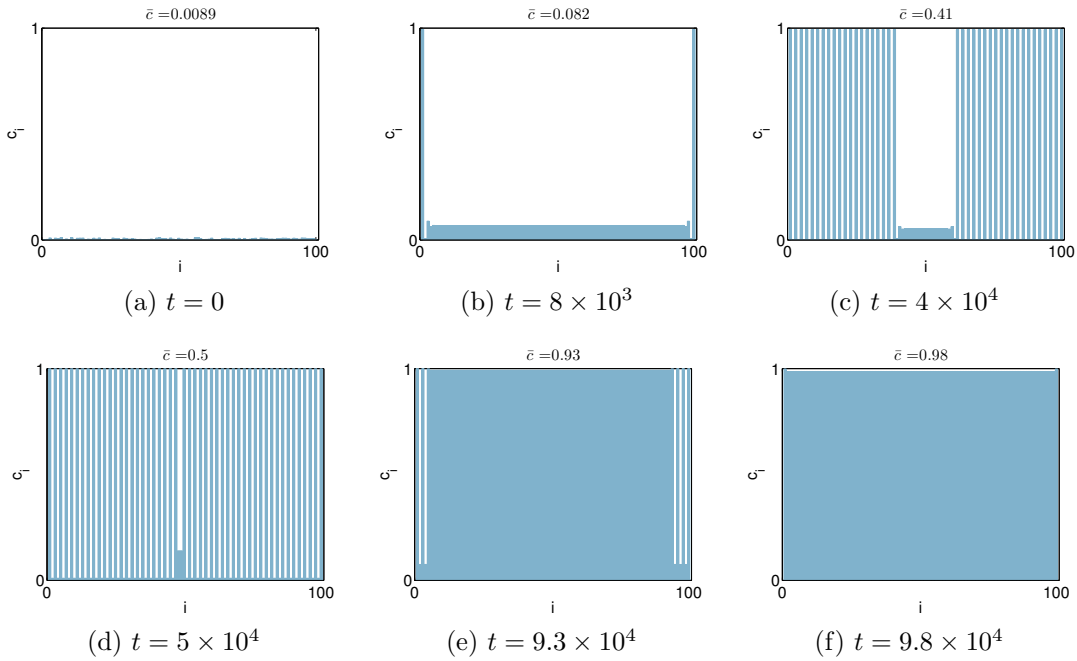
4.2 Numerical simulation of the nearest-neighbour M-compartment model

We first run numerical simulations with a large number of compartments to reveal the key dynamic properties of the gradient flow model (4.8). Then, we investigate these properties in more detail through a careful bifurcation analysis of a three-compartment system.

We solve the ODE system (4.8) with Matlab **ode15s**. It is highly stiff because of the logarithmic terms in $g(c)$, so we set $\epsilon = 0.25$ to ensure numerical convergence. Although this is bigger than its value in reality, $\epsilon = 0.25$ retains the double well energy structure in $g(c)$, thus capturing the key characteristics of the discrete M-compartment model. For numerical simplicity, we assume that the total concentration $C(t)$ changes linearly with time: $C(t) = C(0) + kt$, where $C(0)$ is the initial total concentration found by summing over the initial concentration $c_i(0)$, and k is the charging rate; $k > 0$ denotes an increase of the total concentration, and $k < 0$ denotes a decrease of the total concentration. To model experimental quasi-equilibrium conditions, we choose $k = 10^{-3}$ so that the filling rate is small. It is noteworthy that such charging rates are likely to be much slower than real-life applications, as the time we used to nondimensionalise the gradient-flow model, $2\epsilon t_{\text{int}}$, was computed to be 8 hours for a 50nm LFP nanoparticle. Simulation results are plotted in Fig. 4.1.

The trend of how the compartments are sequentially filled is shown in Fig. 4.1. Initially, the system is randomly distributed with a low concentration (a). This initial randomness is soon smoothed out and the concentrations of all compartments start to grow uniformly. The uniform filling stage ends when an average concentration of around 0.06 is reached, which happens slightly before (b). Having filled the outside compartments first, the compartments start to fill systematically with every other compartment being filled (c). At the end of this stage, the system is half-full – every almost-full compartment is adjacent to an almost-empty compartment. As the influx of ions continues, they begin to fill the sandwiched empty compartments (d). In this case, centre compartments are filled first, with a wave of filled compartments expanding to the outer boundaries (e). Finally, before reaching the full intercalated state, the non-uniform distribution is again smoothed out (f). The final stage sees a uniform increase of all compartments.

We plot the total energy versus the averaged concentration in blue in the left panel of Fig. 4.2. We can spot three different stages. The total energy first increases until $\bar{c} \approx 0.06$, which corresponds to the initial uniform filling. This is followed by a



(a) $t = 0$ (b) $t = 8 \times 10^3$ (c) $t = 4 \times 10^4$

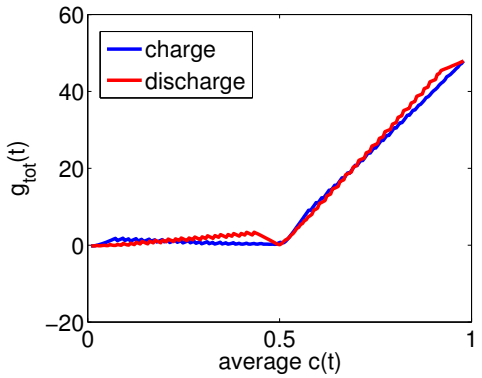
(d) $t = 5 \times 10^4$ (e) $t = 9.3 \times 10^4$ (f) $t = 9.8 \times 10^4$

Figure 4.1: Numerical simulation of a lithiation process using the gradient flow model (4.8) with $C(t) = C(0) + 10^{-3}t$, where the initial concentration $c_i(0)$ is randomly distributed in $[0, 0.01]$ and $C(0)$ is the sum of $\sum c_i(0)$. Parameters are set to be $\epsilon = 0.25$, $M = 100$, and $\sigma = 0.5$.

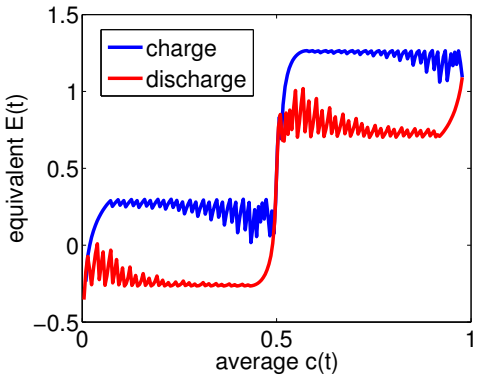
decrease, featuring the filling of non-adjacent compartments. The system continues filling every second compartment until the system is half full, beyond which the total energy starts to increase again. In the right panel of Fig. 4.2, we show in blue the value of $-\lambda(t)$ as computed from equation (4.7). We will later show that $-\lambda(t)$ is equivalent to the voltage required to maintain the system at a given state of charge, and so we label it as $E(t) = -\lambda(t)$.

The jump in potential at $\bar{c} = \frac{1}{2}$ is clearly evident, and there are also small fluctuations in potential due to the constant current assumption. This is because the equivalent voltage needs to be adjusted in such a way to satisfy the linear concentration increase constraint. As discussed in Section 1.3, similar predictions have been proposed in a particle-to-particle filling process [14]. The C-V curve is a very jagged one if there are limited number of particles present, and it would be smoothed by averaging over a large number of particles, as in Fig. 1.9.

Comparing the blue C-V curve in Fig. 4.2(b) with Fig. 1.10, we see that the "staircase" behaviour of lithium graphite is captured by our very simple model. In our model, the nearest-neighbour interaction simply divides all compartments into two alternating groups. During the lithiation/delithiation process, one group fills/empties



(a) Total energy g_{tot} versus average concentration c.



(b) Equivalent potential $E(t) = -\lambda(t)$ versus average concentration c.

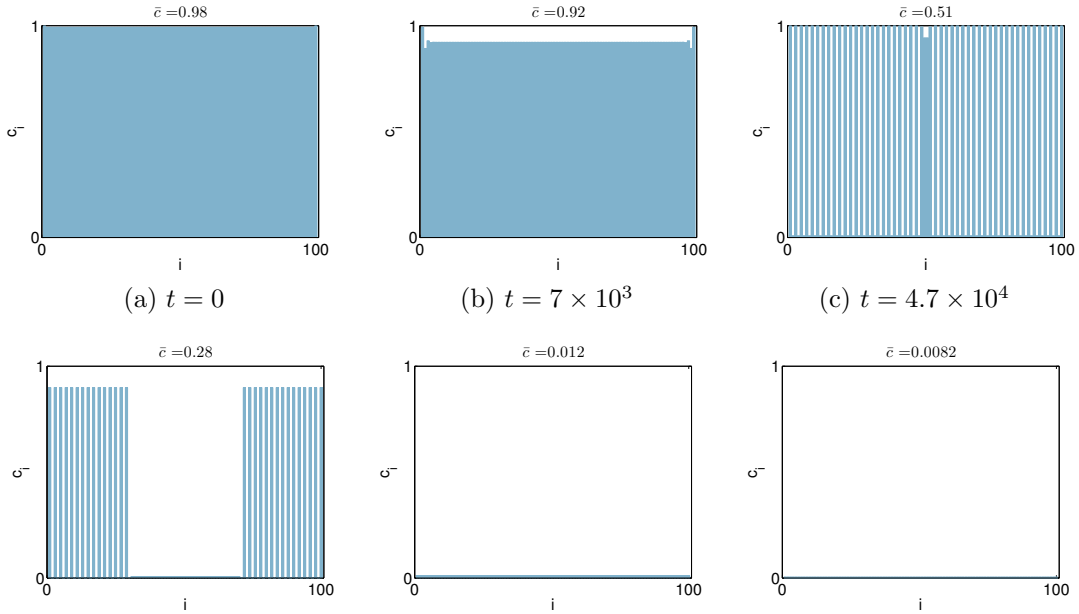
Figure 4.2: Hysteresis in a complete lithiation/delithiation cycle cycle. The blue curve plots evolution of energy and equivalent potential versus the average concentration of the lithiation process corresponding to Fig. 4.1, and the red curve plots the delithiation process corresponding to Fig. 4.3.

first, in a sequential manner. The filling/emptying of the other group does not start until the first group is near full/empty. Consequently, the two plateaus in the C-V curve corresponds to the two-stage process. In reality, the oxidation of graphite shows more transition stages than our very simple model. Equivalently, this requires us to include longer-range inter-compartment interaction energy into the model in order to group all compartments into more than 2 groups. This modified model is discussed in Chapter 7.

We next conduct simulations to show how a fully intercalated system is emptied (deintercalated), showing the results in Fig. 4.3. The total energy evolution versus total concentration is plotted in red in the left panel of Fig. 4.2, and the equivalent potential $E(t) = -\lambda(t)$ is plotted in red in the right panel. The parameters are identical to the simulation of intercalation shown in Fig. 4.1, except that initially c_i is the same distribution as (f) of Fig. 4.1 and that $k = -10^{-3}$. The deintercalation process is a similar process but in a reverse direction to the intercalation process in Fig. 4.1: firstly the concentration decreases uniformly across all compartments (b); then outside compartments are emptied first, with ions moving out from every other compartment until the whole system is half full of lithium (c); after that, the concentration of remaining compartment is reduced (e). In the final stage, a uniform reduction is again observed (e)-(f).

However, comparing the evolution profiles with the lithiation process in Fig. 4.1, we see that the two process are not completely reversible. In the lithiation process,

the uniform increase/decrease of all compartments when the system is near full is approximately in the regime $\bar{c} > 0.99$ as in Fig. 4.1(f), while in the delithiation process this happens in $\bar{c} > 0.9$ as in Fig. 4.1(b). When near empty the uniform increase/decrease regime is $\bar{c} < 0.1$ for lithiation and $\bar{c} < 0.01$ for delithiation.



(a) $t = 0$ (b) $t = 7 \times 10^3$ (c) $t = 4.7 \times 10^4$

(d) $t = 7.2 \times 10^4$ (e) $t = 9.8 \times 10^4$ (f) $t = 9.9 \times 10^4$

Figure 4.3: Numerical simulation of a delithiation process using the gradient flow model (4.8) with $C(t) = C(0) - 10^{-3}t$, where the initial concentration $c_i(0)$ is Fig. 4.1(f) and $C(0)$ is the sum of $\sum c_i(0)$. Parameters are set to be $\epsilon = 0.25$, $M = 100$, and $\sigma = 0.5$.

This is also evident in the comparison between the energy-concentration and potential-concentration diagrams of the lithiation/delithiation processes in Fig. 4.2. First, the potential-concentration diagram in the left panel exhibits 3 hysteresis loops in a complete cycle, indicating that the model predicts multiple stable states at certain values of concentration. For instance, at $\bar{c} = 0.9$, in the lithiation process the concentration is non-uniform, however in the delithiation process the concentration is uniform. On the other hand, the potential-concentration relation plotted in the right panel shows that the voltage plateaus in the lithiation and delithiation differs by a fixed amount. Such hysteresis is very similar to the hysteresis of LFP nanoparticle cathodes as discussed in [14], which is due to the N-shape of the logarithmic double-well potential, and would always exists regardless of laboratory conditions.

4.3 Bifurcation analysis of a three-compartment model

In order to understand the simulation results presented in Section 4.2, we perform some analysis on a system containing only three compartments. Substituting $M = 3$ and

$$g_{\text{tot}} = \sum_{i=1}^{3} g(c_i) + \sigma(c_1c_2 + c_2c_3) \tag{4.9}$$

into system (4.8), it is then reduced to

$$\frac{\mathrm{d}c_1}{\mathrm{d}t} = \frac{1}{3}\left(-2g'(c_1) + g'(c_2) + g'(c_3) + \sigma(c_1 - c_2 + c_3)\right) + \frac{1}{3}\frac{\mathrm{d}C(t)}{\mathrm{d}t}, \tag{4.10a}$$

$$\frac{\mathrm{d}c_2}{\mathrm{d}t} = \frac{1}{3}\left(g'(c_1) - 2g'(c_2) + g'(c_3) + \sigma(-2c_1 + 2c_2 - 2c_3)\right) + \frac{1}{3}\frac{\mathrm{d}C(t)}{\mathrm{d}t}, \tag{4.10b}$$

$$\frac{\mathrm{d}c_3}{\mathrm{d}t} = \frac{1}{3}\left(g'(c_1) + g'(c_2) - 2g'(c_3) + \sigma(c_1 - c_2 + c_3)\right) + \frac{1}{3}\frac{\mathrm{d}C(t)}{\mathrm{d}t}, \tag{4.10c}$$

where $g'(c) = 1-2c+\epsilon\log(c/(1-c))$. We let c_1 and c_3 denote the concentration in the two outside compartments, while c_2 denotes concentration in the centre compartment. Note that we choose a non-periodic boundary condition, so that compartment-1 and compartment-3 do not interact. As a result, there is an asymmetry between the outside compartments and the centre compartment, although c_1 and c_3 are equivalent by the system's inherent symmetry.

Because of the constraint that $c_1 + c_2 + c_3 = C$, the system is fundamentally two-dimensional. Writing $c_2 = C - (c_1 + c_3)$ and treating C as a given function of time, the dynamical system we are solving becomes

$$\frac{\mathrm{d}c_1}{\mathrm{d}t} = f_1(c_1, c_3, C), \tag{4.11a}$$

$$\frac{\mathrm{d}c_3}{\mathrm{d}t} = f_2(c_1, c_3, C), \tag{4.11b}$$

with

$$\begin{aligned} f_1(c_1, c_3, C) = {} & (6 + 2\sigma)c_1 + 2\sigma c_3 - (2 + \sigma)C \\ & - 2\epsilon\log\frac{c_1}{1 - c_1} + \epsilon\log\frac{C - (c_1 + c_3)}{1 - C + (c_1 + c_3)} + \epsilon\log\frac{c_3}{1 - c_3}, \end{aligned} \tag{4.11c}$$

$$\begin{aligned} f_2(c_1, c_3, C) = {} & 2\sigma c_1 + (6 + 2\sigma)c_3 - (2 + \sigma)C \\ & + \epsilon\log\frac{c_1}{1 - c_1} + \epsilon\log\frac{C - (c_1 + c_3)}{1 - C + (c_1 + c_3)} - 2\epsilon\log\frac{c_3}{1 - c_3}. \end{aligned} \tag{4.11d}$$

For the purpose of analysing the steady state of this system, we assume that C is slowly-varying, so that the system is always in quasi-equilibrium, with C effectively treated as a constant parameter. We then find the equilibria (c_1, c_3) of the dynamical system by solving $f_1 = 0$ and $f_2 = 0$. The rest of this chapter is devoted to finding all the equilibria as C varies between 0 and 3 and investigating how they relate to each other through bifurcations.

Once we have identified an equilibrium, we need to determine its stability with the Jacobian matrix J defined by [19]

$$J = \begin{pmatrix} \dfrac{\partial f_1}{\partial c_1} & \dfrac{\partial f_1}{\partial c_3} \\ \dfrac{\partial f_2}{\partial c_1} & \dfrac{\partial f_2}{\partial c_3} \end{pmatrix}. \tag{4.12}$$

Writing c_2 instead of $C - (c_1 + c_3)$ for brevity, the elements of the Jacobian matrix are given by

$$J_{11} = \frac{\partial f_1}{\partial c_1} = \left(2 + \frac{2}{3}\sigma\right) - \frac{2}{3}\epsilon\frac{1}{c_1(1-c_1)} - \frac{1}{3}\epsilon\frac{1}{c_2(1-c_2)}, \tag{4.13a}$$

$$J_{12} = \frac{\partial f_1}{\partial c_3} = \frac{2}{3}\sigma - \frac{1}{3}\epsilon\frac{1}{c_2(1-c_2)} + \frac{1}{3}\epsilon\frac{1}{c_3(1-c_3)}, \tag{4.13b}$$

$$J_{21} = \frac{\partial f_2}{\partial c_1} = \frac{2}{3}\sigma + \frac{1}{3}\epsilon\frac{1}{c_1(1-c_1)} - \frac{1}{3}\epsilon\frac{1}{c_2(1-c_2)}, \tag{4.13c}$$

$$J_{22} = \frac{\partial f_2}{\partial c_3} = \left(2 + \frac{2}{3}\sigma\right) - \frac{1}{3}\epsilon\frac{1}{c_2(1-c_2)} - \frac{2}{3}\epsilon\frac{1}{c_3(1-c_3)}. \tag{4.13d}$$

The trace and the determinant of the Jacobian matrix are given by

$$\mathrm{tr}J = J_{11} + J_{22}, \tag{4.14a}$$

$$\det J = J_{11}J_{22} - J_{12}J_{21}, \tag{4.14b}$$

whose signs determine the stability of the equilibrium [19].

To find all the equilibria of system (4.10), it is easier to investigate the equivalent system by retaining c_1, c_2, and c_3 as the unknowns:

$$C = c_1 + c_2 + c_3, \tag{4.15a}$$

$$0 = (4+\sigma)c_1 - (2+\sigma)c_2 + (-2+\sigma)c_3 - 2\epsilon\log\frac{c_1}{1-c_1} + \epsilon\log\frac{c_2}{1-c_2} + \epsilon\log\frac{c_3}{1-c_3}, \tag{4.15b}$$

$$0 = (-2+\sigma)c_1 - (2+\sigma)c_2 + (4+\sigma)c_3 + \epsilon\log\frac{c_1}{1-c_1} + \epsilon\log\frac{c_2}{1-c_2} - 2\epsilon\log\frac{c_3}{1-c_3}. \tag{4.15c}$$

The transcendental system (4.15) is not easily solvable. Exploiting the fact that ϵ is small, we look for asymptotic solutions instead of exact solutions. Our approach is to initially balance terms of order $\mathcal{O}(1)$ assuming ϵ is negligible. The logarithmic term $\epsilon \log \frac{c_i}{1-c_i}$ is of order $\mathcal{O}(1)$ only when c_i is exponentially close to 0 or 1. This divides c_i into 3 regimes: close to 0, close to 1, and the regime in between. For simplicity we denote them as $c_i \sim 0$, $c_i \sim 1$, and $c_i \sim X$ respectively. Altogether we will have $3^3 = 27$ different combinations of (c_1, c_2, c_3), although the symmetry means that we only need to consider 15 separate combinations. These are enumerated in Table 4.1. In each case, we give the equilibrium an alphabetic label, and list the corresponding value of C. When C is small, it is necessary to consider exponentially small and algebraically small separately.

	(c_1, c_2, c_3)	symmetric equivalent	range of C
A	$(0, 0, 0)$		exponentially small
B	$(0, 0, 0)$		algebraically small
C	$(X, 0, 0)$	$(0, 0, X)$	$C \in (0, 1)$
D	$(0, X, 0)$		$C \in (0, 1)$
E	$(X, X, 0)$	$(0, X, X)$	$C \in (0, 2)$
F	$(1, X, 0)$	$(0, X, 1)$	$C \in (1, 2)$
G	$(X, 1, 0)$	$(0, 1, X)$	$C \in (1, 2)$
H	$(X, 0, X)$		$C \in (0, 2)$
I	$(1, 0, X)$	$(X, 0, 1)$	$C \in (1, 2)$
J	(X, X, X)		$C \in (0, 3)$
K	$(1, X, X)$	$(X, X, 1)$	$C \in (1, 3)$
L	$(X, 1, X)$		$C \in (1, 3)$
M	$(1, 1, X)$	$(X, 1, 1)$	$C \in (2, 3)$
N	$(1, X, 1)$		$C \in (2, 3)$
O	$(1, 1, 1)$		$C \sim 3$
P	$(1, 0, 0)$	$(0, 0, 1)$	$C \sim 1$
Q	$(0, 1, 0)$		$C \sim 1$
R	$(1, 1, 0)$	$(0, 1, 1)$	$C \sim 2$

Table 4.1: Enumeration of possible (c_1, c_2, c_3) combinations. To simplify the notation, we follow the convention that $T \in (a, b)$ means T is a value between a and b, but not close to a or b.

4.3.1 A simple case when $c_1 \sim X$, $c_2 \sim X$, and $c_3 \sim X$

Here we exemplify the basic steps of our analysis with the simplest case when $c_1 \sim X$, $c_2 \sim X$, and $c_3 \sim X$. At the leading order, we can neglect all logarithmic terms in

the system (4.15) and reduce it to a simple algebraic system:

$$c_1 + c_2 + c_3 = C, \tag{4.16a}$$

$$(4+\sigma)c_1 - (2+\sigma)c_2 + (-2+\sigma)c_3 = 0, \tag{4.16b}$$

$$(-2+\sigma)c_1 - (2+\sigma)c_2 + (4+\sigma)c_3 = 0. \tag{4.16c}$$

It is easy to solve equation (4.16) to get

$$c_1 = c_3 = \left(\frac{1}{3} - \frac{\sigma}{6(3+2\sigma)}\right) C, \tag{4.17a}$$

$$c_2 = \left(\frac{1}{3} + \frac{\sigma}{3(3+2\sigma)}\right) C, \tag{4.17b}$$

which corresponds to the case J in Table 4.1.

Substituting c_1, c_2, and c_3 into equation (4.12), the Jacobian matrix is approximately

$$J = \begin{pmatrix} 2+\frac{2}{3}\sigma & \frac{2}{3}\sigma \\ \frac{2}{3}\sigma & 2+\frac{2}{3}\sigma \end{pmatrix}, \tag{4.18}$$

and

$$\mathrm{t}r(J) = 4 + \frac{4}{3}\sigma > 0, \tag{4.19a}$$

$$\mathrm{d}et(J) = 4 + \frac{8}{3}\sigma > 0, \tag{4.19b}$$

thus this equilibrium point $(c_1, c_2, c_3) = (X, X, X)$ is an **unstable node**.

Furthermore, for the assumption $(c_1, c_2, c_3) \sim (X, X, X)$ to hold, we require $0 < C < 3 - \frac{\sigma}{1+\sigma}$. As C approaches $3 - \frac{\sigma}{1+\sigma}$, c_1 and c_3 approach 1, and the logarithmic term is no longer negligible. This suggests that 0 and $3 - \frac{\sigma}{1+\sigma}$ are critical values for C. The transition regions will be studied in later sections.

4.3.2 Brief summary of the equilibria

We carry out detailed analysis for all cases in Table 4.1 following the same steps as in Section 4.3.1. We list the solutions in Table 4.2 and leave the calculations in Appendix C.

Table 4.2 shows the stability of each equilibrium, the range of C that can see this equilibrium, the asymptotic solutions of (c_1, c_2, c_3), and the section number where the analysis can be found.

	Type	c_1	c_2	c_3	C	Appendix
A	stable node	$\frac{C}{3}$	$\frac{C}{3}$	$\frac{C}{3}$	$\sim \mathcal{O}(e^{-1/\epsilon})$	C.1
B	stable node	$\frac{2+\sigma}{2(3+2\sigma)}C$	$\frac{1+\sigma}{3+2\sigma}C$	$\frac{2+\sigma}{2(3+2\sigma)}C$	$\sim \mathcal{O}(\epsilon)$	C.2
C	stable node	C	$e^{-(2+\sigma)C/\epsilon}$	$e^{-2C/\epsilon}$	$(0,1)$	C.3
D	stable node	$e^{\left(-\frac{2+\sigma}{\epsilon}C\right)}$	C	$e^{\left(-\frac{2+\sigma}{\epsilon}C\right)}$	$(0,1)$	C.5
E	saddle	$\frac{C}{2}$	$\frac{C}{2}$	$e^{-C/\epsilon}$	$(0,2)$	C.7
F	stable node	$1-e^{-\frac{2+\sigma}{\epsilon}(2-C)}$	$C-1$	$e^{\frac{2+\sigma}{\epsilon}(2-C)-\frac{2}{\epsilon}}$	$(1,2)$	C.8
G	stable node	$C-1$	$1-e^{-\frac{(2+\sigma)(C-1)}{\epsilon}}$	$e^{-\frac{2(C-1)}{\epsilon}}$	$(1,2)$	C.9
H	saddle	$\frac{C}{2}$	$e^{-\frac{(1+\sigma)C}{\epsilon}}$	$\frac{C}{2}$	$(0,2)$	C.11
I	stable node	$1-e^{-\frac{4-2C}{\epsilon}}$	$e^{-\frac{(2+\sigma)(C-1)-\sigma}{\epsilon}}$	$C-1$	$(1,2)$	C.12
J	unstable node	$\frac{2+\sigma}{2(3+2\sigma)}C$	$\frac{1+\sigma}{3+2\sigma}C$	$\frac{2+\sigma}{2(3+2\sigma)}C$	$(0,3-\frac{\sigma}{1+\sigma})$	C.13
K	saddle	$1-e^{-\frac{3-C}{\epsilon}}$	$\frac{C-1}{2}+\frac{\sigma}{2(2+\sigma)}$	$\frac{C-1}{2}-\frac{\sigma}{2(2+\sigma)}$	$(1+\frac{\sigma}{2+\sigma},3-\frac{\sigma}{2+\sigma})$	C.14
L	saddle	$\frac{C-1}{2}$	$1-e^{\frac{(1+\sigma)(C-1)-2-\sigma}{\epsilon}}$	$\frac{C-1}{2}$	$(1,3-\frac{\sigma}{1+\sigma})$	C.15
M	stable node	$1-e^{-\frac{2(3-C)}{\epsilon}}$	$1-e^{-\frac{2(3-C)}{\epsilon}}$	$C-2$	$(2,3)$	C.16
N	stable node	$1-e^{-\frac{2(3-C-2\sigma)}{\epsilon}}$	$C-2$	$1-e^{-\frac{2(3-C-2\sigma)}{\epsilon}}$	$(2,3)$	C.17
O	stable node	$1-\frac{1}{2+e^{\sigma/\epsilon}}(3-C)$	$1-\frac{e^{\sigma/\epsilon}}{2+e^{\sigma/\epsilon}}(3-C)$	$1-\frac{1}{2+e^{\sigma/\epsilon}}(3-C)$	~ 3	C.18

Table 4.2: Equilibria of the three-compartment system.

To better communicate the information in Table 4.2, we draw complementary diagrams in Fig. 4.4, which plots the equilibria on the $c_1 - c_3$ plane for 9 typical values of C. The shaded area is the range in which c_1 and c_3 can vary for the given value of C, since $0 < c_i < 1, i = 1, 2, 3$ imposes additional constraints as

$$c_1 + c_2 < C, \qquad \text{when } 0 < C < 1; \tag{4.20a}$$

$$C - 1 < c_1 + c_2 < C, \qquad \text{when } 1 < C < 2; \tag{4.20b}$$

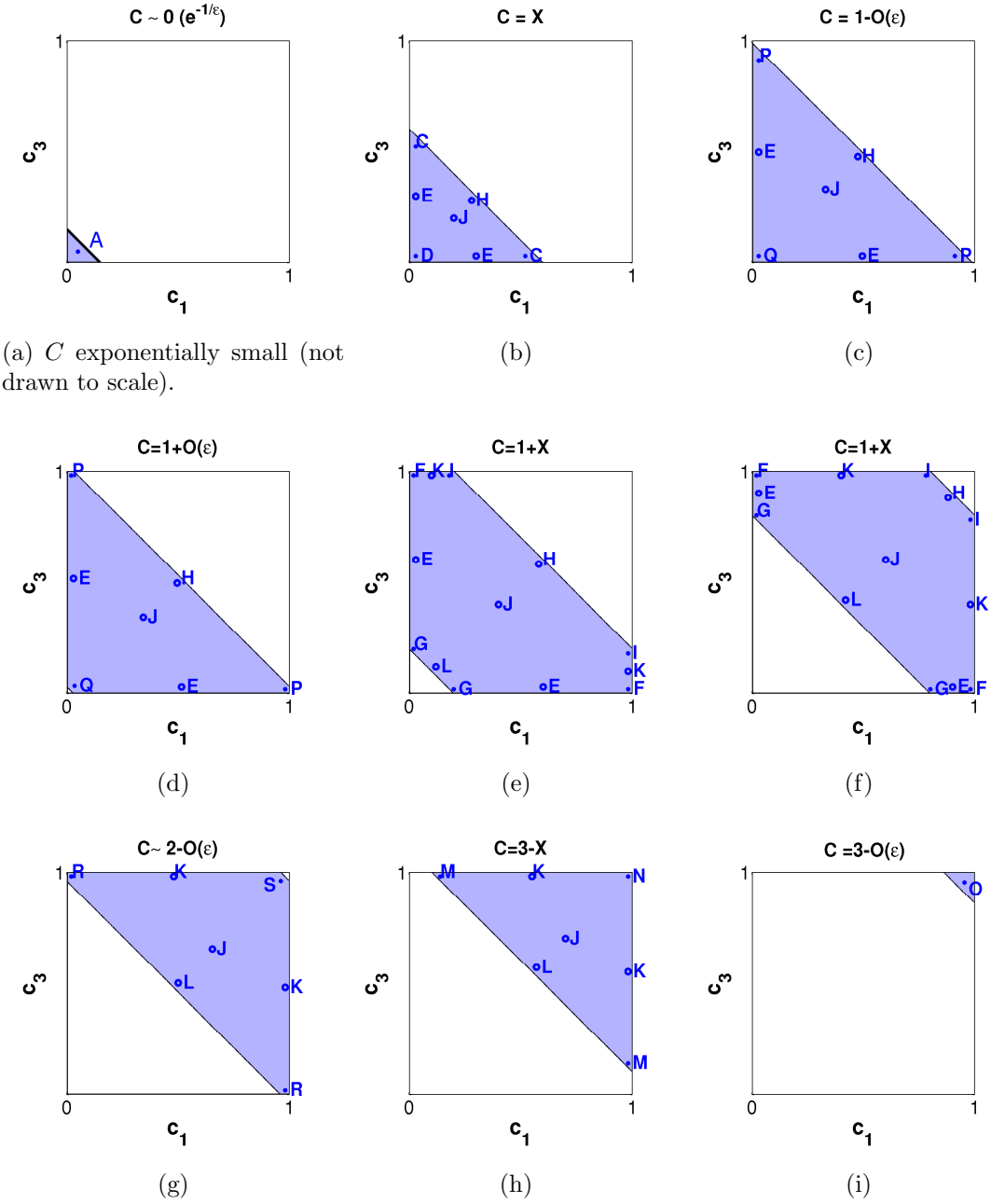
$$C - 1 < c_1 + c_2, \qquad \text{when } 2 < C < 3. \tag{4.20c}$$

Figure 4.4 confirms one aspect of the filling pattern we observed in the numerical simulations of Section 4.2: it is always preferred that some compartments are near full and other compartments are near empty. A uniform concentration across all compartments is not preferred, except when the system is near full or near empty. For instance, in Figure 4.4(a) and (i), which show a very low concentration and a very high concentration, there is only one equilibrium in the system. In contrast, when the concentration is in the intermediate range as in Figure 4.4(b - h), there are multiple stable nodes, all of which share the same property that at least one of c_1, c_2, and c_3 is close to zero or one. Physically this suggests that to minimise the total energy, the system always wants a compartment to be empty/full, while the logarithmic double well prevents it from being completely empty/full. It is also noticeable that $c_1 \approx c_2 \approx c_3$ is always an equilibrium (give by (4.17)), although due to the high interaction energy associated with this state it is unstable except when $C \approx 0$ or $C \approx 3$.

As C increases from 0 to 3, the system undergoes very complicated transitions, which will be explored in the following sections.

4.3.3 Equilibria when C is close to 0

In this section we analyse the transition from (a) to (b) in Fig. 4.4. When C is exponentially small (a), the only equilibrium is the stable node A, where $c_1 = c_2 = c_3 = \frac{C}{3}$. This explains why starting from a very small random distribution, we would see the system quickly redistribute to a uniform distribution. When C grows to order $\mathcal{O}(1)$ (b), the system has 7 equilibria (stable node C, D; saddle E, H; and unstable node J). So the system can take two stable configurations, C and D : C is associated with $[X, 0, 0]$, suggesting the lithium flows entirely into the outside compartment; D is associated with $[0, X, 0]$, suggesting the lithium flows entirely into the centre compartment.



(a) C exponentially small (not drawn to scale). (b) (c)

(d) (e) (f)

(g) (h) (i)

Figure 4.4: Plots of equilibria on the $c_1 - c_3$ plane, as C increases from near 0 in the top-left panel to near 3 in the bottom-right panel. X denotes a value that is not close to 0 or 1, and the shaded area is the region allowed for $[c_1, c_3]$ given the total concentration C, as given by (4.20). Round dots represent stable nodes in the $c_1 - c_3$ plane given the total concentration specified, and empty circles represent unstable nodes and saddles. The equilibria are labelled in accordance with Table 4.2.

To understand the system evolution when C exceeds the exponentially small regime, we need to analyse the behaviour when C grows from exponentially small to algebraically small. We make the transformation of $X_1 = c_1/\epsilon$, $X_2 = c_2/\epsilon$, $X_3 = c_3/\epsilon$, $\Gamma = C/\epsilon$ and rewrite equation (4.15) as

$$\Gamma = X_1 + X_2 + X_3, \tag{4.21a}$$

$$\mathcal{O}(\epsilon) = (4+\sigma)X_1 - (2+\sigma)X_2 + (-2+\sigma)X_3 - 2\log X_1 + \log X_2 + \log X_3, \tag{4.21b}$$

$$\mathcal{O}(\epsilon) = (-2+\sigma)X_1 - (2+\sigma)X_2 + (4+\sigma)X_3 + \log X_1 + \log X_2 - 2\log X_3. \tag{4.21c}$$

Subtracting equation (4.21b) from equation (4.21c) gives:

$$2X_1 - \log X_1 = 2X_3 - \log X_3. \tag{4.22}$$

There are two solution branches for equation (4.22): $X_1 = X_3$ and $X_1 \neq X_3$. The solution $X_1 = X_3$ corresponds to the symmetric line $c_1 = c_3$ on the $c_1 - c_3$ plane, and we will refer to this as the symmetric branch. The solution where $X_1 \neq X_3$ is the asymmetric branch, and due to the symmetry between X_1 and X_3, we expect this branch to be associated with a pair of solutions which are symmetric about the $c_1 = c_3$ line. By analysing the two branches, we will show that four bifurcations happen in sequence for the equilibria to change from (a) to (b) in Fig. 4.4. Although configuration of the final equilibria when C grows to order $\mathcal{O}(1)$ is fixed regardless of the value of σ, the properties and sequence of the four bifurcations can differ depending on σ.

4.3.3.1 The symmetric branch

On this branch $X_1 = X_3$ so that equation (4.22) always holds. We solve equation (4.21b, 4.21c) parametrically by introducing a parameter $\mu = X_1/\Gamma$ (so $\mu < 1/2$). Solutions are given by

$$X_1 = X_3 = \mu\frac{\log\mu - \log(1-2\mu)}{(6+4\sigma)\mu - (2+\sigma)}, \tag{4.23a}$$

$$\Gamma = \frac{\log\mu - \log(1-2\mu)}{(6+4\sigma)\mu - (2+\sigma)}. \tag{4.23b}$$

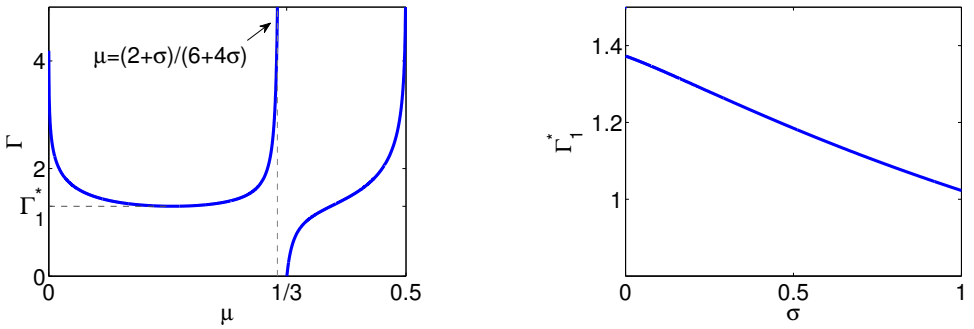
We plot Γ in terms of μ in the left panel of Fig. 4.5. Clearly there is a critical value for Γ, which we call Γ_1^*. When $\Gamma < \Gamma_1^*$, there is only a single solution for μ, and $\mu \in (1/3, 1/2)$. On the other hand, three solutions of μ exist when $\Gamma > \Gamma_1^*$, two in the region $(0, (2+\sigma)/(6+4\sigma))$ and one in $(1/3, 1/2)$.

The value Γ_1^* is the critical value for of a bifurcation that preserves the symmetry of X_1 and X_3. We note that Γ_1^* is associated with a minimum of Γ with respect to μ. Hence, we seek μ_1^* that makes $\frac{d\Gamma}{d\mu}|_{\mu_1^*} = 0$ and substitute it back to (4.23), which yields parametric solutions for σ and Γ_1^*

$$\sigma = -\frac{3}{2} + \frac{1}{2\left[4\mu - 1 + 4\mu(1-2\mu)\log\left(\frac{1-2\mu}{\mu}\right)\right]}, \tag{4.24a}$$

$$\Gamma_1^* = \frac{4\mu - 1 + 4\mu(1-2\mu)\log\left(\frac{1-2\mu}{\mu}\right)}{2\mu(1-2\mu)}. \tag{4.24b}$$

We plot Γ_1^* versus σ in the right panel of Fig. 4.5, for $\mu \in (0.087864, 0.2076)$. We see that Γ_1^* is $\mathcal{O}(1)$ for all $\sigma \in (0,1)$, suggesting that the symmetry-preserving bifurcation happens when C grows be $\mathcal{O}(\epsilon)$.

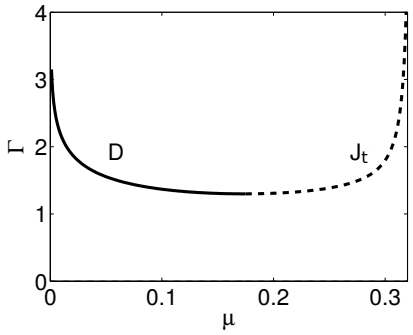


(a) $\Gamma = \frac{C}{\epsilon}$ in terms of $\mu = \frac{c_1}{C}$ when C is algebraically small and when $c_1 = c_3$.

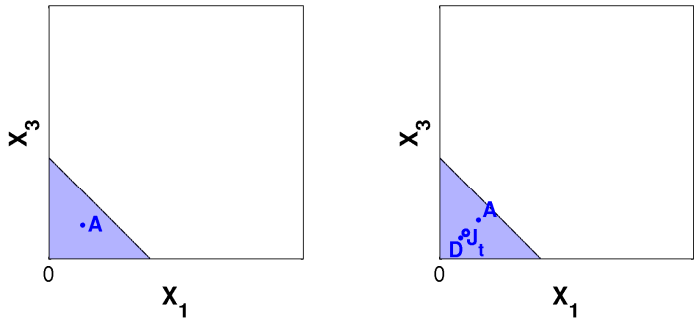
(b) The critical value of Γ_1^* when a symmetry-preserving bifurcation happens, plotted versus σ.

Figure 4.5: Symmetry-preserving bifurcation when the total concentration is algebraically small.

We call this symmetry-preserving bifurcation B_{I}. By examining the trace and determinant (4.14) of the Jacobian matrix of the symmetric solution, we identify it as a saddle-node bifurcation, shown in Fig. 4.6(a). In the region $\mu < (2+\sigma)/(6+4\sigma)$, smaller μ is associated with the stable node D, and larger μ is associated with the saddle J_{t}. On the other hand, the solution branch of $\mu \in (1/3, 1/2)$ is associated with the stable node A, which is also the only equilibrium when C is exponentially small. Additionally, Fig. 4.5(a) suggests that as the scaled total concentration Γ increases, μ goes up. As μ gets closer to $1/2$, the stable node A gets farther away from the centre of the triangle ($c_1 = c_2 = c_3$ when C is exponentially small) and moves closer to the line $X_1 + X_3 = \Gamma$. Combining the above analysis, we show the equilibria before and after the B_{I} bifurcation in Fig. 4.6(b).



(a) The symmetry-preserving bifurcation B_{I} is a saddle node bifurcation.



(b) Equilibria of the three-compartment system before and after the bifurcation B_{I}. Here only the equilibria associated with this bifurcation are shown.

Figure 4.6: Illustration of the symmetry-preserving bifurcation B_{I} when the total concentration is algebraically small. We use round dots for stable nodes and empty circles for unstable nodes and saddles.

4.3.3.2 The asymmetric branch

To find solutions to equation (4.22) where $X_1 \neq X_3$, we let $\alpha = X_1/X_2, \beta = X_3/X_2$ and subtract/add (4.21b) and (4.21c) to obtain

$$X_2\left((2+2\sigma)(\alpha+\beta) - 2(2+\sigma)\right) = \log\alpha + \log\beta, \tag{4.25a}$$

$$2X_2(\alpha-\beta) = \log\alpha - \log\beta, \tag{4.25b}$$

so that X_1, X_2, and X_3 are given parametrically by α and β. Meanwhile, (4.25) requires α and β to satisfy

$$(\log\alpha - \log\beta)\left((1+\sigma)(\alpha+\beta) - (2+\sigma)\right) = (\alpha-\beta)(\log\alpha + \log\beta). \tag{4.26}$$

Two branches of asymmetric solution pairs First of all, (4.26) indicates two branches of asymmetric solution pairs. To show this, we note that equation (4.26)

specifies a parametric representation of σ in terms of α and β:

$$\sigma = -1 + \frac{1}{\alpha+\beta-1} + \frac{\alpha-\beta}{\alpha+\beta-1}\frac{\log(\alpha)+\log(\beta)}{\log(\alpha)-\log(\beta)}. \tag{4.27}$$

The contours of σ given by (4.27) are plotted in Fig. 4.7, indicating that given a fixed value of σ, two branches of asymmetric solution pairs exist, one in the regime $\alpha > 1, \beta > 1$, and one in the regime $\alpha < 1, \beta < 1$.

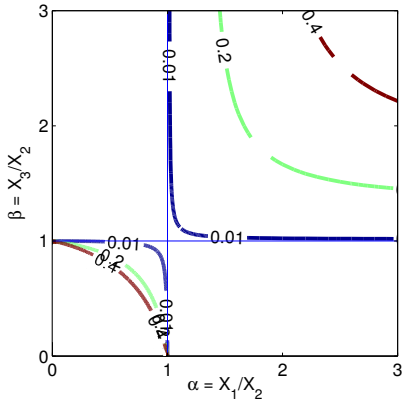


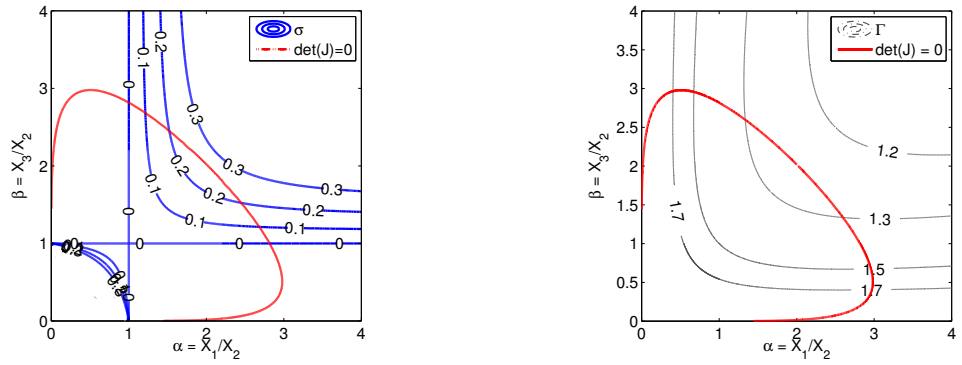
Figure 4.7: Contour plot of σ in the $\alpha - \beta$ plane as given by (4.27).

The scaled total concentration $\Gamma = X_2(1+\alpha+\beta)$ is given by (4.25),

$$\Gamma = \frac{(1+\alpha+\beta)(\log\alpha - \log\beta)}{2(\alpha-\beta)}. \tag{4.28}$$

Its contours are plotted in Fig. 4.8(b). Clearly, the solution branch in $\alpha < 1, \beta < 1$ corresponds to higher concentration than the solution branch in $\alpha > 1, \beta > 1$.

In addition, at each point in the $\alpha - \beta$ plane, we can find the solution numerically with (4.25), and then use it to determine its stability. We find that there is a critical line on which $\det(J) = 0$, which divides the $\alpha - \beta$ plane into a stable region and an unstable region. This line is shown in red in the plot of Fig. 4.8(b); the region enclosed by this line is unstable, and the region outside the line is stable. Evidently, the branch of asymmetric solutions in the regime $\alpha < 1, \beta < 1$ is always unstable, but the other branch in the regime $\alpha > 1, \beta > 1$ can be either stable or unstable. We incorporate the critical line $\det(J) = 0$ into the σ contour in Fig. 4.8(a), which suggests an an apparent critical value for σ: if σ is above this value (around 0.26), the asymmetric solution in $\alpha > 1, \beta > 1$ is always stable; otherwise, its stability depends on the value of Γ.



(a) Contour of σ given by (4.27). (b) Contour of Γ given by (4.28).

Figure 4.8: Contour plots for σ and Γ in the $\alpha - \beta$ plane. In both panels the red line $\det(J) = 0$ is computed from numerics, and it divides the plane into a stable region (outside the red line) and an unstable region (inside the red line).

Saddle-node bifurcations To understand how the stability of the asymmetric branch is determined by σ, we examine the contour plots of σ and Γ side-by-side. The two contour plots are illuminating in that their intersections are the solutions in the $\alpha - \beta$ plane. We will show that in the regime $\alpha > 1, \beta > 1$, the intersection of the two contours have two different configurations depending on the value of σ, hence leading to the different stability properties.

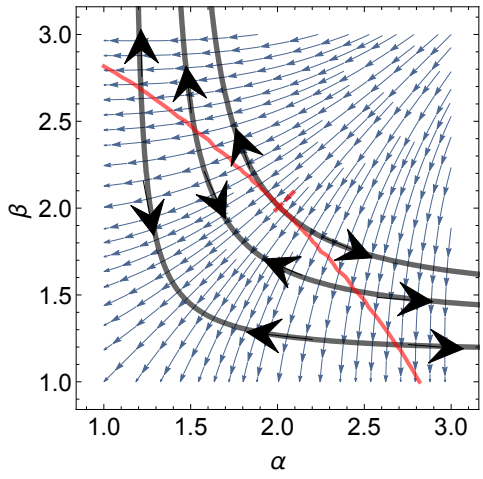
In Fig. 4.9(a), we show three contours of $\sigma = 0.1$, $\sigma = 0.2$ and $\sigma = 0.26$ in black and plot the streamlines of the gradient of Γ in blue. The $\det J = 0$ line in shown in red. We deduce that along the $\det J = 0$ line, the gradient of Γ is perpendicular to the $\sigma = \text{const}$ line. To confirm this, we plot the line where $\sigma = \text{const}$ is parallel to $\Gamma = \text{const}$ in Fig. 4.9(b), which is found by numerically solving

$$\frac{\partial \Gamma}{\partial \alpha}\frac{\partial \sigma}{\partial \beta} - \frac{\partial \Gamma}{\partial \beta}\frac{\partial \sigma}{\partial \alpha} = 0 \tag{4.29}$$

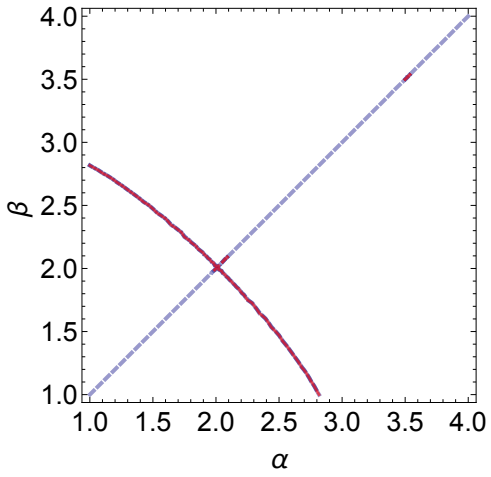
in the $\alpha - \beta$ plane. Clearly this line coincides with the red $\det J = 0$ line given that $\alpha \neq \beta$.

In this plot, along each contour of σ, the black arrows indicate the direction along which Γ increases. Clearly, for larger σ whose contour line lies entirely in the stable region and hence does not intersect with $\det J = 0$, the point of minimum Γ lies at the $\alpha = \beta$ line, indicating that the asymmetric solution pair bifurcates from the symmetric solution.

In contrast, for smaller values of σ whose contours intersect with the $\det J = 0$ line, the points of minimum Γ are at the intersection points and generally not on the $\alpha = \beta$ line. Each of the two intersection points is associated with a saddle-node



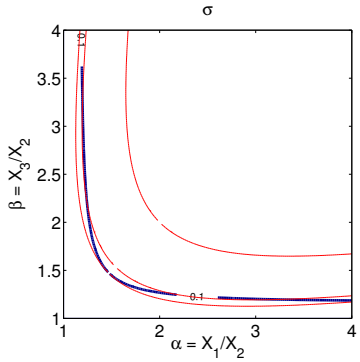
(a) Three contours of $\sigma = 0.1, 0.2, 0.26$ in black, $\det J = 0$ in red, as well as the streamlines of the gradient of Γ.



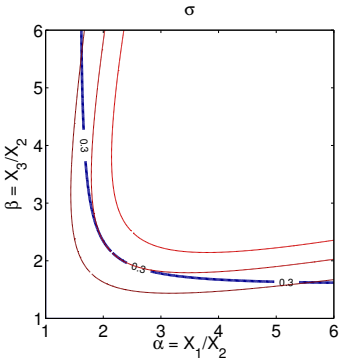
(b) The line where σ contours are parallel to Γ contours (blue dashed line) with $\det J = 0$ (red solid line) when $\alpha \neq \beta$.

Figure 4.9: Contour plot of σ and Γ, given by (4.27) and (4.28).

bifurcation. As Γ increases, the nodes move further away from the symmetric line, while the saddles move towards the symmetric line, and potentially annihilates with each other as well as the symmetric solution when Γ increases further. The two distinctive intersection patterns are illustrated in Fig. 4.10, where we plot how the Γ contours intersect with a fixed σ contour for $\sigma = 0.1$ and $\sigma = 0.3$.



(a) $\sigma = 0.1$, there exist up to four intersections for appropriate values of Γ.



(b) $\sigma = 0.3$ has at most two intersections.

Figure 4.10: Contour plots showing the intersections of a fixed σ contour and various Γ contours.

In summery, we have identified two different bifurcations that lead to the existence of asymmetric solution pairs. One is by breaking the symmetry of X_1 and X_3, which we call symmetry-breaking bifurcation, and it happens in both the $\alpha > 1, \beta > 1$ regime and $\alpha < 1, \beta < 1$ regime. The other is a saddle-node bifurcation on the

asymmetric solution branch, which only exist in the $\alpha > 1, \beta > 1$ regime, and only when $\sigma < 0.26$. We denote this saddle-node bifurcation as B_{o}. The critical value of Γ_0^* for this saddle-node bifurcation can be found by combining (4.28), (4.27), and (4.29), as plotted in Fig. 4.11.

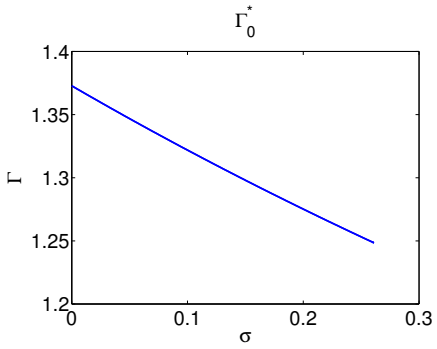


Figure 4.11: Plot of the critical value Γ verus σ for the saddle-node bifurcation B_{o}, which only occurs when $\sigma < 0.26$.

Symmetry-breaking bifurcations Now we focus on the symmetry-breaking bifurcations, identifying their critical values as well as establishing their change of stability property. To find the critical value of Γ, we linearise the two variables around the critical values by $\alpha = \beta = \alpha^*$ by by letting

$$\alpha = \alpha^* + \gamma, \qquad \beta = \alpha^* + \delta, \tag{4.30}$$

where we assume δ and γ are small quantities of the same order. Substituting (4.30) into (4.26) and carrying out Taylor expansions, we obtain

$$\begin{aligned}
&(\gamma - \delta)\left(2\log\alpha^* + \frac{\delta}{\alpha^*} - \frac{\delta^2}{2(\alpha^*)^2} - \frac{\gamma}{\alpha^*} - \frac{\gamma^2}{2(\alpha^*)^2} + \cdots\right) \\
&= \left(-\frac{\delta}{\alpha^*} + \frac{\delta^2}{2(\alpha^*)^2} + \frac{\gamma}{\alpha^*} - \frac{\gamma^2}{2(\alpha^*)^2} + \cdots\right)\left(2(1+\sigma)\alpha^* + (1+\sigma)(\delta+\gamma) - (2+\sigma)\right).
\end{aligned} \tag{4.31}$$

Matching at order $\mathcal{O}(\delta)$ requires that

$$(\gamma - \delta)2\log\alpha^* = \frac{\gamma - \delta}{\alpha^*}\left(2(1+\sigma)\alpha^* - (2+\sigma)\right), \tag{4.32}$$

so that α^* is related to σ by

$$\sigma = \frac{2\alpha^*\log\alpha^* - 2\alpha^* + 2}{2\alpha^* - 1}. \tag{4.33}$$

Meanwhile matching at order $\mathcal{O}(\delta^2)$ requires that

$$\frac{\gamma^2-\delta^2}{\alpha^*}=\frac{2+\sigma}{2(\alpha^*)^2}(\gamma^2-\delta^2). \tag{4.34}$$

Because α^* is determined at order $\mathcal{O}(\delta)$ and generally not equal to $1+\sigma/2$, for (4.34) to hold, we need

$$\gamma^2-\delta^2=0, \tag{4.35}$$

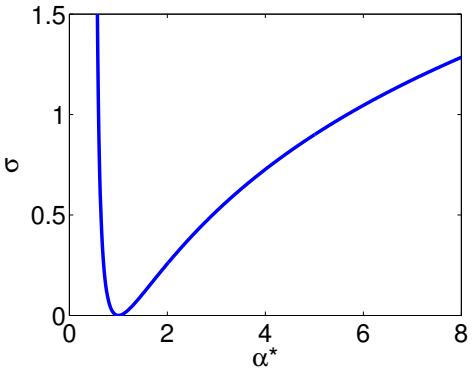
and asymmetric solutions that we seek correspond to

$$\gamma=-\delta. \tag{4.36}$$

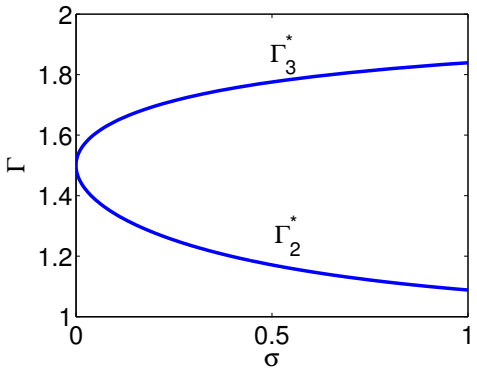
Now equation (4.33) specifies the critical value of α and β for the two symmetry-breaking bifurcations. We combine (4.33) with (4.25a), and use $\Gamma=X_2(1+\alpha+\beta)$ to find the corresponding critical value in Γ^* as

$$\Gamma^*=1+\frac{1}{2\alpha^*}. \tag{4.37}$$

The relations of α^* and Γ^* with σ given by equations (4.33) and (4.37) are plotted in Fig. 4.12. As shown Fig. 4.12(a), for every given value of σ, there are two possible solutions for α^*: $\alpha^*>1$ or $\frac{1}{2}<\alpha^*<1$, and these two solutions for α^* correspond to the two branches of solution pairs in the $\alpha-\beta$ plane shown in Fig. 4.7.



(a) Plot of σ versus α^* given by (4.33). This specifies the critical value for $\alpha=X_1/X_2$ when the two symmetry-breaking bifurcations happen.

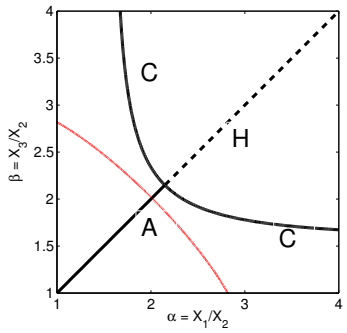


(b) Plot of the critical value Γ versus σ, given by (4.33) and (4.37). Each σ is associated with two values of Γ: the larger $\Gamma=\Gamma_3^*$ corresponds to the bifurcation when $\alpha^*<1$, and a smaller $\Gamma=\Gamma_2^*$ corresponds to the bifurcation when $\alpha^*>1$.

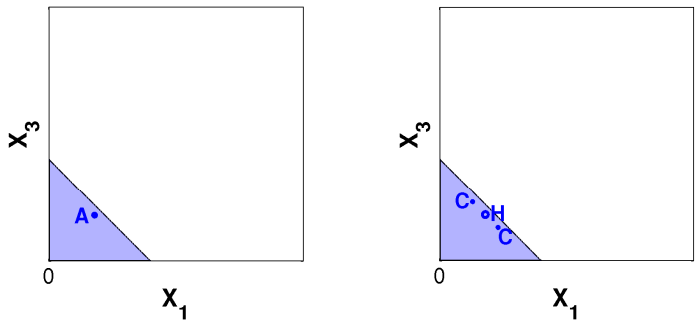
Figure 4.12: Critical parameter values for the two bifurcations that break symmetry when the total concentration is algebraically small.

We label the bifurcation at $\alpha^*>1$ as B_{II} and the corresponding critical value as Γ_2^*, and the bifurcation at $\alpha^*<1$ as B_{III} and the critical value as Γ_3^*.

The symmetry-breaking bifurcation B_{II} The symmetry-breaking bifurcation at $\alpha > 1, \beta > 1$ is marked as B_{II}. As discussed earlier, when $\sigma > 0.26$, the asymmetric solution pair bifurcated from B_{II} are always stable. By checking the change of stability of the equilibrium A, we can confirm that B_{II} is a supercritical pitchfork bifurcation. This bifurcation is illustrated in Fig. 4.13(a) in the $\alpha - \beta$ plane with $\sigma = 0.3$. The symmetric solutions before and after B_{II} are A and H, and the asymmetric solution C is the contour of $\sigma = 0.3$. The red line on which $\det(J) = 0$ is retained to highlight that the asymmetric branch C is always stable in this case. In Fig. 4.13(b) we also show the change of equilibria (associated with B_{II}) in the $X_1 - X_3$ plane.



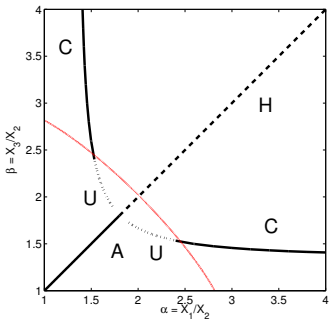
(a) The symmetry-breaking bifurcation B_{II} is a supercritical pitchfork bifurcation when $\sigma > 0.26$.



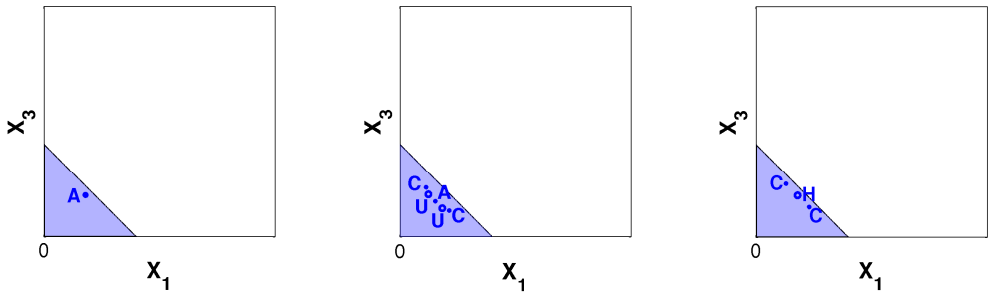
(b) The change of equilibria of the bifurcation B_{II}. Here only the equilibria associated with this bifurcation are shown.

Figure 4.13: Illustration of the symmetry-breaking bifurcation B_{II} when $\sigma > 0.26$. We use round dots for stable nodes and empty circles for unstable nodes and saddles.

On the other hand, when $\sigma < 0.26$, we find the bifurcation B_{II} to be a subcritical bifurcation. In this case, the stable symmetric equilibrium A collides with the two saddles of the saddle-node bifurcation B_{o}. We show the bifurcation plot and the change of equilibria in Fig. 4.14.



(a) The symmetry-breaking bifurcation B_{II} is a subcritical pitchfork bifurcation when $\sigma < 0.26$. A saddle-node bifurcation B_{o}happens first before B_{II}.



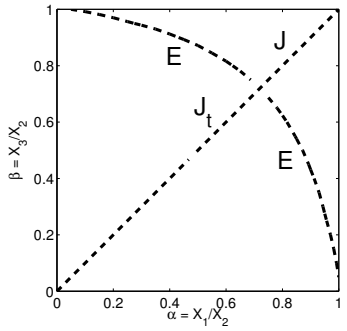
(b) The change of equilibria of the bifurcation B_{II} and the saddle-node bifurcation. Here only the equilibria associated with this bifurcation are shown.

Figure 4.14: Illustration of the symmetry-breaking bifurcation B_{II} when $\sigma < 0.26$. We use round dots for stable nodes and empty circles for unstable nodes and saddles.

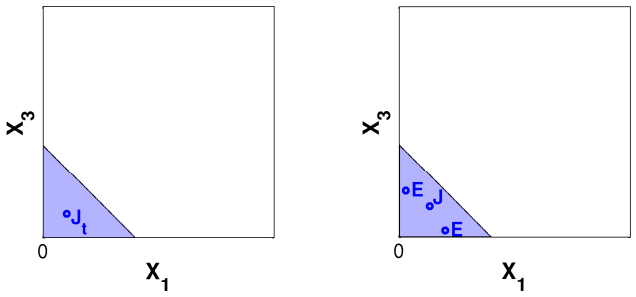
The symmetry-breaking bifurcation B_{III} The other symmetry-breaking bifurcation B_{III} is relatively simple. Since it bifurcates from a symmetric solution of $\alpha = \beta < 1$, it has to bifurcate from the saddle point J_{t}. Meanwhile examination of the trace and determinant of its Jacobian suggests that the asymmetric solutions are of saddle type. This leads to the bifurcation plot and the change of equilibria illustrated in Fig. 4.15. At the bifurcation, the saddle point J_{t} becomes an unstable node J; meanwhile two new saddles E come into existence.

4.3.3.3 Summary of bifurcations when T is algebraically small

In summary, as C increases from exponentially small to algebraically small, up to four bifurcations could happen: a symmetry-preserving bifurcation B_{I}, two symmetry-breaking ones B_{II} and B_{III}, and a saddle-node bifurcation B_{o} on the asymmetric solution branch which only occurs when $\sigma < 0.26$.



(a) The symmetry-breaking bifurcation B_{III}.



(b) The change of equilibria of the bifurcation B_{III}. Here only the equilibria associated with this bifurcation is shown.

Figure 4.15: Illustration of the symmetry-breaking bifurcation B_{III}. We use round dots for stable nodes and empty circles for unstable nodes and saddles.

To determine the bifurcation sequence, we notice that the two symmetry-breaking bifurcations B_{II} and B_{III} have to bifurcate from a symmetric equilibrium: B_{II} bifurcations from the stable node A and B_{III} bifurcates from the saddle node J_{t}. Because the saddle node J_{t} only exists after the B_{I} bifurcation, and because we know B_{III} happens after B_{II}, B_{III} has to be the last bifurcation of the three. On the other hand, which one of B_{o}, B_{I} and B_{II} happens first again depends on the value of σ.

We have obtained parametric solutions, (4.24b), (4.33), (4.37) for the three critical values of Γ for B_{I}, B_{II}, and B_{III}. We have also found numerical solution of the critical value for B_{o}. Plotting them together with respect to σ in Fig. 4.16 suggests that B_0 always happens first. For $\sigma \in (0.108, 0.603)$, $\Gamma_2^* < \Gamma_1^*$ and B_{II} happens before B_{I}. Otherwise $\Gamma_2^* > \Gamma_1^*$ and B_{I} happens before B_{II}. This introduces four possible scenarios, which we summarise in Table 4.3.

The changes of the equilibria of the four different scenarios are illustrated in Fig. 4.17. Suppose that when any bifurcation happens the system prefers to stay in

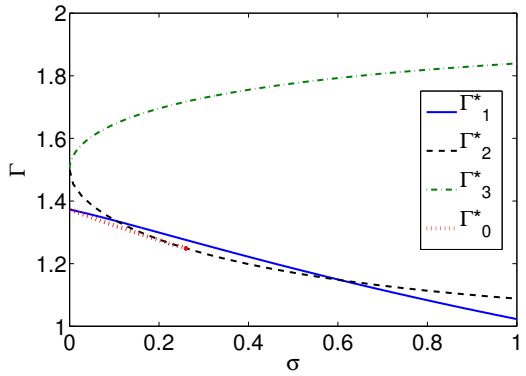


Figure 4.16: Critical values when C is small.

	Sequence	Bifurcation properties of B_{II}	In Fig. 4.17
$\sigma < 0.108$	B_{o}, B_{I}, B_{II}, B_{III}	subcritical pitchfork	(a)
$0.108 < \sigma < 0.26$	B_{o}, B_{II}, B_{I}, B_{III}	subcritical pitchfork	(b)
$0.26 < \sigma < 0.603$	B_{II}, B_{I}, B_{III}	supercritical pitchfork	(c)
$\sigma > 0.603$	B_{I}, B_{II}, B_{III}	supercritical pitchfork	(d)

Table 4.3: Four possible bifurcation scenarios depending on σ.

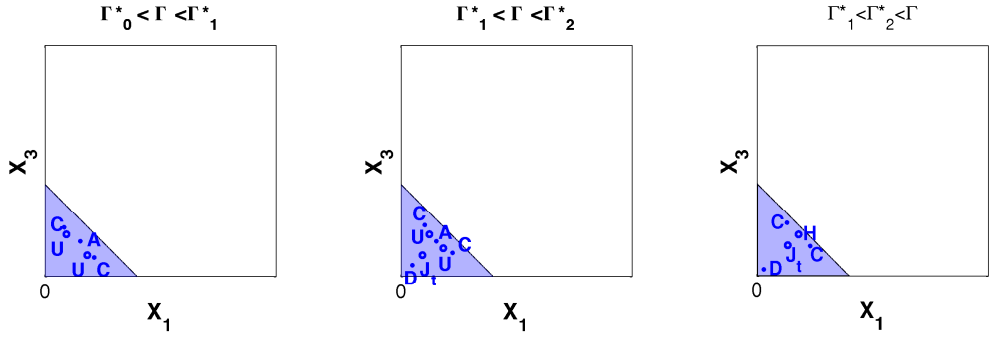
the original stable equilibrium if it still exists after the bifurcation, and the system would only switch to a different stable equilibrium if the original equilibrium changes its stability. Among the four possible scenarios, only in case (a) would the system start from state A but could end up in state D as the concentration grows to $\mathcal{O}(1)$, in which case only the centre compartment is filled. In cases (b-d), the 3-compartment system ends up in the stable equilibrium C, i.e. one outside compartment is filled and the other two are almost empty.

4.3.4 Equilibria when C approaches 1

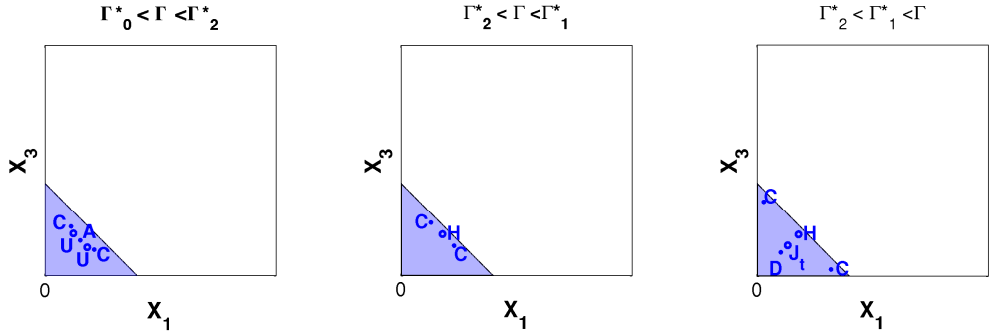
In Section 4.3.3, we analysed the transition from (a) to (b) in Fig. 4.4, and in this section we illustrate the process from (b) to (e), namely when the concentration grows from $\mathcal{O}(\epsilon)$ to $1 + \mathcal{O}(\epsilon)$.

As can be seen in (b) and (c), no new equilibrium states are added into the system as C grows from $\mathcal{O}(\epsilon)$ to $1 - \mathcal{O}(\epsilon)$. In this regime, it has the stable nodes $C(X, 0, 0)$ ($P(1, 0, 0)$ as C approaches 1) and $D(0, X, 0)$ ($Q(0, 1, 0)$ as C approaches 1), the saddles $E(X, X, 0)$ and $H(X, 0, X)$, and the unstable node $J(X, X, X)$.

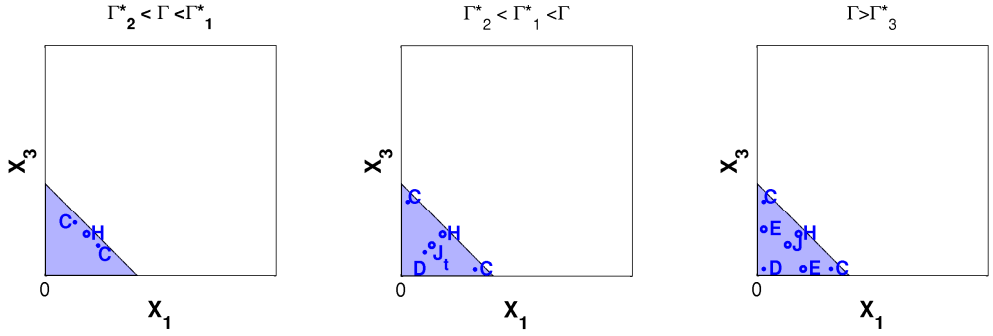
When C increases to $1 + \mathcal{O}(\epsilon)$, new equilibria are added into the system. We can show in a similar manner as in Section 4.3.3 that the stable node $Q(0, 1, 0)$ (in (d))



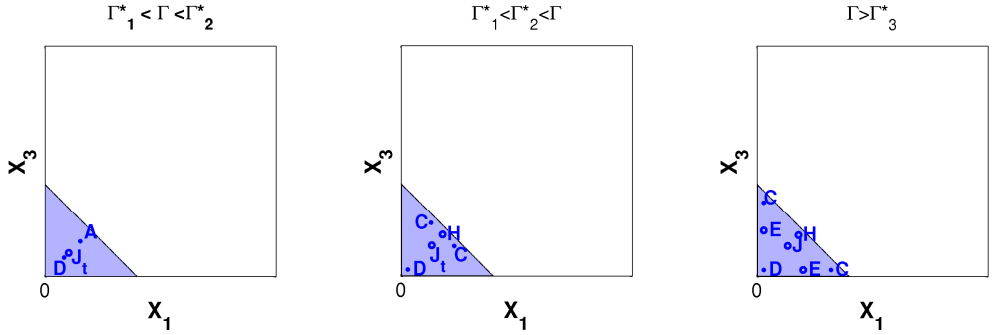
(a) $\sigma < 0.1$, so the saddle-node bifurcation on the asymmetric branch B_{o} occurs first, followed by the symmetry-preserving bifurcation B_{I}.



(b) $0.1 < \sigma < 0.26$, so the saddle-node bifurcation on the asymmetric branch B_{o} occurs first, followed by the symmetry-breaking bifurcation B_{II}. The symmetry-preserving bifurcation B_{o} happens later.



(c) $0.26 < \sigma < 0.6$. The symmetry-breaking bifurcation B_{II} occurs first. It is followed by the symmetry-preserving bifurcation B_{I}



(d) $\sigma > 0.6$. The symmetry-preserving bifurcation B_{I} happens first, followed by a supercritical pitchfork bifurcation B_{II}.

Figure 4.17: Four possible bifurcation scenarios when C is algebraically small.

undergoes a pitchfork bifurcation and becomes the stable node $G(X,1,0)(0,1,X)$ and the saddle $L(X,1,X)$ (in (e)). In contrast, the stable node $P(1,0,0)$ (in (d)) is always an equilibrium and transits smoothly into the stable node $I(1,0,X)$ (in (e)) as C increases. Meanwhile, a saddle-node bifurcation generates two more equilibria, namely the stable node $F(1,X,0)$ and the saddle $K(1,X,X)$ as in (e) of Fig. 4.4.

If we assume that when each bifurcation happens the system always jumps to the nearest steady state, then the above process can be interpreted as follows. Suppose at $C=1$ the system is initially in the stable state $Q(0,1,0)$ (associated with $D(0,X,0)$ when C is algebraically small), i.e. only the centre compartment is filled. Then as C increases, the nearest symmetric equilibrium becomes the saddle $L(X,1,X)$, so the system goes into the stable state $G(X,1,0)$ and hence the symmetry is broken. After that the system keeps the centre compartment full, one outside compartment empty, and all incoming flux goes into the other outside compartment. On the other hand, if the system is initially in the stable state $P(1,0,0)$ (associated with $C(X,0,0)$ when C is algebraically small), i.e. only one outside compartment is filled, then as C increases, the system moves smoothly to $I(1,0,X)$. Another neighbouring stable state $F(1,X,0)$ can never be reached.

4.3.5 Equilibria when C approaches 2

In the regime of $C=1+X$ as in (e) and (f) in Fig. 4.4, the system has the stable nodes $G(X,1,0)$, $F(1,X,0)$, $I(1,0,X)$; the saddles $L(X,1,X)$, $E(X,X,0)$, $K(1,X,X)$, $H(X,0,X)$; and the unstable nodes $J(X,X,X)$.

Similar analysis to Section 4.3.3 suggests that when C grows to around $2-\mathcal{O}(\epsilon)$, the stable node I and saddle H undergo a pitchfork bifurcation and become the stable node $S(1,0,1)$ ($N(1,X,1)$ as C increases further). The stable nodes G, F and the saddle E undergo another pitchfork bifurcation and become the stable node $R(1,1,0)$ ($M(1,1,X)$ as C increases further). So when $C=2+X$, the only two stable states are $M(1,1,X)$ (associated with $G(X,1,0)$ when $C=1+X$) and $N(1,X,1)$ (associated with $I(1,0,X)$ when $C=1+X$).

4.3.6 Equilibria when C approaches $3-\frac{\sigma}{1+\sigma}$

In this section we consider the final stage of the three-compartment intercalation problem, when C approaches $3-\sigma/(1+\sigma)$ and the system is close to full. We make the transformation $y_1=1-c_1$, $y_2=1-c_1$, and $y_3=1-c_3$, so equation (4.15)

becomes

$$3 - C = y_1 + y_2 + y_3, \tag{4.38a}$$

$$\mathcal{O}(\epsilon) = -\sigma + (4+\sigma)y_1 - (2+\sigma)y_2 + (-2+\sigma)y_3 - 2\epsilon \log y_1 + \epsilon \log y_2 + \epsilon \log y_3, \tag{4.38b}$$

$$\mathcal{O}(\epsilon) = -\sigma + (-2+\sigma)y_1 - (2+\sigma)y_2 + (4+\sigma)y_3 + \epsilon \log y_1 + \epsilon \log y_2 - 2\epsilon \log y_3. \tag{4.38c}$$

Comparing equation (4.38) to the leading order equations (4.21) when C is algebraically small, we notice an extra $-\sigma$ term, which signifies the importance of inter-compartment interactions when all compartments are filled. Meanwhile, as all bifurcations occur in the vicinity of $C \sim 3 - \sigma/(1+\sigma)$ instead of 3, we do not need to consider the transition from algebraically small y_i to exponentially small y_i $(i = 1, 2, 3)$, which reduces the analysis greatly. Following a similar but much simpler approach to that in Section 4.3.3, we find that when C approaches $3 - \sigma/(1+\sigma)$, the stable node $N(1, X, 1)$ becomes $O(1, 1, 1)$ when C gets closer to 3. Meanwhile, two saddle-node bifurcations happen between the unstable node $J(X, X, X)$ and the saddle $L(X, 1, X)$, and between the stable node $M(1, 1, X)$ and the saddle $K(1, X, X)$. That is to say, when C grows to $3 - \sigma/(1+\sigma)$, the symmetric stable node $N(1, X, 1)$ becomes $O(1, 1, 1)$, while the asymmetric stable node $M(1, 1, X)$ disappears through the saddle-node bifurcation. As a result, the system does not have any asymmetric stable states, which explains that in the end of the intercalation simulation, the concentrations of all compartments increase uniformly. We show the equilibria when C is close to 3 in Fig. 4.18.

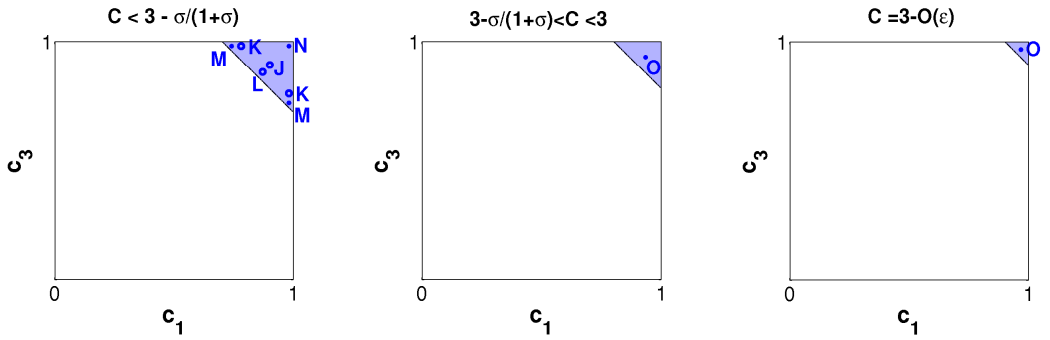


Figure 4.18: Equilibria when C is close to 3.

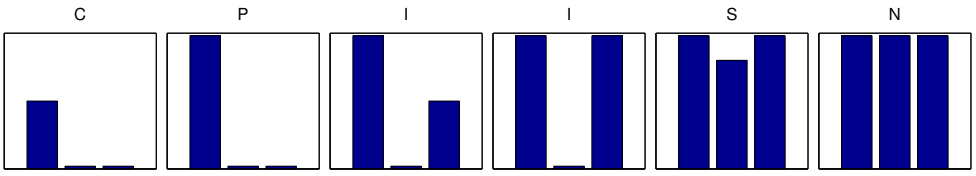
4.3.7 Summary of a complete intercalation/deintercalation cycle

As a summary, we list the number of stable nodes for different concentrations of C.

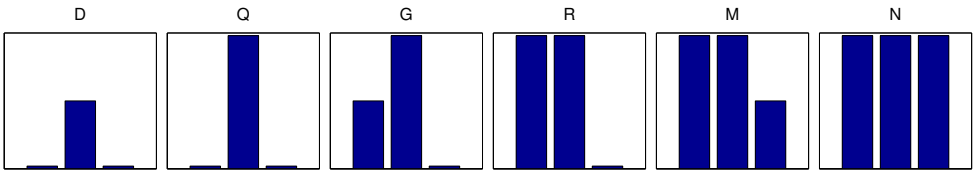
Range of C	$\mathcal{O}(e^{-1/\epsilon})$	X	$1+X$	$2+X$	$3-\frac{\sigma}{1+\sigma}$
Number of symmetric stable nodes	1	1	0	1	1
Number of asymmetric stable nodes	0	1	3	1	0

We can see that in the low/high concentration regime, the system only has symmetric stable states. In sharp contrast, in the intermediate concentration regime, all the stable nodes are highly asymmetric, as the system tends to keep an individual compartment either almost full or almost empty, which agrees with our numerical simulation observation in Section 4.2.

When $C = X$, both symmetric and asymmetric stable states exists. As found in Section 4.3.3.3, the system could only be at the asymmetric state C if $\sigma > 0.108$, and is definitely at the symmetric state D if $\sigma < 0.108$, as emerging from the same states at algebraically small C. We start from each state, follow the smooth transition of equilibria (or jump to the nearest stable equilibrium), and identify two possible ways to fill up the three-compartment system. We show the two different paths in Fig. 4.19. In (a) the system is initially in the asymmetric state when $C = X$, however this later translates into a symmetric configuration at $C = 2+X$. In (b) the system is initially in the symmetric state when $C = X$, however at $C = 2 + X$ the stable state is symmetric. This change of symmetry properties as C increases is very interesting.



(a) When $\sigma > 0.108$, so the system is initially in an asymmetric state.



(b) When $\sigma < 0.108$, so the system is initially in a symmetric state.

Figure 4.19: Two possible approaches to fill up 3 compartments.

4.4 Summary

In this chapter, we examine an interacting multicompartment system in which the interaction only occurs between adjacent compartments. We start with linear dynamics and adopt a gradient flow model, assuming that the total lithium concentration of the system is controlled.

Numerical experiments reveal that the nearest-neighbour interaction leads to a two-stage process: before reaching half-full, the system fills by every other compartment; after reaching half-full, the system fills the remaining compartments sequentially. In the beginning of the two-stage process, because the two compartments at the boundaries can only interact with one compartment, the system prefers to fill from the outside. In addition, when the system is near empty or near full, all compartments fill at the same rate. This agrees with the physical intuition that the steepness of the chemical potential $\mu(c)$ dominates when the lithium concentration is extremely low or high, so that the contribution from the interaction is repressed; while for intermediate lithium concentration, the interaction energy determines the filling pattern.

The observed behaviour is supported by the detailed bifurcation analysis of a three-compartment system, which indicates the existence of multiple equilibria at intermediate lithium concentration as well as a single equilibrium at extremely low or high lithium concentration. We also find that bifurcations that connect these equilibria are extremely subtle, and are controlled by the relative importance of the interaction: if the interaction is weak, the three-compartment system tend to fill the centre compartment first, otherwise the two outside compartments are always filled before the centre compartment.

Due to the complicated bifurcation structure, we expect the concentration profile at intermediate concentration to depend on the initial condition. Starting from different initial conditions, the quasi-equilibrium evolution of the concentration profile follows different paths. Potentially, this will also be influenced by the charging speed. Nevertheless, as will be shown in Section 5.1, in the gradient-flow model, t is scaled by the characteristic time scale $2\epsilon t_{\text{int}}$, where t_{int} is the time required to deplete a fully-lithiated compartment introduced in Chapter 2, computed to be around 17 hours for a 50nm LFP nanoparticle. Therefore, as long as ϵ is a small number, the characteristic time for the gradient flow model is small, and it is reasonable to assume that the system evolves near equilibrium. The influence of the charging speed will be

analysed in the Butler–Volmer dynamics, where the characteristic time is relatively large.

Finally, it is noteworthy that the bifurcation analysis of the three-compartment dynamics applies in a reverse process, ie. the deintercalation process. In the analysis, however, we do not observe hysteresis. The hysteresis observed in simulating a 200-compartment system could be explained by the delay and memory effect during slow transition through bifurcations [3, 36].

Chapter 5

A deterministic multicompartment model with nonlinear dynamics

In the gradient flow model in Chapter 4, we investigated the evolving concentration profile of a multicompartment system under the assumption that the total concentration at any point in time is specified. This corresponds physically to experiments with current control.

In this chapter, we consider the problem of voltage control. The deterministic version of the multicompartment voltage control model is very similar to the single-compartment voltage control model; the only difference is the addition of an interaction energy that modifies the chemical potential of individual compartment. However, the resulting behaviour are extremely subtle and complicated, which we will illustrate first by analysing the bifurcation structure of a two-compartment system, and by examining the dynamics. This detailed bifurcation analysis again raises the question of whether such a delicate structure is robust in the presence of thermal noise, which motivates us to study stochastic multicompartment models with voltage control in the next chapter.

5.1 Setting up the Butler–Volmer style model

As in the single-compartment system, we assume that the multicompartment system is immersed in an electrolyte which is sufficiently large that it can be considered a bath of lithium ions, with its potential unaffected by the electrochemical reactions. We also assume that all compartments in the system are identical, and that any secondary effects including position within the electrode, potential gradient in the electrolyte, and size of the particle, are neglected.

In addition, we assume that each compartment can only react with the electrolyte bath, as shown in Fig. 5.1. In other words, there is no direct pathway for any two compartments to exchange lithium ions with each other; all exchanges of lithium ions have to happen via the electrolyte.

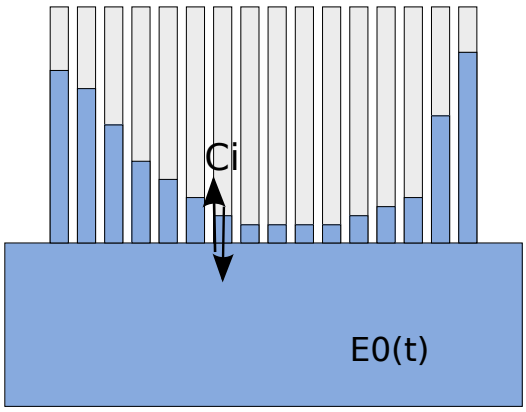


Figure 5.1: In the voltage control model, each compartment can only exchange lithium ions with the electrolyte bath.

.

The dynamics of this system is described by the Butler–Volmer model. In Chapter 2, we introduced the dynamics of a single compartment as

$$\frac{\mathrm{d}c}{\mathrm{d}t} = \sinh\left(\frac{E(t) - \mu\big[c(t)\big]}{2\epsilon}\right),$$
$$\mu(c) = \frac{\mathrm{d}g}{\mathrm{d}c} = 1 - 2c + \epsilon \log\left(\frac{c}{1-c}\right),$$

where $\mu(c)$ is the chemical potential of the compartment. It represents the nondimensionalised change in free energy associated with removing a lithium ion from the compartment. Now consider an M-compartment system. The chemical potential of the i-th compartment can be defined as the change in free energy of the entire system associated with adding lithium to the i-th compartment, namely

$$\mu_i(\mathbf{c}, t) = \frac{\partial g_{\mathrm{tot}}}{\partial c_i} = \mu(c_i) + \frac{\partial g_{\mathrm{int}}}{\partial c_i}, \tag{5.2}$$

where the column vector $\mathbf{c} = [c_1, c_2, \cdots, c_M]'$ denotes the concentration of each compartment, g_{tot} represents the total energy of the system, and g_{int} represents the interaction energy. We adopt the same interaction law as Chapter 4 and model g_{tot} by

$$g_{\mathrm{tot}} = \sum_{i=1}^{M} g(c_i) + g_{\mathrm{int}}(\mathbf{c}) = \sum_{i=1}^{M} g(c_i) + \sigma \sum_{i=1}^{M-1} c_i c_{i+1}. \tag{5.3}$$

The dynamics of each compartment is then specified by the Butler–Volmer equation, giving the ODE system

$$\frac{\mathrm{d}c_i}{\mathrm{d}t} = \sinh\left(\frac{E(t) - \mu_i\big[\mathbf{c}(t)\big]}{2\epsilon}\right), \tag{5.4a}$$

$$\mu_i\big[\mathbf{c}(t)\big] = 1 - 2c_i + \epsilon\log\left(\frac{c_i}{1-c_i}\right) + \sigma c_{i-1}(1-\delta_{i1}) + \sigma c_{i+1}(1-\delta_{iM}), \quad i = 1, \cdots, M \tag{5.4b}$$

where δ_{ij} is the Kronecker delta.

Connection to the gradient flow model If $E(t) - \mu_i\big[\mathbf{c}(t)\big] \ll \mathcal{O}(\epsilon)$, the Butler–Volmer equation (5.4) can be approximated by its linear form

$$\frac{\mathrm{d}c_i}{\mathrm{d}t} = \frac{E(t) - \mu_i\big[\mathbf{c}(t)\big]}{2\epsilon}, \tag{5.5}$$

or, letting $t = 2\epsilon\bar{t}$,

$$\frac{\mathrm{d}c_i}{\mathrm{d}\bar{t}} = E(\bar{t}) - \mu_i\big[\mathbf{c}(\bar{t})\big]. \tag{5.6}$$

Comparing this with the gradient flow model in Chapter 4 that

$$\frac{dc_i}{dt} = -\frac{\partial g_{\mathrm{tot}}(t)}{\partial c_i(t)} - \lambda(t) = -\lambda(t) - \mu_i\big[\mathbf{c}(t)\big], \tag{5.7}$$

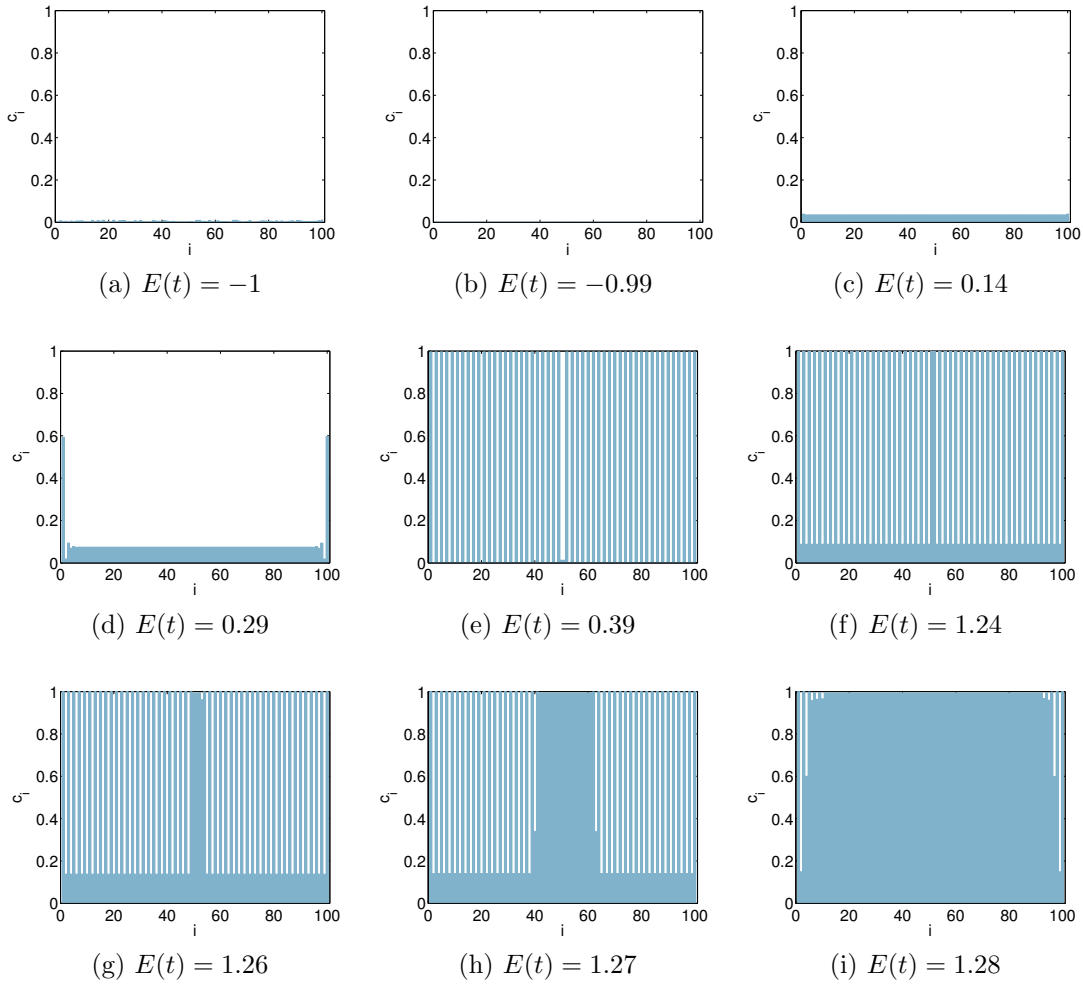
we infer that the Lagrange multiplier in the gradient flow model corresponds to the negative of the electrolyte potential of the Butler–Volmer model. In addition, the relation $t = 2\epsilon\bar{t}$ suggests that the dimensional time constant we used to nondimensionalise the gradient flow model in (4.5) must satisfy $1/L = 2\epsilon t_{\mathrm{int}}$, where t_{int} is the time constant we chose to nondimensionalise the Butler–Volmer equation. The only difference is that in analysing the gradient flow model in Chapter 4, we assume that the total concentration $C(t)$ is given, and $\lambda(t) = -E(t)$ is implicitly determined. In contrast, when using the Butler–Volmer model, it is convenient to model $E(t)$ as explicitly given over time, and $C(t)$ could be determined a posteriori.

5.2 Numerical simulations

5.2.1 Very slowly varying $E(t)$

Now that the gradient flow model can be viewed as a linearisation of the Butler–Volmer model, we expect the dynamics of the two models to generate similar C-V curves when the voltage varies slowly enough.

First, we run simulations to reveal this. We solve the ODE system (5.4) with Matlab solver **ode15s**, using the same parameters as the simulation of the current-control gradient flow model as in Fig. 4.1. Comparing the voltage-control process in Fig. 5.2 with the current control process in Fig. 4.1, we see that the two dynamics are qualitatively similar. In both processes, the initial stage is uniform growth across all compartments, followed by the filling of every other compartment until half full, and then the filling of the remaining compartments one by one.



(a) $E(t) = -1$ (b) $E(t) = -0.99$ (c) $E(t) = 0.14$

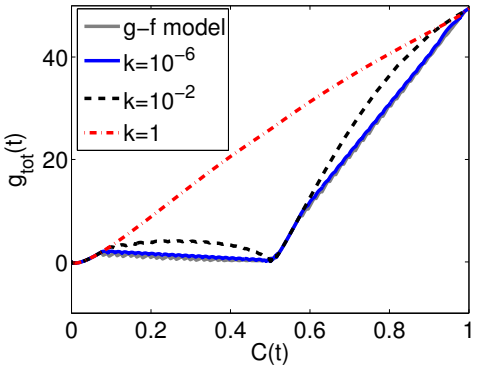
(d) $E(t) = 0.29$ (e) $E(t) = 0.39$ (f) $E(t) = 1.24$

(g) $E(t) = 1.26$ (h) $E(t) = 1.27$ (i) $E(t) = 1.28$

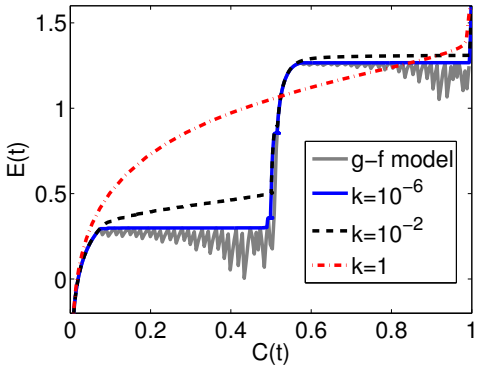
Figure 5.2: Numerical simulation of the nearest-neighbour interaction Butler–Volmer model of equation (5.4) with $E(t) = 10^{-6}t$. Parameter values are $\epsilon = 0.25$, $N = 100$ and $\sigma = 0.5$, and the initial concentration of each compartment is randomly distributed in $[0, 0.01]$.

We plot the total energy and the potential $E(t)$ against the total concentration of the simulation in Fig. 5.3, and compare them with those found by simulating a gradient flow model with a charging rate of $\mathrm{d}C(t)/\mathrm{d}t = 10^{-3}$. In this very slowly

varying $E(t)$ case, both the $g_{\text{tot}}(t)$-$C(t)$ curve and the $E(t)$-$C(t)$ curve agree with those found by the gradient flow model, and a two-stage process is evident.



(a) Total energy g_{tot} versus the total concentration.



(b) Potential $E(t)$ versus the total concentration.

Figure 5.3: Total energy and potential versus the total concentration of the three simulations plotted in Fig. 5.2, 5.4 and 5.5. The blue solid line, the black dashed line, and the red dash-dotted line plots $E(t) = 10^{-6}t$, $E(t) = 10^{-2}t$, and $E(t) = t$ respectively. The grey solid line plots the results found by simulating the gradient flow model (4.8), using the same parameters as Fig. 5.2 and a charging rate of $\mathrm{d}C(t)/\mathrm{d}t = 10^{-3}$.

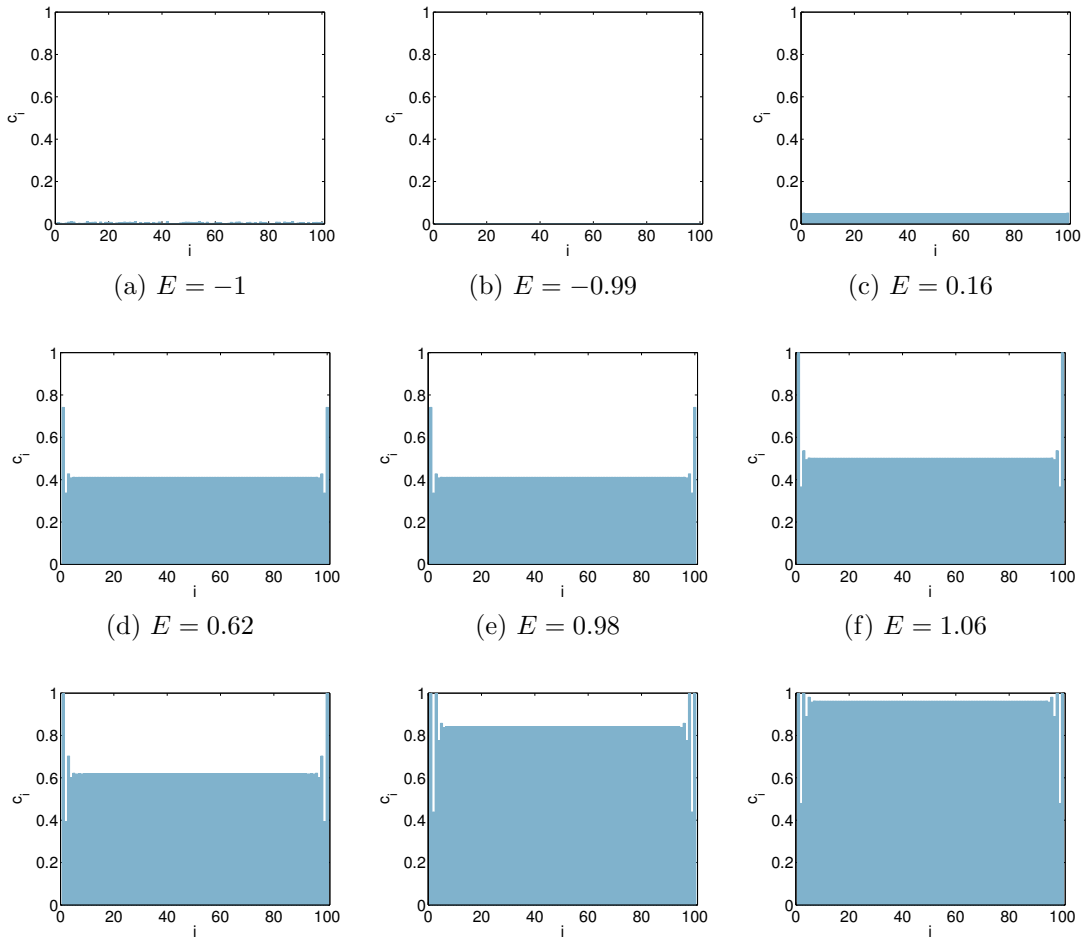
5.2.2 Intermediate charging rate

In contrast, at a faster charging speed, the dynamics of the Butler–Volmer model can be quite different from the dynamics of the gradient flow model.

Here we assume a dimensionless charging rate of $E(t) = t$ and rerun the simulation, which corresponds to a dimensional charging rate where the voltage varies on the intrinsic time-scale t_{int} as defined in (2.8). The results are shown in Fig. 5.4. Surprisingly, the stage of filling by every other compartment disappears, and it appears that a much more uniform growth is preferred when $\mathrm{d}E/\mathrm{d}t = 1$.

5.2.3 Slowly varying $E(t)$

We carry out a further numerical simulation with $E = 10^{-2}t$. As plotted in Fig. 5.5, the resulting dynamics resembles both the very slow charging and the intermediate charging rate dynamics. Initially, its dynamics are similar to the very slowly varying $E(t)$ case. At very low concentration, all compartment at the same rate, as in panels (b)-(c). It then follows the asymmetric growth stage when every other compartment is filled, as in panels (d)-(f). This stage ends when the system reaches around



(a) $E = -1$ (b) $E = -0.99$ (c) $E = 0.16$

(d) $E = 0.62$ (e) $E = 0.98$ (f) $E = 1.06$

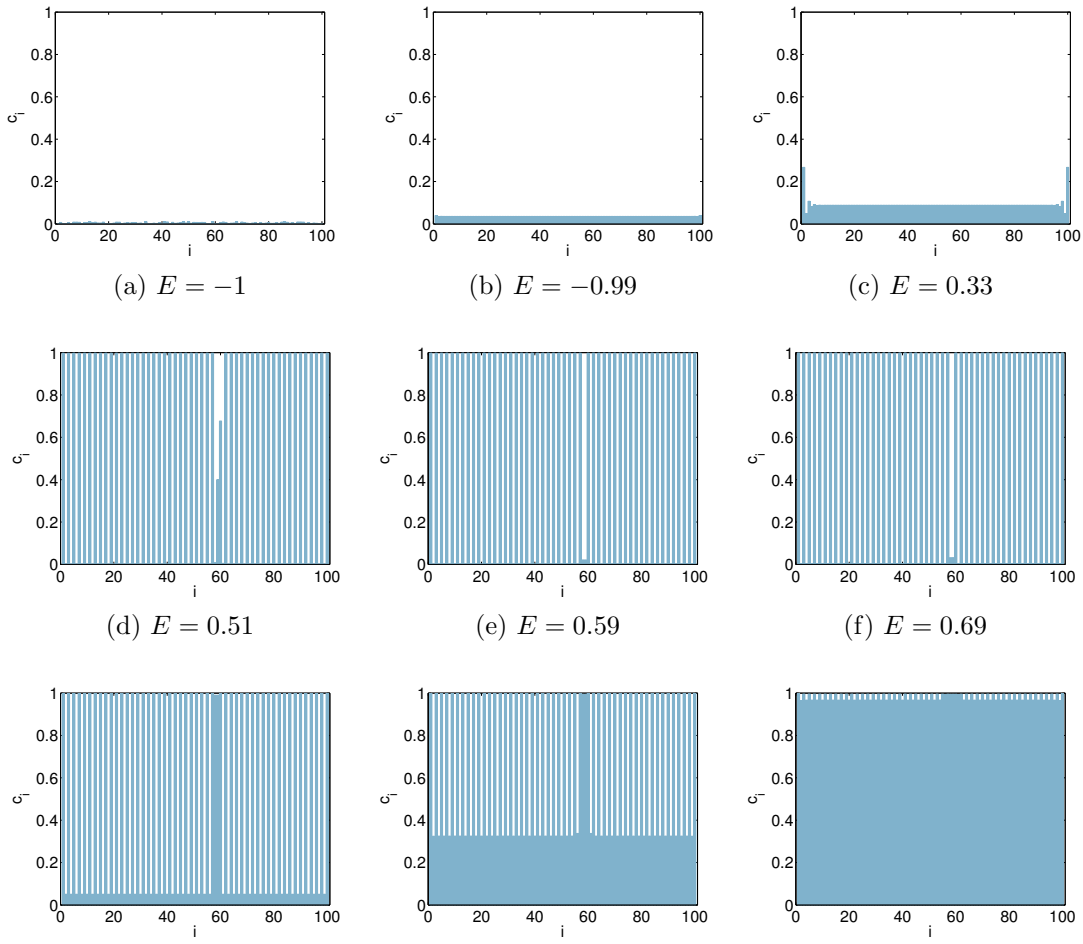
(g) $E = 1.14$ (h) $E = 1.26$ (i) $E = 1.34$

Figure 5.4: Numerical simulation of the nearest-neighbour interaction Butler–Volmer model of equation (5.4) with $E(t) = t$. Parameter values are $\epsilon = 0.25$, $N = 100$ and $\sigma = 0.5$, and the initial concentration of each compartment is randomly distributed in $[0, 0.01]$.

half full. After that, as shown in panels (g)-(i), all the remaining compartments start to grow at the same rate.

The dynamics of the slowly varying $E(t)$ are similar to the very slowly varying $E(t)$ before the system reaches half-full, featuring a compartment-by-compartment filling. After half-full, the dynamics feature uniform filling across the remaining compartments, which resembles the case where $E = t$.

We also plot the total energy and the potential $E(t)$ against the total concentration of the two simulations with $E = t$ and $E = 10^{-2}t$ in Fig. 5.3. Now with the intermediate charging speed $E(t) = t$, we see near-uniform growth instead of a two-stage process, and the $E(t)$ versus $C(t)$ plot shows smooth increase without



(a) $E = -1$ (b) $E = -0.99$ (c) $E = 0.33$

(d) $E = 0.51$ (e) $E = 0.59$ (f) $E = 0.69$

(g) $E = 1.16$ (h) $E = 1.30$ (i) $E = 1.31$

Figure 5.5: Numerical simulation of the nearest-neighbour interaction Butler–Volmer model of equation (5.4) with $E(t) = 10^{-2}t$. Parameter values are $\epsilon = 0.25$, $N = 100$ and $\sigma = 0.5$, and the initial concentration of each compartment is randomly distributed in $[0, 0.01]$.

abrupt jumps. The slow charging curve sits inbetween the very slow charging and the intermediate charging rate curves.

5.2.4 Implications

The above comparison between three simulations with different charging speeds has several implications. First, it indicates that the equilibrium path and out-of-equilibrium path of the multicompartment system are qualitatively different, while in the single-compartment model we have shown that the two paths are similar and only differ by a delay of order $\mathcal{O}(\epsilon)$. Second, it is suggestive of the existence of multiple equilibria,

and it indicates that the choice of equilibrium branch may be strongly affected by the charging speed. All of these factors add extra complexity to the multicompartment model.

5.3 A deterministic two-compartment model

In Section 5.2, we show by direct simulation that the dynamics of the multicompartment model can bear very little resemblance to its quasi-equilibrium behaviour. In this section, we will use a two-compartment system as a paradigm to illustrate this analytically. First, we will perform bifurcation analysis of the two-compartment system, and demonstrate that studying the quasi-equilibrium evolution is extremely demanding. Then we will then give an heuristic argument on how the dynamics are further affected by charging speed.

The two-compartment system is given by (5.4) with $M = 2$, specifically

$$\frac{\mathrm{d}c_1}{\mathrm{d}t} = \sinh\left[\frac{E - 1 + 2c_1 - \epsilon\log\left(\frac{c_1}{1-c_1}\right) - \sigma c_2}{2\epsilon}\right], \tag{5.8a}$$

$$\frac{\mathrm{d}c_2}{\mathrm{d}t} = \sinh\left[\frac{E - 1 + 2c_2 - \epsilon\log\left(\frac{c_2}{1-c_2}\right) - \sigma c_1}{2\epsilon}\right]. \tag{5.8b}$$

5.3.1 Bifurcation analysis

Equilibria of (5.8) satisfy

$$E - 1 + 2c_1 - \epsilon\log\left(\frac{c_1}{1-c_1}\right) - \sigma c_2 = 0, \tag{5.9a}$$

$$E - 1 + 2c_2 - \epsilon\log\left(\frac{c_2}{1-c_2}\right) - \sigma c_1 = 0. \tag{5.9b}$$

Using the same technique as in Section 4.3, we find asymptotic solutions to this system and then evaluate the Jacobian matrix to determine the type and stability of the equilibria. Possible equilibria and their types are listed in Table 5.1.

Based on the relationship between E and the equilibria, we sketch the bifurcation diagram on the $(c_1 + c_2) - E$ plane as shown in Fig. 5.6. Stable (unstable) branches are plotted as solid (dashed) lines and marked accordingly. Note that due to the symmetry between c_1 and c_2, the solution branches labelled as $(0, X)$, $(1, 0)$, and $(1, X)$ also represent $(X, 0)$, $(0, 1)$, and $(X, 1)$ respectively.

(c_1, c_2)	c_1	c_2	range of E	stability
$(0,0)$	$e^{-(1-E)/\epsilon}$	$e^{-(1-E)/\epsilon}$	$E<1$	stable node
$(0,X)$	$e^{-(2+\sigma)(1-E)/(2\epsilon)}$	$\frac{1-E}{2}$	$-1<E<1$	saddle
$(0,1)$	$e^{-(1+\sigma-E)/\epsilon}$	$1-e^{-(1+E)/\epsilon}$	$-1<E<1+\sigma$	stable node
(X,X)	$\frac{1-E}{2-\sigma}$	$\frac{1-E}{2-\sigma}$	$-1+\sigma<E<1$	unstable node
$(X,1)$	$\frac{1-E+\sigma}{2}$	$1-e^{-\frac{E+1-\sigma}{\epsilon}(1+\frac{\sigma}{2})}$	$-1+\sigma<E<1+\sigma$	saddle
$(1,1)$	$1-e^{-(1+E-\sigma)/\epsilon}$	$1-e^{-(1+E-\sigma)/\epsilon}$	$E>-1+\sigma$	stable node

Table 5.1: Enumeration of possible solutions to the algebraic system (5.9) as a function of E. In the first column, 0, X, and 1 should be read as "near-0", "neither near-0 nor near-1", and "near-1" respectively; in the fourth column, $<(>)$ should be read as smaller (bigger) than, but not close to. As noted below, many branches cease to exist when E is within $\mathcal{O}(\epsilon)$ of the limits specified.

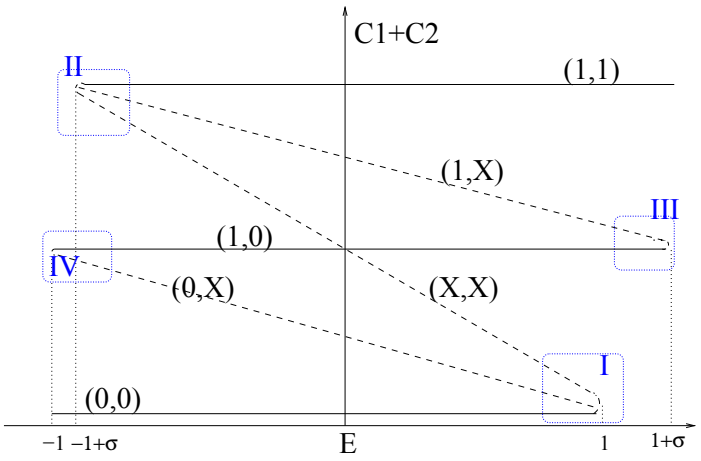


Figure 5.6: Bifurcation diagram of the system (5.8) in the c_1+c_2 versus E plane. All the solution branches labelled are the same as listed in Table 5.1.

To construct the bifurcation plot of Fig. 5.6, it suffices to consider each of the four bifurcations labelled as I, II, III, and IV. A detailed analysis of the four bifurcations are presented in Sections 5.3.1.1 to 5.3.1.4.

5.3.1.1 Bifurcation I

In Bifurcation I, c_1 and c_2 are near 0 and E is near 1. We make the local transformation

$$c_1 = \epsilon c_1^{\mathrm{I}}, \qquad c_2 = \epsilon c_2^{\mathrm{I}}, \qquad E = 1 + \epsilon \log \epsilon + \epsilon E^{\mathrm{I}} \tag{5.10}$$

and substitute into (5.9) to get

$$E^{\mathrm{I}} = -2c_1^{\mathrm{I}} + \log c_1^{\mathrm{I}} + \sigma c_2^{\mathrm{I}} + \mathcal{O}(\epsilon), \tag{5.11a}$$

$$E^{\mathrm{I}} = -2c_2^{\mathrm{I}} + \log c_2^{\mathrm{I}} + \sigma c_1^{\mathrm{I}} + \mathcal{O}(\epsilon). \tag{5.11b}$$

The leading-order Jacobian matrix corresponding to a solution (c_1^I, c_2^I) is

$$J = \frac{1}{2\epsilon} \begin{pmatrix} 2 - \frac{1}{c_1^I} & -\sigma \\ -\sigma & 2 - \frac{1}{c_2^I} \end{pmatrix}. \tag{5.12}$$

The symmetric branch System (5.11) admits both a symmetric solution branch $c_1^{\mathrm{I}} = c_2^{\mathrm{I}}$ and an asymmetric solution branch $c_1^{\mathrm{I}} \neq c_2^{\mathrm{I}}$. For the symmetric branch $c_1^{\mathrm{I}} = c_2^{\mathrm{I}}$, the leading order equation is

$$E^I \sim -(2-\sigma)c_1^I + \log c_1^I. \tag{5.13}$$

When $E^I < -1 - \log(2-\sigma)$, (5.13) has two real solutions, which are plotted in blue in Fig. 5.7(a).

The trace and determinant of the Jacobian (5.12) are given by

$$\det(J) = \frac{1}{4\epsilon^2}\left(\left(2 - \frac{1}{c_1^1}\right)^2 - \sigma^2\right), \tag{5.14a}$$

$$\mathrm{tr}(J) = \frac{1}{\epsilon}\left(2 - \frac{1}{c_1^1}\right). \tag{5.14b}$$

Therefore it is straightforward to find out that this symmetric branch is a stable node when $c_1^{\mathrm{I}} = c_2^{\mathrm{I}} < \frac{1}{2+\sigma}$, a saddle when $\frac{1}{2+\sigma} < c_1^{\mathrm{I}} < \frac{1}{2-\sigma}$, and an unstable node when $c_1^{\mathrm{I}} > \frac{1}{2-\sigma}$. These three cases are labelled in blue in Fig. 5.7(a).

The asymmetric branch For the asymmetric branch, we solve for c_1^{I} and c_2^{I} parametrically by setting $\alpha = c_1^{\mathrm{I}}/c_2^{\mathrm{I}}$ and get

$$c_1^{\mathrm{I}} = \frac{1}{2+\sigma}\frac{\alpha\log\alpha}{\alpha-1}, \tag{5.15a}$$

$$c_2^{\mathrm{I}} = \frac{1}{2+\sigma}\frac{\log\alpha}{\alpha-1}. \tag{5.15b}$$

Determinant of its Jacobian satisfies

$$\frac{4\epsilon^2\alpha(\log\alpha)^2}{2+\sigma}\det(J) = \left[(\alpha-1)^2 - \alpha(\log\alpha)^2\right]\sigma - 2(\alpha - 1 - \log\alpha)(1 - \alpha + \alpha\log\alpha). \tag{5.16}$$

Clearly $\det(J) > 0$ only if

$$\sigma > \frac{2(\alpha - 1 - \log\alpha)(1 - \alpha + \alpha\log\alpha)}{(\alpha-1)^2 - \alpha(\log\alpha)^2} \geq 6, \tag{5.17}$$

so that $\det(J) \leq 0$ provided $\sigma < 6$. Therefore this asymmetric solution is always a saddle. This branch is shown in black in Fig. 5.7(a).

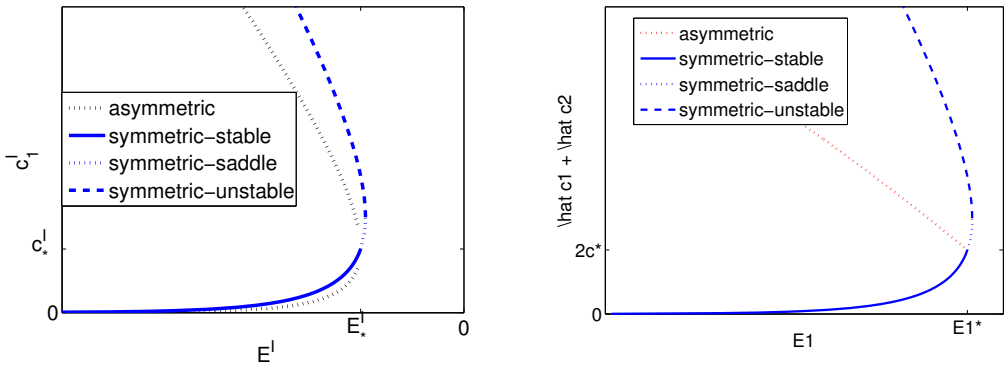
Bifurcation diagram Combining the symmetric branch and the asymmetric branch together gives us the bifurcation plot on the c_1^{I} versus E^{I} plane as in Fig. 5.7(a). Note that bifurcation I actually involves two bifurcations: a subcritical pitchfork bifurcation, at

$$E^{\mathrm{I}} = -\frac{2-\sigma}{2+\sigma} - \log(2+\sigma), \qquad c_1^{\mathrm{I}} = \frac{1}{2+\sigma}, \tag{5.18}$$

and a saddle-node bifurcation, at

$$E^{\mathrm{I}} = -1 - \log(2-\sigma), \qquad c_1^{\mathrm{I}} = \frac{1}{2-\sigma}. \tag{5.19}$$

We re-plot the two bifurcations in the $(c_1^{\mathrm{I}} + c_2^{\mathrm{I}})$ versus E^{I} plane in Fig. 5.7(b). This corresponds to bifurcation I in Fig. 5.6.



(a) The c_1^{I}-E^{I} plane. (b) The $c_1^{\mathrm{I}} + c_2^{\mathrm{I}}$-$E^{\mathrm{I}}$ plane.

Figure 5.7: Bifurcation I includes a pitchfork bifurcation of (5.18) and a saddle-node bifurcation of (5.19), plotted with $\sigma = 0.4$. Solid lines denote stable solutions, and dotted and dashed lines denote unstable solutions.

5.3.1.2 Bifurcation II

The structure of bifurcation II is very similar to that of bifurcation I. This can be shown by making the local expansion

$$c_1 = 1 - \epsilon c_1^{\mathrm{II}}, \qquad c_2 = 1 - \epsilon c_2^{\mathrm{II}}, \qquad E = -(1 - \sigma + \epsilon\log\epsilon) + \epsilon E^{\mathrm{II}}. \tag{5.20}$$

This gives us the leading order equation

$$-E^{\mathrm{II}} = -2c_1^{\mathrm{II}} + \log(c_1^{\mathrm{II}}) + \sigma c_2^{\mathrm{II}} + \mathcal{O}(\epsilon), \tag{5.21a}$$

$$-E^{\mathrm{II}} = -2c_2^{\mathrm{II}} + \log(c_2^{\mathrm{II}}) + \sigma c_1^{\mathrm{II}} + \mathcal{O}(\epsilon), \tag{5.21b}$$

which is identical to equation (5.11) except for a difference in sign of the left-hand side. Thus the bifurcation diagram in terms of $(c_1^{\mathrm{II}} + c_2^{\mathrm{II}})$ versus E^{II} is the same as Bifurcation I but in a different direction, as plotted in Fig. 5.8.

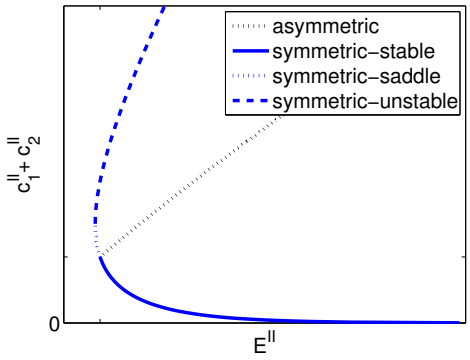


Figure 5.8: Bifurcation II is similar to bifurcation I, plotted with $\sigma = 0.4$. Solid lines denote stable solutions, and dotted and dashed lines denote unstable solutions.

5.3.1.3 Bifurcation III

In bifurcation III, c_1 is near 1, c_2 is near 0, and E is near $1 + \sigma$. We make the local expansion

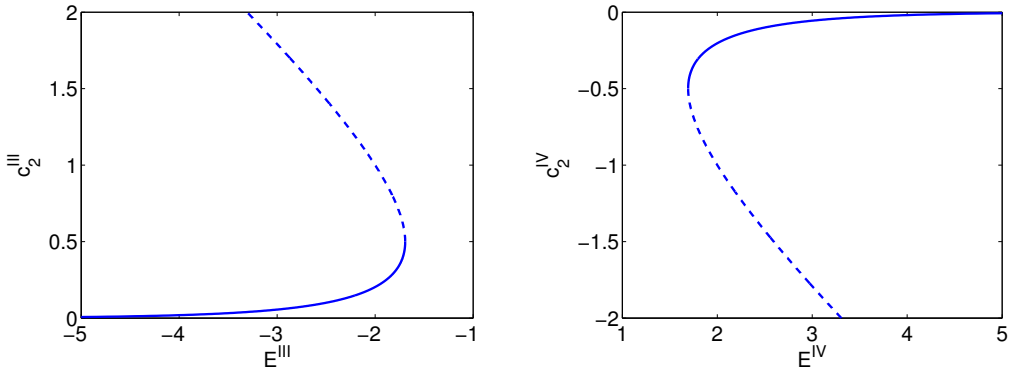
$$c_1 = 1 - e^{-c_1^{\mathrm{III}}/\epsilon}, \qquad c_2 = \epsilon c_2^{\mathrm{III}}, \qquad E = 1 + \sigma + \epsilon \log \epsilon + \epsilon E^{\mathrm{III}} \tag{5.22}$$

and find the leading-order equations

$$E^{\mathrm{III}} = -1 + c_1^{\mathrm{III}} + \mathcal{O}(\epsilon), \tag{5.23a}$$

$$E^{\mathrm{III}} = -2c_2^{\mathrm{III}} + \log c_2^{\mathrm{III}} + \mathcal{O}(\epsilon). \tag{5.23b}$$

Therefore the bifurcation is in terms of c_2^{III} and is independent of c_1^{III}. It is straightforward to identify (5.23b) as a saddle-node bifurcation at $c_2^{\mathrm{III}} = 1/2$, which we plot in Fig. 5.9(a).



(a) Bifurcation III specified by (5.23b). (b) Bifurcation IV specified by (5.25b).

Figure 5.9: Both bifurcations III and IV are independent of σ.

5.3.1.4 Bifurcation IV

Finally, bifurcation IV is equivalent to bifurcation III. Letting

$$c_1 = e^{-c_1^{\mathrm{IV}}/\epsilon}, \qquad c_2 = 1 + \epsilon c_2^{\mathrm{IV}}, \qquad E = -1 - \epsilon \log \epsilon + \epsilon E^{\mathrm{IV}}, \tag{5.24}$$

we get

$$E^{\mathrm{IV}} = 1 - c_1^{\mathrm{IV}} + \sigma + \mathcal{O}(\epsilon), \tag{5.25a}$$

$$E^{\mathrm{IV}} = -2c_2^{\mathrm{IV}} - \log(-c_2^{\mathrm{IV}}) + \mathcal{O}(\epsilon). \tag{5.25b}$$

This introduces a saddle-node bifurcation in the c_2^{IV} versus E^{IV} plane, as in Fig. 5.9(b).

5.3.1.5 Implications of the bifurcation plot

The bifurcation diagram Fig. 5.6 suggests that when E is extremely low or extremely high, the two-compartment system has only one equilibrium. However, when E is in the intermediate regime $-1 + \epsilon(1 + \log 2\epsilon) < E < 1 + \sigma + \epsilon(-1 - \log 2\epsilon)$, the system can have multiple stable equilibria and multiple unstable equilibria.

5.3.2 Dynamics

We consider the case when $E(t) = t$, with an initial condition $E(-t_0) = E_0$ imposed at some $t_0 > 1$. Following asimilar analysis as for the single-compartment model, we can say that regardless of their initial concentration, both compartments would quickly deplete themselves and join the stable manifold $(0, 0)$. The $(0, 0)$ manifold ceases to exist as bifurcation I happens. Then the system exits this manifold and jumps to the next stable manifold. However, due to the existence of two stable equilibria in

$E \in (1, 1+\sigma)$, it remains unclear which manifold, $(0,1)$ or $(1,1)$, would be the next state.

To try and probe this problem, we consider a simple problem when a general linear charging voltage is applied, with

$$E(t) = \kappa t,$$

and we consider its local behaviour in the critical transition stage by making the transformation

$$E(t) = \kappa t = 1 + \epsilon \log \epsilon + \epsilon T \tag{5.26}$$

and

$$c_1 = \epsilon X_1, \qquad c_2 = \epsilon X_2. \tag{5.27}$$

Substituting the local expansions into (5.8),

$$\kappa \frac{\mathrm{d}X_1}{\mathrm{d}T} = \sinh\left(\frac{T + 2X_1 - \log X_1 - \sigma X_2}{2} + \mathcal{O}(\epsilon)\right), \tag{5.28a}$$

$$\kappa \frac{\mathrm{d}X_2}{\mathrm{d}T} = \sinh\left(\frac{T + 2X_2 - \log X_2 - \sigma X_1}{2} + \mathcal{O}(\epsilon)\right). \tag{5.28b}$$

By subtracting equation (5.28b) from (5.28a) and using the addition formula for hyperbolic functions, we obtain that their difference

$$\Delta X = X_1 - X_2$$

satisfies

$$\begin{aligned}\kappa \frac{\mathrm{d}\Delta X}{\mathrm{d}T} = 2\sinh&\left(\frac{(2+\sigma)(X_1 - X_2) - \log\left(\frac{X_1}{X_2}\right)}{4} + \mathcal{O}(\epsilon)\right) \\ &\cdot \cosh\left(\frac{2T + 2(2-\sigma)(X_1 + X_2) - \log X_1 - \log X_2}{4} + \mathcal{O}(\epsilon)\right).\end{aligned} \tag{5.29}$$

We are interested in the initial condition when the two-compartment system is on the $(0,0)$ branch as $T \to -\infty$, so that $X_1 \sim X_2$ and $\Delta X \ll X_1$ as $T \to -\infty$. Given a very small but nonzero ΔX as $T \to -\infty$, it is important to find out whether or not ΔX would grows more quickly than X_1. If it always holds that $\Delta X \ll X_1$, then it is highly suggestive that the two-compartment system grows symmetrically; otherwise it indicates an asymmetric growth.

Assuming that $\Delta X \ll X_1$ is satisfied, (5.28 - 5.29) can be approximated by

$$\kappa \frac{\mathrm{d}X_1}{\mathrm{d}T} \sim \sinh\left(\frac{T + (2-\sigma)X_1 - \log X_1}{2}\right), \tag{5.30a}$$

$$\begin{aligned}\kappa \frac{\mathrm{d}\Delta X}{\mathrm{d}T} &\sim 2\sinh\left(\frac{(2+\sigma)\Delta X}{4} - \frac{\Delta X}{4X_1}\right)\cosh\left(\frac{T + (2-\sigma)X_1 - \log X_1}{2}\right) \\ &\approx \frac{1}{2}\left(2 + \sigma - \frac{1}{X_1}\right)\cosh\left(\frac{T + (2-\sigma)X_1 - \log X_1}{2}\right)\Delta X. \end{aligned} \tag{5.30b}$$

Equation (5.30a) is similar to the dynamics of a single-compartment model in its jump regime with a charging rate κ, except for the change in the coefficient from 2 to $2 - \sigma$. Therefore its trajectory is similar to the single-compartment dynamics, as plotted in Fig. 2.7. Following a similar argument as in Section 2.3.1.3, we can see that for T that is large and negative, $X_1(T)$ is exponentially small. As T approachers a critical value that is of order $\mathcal{O}(1)$, $X_1(T)$ blows up. And in this case this critical value in time also depends on the charging speed κ and the interaction coefficient σ.

Meanwhile, ΔX from (5.30b) can be solved directly now that $X_1(T)$ is known, yielding

$$\Delta X(T) = \Delta X(T_0) e^{\int_{T_0}^{T} l(s)ds/\kappa}, \tag{5.31}$$

with

$$l(T) = \frac{1}{2}\left(2 + \sigma - \frac{1}{X_1(T)}\right)\cosh\left(\frac{T + (2-\sigma)X_1(T) - \log X_1(T)}{2}\right). \tag{5.32}$$

Generally, for $X_1(T)$ that is exponentially small, $l(T)$ is negative and exponentially large, which, in turn, makes $\Delta X(T)$ double exponentially small, so that the assumption $\Delta X \ll X_1$ is still valid. But in the mean time, preliminary analysis reveals that the double exponentially small term in the expansion of ΔX has an order 1 effects on the final behaviour of $\Delta X(T)$ near the blow-up regime. Since the exponent of the double exponentially small term depends linearly on the initial condition, whether or not ΔX grows faster than X_1 depends parametrically on the initial condition.

Moreover, the double exponentially small term also poses difficulties to the numerics. ΔX can grow much smaller than machine precision, hence the numerical error accumulates over time, and in the end it might be the numerical error to determine the behaviour. In Appendix D, we illustrate the numerical challenge by solving (5.28) and (5.30) with different Matlab solvers. Basically, with the same parameters and the same initial condition, some solver predicts a symmetric growth, while others predicts an asymmetric growth.

In summary, asymptotic analysis for the dynamics is delicate, and it is very difficult for it to be captured numerically. It is not clear whether the solution will leave the vicinity of bifurcation I on a trajectory that leads to the $(0, 1)$ equilibrium. In practice, this makes us to doubt whether such delicate behaviour can survive thermal noise.

5.4 Discussions

Using a two-compartment system as an example, we have shown the delicacy of a deterministic voltage-control model by carrying out asymptotic analysis for both the equilibrium and dynamics. In the case of a large number of interacting compartments, the situation becomes even more complicated, since the number of possible equilibria increases as well as the complexity of the bifurcation structure.

In addition, the delicate bifurcations structure means that the two-compartment system is likely to be significantly influenced by stochastic effects, and the deterministic model may fail to be accurate. In the next chapter, we will consider the effects of thermal noise on a two-compartment model. We hope by doing so we can gain insights into a multicompartment system, and then generalise our analysis to the multicompartment system.

Chapter 6

A stochastic multicompartment model

The deterministic Butler-Volmer equation predicts an extremely complicated bifurcation structure, and the existence of multiple equilibria introduces uncertainty even into the dynamics of a two-compartment system. It is therefore necessary to find out to what degree the solution structure of the deterministic model would be changed by thermal noise.

In this chapter we apply the framework of the stochastic model to two and more interacting compartments. We first begin with a two-compartment system and present a two-dimensional chemical master equation, which enables us to obtain a complete lithiation/delithiation profile in both the discrete limit and the continuum limit. We then use the insights from analysing the two-compartment stochastic model to generalise to multiple compartments. The comparison with the deterministic model suggests that the stochastic effects may lead to a profoundly different lithiation/delithiation process.

6.1 A stochastic two-compartment model

6.1.1 Chemical master equation for a two-compartment system

In the two-compartment model, we consider the concentration of each compartment as a random variable over the discrete concentration state space

$$c_i = i\Delta C, \qquad i = 1, \cdots, N,$$

and $\Delta C = 1/(N+1)$, as defined in Section 3.1.1, where N is the number of lithium ions that each individual compartment can accommodate. The state of this two-

compartment system is described by an integer vector (i, j), where

$$C_1 = i\Delta C, \qquad C_2 = j\Delta C \tag{6.1}$$

are the two random variables representing the concentrations in each compartment. The subject under study is the joint probability mass function

$$p_{i,j}(t) = P(C_1(t) = i\Delta C, C_2(t) = j\Delta C), \tag{6.2}$$

which must satisfy the normalisation requirement

$$\sum_{i=1}^{N}\sum_{j=1}^{N} p_{i,j} = 1. \tag{6.3}$$

The marginal distribution for each random variable is denoted as

$$P(C_1(t) = i\Delta C) = p_X(i) = \sum_{j=1}^{N} p_{i,j}, \tag{6.4a}$$

$$P(C_2(t) = j\Delta C) = p_Y(j) = \sum_{i=1}^{N} p_{i,j}. \tag{6.4b}$$

We follow a similar approach to the single-compartment model and study $p_{i,j}(t)$ using the chemical master equation. Assume that if the system is currently in state (i, j), in a small enough time it can make at most one jump to one of its four neighbouring states: $(i-1, j)$, $(i+1, j)$, $(i, j-1)$, and $(i, j+1)$, or remain in state (i, j). We denote the probability per unit time for the system to jump from state (i, j) to the four neighbouring states accordingly as $q^-_{i,j}$, $q^+_{i,j}$, $h^-_{i,j}$, and $h^+_{i,j}$, as illustrated in Fig. 6.1. The change of state is either in the parallel direction or in the vertical direction, i.e. only one of the two variables C_1 and C_2 can change its value. This model does not allow jumps in diagonal directions, that is to say, we do not permit the two random variables to change states simultaneously.

The chemical master equation for the joint probability mass function is

$$\begin{aligned}\frac{\mathrm{d}p_{i,j}}{\mathrm{d}t} &= q^+_{i-1,j}p_{i-1,j} - q^-_{i,j}p_{i,j} - q^+_{i,j}p_{i,j} + q^-_{i+1,j}p_{i+1,j} \\ &\quad + h^+_{i,j-1}p_{i,j-1} - h^+_{i,j}p_{i,j} - h^-_{i,j}p_{i,j} + h^-_{i,j+1}p_{i,j+1}, \quad i, j = 1, 2, \cdots, N,\end{aligned} \tag{6.5a}$$

with no flux boundary condition

$$q^-_{1,j} = q^+_{N,j} = h^-_{i,1} = h^+_{i,N} = 0, \quad i, j = 1, 2, \cdots, N, \tag{6.5b}$$

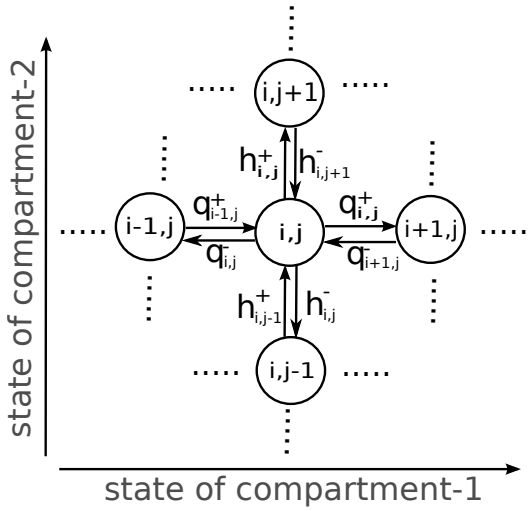


Figure 6.1: One-step process for a two-compartment model and the transition probabilities. Values inside the circles represent the state of the system, and the labelled arrows denote possible jumps between the states as well as the corresponding transition probabilities.

as well as boundary conditions to ensure that completely empty or full states are never reached:

$$p_{0,j} = p_{N+1,j} = p_{i,0} = 0 = p_{i,N+1} = 0, \quad i, j = 1, 2, \cdots, N. \tag{6.5c}$$

To determine the functional form for the transition probabilities, we follow a similar procedure to that in Section 3.1.1. First, due to symmetry between the two compartments, we assume that

$$q^+_{i,j} = h^+_{j,i}, \qquad q^-_{i,j} = h^-_{j,i}, \tag{6.6}$$

so it suffices to consider functional forms for $q^+_{i,j}$ and $q^-_{i,j}$. The mean concentration of compartment-1 is

$$\bar{c}_1(t) = \sum_{i=1}^{N} c_i p_X(i) = \sum_{i=1}^{N} c_i \sum_{j=1}^{N} p_{i,j} = \Delta C \sum_{i=1}^{N} i \sum_{j=1}^{N} p_{i,j}, \tag{6.7}$$

and

$$\frac{\mathrm{d}\bar{c}_1(t)}{\mathrm{d}t} = \Delta C \sum_{i=1}^{N} i \sum_{j=1}^{N} \frac{\mathrm{d}p_{i,j}}{\mathrm{d}t}. \tag{6.8}$$

Substituting (6.5) into (6.8) and after cancelling inside the summation, we can show

that

$$\begin{aligned}\frac{\mathrm{d}\bar{c}_1(t)}{\mathrm{d}t} &= \Delta C \sum_{i=1}^{N} i \sum_{j=1}^{N} \left(q^+_{i-1,j}p_{i-1,j} - q^-_{i,j}p_{i,j} - q^+_{i,j}p_{i,j} + q^-_{i+1,j}p_{i+1,j}\right) \\ &\quad + \Delta C \sum_{i=1}^{N} i \sum_{j=1}^{N} \left(h^+_{i,j-1}p_{i,j-1} - h^+_{i,j}p_{i,j} - h^-_{i,j}p_{i,j} + h^-_{i,j+1}p_{i,j+1}\right) \\ &= \Delta C \sum_{i=1}^{N}\sum_{j=1}^{N}(q^+_{ij} - q^-_{ij})p_{i,j}. \end{aligned} \tag{6.9}$$

In the deterministic limit, we let $\bar{c}_1(t) = i_0\Delta C$, $\bar{c}_2(t) = j_0\Delta C$, and $p_{i,j} = \delta(i,i_0)\delta(j,j_0)$, hence

$$\frac{\mathrm{d}\bar{c}_1(t)}{\mathrm{d}t} = \Delta C(q^+_{i_0j_0} - q^-_{i_0j_0}). \tag{6.10}$$

Comparing (6.10) with the deterministic dynamics of the two-compartment model

$$\frac{\mathrm{d}\bar{c}_1(t)}{\mathrm{d}t} = \frac{1}{2}\exp\left[\frac{E-\mu(\bar{c}_1)-\sigma\bar{c}_2}{2\epsilon}\right] - \frac{1}{2}\exp\left[-\frac{E-\mu(\bar{c}_1)-\sigma\bar{c}_2}{2\epsilon}\right] \tag{6.11}$$

suggests

$$q^+_{i,j} = \frac{1}{2\Delta C}\exp\left[\frac{1}{2\epsilon}\left(E - \frac{g_{i+1}-g_i}{\Delta C} - \sigma j\Delta C\right)\right], \tag{6.12a}$$

$$q^-_{i,j} = \frac{1}{2\Delta C}\exp\left[\frac{1}{2\epsilon}\left(-E + \frac{g_i-g_{i-1}}{\Delta C} + \sigma j\Delta C\right)\right]. \tag{6.12b}$$

This can be simplified to

$$q^+_{i,j} = q^+_i \exp\left(-\frac{1}{2}\alpha\sigma j\right), \tag{6.13a}$$

$$q^-_{i,j} = q^-_i \exp\left(\frac{1}{2}\alpha\sigma j\right), \tag{6.13b}$$

where $q^\pm_i$ are the transition probabilities defined in the single-compartment stochastic model equation (3.10).

6.1.2 Stationary distribution

In steady state, the detailed balance condition states that

$$q^+_{i-1,j}p_{i-1,j} - q^-_{i,j}p_{i,j} = q^+_{i,j}p_{i,j} - q^-_{i+1,j}p_{i+1,j} = 0 \tag{6.14}$$

and

$$h^+_{i,j-1}p_{i,j-1} - h^-_{i,j}p_{i,j} = h^+_{i,j}p_{i,j} - h^-_{i,j+1}p_{i,j+1} = 0. \tag{6.15}$$

Therefore

$$\begin{aligned} p_{i,j} &= \frac{q^+_{i-1,j}}{q^-_{i,j}} p_{i-1,j} \\ &= \exp\left[\frac{1}{\epsilon}\left(E - \frac{g_i - g_{i-1}}{\Delta C} - \sigma j \Delta C\right)\right] p_{i-1,j} && \text{by substituting (6.12)} \\ &= \exp\left[\frac{1}{\epsilon}\left((i-1)E - \frac{g_i - g_1}{\Delta C} - \sigma(i-1) j \Delta C\right)\right] p_{1,j} && \text{by iteration} \end{aligned}$$

and

$$\begin{aligned} p_{i,j} &= \frac{h^+_{i,j-1}}{h^-_{i,j}} p_{i,j-1} \\ &= \exp\left[\frac{1}{\epsilon}\left(E - \frac{g_j - g_{j-1}}{\Delta C} - \sigma i \Delta C\right)\right] p_{i,j-1} && \text{by substituting (6.12)} \\ &= \exp\left[\frac{1}{\epsilon}\left((j-1)E - \frac{g_j - g_1}{\Delta C} - \sigma(j-1) i \Delta C\right)\right] p_{i,1}. && \text{by iteration} \end{aligned}$$

Altogether this gives

$$p_{i,j} = \exp\left[\frac{1}{\epsilon}\left((i+j-2)E - \frac{g_i + g_j - 2g_1}{\Delta C} - \sigma(ij-1)\Delta C\right)\right] p_{1,1}, \tag{6.16}$$

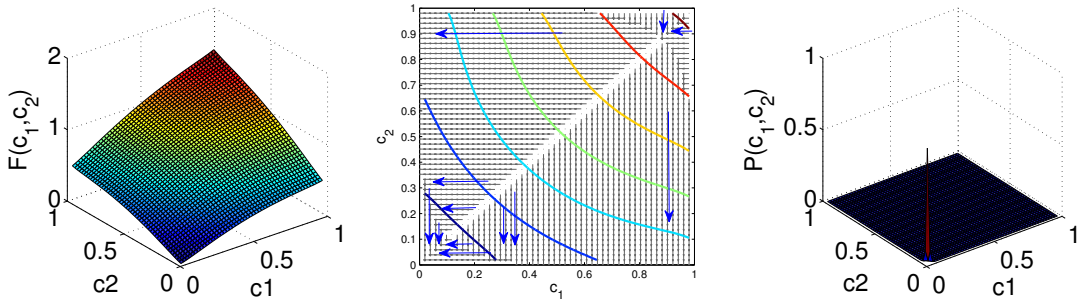
where $p_{1,1}$ is fixed by normalisation. Hence, as with the stationary distribution of the single-compartment model discussed in Section 3.2, the stationary distribution is a Boltzmann distribution $p_{i,j} \propto e^{-F_{i,j}/(k_B T)}$, and the energy associated with state (i, j) is

$$F_{i,j} = \frac{\Omega}{\Delta C}(g_i + g_j + \sigma c_i c_j - (c_i + c_j)E), \tag{6.17}$$

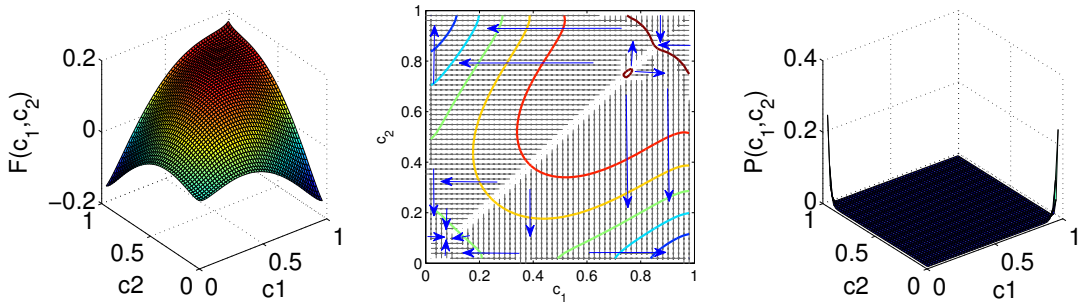
where Ω is enthalpy of mixing as defined in Section 2.1.1.

The equivalent energy and its contour are plotted in Fig. 6.2 for three different values of E, with $N = 50$, $\epsilon = 0.25$, $\sigma = 0.5$. Depending on the value of E, the energy minimum of the two-compartment system is at state $(1, 1)$ (when $E < 0$), as in Fig. 6.2(a); at states $(1, N)$ and $(N, 1)$ (when $0 < E < \sigma$), as in Fig. 6.2(b); or at state (N, N) (when $E > \sigma$), as in Fig. 6.2(c). In addition, the stationary distribution is highly localised around the four corner regions. This indicates that, in equilibrium, each compartment is near empty or near full; no intermediate state of either of the two compartments is preferred.

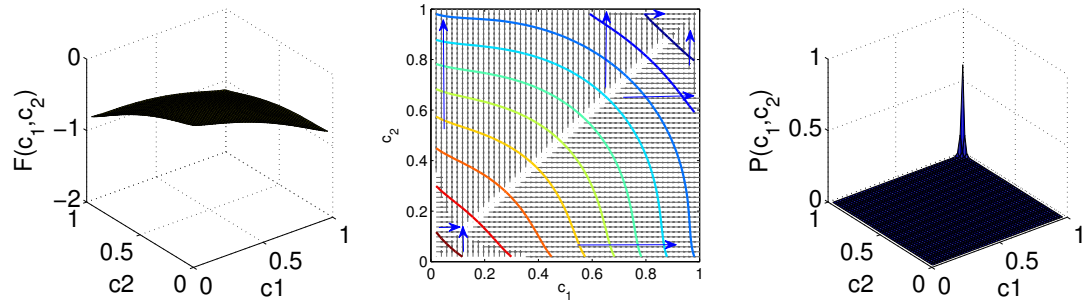
In terms of the mean concentration, the probability distribution in Fig. 6.2(a) suggests that both compartments are near-empty when $E < 0$, and hence $\bar{c}_1 + \bar{c}_2 \approx 0$. Fig. 6.2(b) suggests that one compartment is near-full and the other is near-empty



(a) $E = -0.5$.



(b) $E = 0.15$.



(c) $E = 0.8$.

Figure 6.2: Illustration of the equilibrium distribution of a two-compartment model according to (6.16) for three different values of E, with $\sigma = 0.2$. In the left-most panel, we show the equivalent energy $F(c_1, c_2) = g(c_1) + g(c_2) + \sigma c_1 c_2 - E(c_1 + c_2)$. In the middle panel, we show its contour in coloured lines, and in the background we plot its gradient in grey. Because in the one-step model only transition in the vertical or horizontal direction is allowed, so the gradient actually plots the larger of two projections of ∇F on to the horizontal and vertical directions. The right-most panel plots the equilibrium distribution.

when $0 < E < \sigma$, hence $\bar{c}_1 + \bar{c}_2 \approx 1$. Fig. 6.3(c) is associated with both compartments near-full when $E > \sigma$, hence $\bar{c}_1 + \bar{c}_2 \approx 2$. Therefore, the C-V curve for quasi-equilibrium should be step-like, with two jumps at $E = 0$ and $E = \sigma$. We can confirm

this by computing the mean concentrations for both compartments using

$$\bar{c}_1 = \sum_{i=1}^{N}\sum_{j=1}^{N} p_{i,j} i\Delta C, \qquad \bar{c}_2 = \sum_{i=1}^{N}\sum_{j=1}^{N} p_{i,j} j\Delta C. \tag{6.18}$$

The sum $\bar{c}_1 + \bar{c}_2$ is plotted with respect to E in Fig. 6.3. It indeed shows two jumps, at $E = 0$ and $E = \sigma$, agreeing with the analysis.

Comparing Fig. 6.3 with the bifurcation plot of the deterministic model in Fig. 5.6, we see that by incorporating stochastic effects, we have eliminated hysteresis, reduced the number of equilibria, and hence removed the subtle equilibrium behaviour observed in the deterministic analysis. Meanwhile, the two critical voltages of lithiation/delithiation are displaced by ∓ 1. These are the same phenomena that were observed in the case of a single compartment.

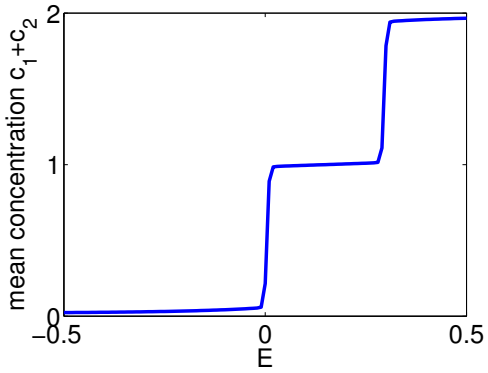


Figure 6.3: Mean concentration $\bar{c}_1 + \bar{c}_2$ corresponding to the stationary distribution (6.16) plotted versus E, with the same parameter values as Fig. 6.2 that $\epsilon = 0.25$, $\sigma = 0.2$, $N = 50$.

Meanwhile, in terms of the effect of discreteness on the equilibrium distribution, all the discussions in Section 3.2 still hold. If discreteness is essential, i.e. when ΔC is relatively large, the local double-well structure will not be captured, and the local distributions at each of the four corner region are always monotonic: the energy minima are at one of the four states $(1, 1)$, $(1, N)$, $(N, 1)$, and (N, N). In contrast, if ΔC is small enough then the logarithmic well structure is retained, and the energy minima are not exactly at the four extreme states but subtly displaced.

6.1.3 Numerical simulations

We first illustrate dynamic properties of the two-compartment stochastic model by numerical simulation. In Fig. 6.4, we present some results obtained by simulating (6.5)

with Matlab **23s**. In each row of Fig. 6.4, from the left-most column to the right-most column, we show the joint probability distribution, the marginal probability distribution of compartment-1, the marginal probability distribution of compartment-2, and the mean concentrations of each compartment. From the top row to the bottom row, E increases from -0.5 to 1.4.

The simulation results show that because initially the potential is low enough, the two-compartment system depletes itself quickly to the lowest state, $(1, 1)$, and becomes approximately a Delta function. After that, the joint probability distribution is always symmetrical with respect to i and j. The Delta function then evolves into a seemingly continuous distribution in the corner region, where both compartments are at their lowest states, and later the majority of the probability mass moves around the two edges, where one compartment is near full but the other is still at the low concentration states. Finally, the probability of the compartment with a low concentration quickly moves to the highest state, and the joint probability function approaches a Delta function at the highest state (N, N). In addition, the evolution of the marginal probability distribution of each compartment resembles that of a single-compartment case, as discussed in Chapter 3.

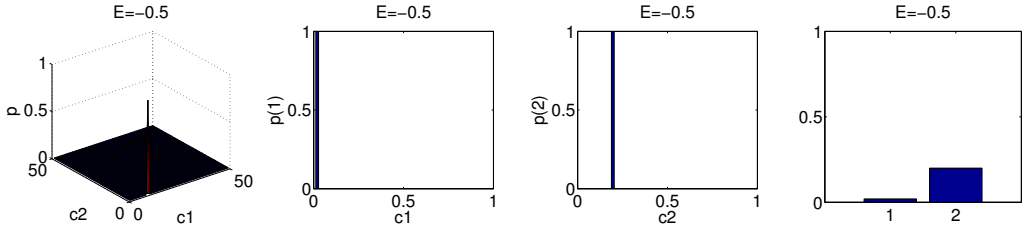
A more prominent feature that is suggested by this evolution profile is the symmetric growth in terms of the mean concentration of each compartment. With probability 1 the dynamic process is asymmetric, as it always happens that one compartment grows to near full while the other stays near empty. However, the mean concentrations of each compartment are always the same. This is a major feature that makes the stochastic model different from the deterministic model.

6.1.4 A discrete-to-continuum model

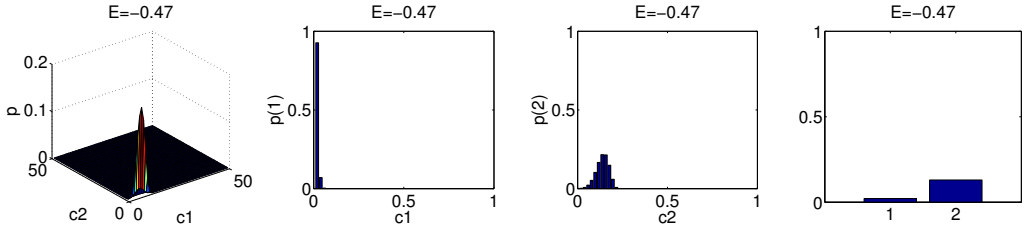
In the two-compartment model, the distinction between discrete and continuum limits still holds, and still depends on the value of α, which we defined in Section 3.3 as

$$\alpha = \frac{\Delta C}{\epsilon}.$$

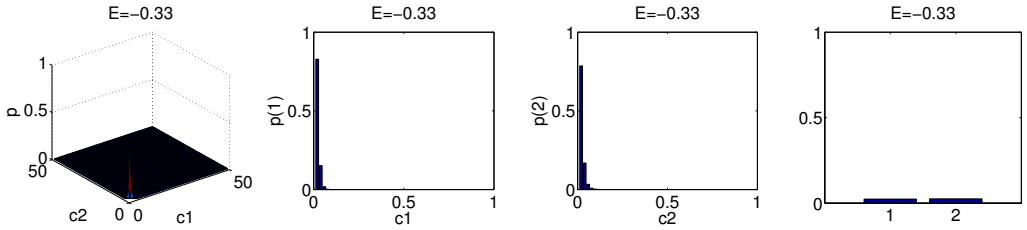
It is possible to develop a discrete-to-continuum model in a similar way to the single-compartment model, using α as the key parameter. However, we believe that this analysis would be analogous to the single-compartment model so we skip the detailed analysis but instead present a heuristic argument for the general case where $\alpha = \mathcal{O}(1)$, using the insights we gained from the single-compartment model in Chapter 3. The two limiting cases, the discrete limit when $\alpha \gg 1$ and the continuum limit when $\alpha \ll 1$, are discussed in detail in Sections 6.1.5 and 6.1.6.



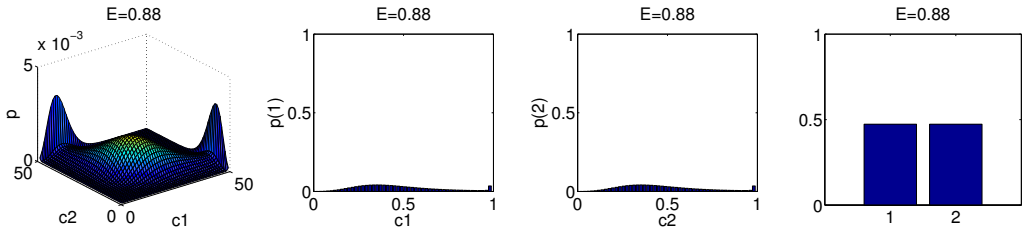
(a) $E = -0.5$.



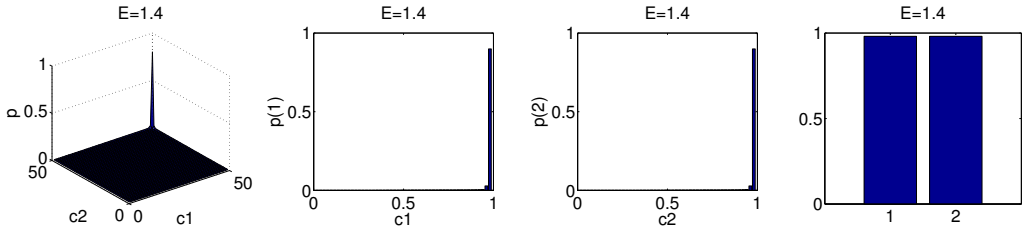
(b) $E = -0.47$.



(c) $E = 0.33$.



(d) $E = 0.88$.



(e) $E = 1.4$.

Figure 6.4: Numerical simulations of the two-dimensional chemical master equation (6.5). Parameter values are $N = 50$, $\sigma = 0.5$, $\epsilon = 0.25$, and $E = t$. An initial condition of a Delta distribution with $p_{ij} = \delta(i = 1)\delta(j = 10)$ is used. From left to right, we show the joint probability distribution, marginal probability distribution for compartment-1, marginal probability distribution for compartment-2, and the mean concentration of each compartment.

A distinguished limit: $\alpha = \mathcal{O}(1)$ As with the single-compartment case, we divide the states of each compartment into three regions: two inner regions near the boundaries and one outer region away from the boundaries. This translates into 9 regions in the two-dimensional (i, j) plane; by symmetry the number of distinct regions can be reduced to 6, as illustrated and labelled in Fig. 6.5.

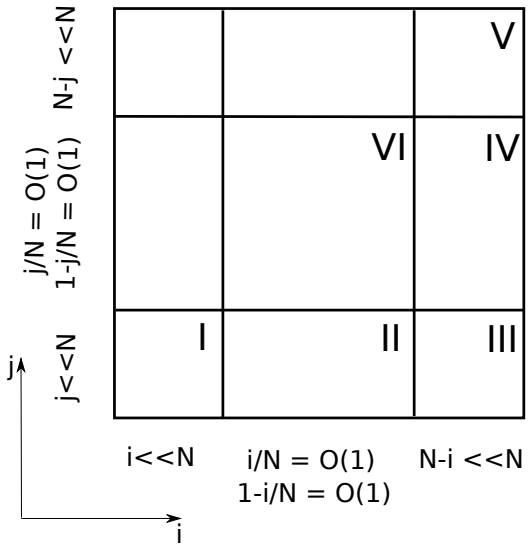


Figure 6.5: A schematic of the 6 regions on the (i, j) plane. This is analogous to the division of inner layers and outer layers in the stochastic single-compartment model.

The canonical dynamic process that we study is

$$E(t) = t.$$

We need to consider only the initial condition of a Delta distribution at the lowest state $(1, 1)$. This is because the numerical experiments of Fig. 6.4 suggest that if initially $E(t)$ is low enough, the system would always quickly relax to its lowest state. Meanwhile, our study of the dynamic problem can be greatly simplified with our knowledge of the single-compartment model. We do not need to analyse the canonical two-dimensional problem in full: it suffices to examine only the transition probabilities in each of the six regions.

In the rest of this section, we illustrate that the dynamics can be divided into two stages. In stage one when E is near 1, the initial Delta distribution splits into two Delta distributions at $(1, N)$ and $(N, 1)$, so that one compartment is near full but the other is near empty. The one-empty, one-full configuration remains till E grows to near $1 + \sigma$, where both compartments become near full.

6.1.4.1 Initial stage: $E \sim 1$

In the initial stage of the dynamic problem that we study, the probability distribution is highly localised in region I, i.e. the boundary states $i, j = 1, 2, \cdots, K$, where $1 \ll K \ll N$. Initially when E is low, the negative fluxes dominates over the positive fluxes in both the horizontal and vertical directions, and the system remains in the lowest state $(1, 1)$. When E increases, the relative strengths of positive and negative fluxes in this region becomes equal in magnitude, and the initial Delta distribution begins to spread out.

This critical value for E is identified by examining the positive and negative transition probabilities. Using the approximation we developed in equation (3.32) that

$$q_i^+ \sim \epsilon^{-3/2} \exp\left(\frac{E-1}{2\epsilon}\right) f_i^+(\alpha), \quad q_i^- \sim \epsilon^{-1/2} \exp\left(-\frac{E-1}{2\epsilon}\right) f_i^-(\alpha), \qquad i \ll N \tag{6.19}$$

where $f_i^\pm$ are defined in (3.33), the two-dimensional transition probabilities in region I can be simplified to

$$q_{i,j}^+ \sim \frac{1}{\epsilon^{3/2}} \exp\left(\frac{E-1}{2\epsilon}\right) f_i^+ \exp\left(-\frac{1}{2}\alpha\sigma j\right), \tag{6.20a}$$

$$q_{i,j}^- \sim \frac{1}{\epsilon^{1/2}} \exp\left(-\frac{E-1}{2\epsilon}\right) f_i^- \exp\left(\frac{1}{2}\alpha\sigma j\right), \tag{6.20b}$$

$$h_{i,j}^+ \sim \frac{1}{\epsilon^{3/2}} \exp\left(\frac{E-1}{2\epsilon}\right) f_j^+ \exp\left(-\frac{1}{2}\alpha\sigma i\right), \tag{6.20c}$$

$$h_{i,j}^- \sim \frac{1}{\epsilon^{1/2}} \exp\left(-\frac{E-1}{2\epsilon}\right) f_j^- \exp\left(\frac{1}{2}\alpha\sigma i\right). \tag{6.20d}$$

Clearly, the positive and negative transition probabilities in (6.20) depend on E in a similar way to the left inner region in the single-compartment model, except for an extra exponential term of order $\mathcal{O}(1)$. Therefore, $E \sim 1$ is a critical value, and the relevant local time variable is (as found previously in Chapters 2 and 3)

$$E = 1 + \epsilon \log \epsilon + \epsilon\tau. \tag{6.21}$$

Dynamics in region I The chemical master equation for region I thus becomes

$$\begin{aligned}\frac{\mathrm{d}p_{i,j}}{\mathrm{d}\tau} &= e^{-\frac{1}{2}\alpha\sigma j + \frac{\tau}{2}} \left(f_{i-1}^+ p_{i-1,j} - f_i^+ p_{i,j}\right) + e^{\frac{1}{2}\alpha\sigma j - \frac{\tau}{2}} \left(f_{i+1}^- p_{i+1,j} - f_i^- p_{i,j}\right) \\ &\quad e^{-\frac{1}{2}\alpha\sigma i + \frac{\tau}{2}} \left(f_{j-1}^+ p_{i,j-1} - f_j^+ p_{i,j}\right) + e^{\frac{1}{2}\alpha\sigma i - \frac{\tau}{2}} \left(f_{j+1}^- p_{i,j+1} - f_j^- p_{i,j}\right), \quad i, j = 1, \cdots K,\end{aligned} \tag{6.22a}$$

with no flux boundary condition

$$q^-_{1,j} = h^-_{i,1} = 0, \quad i, j = 1, 2, \cdots, K, \tag{6.22b}$$

as well as boundary conditions to ensure that completely empty or full states are never reached:

$$p_{0,j} = p_{i,0} = 0, \quad i, j = 1, 2, \cdots, K. \tag{6.22c}$$

The system (6.22) has to be solved numerically for each fixed value of σ and α.

We present an example solution in region I in Fig. 6.6, with $\alpha = 0.5$, $\sigma = 0.4$, and $K = 25$. The shape of the probability distribution differs depending on the values of α and σ, but the dynamic properties are qualitatively similar. The probability mass in region I is not conserved, and the probability flux flows out from region I to its neighbouring region II.

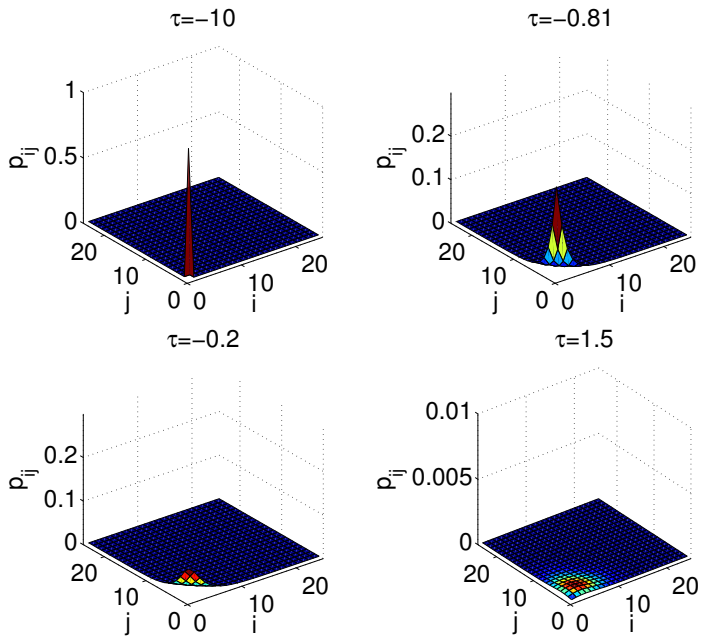


Figure 6.6: Probability distribution evolutoin of region I by simulating (6.22) with $\alpha = 0.5$, $\sigma = 0.4$, and $K = 25$.

Regime II and III: quasi-equilibrium The probability mass flowing out of region I all flows into region II (as well as its mirror region $j/N, 1 - j/N \sim \mathcal{O}(1)$ and $1 \ll i \ll N$). To study the dynamic problem in this region in full, we need to define a mixed joint density because the distribution of compartment-1 can be approximated as a continuum model but the distribution of compartment-2 needs to be treated

discretely. However, since this region is in quasi-equilibrium, we do not study its behaviour in detail.

Instead, inspired by the single-compartment dynamics, we can argue that both this region and region III (except for the corner state $(N, 1)$) are in quasi-equilibrium. If the argument holds, the probability mass from region I just passes through region II and enters region III. In addition, since all states in region III, other than the bottom-leftmost state $(N, 1)$, are in quasi-equilibrium, the probability mass flowing out of region I simply accumulates at state $(N, 1)$.

To verify that both region II and III are in quasi-equilibrium, it remains to check the transition probabilities in both regions. In region II, we let $c_1 = i\Delta C$ and use the rescaling of (6.21) to find the transition probabilities in this region to be

$$q^+_{i,j} = \frac{\epsilon^{1/2}}{2\Delta C}\sqrt{\frac{1-c_1}{c_1}}\exp\left(\frac{\tau}{2} - \frac{1}{2}\alpha\sigma j\right)\exp\left(\frac{c_1}{\epsilon}\right), \tag{6.23a}$$

$$q^-_{i,j} = \frac{\epsilon^{-1/2}}{2\Delta C}\sqrt{\frac{c_1}{1-c_1}}\exp\left(-\frac{\tau}{2} + \frac{1}{2}\alpha\sigma j\right)\exp\left(-\frac{c_1}{\epsilon}\right), \tag{6.23b}$$

$$h^+_{i,j} = \epsilon^{-1} f^+_j \exp\left(\frac{\tau}{2}\right)\exp\left(-\frac{\sigma c_1}{2\epsilon}\right), \tag{6.23c}$$

$$h^-_{i,j} = \epsilon^{-1} f^-_j \exp\left(-\frac{\tau}{2}\right)\exp\left(\frac{\sigma c_1}{2\epsilon}\right). \tag{6.23d}$$

Therefore $q^+_{i,j} \gg q^-_{i,j}$ and $h^-_{i,j} \gg h^+_{i,j}$, so that all states in region II are indeed in quasi-equilibrium.

In region III, compartment-1 is near full and compartment-2 is near empty, so that both random variables needs to be treated discretely. We denote $i' = N + 1 - i$ and find transition probabilities in this region as

$$q^+_{i,j} = f^-_{i'} \exp\left(\frac{\tau}{2} - \frac{1}{2}\alpha\sigma j\right)\exp\left(\frac{1}{\epsilon}\right), \tag{6.24a}$$

$$q^-_{i,j} = \frac{1}{\epsilon^2} f^+_{i'} \exp\left(-\frac{\tau}{2} + \frac{1}{2}\alpha\sigma j\right)\exp\left(-\frac{1}{\epsilon}\right), \tag{6.24b}$$

$$h^+_{i,j} = \frac{1}{\epsilon} f^+_j \exp\left(\frac{\tau}{2} + \frac{1}{2}\alpha\sigma i'\right)\exp\left(-\frac{\sigma}{2\epsilon}\right), \tag{6.24c}$$

$$h^-_{i,j} = \frac{1}{\epsilon} f^-_j \exp\left(-\frac{\tau}{2} - \frac{1}{2}\alpha\sigma i'\right)\exp\left(\frac{\sigma}{2\epsilon}\right). \tag{6.24d}$$

Again $q^+_{i,j} \gg q^-_{i,j}$ and $h^-_{i,j} \gg h^+_{i,j}$ also hold in region III.

A brief summary of the initial stage Combining the above descriptions of region I, II and III, it is clear that all the probability mass which leaks from region I accumulates at $(N, 1)$. By symmetry, the Delta distribution at the lowest state $(1, 1)$

finally evolves into two Delta distributions, at state $(1, N)$ and state $(N, 1)$. Therefore, in the end of this stage, one of the two compartments must be near empty, while the other must be near full.

We further note that in region III, $q^+_{i,j} \gg q^-_{i,j}$ continues to hold as E increases, but $h^-_{i,j} \gg h^+_{i,j}$ ceases to hold when E approaches $1 + \sigma + \epsilon \log \epsilon$. As a result, the Delta distribution at state $(1, N)$ will no long remain.

6.1.4.2 Second stage: $E \sim 1 + \sigma$

As E approaches $1 + \sigma$, we expect the probability distribution to flow out from region III, pass through region IV, and eventually reach region V.

To show this, we make the local expansion

$$E = 1 + \sigma + \epsilon \log \epsilon + \epsilon \tau'. \tag{6.25}$$

The transition probabilities in the horizontal direction in all three regions III, IV,and V are given by

$$q^+_{i,j} = f^-_{i'} \exp\left(\frac{\tau'}{2} - \frac{1}{2}\alpha\sigma j\right) \exp\left(\frac{1+\sigma}{\epsilon}\right), \tag{6.26a}$$

$$q^-_{i,j} = \frac{1}{\epsilon^2} f^+_{i'} \exp\left(-\frac{\tau'}{2} + \frac{1}{2}\alpha\sigma j\right) \exp\left(-\frac{1+\sigma}{\epsilon}\right), \tag{6.26b}$$

where $i' = N + 1 - i$. Hence $q^+_{i,j}$ always dominates over $q^-_{i,j}$, suggesting that the probability distribution is highly localised in the right-most states, and compartment-1 always remains near full, i.e.

$$p_{ij} \sim 0, \quad \text{if } i \neq N. \tag{6.27}$$

This reduces the chemical master equation to the one-dimensional system

$$\frac{\mathrm{d}p_{N,j}}{\mathrm{d}t} = h^+_{N,j-1} p_{N,j-1} - h^+_{N,j} p_{N,j} - h^-_{N,j} p_{N,j} + h^-_{N,j+1} p_{N,j+1}, \quad j = 1, 2, \cdots, N. \tag{6.28a}$$

where

$$h^+_{N,j} = q^+_j \exp(-\alpha N \sigma/2) \approx q^+_j \exp(-\sigma/2\epsilon), \tag{6.28b}$$

$$h^-_{N,j} = q^-_j \exp(\alpha N \sigma/2) \approx q^+_j \exp(\sigma/2\epsilon). \tag{6.28c}$$

System (6.28) resembles the chemical master equation (3.1) of the single-compartment model except for a shift in the critical voltage by σ. Therefore, in the second stage where $E \sim 1 + \sigma$, the probability distribution becomes purely one-dimensional. More

importantly, the one-dimensional process is identical to the single-compartment model dynamics.

In sum, in the second stage as E approaches $1 + \sigma + \epsilon \log \epsilon$, one compartment remains full, and the other compartment undergoes an identical process to the single-compartment case and fills up from near empty to near full.

6.1.5 The discrete limit: $\alpha \gg 1$

All the discussions of the general case of $\alpha \sim \mathcal{O}(1)$ still apply to the two limiting cases of $\alpha \gg 1$ and $\alpha \ll 1$. The two critical transitions still happen at $E \sim 1$ and $E \sim 1 + \sigma$.

In the discrete limit $\alpha \gg 1$, the single-compartment model suggests that only the lowest and the highest state are significant, and meanwhile all other states are negligible. For a two-compartment model, we need to consider only the four states: $(1, 1)$, $(1, N)$, $(N, 1)$, and (N, N). In addition, the single-compartment model suggests that the positive probability flux always dominates over the negative probability flux; hence the leading order chemical master equation can be reduced to

$$\frac{\mathrm{d}p_{11}}{\mathrm{d}t} \sim -(q_{11}^+ + h_{11}^+)p_{11}, \tag{6.29a}$$

$$\frac{\mathrm{d}p_{N1}}{\mathrm{d}t} \sim q_{11}^+ p_{11} - h_{N1}^+ p_{N1}, \tag{6.29b}$$

$$\frac{\mathrm{d}p_{1N}}{\mathrm{d}t} \sim h_{11}^+ p_{11} - q_{1N}^+ p_{1N}, \tag{6.29c}$$

$$\frac{\mathrm{d}p_{NN}}{\mathrm{d}t} \sim q_{1N}^+ p_{1N} + h_{N1}^+ p_{N1}, \tag{6.29d}$$

subject to the initial condition that $p_{i,j} = \delta_{1i}\delta_{1j}$.

Now only the two transition probabilities $q_{11}^+ (= h_{11}^+)$ and $q_{1N}^+ (= h_{N1}^+)$ are relevant, namely

$$q_{11}^+ = q_1^+ e^{-\sigma \Delta C} \sim \epsilon^{-3/2} f_1^+ \exp\left(\frac{E-1}{2\epsilon} - \frac{1}{2}\alpha\sigma\right) \tag{6.30a}$$

$$q_{1N}^+ = q_1^+ e^{-\sigma N \Delta C} \sim \epsilon^{-3/2} f_1^+ \exp\left(\frac{E-1-\sigma}{2\epsilon}\right). \tag{6.30b}$$

Their values confirm that the two critical values for E are 1 and $1 + \sigma$.

Initial stage: $E \sim 1$ When $E \sim 1$, the local expansion of

$$E = 1 + \epsilon \log \epsilon + \epsilon\tau \tag{6.31}$$

gives the leading order chemical master equation

$$\frac{\mathrm{d}p_{11}}{\mathrm{d}\tau} \sim -2f_1^+ e^{-\alpha\sigma/2} e^{\tau/2} p_{11}, \tag{6.32a}$$

$$\frac{\mathrm{d}p_{N1}}{\mathrm{d}t} = \frac{\mathrm{d}p_{1N}}{\mathrm{d}t} \sim f_1^+ e^{-\alpha\sigma/2} e^{\tau/2} p_{11}, \tag{6.32b}$$

$$\frac{\mathrm{d}p_{NN}}{\mathrm{d}t} \sim 0, \tag{6.32c}$$

subject to the initial condition that $p_{i,j} = \delta_{1i}\delta_{1j}$ as $\tau \to -\infty$. The leading order solution is,

$$p_{11} \sim e^{-4f_1^+ e^{-\alpha\sigma/2} e^{\tau/2}}, \tag{6.33a}$$

$$p_{1N} = p_{N1} \sim \frac{1}{2}\left(1 - e^{-4f_1^+ e^{-\alpha\sigma/2} e^{\tau/2}}\right), \tag{6.33b}$$

$$p_{NN} \sim 0. \tag{6.33c}$$

Therefore, in this stage, the probability of the lowest state $(1,1)$ decays to 0, while the probabilities of the states $(1,N)$ and $(N,1)$ grow to $1/2$. The initial and final state of this stage are the same as the general $\alpha \sim \mathcal{O}(1)$ case, but only three states ($(1,1)$, $(1,N)$, and $(N,1)$) are involved.

Second stage: $E \sim 1+\sigma$ Close to the critical value of $E \sim 1+\sigma$, we rescale E by

$$E = 1 + \sigma + \epsilon \log \epsilon + \epsilon\tau'. \tag{6.34}$$

The leading order system is

$$\frac{\mathrm{d}p_{11}}{\mathrm{d}\tau} \sim 0, \tag{6.35a}$$

$$\frac{\mathrm{d}p_{N1}}{\mathrm{d}t} = \frac{\mathrm{d}p_{1N}}{\mathrm{d}t} \sim -f_1^+ e^{-\alpha\sigma/2} e^{\tau'/2} p_{N1}, \tag{6.35b}$$

$$\frac{\mathrm{d}p_{NN}}{\mathrm{d}t} \sim 2f_1^+ e^{-\alpha\sigma/2} e^{\tau'/2} p_{N1}. \tag{6.35c}$$

Matching with the previous stage (6.33) suggests that the initial condition is

$$p_{11} \to 0, \quad p_{N1} = p_{1N} \to \frac{1}{2}, \quad p_{NN} \to 0, \quad \text{as } \tau' \to -\infty.$$

The leading order solution is

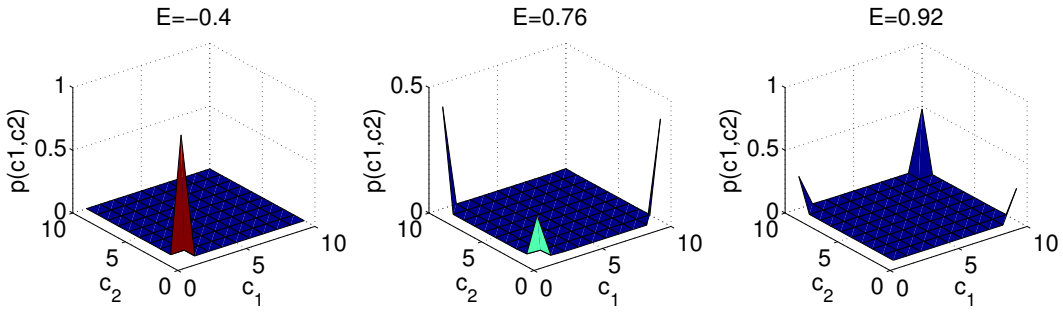
$$p_{11} \sim 0, \tag{6.36a}$$

$$p_{1N} = p_{N1} \sim \frac{1}{2} e^{-2f_1^+ e^{-\alpha\sigma/2} e^{\tau'/2}}, \tag{6.36b}$$

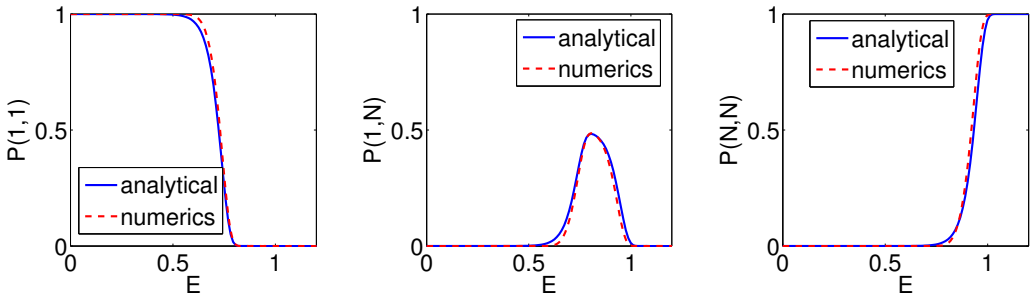
$$p_{N1} \sim 1 - e^{-2f_1^+ e^{-\alpha\sigma/2} e^{\tau'/2}}. \tag{6.36c}$$

Again it confirms that near $E \sim 1 + \sigma$ the probability becomes completely concentrated in the highest state (N, N). We consolidate this heuristic argument by comparing the analytical solutions (6.33) and (6.36) with numerical solutions in Fig. 6.7.

In Fig. 6.7(a), the numerical solution of the joint probability distribution is shown, and it can be seen that the probability is always concentrated in the four corners. In Fig. 6.7(b), we plot asymptotic solutions of the probability of the four corner states and compare them with numerical solutions and see good agreement.



(a) Evolution of the joint probability distribution by numerically solving the chemical master equation (6.5).



(b) Comparisons of the probability of states $(1,1)$, $(1,N)(N,1)$, and (N,N) between the numerical results and the asymptotic solution (6.33) and (6.36).

Figure 6.7: Evolution of the joint probability distribution of a two-compartment system in the discrete limit. The parameter values are $\sigma = 0.2$, $N = 10$, $\epsilon = 0.02$, $E = t$ and $\alpha = 4.45$, with a Delta distribution at $t = -5$ as the initial condition.

6.1.6 The continuum limit: $\alpha \ll 1$

In the continuum limit, it is again possible to obtain asymptotic solutions for the two critical transitions. First, the transition around $E \sim 1 + \sigma$ is essentially a one-dimensional process, in that one compartment is always near full while the other fills up from near empty to near full in a process that is identical to the single-compartment model. Therefore, the transition around $E \sim 1 + \sigma$ is well understood, and it only remains to study the transition near $E \sim 1$. In this transition, the initial

delta distribution first develops into a continuous Gaussian distribution, and then the Gaussian evolves into two delta distributions concentrated at the two corner states $(1, N)$ and $(N, 1)$.

Here we show that the analysis near $E \sim 1$ is very similar to a single compartment model in the continuum limit, as presented in Section 3.4.3. The region of interest is region I, and the transition near $E \sim 1$ can be decomposed into two steps. In the first step, the delta distribution spreads into a Gaussian distribution. In the second step, the Gaussian distribution evolves according to a Fokker-Planck PDE.

6.1.6.1 Sub-stage 1: discrete law

Initially, the distribution is highly localised in the lowest states, so we consider a small region inside region I that satisfies $i\alpha \ll 1$, $j\alpha \ll 1$. We rescale E with

$$E = 1 + \epsilon \log \epsilon + \epsilon \log \alpha + \epsilon \bar{\tau}, \quad \text{or} \quad \bar{\tau} = \tau - \log \alpha. \tag{6.37}$$

In this region, we can neglect α-dependence in the exponentials of $q_i^{\pm}$, giving

$$q_{i,j}^{+} \sim \frac{1}{\epsilon\alpha} \tilde{f_i^{+}} \exp(\bar{\tau}/2), \qquad q_{i,j}^{-} \sim \frac{1}{\epsilon\alpha} \tilde{f_i^{-}} \exp(-\bar{\tau}/2), \tag{6.38}$$

where the coefficients $\tilde{f_i^{\pm}}$ are as defined in (3.54). The chemical master equation becomes

$$\begin{aligned} \alpha \frac{\mathrm{d}p_{i,j}}{\mathrm{d}\bar{\tau}} &= \tilde{f_{i-1}^{+}} e^{\bar{\tau}/2} p_{i-1,j} - \tilde{f_i^{-}} e^{-\bar{\tau}/2} p_{i,j} - \tilde{f_i^{+}} e^{\bar{\tau}/2} p_{i,j} + \tilde{f_{i+1}^{-}} e^{-\bar{\tau}/2} p_{i,j} \\ &\quad + \tilde{f_{j-1}^{+}} e^{\bar{\tau}/2} p_{i,j-1} - \tilde{f_j^{-}} e^{-\bar{\tau}/2} p_{i,j} - \tilde{f_j^{+}} e^{\bar{\tau}/2} p_{i,j} + \tilde{f_{i+1}^{-}} e^{-\bar{\tau}/2} p_{i,j+1}. \end{aligned} \tag{6.39}$$

In the limit $\alpha \downarrow 0$, the system is in quasi-equilibrium.

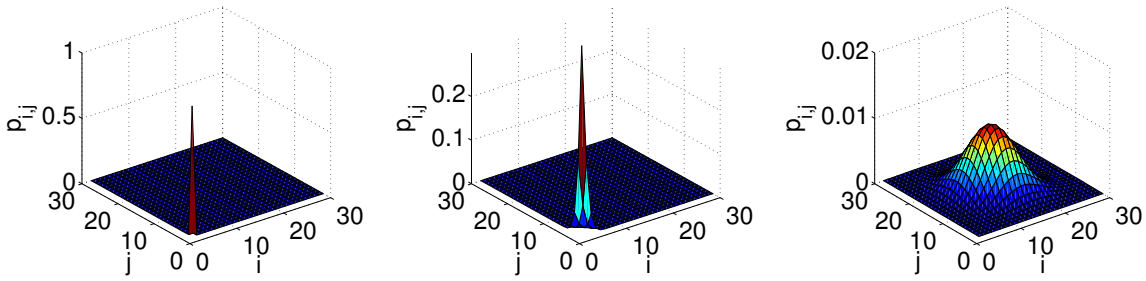
Using the stationary distribution found in (6.16) and using the approximation of $g(c_i)$ for $i \ll N$ that is presented in Appendix B.1, it can be shown

$$p_{i,j}(\bar{\tau}) \propto e^{(i-1)\bar{\tau}} e^{i-1-i\log i} e^{(j-1)\bar{\tau}} e^{j-1-j\log j} e^{-\alpha\sigma ij} \tag{6.40}$$

up to a normalization factor. The density function (6.40) is plotted in Fig. 6.8 to show how a Delta distribution gradually develops into a Gaussian as $\bar{\tau}$ increases.

To verify that (6.40) is indeed a Gaussian when $\bar{\tau}$ as well as i, j tend to infinity, we make the local transformation

$$i = e^{\bar{\tau}} + s, \qquad j = e^{\bar{\tau}} + u \tag{6.41}$$



(a) $\bar{\tau} = -10$. (b) $\bar{\tau} = 0$. (c) $\bar{\tau} = 3$.

Figure 6.8: Quasi-equilibrium distribution given by (6.40) with the sum $\sum p_i$ normalised to 1. Here $\alpha = 0.05$ and $\sigma = 0.2$.

where s and u are small compared to $e^{\bar{\tau}}$. It can then be shown that

$$p(s, u, \bar{\tau}) := p_{i,j}(\bar{\tau}) \propto \exp\left[-\frac{1}{2}e^{-\bar{\tau}}s^2 - \frac{1}{2}e^{-\bar{\tau}}u^2 - \alpha\sigma e^{\bar{\tau}}(s+u) - \alpha\sigma su\right] \tag{6.42}$$

up to a normalisation factor, which is indeed a Gaussian. (6.42) can be rearranged to give

$$p(s, u, \bar{\tau}) = \frac{\sqrt{1-(\alpha\sigma e^{\bar{\tau}})^2}}{2\pi} e^{-\bar{\tau}} e^{-\frac{1}{2}e^{-\bar{\tau}}((s-s_0)^2+(u-u_0)^2)-\alpha\sigma(s-s_0)(u-u_0)}, \tag{6.43a}$$

where

$$s_0 = u_0 = -\frac{\alpha\sigma e^{2\bar{\tau}}}{1+\alpha\sigma e^{\bar{\tau}}}. \tag{6.43b}$$

The pre-factor is determined by the normalisation requirement $\sum p_{i,j}(\bar{\tau}) = 1$, or equivalently $\iint p(s, u, \bar{\tau})\mathrm{d}s\mathrm{d}u = 1$. The normalisation requirement holds as long as the probability mass flowing out from region I can be neglected, which is true in the beginning stage of the transition.

The expansions (6.43) can be rewritten in terms of τ as

$$p(\xi, \eta, \tau) := p(s, u, \bar{\tau}) = \frac{\alpha\sqrt{1-\sigma^2 e^{2\tau}}}{2\pi} e^{-\tau} e^{-\frac{1}{2}e^{-\tau}\xi^2 - \frac{1}{2}e^{-\tau}\eta^2 - \sigma\xi\eta}, \tag{6.44a}$$

where

$$\xi = \frac{i\alpha - e^{\tau} - \alpha s_0}{\sqrt{\alpha}}, \qquad \eta = \frac{j\alpha - e^{\tau} - \alpha u_0}{\sqrt{\alpha}} \tag{6.44b}$$

and

$$s_0 = u_0 = -\frac{\sigma e^{2\tau}}{1+\sigma e^{\tau}}. \tag{6.44c}$$

6.1.6.2 Sub-stage 2: the F-P equation

At the end of the previous stage, the distribution has moved to a region of $N \gg i, j \gg 1$ and the approximation (6.39) breaks down. Now by defining $x = i\alpha$, $y = j\alpha$ (so $x, y \gg \alpha$) and $p(x, y, \tau) = p_{i,j}(\tau)$, and exploiting large i asymptotics for f_i^+ and f_i^-, we find a Fokker-Planck PDE

$$\begin{aligned}\frac{\partial p}{\partial \tau} = &-\frac{\partial}{\partial x}\left[\sinh\left(\frac{\tau - \sigma y + 2x - \log x}{2}\right)p\right] + \frac{\alpha}{2}\frac{\partial^2}{\partial x^2}\left[\cosh\left(\frac{\tau - \sigma y + 2x - \log x}{2}\right)p\right] \\ &-\frac{\partial}{\partial y}\left[\sinh\left(\frac{\tau - \sigma x + 2y - \log y}{2}\right)p\right] + \frac{\alpha}{2}\frac{\partial^2}{\partial y^2}\left[\cosh\left(\frac{\tau - \sigma x + 2y - \log y}{2}\right)p\right]\end{aligned} \tag{6.45}$$

As in the linear noise approximation that we performed in Section 3.4.3.2, we make a local expansion

$$\sqrt{\alpha}\Phi(\xi, \eta, \tau) = p(x, y, \tau), \qquad \text{where } x = \bar{x}(\tau) + \sqrt{\alpha}\xi, \quad y = \bar{y}(\tau) + \sqrt{\alpha}\eta. \tag{6.46}$$

Now the definition of the local variables ξ and η are consistent with that defined in (6.44b), the Gaussian approximation of sub-stage 1. By the chain rule,

$$\begin{cases} \dfrac{\partial}{\partial x} &= \dfrac{1}{\sqrt{\alpha}}\dfrac{\partial}{\partial \xi}, \\ \dfrac{\partial}{\partial y} &= \dfrac{1}{\sqrt{\alpha}}\dfrac{\partial}{\partial \eta}, \\ \dfrac{\partial}{\partial \tau} &= -\dfrac{1}{\sqrt{\alpha}}\dfrac{\mathrm{d}\bar{x}(\tau)}{\mathrm{d}\tau}\dfrac{\partial}{\partial \xi} - \dfrac{1}{\sqrt{\alpha}}\dfrac{\mathrm{d}\bar{y}(\tau)}{\mathrm{d}\tau}\dfrac{\partial}{\partial \eta} + \dfrac{\partial}{\partial \tau'}, \end{cases} \tag{6.47}$$

where $\tau' = \tau$ represents the new time variable, so that the left-hand side of (6.45) becomes

$$\frac{\partial p}{\partial \tau} = -\frac{\mathrm{d}\bar{x}}{\mathrm{d}\tau}\frac{\partial \Phi}{\partial \xi} - \frac{\mathrm{d}\bar{y}}{\mathrm{d}\tau}\frac{\partial \Phi}{\partial \eta} + \sqrt{\alpha}\frac{\partial \Phi}{\partial \tau}. \tag{6.48}$$

Meanwhile, we expand the right-hand side of (6.45) using $x = \bar{x}(\tau) + \sqrt{\alpha}\xi$ and $y = \bar{y}(\tau) + \sqrt{\alpha}\eta$ to obtain

$$\begin{aligned}\frac{\partial}{\partial x}[\sinh(\tau/2 - \epsilon y/2 + x - \log x/2)p(x, y, \tau)] = &\sinh(\tau/2 - \sigma y/2 + \bar{x} - \log \bar{x}/2)\frac{\partial \Phi}{\partial \xi} \\ &- \frac{1}{2}\sqrt{\alpha}\sigma\cosh(\tau/2 - \sigma y/2 + \bar{x} - \log \bar{x}/2)\eta\frac{\partial \Phi}{\partial \xi} \\ &+ \sqrt{\alpha}\cosh(\tau/2 - \sigma y/2 + \bar{x} - \log \bar{x}/2)\left(1 - \frac{1}{2\bar{x}}\right)\frac{\partial}{\partial \xi}(\xi\Phi) + \mathcal{O}(\alpha)\end{aligned} \tag{6.49}$$

and

$$\frac{\alpha}{2}\frac{\partial^2}{\partial x^2}[\cosh(\tau/2-\sigma y/2+x-\log x/2)p] = \frac{\sqrt{\alpha}}{2}\cosh(\tau/2-\sigma y/2+\bar{x}-\log\bar{x}/2)\frac{\partial^2\Phi}{\partial\xi^2}+\mathcal{O}(\alpha). \quad (6.50)$$

The other two terms in the right-hand side of (6.45) are expanded similarly. Substituting them altogether into the F-P equation (6.45) and matching terms at order $\mathcal{O}(1)$ and $\mathcal{O}(\sqrt{\alpha})$ gives us the following equations:

$$\frac{\mathrm{d}\bar{x}}{\mathrm{d}\tau} = \sinh\left(\frac{\tau-\sigma\bar{y}+2\bar{x}-\log\bar{x}}{2}\right), \quad (6.51a)$$

$$\frac{\mathrm{d}\bar{y}}{\mathrm{d}\tau} = \sinh\left(\frac{\tau-\sigma\bar{x}+2\bar{y}-\log\bar{y}}{2}\right), \quad (6.51b)$$

$$\frac{\partial\Phi}{\partial\tau} = \cosh\left(\frac{\tau-\sigma\bar{y}+2\bar{x}-\log\bar{x}}{2}\right)\left(\frac{1}{2}\frac{\partial^2\Phi}{\partial\xi^2}-\left(1-\frac{1}{2\bar{x}}\right)\frac{\partial}{\partial\xi}(\xi\Phi)+\frac{\sigma\eta}{2}\frac{\partial\Phi}{\partial\xi}\right) + \cosh\left(\frac{\tau-\sigma\bar{x}+2\bar{y}-\log\bar{y}}{2}\right)\left(\frac{1}{2}\frac{\partial^2\Phi}{\partial\eta^2}-\left(1-\frac{1}{2\bar{y}}\right)\frac{\partial}{\partial\eta}(\eta\Phi)+\frac{\sigma\xi}{2}\frac{\partial\Phi}{\partial\eta}\right). \quad (6.51c)$$

Now equations (6.51a - 6.51b) are exactly the deterministic law for a two-compartment model, and (6.51c) is the linear noise approximation, which depends on the solutions for $\bar{x}(\tau)$ and $\bar{y}(\tau)$. The symmetry between $\bar{x}$ and $\bar{y}$ in terms of the dynamics as well as the initial condition requires that

$$\bar{x}(\tau) = \bar{y}(\tau), \quad (6.52)$$

reducing (6.51) to

$$\frac{\mathrm{d}\bar{x}}{\mathrm{d}\tau} = \sinh\left(\frac{\tau+(2-\sigma)\bar{x}-\log\bar{x}}{2}\right), \quad (6.53a)$$

$$\frac{\partial\Phi}{\partial\tau} = \cosh\left(\frac{\tau+(2-\sigma)\bar{x}-\log\bar{x}}{2}\right)\left(\frac{1}{2}\frac{\partial^2\Phi}{\partial\xi^2}+\frac{1}{2}\frac{\partial^2\Phi}{\partial\eta^2}+\frac{\sigma\eta}{2}\frac{\partial\Phi}{\partial\xi}+\frac{\sigma\xi}{2}\frac{\partial\Phi}{\partial\eta}\right) - \cosh\left(\frac{\tau+(2-\sigma)\bar{x}-\log\bar{x}}{2}\right)\left(1-\frac{1}{2\bar{x}}\right)\left(\frac{\partial}{\partial\xi}(\xi\Phi)+\frac{\partial}{\partial\eta}(\eta\Phi)\right). \quad (6.53b)$$

Now the mean concentration $\bar{x}(\tau) = \bar{y}(\tau)$ needs to be solved by numerics. Provided $\sigma < 2$, the solution is qualitatively similar to the deterministic model (2.48a) for a single compartment when it transits from the lower branch to the higher branch. As in Section 2.3.1.3, $\bar{x}(\tau)$ blows up in finite time, and the blow-up time is a numerically determined function of σ.

Once $\bar{x}(\tau)$ is known, we seek a Gaussian ansatz for $\Phi(\xi, \eta, \tau)$, i.e.

$$\Phi(\xi, \eta, \tau) = C(\tau) \exp[-A(\tau)(\xi^2 + \eta^2) + B(\tau)\xi\eta]. \tag{6.54}$$

Comparing it with a standard bivariate Gaussian distribution, we see that the variance of the Gaussian is

$$\mathrm{Var}(\tau) = \frac{A(\tau)}{2\pi^2 C(\tau^2)}, \tag{6.55}$$

its correlation is

$$\mathrm{Corr}(\tau) = \frac{B(\tau)}{2A(\tau)} = \frac{\sqrt{A(\tau)^2 - \pi^2 C(\tau)^2}}{A(\tau)}, \tag{6.56}$$

and the conservation of probability mass requires that

$$B(\tau)^2 + 4\pi^2 C(\tau)^2 = 4A(\tau)^2. \tag{6.57}$$

Substituting (6.54) into (6.53b), we obtain the following equations for $A(\tau)$ and $B(\tau)$:

$$\frac{\mathrm{d}A}{\mathrm{d}\tau} = -\cosh\left(\frac{\tau + (2-\sigma)\bar{x} - \log\bar{x}}{2}\right)\left[2A^2 + \frac{B^2}{2} + \frac{\sigma}{2}B + 2A\left(1 - \frac{1}{2\bar{x}}\right)\right], \tag{6.58a}$$

$$\frac{\mathrm{d}B}{\mathrm{d}\tau} = -\cosh\left(\frac{\tau + (2-\sigma)\bar{x} - \log\bar{x}}{2}\right)\left[4AB + 2\sigma A + 2B\left(1 - \frac{1}{2\bar{x}}\right)\right], \tag{6.58b}$$

and matching with (6.44) provides the initial conditions:

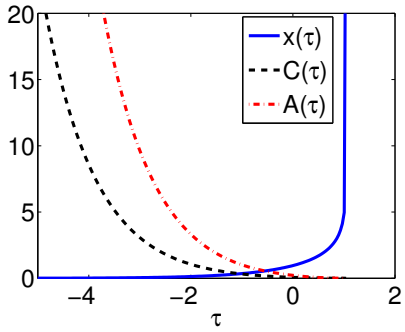
$$\bar{x}(\tau) = \frac{e^\tau}{1 + \sigma e^\tau}, \qquad A(\tau) = \frac{1}{2}e^{-\tau}, \qquad B(\tau) = -\sigma, \quad \text{as } \tau \to -\infty. \tag{6.58c}$$

Note that the equations (6.58 do not include $C(\tau)$, so we can solve for $A(\tau)$ and $B(\tau)$, and use (6.57) to find $C(\tau)$. The dynamics in this region reduces to two nonlinear ODEs, with the only parameter being σ.

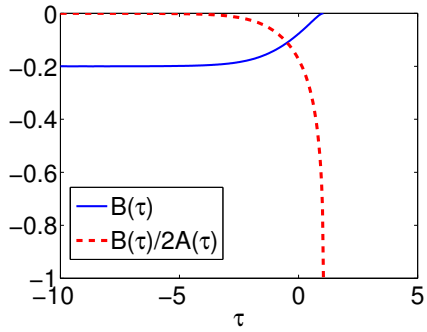
We then solve for $A(\tau)$, $B(\tau)$ and $C(\tau)$ numerically, subject to the initial condition (6.58c). Some results are plotted in Fig. 6.9. As the mean of the distribution $\bar{x}$ blows up, the amplitude of the distribution goes to zero as expected, suggesting that the probability flux flows into region II.

In the meantime, the correlation decreases from 0 to -1, which indicates the increasing importance of the interaction as the probability distribution moves from the region of the lowest concentration to the region of higher concentration. Initially, the probability mass is at the extremely low concentration state and the interaction is weak, so the probability distribution of the two compartments can be regarded as

independent. As the probability mass moves to higher states, the strength of the interaction between the two compartments makes one compartment unlikely to be near-full if the other compartment if near-full, thereby introducing a correlation of -1.



(a) Numerical solutions for $\bar{x}(\tau)$, $A(\tau)$, and $C(\tau)$.



(b) Numerical solutions for $B(\tau)$ and the correlation $B(\tau)/(2A(\tau))$.

Figure 6.9: Numerical solution of the system (6.58) subject to the initial condition (6.58c), using Matlab solver **ODE15s**. Values of the parameters are $\tau_0 = -10$ and $\sigma = 0.2$.

6.1.7 Dynamic trajectories of the mean concentration

The dynamic trajectory for the mean concentration corresponds to the asymmetric path of the deterministic model. In the continuum limit, equations (6.51a) and (6.51b) specify the dynamics for the mean concentration in the initial stage where $E \sim 1 + \epsilon \log \epsilon$. Comparing with the bifurcation analysis for Bifurcation I, in Section 5.3.1.1, we conclude that the differences between the dynamic trajectory for the mean concentration of the stochastic model and the equilibrium trajectory of the deterministic model have a similar structure to the single compartment case studied in Section 3.4. Again, the trajectory of the mean concentration in the dynamic stochastic model jumps later than the deterministic equilibrium, by an amount that depends on σ and needs to be numerically determined.

The similarities between the two-compartment model and the single-compartment model also extend to the transition between empty and full occurring around $E \sim 1 + \epsilon \log \epsilon + \sigma$. In this transition, the dynamic trajectory of the mean concentration in the stochastic model also jumps later than the deterministic equilibrium.

Fig. 6.10 illustrates the dynamic trajectories for $\bar{c}_1 + \bar{c}_2$ together with the equilibrium trajectories. The dynamic trajectories of a delithiation process are also shown

to illustrate hysteresis. Evidently, in dynamics, the hysteresis between lithiation and delithiation is retained, although in equilibrium the hysteresis is wiped out.

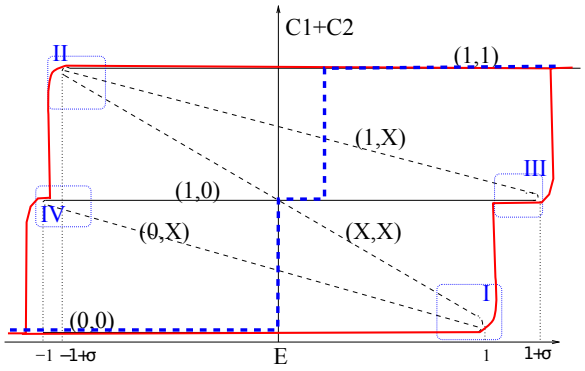


Figure 6.10: Comparison between the equilibrium and dynamic trajectories of $C_1 + C_2$ of the stochastic model. The blue dashed line plots the equilibrium relation, as revealed in Fig. 6.3, indicating no hysteresis. The red solid line plots the dynamic trajectories of the continuum limit. Lithiation and delithiation follows different paths, suggesting hysteresis. Grey lines in the background is the bifurcation structure found in Fig. 5.6.

Finally, note that the equilibrium behaviour in Fig. 6.10 applies to a general problem regardless of α, while the dynamic trajectories only applies to the continuum limit. For a general problem of $\alpha = \mathcal{O}(1)$, the dynamic trajectories will depend on the value of α, and generally differ from the highly asymmetric path of the deterministic model. However, the general structure remains the same, that hysteresis remains, and the voltage jumps occur in the same neighbourhood, around $E \sim 1 + \epsilon \log \epsilon$ and $E \sim 1 + \epsilon \log \epsilon + \sigma$.

6.2 Summary of the two-compartment model

So far, we have analysed deterministic and stochastic models for a two-compartment system, both assuming the Butler–Volmer dynamics. A comparison of the two models in Fig. 6.10 provides many insights.

First, the equilibrium behaviour of the two models differs. In the deterministic setting, in the range of $-1 + \sigma < E < 1 + \sigma$, each of the two compartments can be in one of three possible states: "near-empty", "near-full", or "neither near-empty nor near-full". As a result, the two-compartment system has as many as $2^3 = 8$ equilibria, and if the number of compartments increases, the number of equilibria grows geometrically. In general, these equilibria are connected by extremely subtle

and complicated bifurcations. Additionally, hysteresis exists between lithiation and delithiation.

In contrast, the stochastic model proposes much simpler equilibrium behaviour: a two-step C-V curve without hysteresis. This is an intrinsic difference between the two models: in the deterministic model, the root of the hysteresis is the N-shaped double-well potential; but the effect of the N-shaped double-well potential on the stochastic model is a multi-modal equilibrium distribution in the vicinity of the critical voltages. In the single-compartment case, a bimodal distribution near $E = 0$ leads to a single voltage jump; in the two-compartment case, a multi-model distribution near $E = 0$ and $E = \sigma$ leads to two voltage jumps.

The dynamics are also simplified by the stochastic model. In the deterministic two-compartment model, we have shown that the highly nonlinear dynamics make it extremely difficult to predict the dynamic trajectory: a slight change in the initial condition, or in the charging rate, could have a profound impact. Because the relationship is extremely subtle, it would be extremely difficult to capture such effects numerically. On the other hand, the stochastic model indicates that the asymmetric trajectory is always selected, which makes it straightforward to obtain the C-V curve.

6.3 Generalising to a M-compartment model

When extending the stochastic model to M-interacting compartments, the full chemical master equation would, in general, consist of NM coupled ODEs or, in the continuous limit, an M-dimensional F-P type PDE. Meanwhile, the deterministic Butler-Volmer model would consist of M stiff ODEs. Such systems would be very difficult to solve in practice. Therefore, we aim to generalise the behaviour of a M-compartment model from our analysis of the single-compartment model and the two-compartment model, instead of analysing the M-compartment model directly.

6.3.1 Equilibrium behaviour

First, we consider the deterministic Butler–Volmer model; here, the bifurcation structure is believed to be similar to that of the two-compartment model presented in Fig. 6.10. The similarity is in the configurations of the equilibria: when E is in the intermediate region, presumably in the region of $-1 + \sigma < E < 1 + \sigma$, each of the M compartments can be "near-full", "near-empty", or "neither near-empty nor near-full", and altogether there are 3^M combinations of possible equilibria. In all cases,

the 3^M equilibria are subject to the influence of the interaction term, making the bifurcations connecting these equilibria extremely complicated.

If our model includes only nearest neighbour interaction, we expect the critical voltages for a M-compartment system to remain the same as for a two-compartment system: in lithiation, the two critical voltages are respectively $E = 1$ and $E = 1 + \sigma$. These two critical values are associated with two basic configurations and the number of compartments is irrelevant: the critical voltage $E = 1$ is associated with a transition from near-empty to half-full, while the second critical voltage of $E = 1+\sigma$ corresponds to the transition from half-full to near-full. Meanwhile, due to the existence of 3^M equilibria, we expect that a spectrum of critical voltages lies between the two critical values. Depending on which equilibrium path the system chooses, the C-V curve can take a variety of different trajectories.

Meanwhile, in the direction of delithiation, we expect a similar structure, with the two critical values in delithiation to be around $E = -1$ and $E = -1 + \sigma$.

Similar arguments apply to the stochastic model: the two critical values for the C-V curve apply irrespective of the number of compartments. Meanwhile, as already discussed, bifurcations are wiped out in the stochastic model, and as a result, we expect the C-V curve to jump near the two critical voltages, which essentially leads to the same C-V curve as found in the two-compartment model.

This can be confirmed by computing the C-V curve in equilibrium directly. The equilibrium distributions of the single-compartment model and the two-compartment model are both Boltzmann distributions, suggesting that the equilibrium distribution of a M-compartment system is also a Boltzmann distribution. Using $P(c_1, c_2, \cdots, c_M)$ to denote the probability that the system is in the state

$$(C_1 = c_1, C_2 = c_2, \cdots, C_M = c_M),$$

and $F(c_1, c_2, \cdots, c_M)$ to denote the energy associated with this state, we can express the equilibrium probability distribution as

$$P(c_1, c_2, \cdots, c_M) \propto e^{-F(c_1, c_2, \cdots, c_M)/(k_B T)} \tag{6.59a}$$

up to a normalisation factor. We also refer to the equivalent energy of the single-compartment model and the two-compartment model, in equation (3.21) and (6.17), to deduce that

$$F(c_1, c_2, \cdots, c_M) = \frac{\Omega}{\Delta C}(g_{\text{tot}} - E\sum_{i=1}^{M} c_i), \tag{6.59b}$$

where g_{tot} is the total energy of the system as specified in (4.1), and Ω is enthalpy of mixing as defined in Section 2.1.1.

Given the equilibrium distribution (6.59), we can obtain the mean concentration by summing over all states. The equilibrium $E - C$ relation of a two-, four-, and six-compartment system are computed and compared in Fig 6.11. In all three cases, the $E - C$ curve overlaps, confirming that the critical voltages are invariant with respect to the number of compartments. In Fig. 6.11, the second jump is at $E = 2\sigma$ instead of $E = \sigma$. This is because we assume extra interaction energy between compartment-1 and M, in order to make the system periodic. In the two-compartment case, this means counting the interaction twice. In addition, we set N, the number of states for each compartment, at the relatively small number $N = 10$. In a six-dimensional space, setting N as a large number would require a significant amount of memory to perform the required computations.

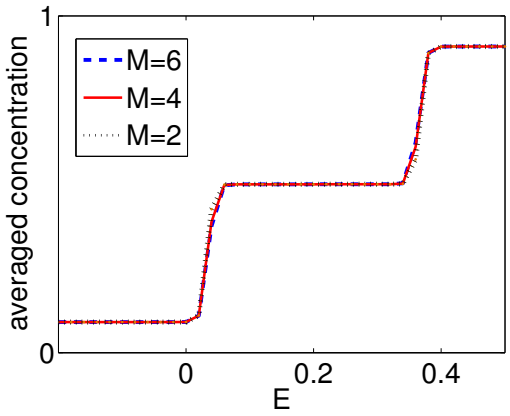


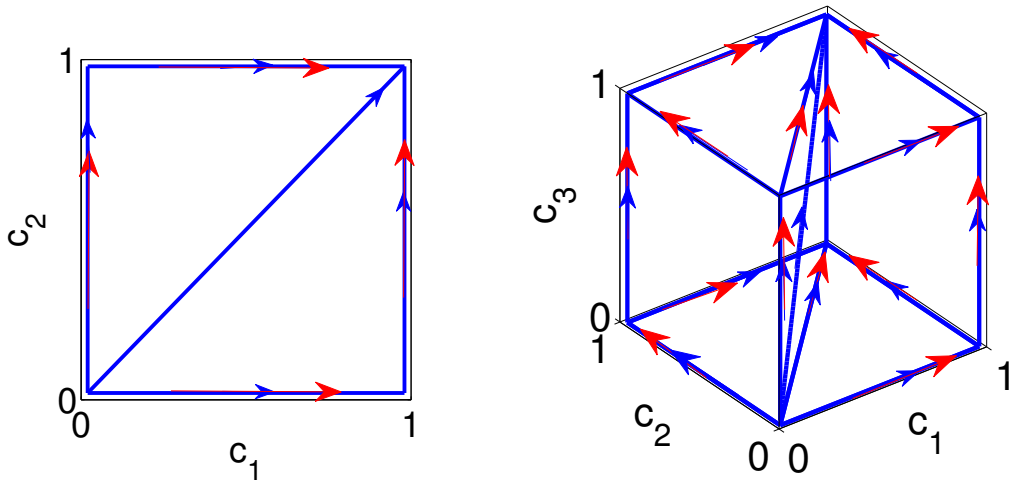
Figure 6.11: The relation between the averaged concentration and the voltage E, associated with the probability distribution of (6.59). We compare the result of a two-, four-, and six-compartment system. Values of the parametes are $\sigma = 0.2$, $N = 10$, and $\epsilon = 0.25$.

6.3.2 Dynamics

Due to the large number of equilibria in the M-compartment system, it is unlikely that the equilibrium profile can be fully captured in the deterministic setting. Analysis of the dynamics is even worse: given an initial condition and a time-varying voltage, it cannot even be predicted whether there is compartment-by-compartment growth, or whether all compartments grow at the same rate.

On the other hand, we expect much of the delicacy to be removed by incorporating thermal noise. First, the stochastic model always selects compartment-by-

compartment growth. In the M-dimensional space, this corresponds to the trajectories that are along the edges of the M-dimensional hypercubes. We illustrate such trajectories in Fig. 6.12, taking two- and three-compartment models as examples. In a deterministic model, the multiple-compartment system selects one of the blue paths according to the initial condition and the charging rate, which includes both uniform growth and compartment-by-compartment growth. Meanwhile, in a stochastic model,only the red paths are selected; all of these correspond to compartment-by-compartment filling.



(a) A two-compartment model. (b) A three-compartment model.

Figure 6.12: Comparison between possible paths of a deterministic model and a stochastic model. In a deterministic model, the multiple-compartment system selects one of the blue paths according to the initial condition and the charging rate. In a stochastic model, the multiple-compartment system selects each of the red paths with equal probability.

The fact that the equilibrium C-V curve does not depend on the value of M indicates that the multicompartment system could have a considerable degree of degeneracy. In the stochastic setting, the two-compartment model could carry all the essential features of the multicompartment system as a result of the nearest-neighbour interaction. As discussed in Chapters 4, the nearest-neighbour interaction divides all compartments into two alternating groups. The two compartments in the $M = 2$ case now represent the two groups of compartments when M is a large number.

Consequently, the four corner states of the two-compartment system, $(1, 1)$, $(1, N)$, $(N, 1)$, and (N, N), are associated with the four "corner states" of a multicompartment system, that is, the states of being "all empty", "group-1 empty, group-2 full",

"group-1 full, group-2 empty", and "all full". Meanwhile, the equilibrium C-V curve suggests that the stationary probability distribution of the multicompartment system could be considered as abrupt changes between the Delta distributions at these "corner states". Similarly, we expect the dynamics of the multicompartment system to occur as transitions between the Delta distributions at these "corner states", and to follow the same dynamic law as the two-compartment model. In addition, we expect the probability for the multicompartment system to be in all other states to be extremely small, except for the "edge states" during the transitions.

Therefore, we suspect that the equilibrium and dynamic paths for the mean concentration identified in Fig. 6.10 continue to hold in a multicompartment system. It would be very interesting to test our intuitions by simulating a high-dimensional chemical master equation, but this is beyond the scope of this work.

6.3.3 Further discussions

In retrospect, the deterministic model is extremely useful in that it predicts the correct voltage for the critical transitions in a lithiation/delithiation process. In a deterministic setting, the multiple critical values correspond to the bifurcations when new equilibria come into the picture or when the old equilibria cease to exist. Switching to a stochastic model, the critical values for dynamics are the same, since they are determined by the leading order effects. So if the critical voltages from the deterministic analysis are combined with a stochastic model, a much simpler picture of the lithiation/delithiation process can be obtained. This would be extremely helpful in analysing a longer-range interaction model in Chapter 7, where multiple critical voltages exist in describing a multiple phase transition.

There is always the issue of discreteness. The effect of thermal noise is to alter both the equilibrium and out-of-equilibrium path near each transition. The details, as in Chapter 3, depend on the "degree of discreteness" of each compartment. The size of each compartment (assumed to be identical in this thesis), or the number of lithium ions that each compartment can accommodate, determines how a quasi-equilibrium is achieved during each critical transition. If the number of lithium ions each compartment can accommodate is limited, the mean concentration of the ensemble of interacting compartments would be different from that predicted by the deterministic model, if the same trajectory is selected by the deterministic model. The dynamics in this case is simple to analyse, since each compartment can only transit between two states, the lowest and the highest. On the other hand, if the number of lithium ions each compartment can accommodate is large enough so that

a continuum model can be used, the mean concentration follows the same law as the deterministic model, if the same trajectory is selected by the deterministic model. And in the mean time the M-dimensional distribution can be studied using the linear noise approximation. Much of the analysis would be similar to that we performed in the single-compartment and two-compartment cases.

Chapter 7

Investigating the interaction law

In Chapters 4, 5, and 6, we investigated the dynamics of a multicompartment system both under current control and under voltage control, assuming that the interaction exists only between adjacent compartments. One consequence of this nearest-neighbour interaction is a two-step process during lithiation/delithiation, since the interaction term separates the system into two groups, and one group fills earlier than the other group. To describe more realistic patterns of the staging phenomenon, such as the 8-4-3-2-1 transition observed in lithium graphite, as described in Section 1.3, we need to include longer-range interactions.

In this chapter, we examine the case where a pair of non-adjacent compartments can also contribute to the interaction energy. First, we assume that the interaction occurs only within a finite range. This is called a finite K-nearest neighbour interaction: the interaction is assumed to exist between any two compartments as long as their distance does not exceed an integer K. In general, this type of interaction divides the M-compartment system into $K+1$ groups, and the system tends to fill/empty group by group provided that the lithiation/delithiation rate is slow enough, therefore leading to a stepped C-V curve with K jumps.

As the range over which two compartments can interact increases, so too does the number of jumps in the C-V curve. If K is a large number, this tends to smooth the C-V curve. In the second part of the chapter, we consider the case where $K=M$, so that interaction occurs between any two compartments, with the interaction strength decaying with distance. We show that, if the interaction decays quickly enough with distance, it is possible to develop a semi-continuous model, allowing for further analysis of the problem.

At the end of this chapter, we show an application of the finite K-nearest neighbour interaction model; we use $K=7$ to investigate the 8-4-3-2-1 transition of lithium graphite. In particular, we focus on the existence of stage-3 material, and examine

how stage-2 or stage-4 material could transit into stage-3 material. We show that the stage-3 configuration could be the energetically favourable state, when the total concentration is around 1/3. However, in dynamic lithiation, where the system undergoes a series of smooth transitions, a stage-4 configuration is more likely to be followed by a mixture of stage-2 and stage-4, rather than the stage-3 configuration, which requires a complete re-ordering of the material. We show by numerics that dynamic transition from stage-4 to stage-3 is extremely difficult in a deterministic process; however, with an appropriate amount of thermal noise that is enough to deviate the system from its original stage-4 configuration, the stage-3 configuration may be observed.

7.1 A general model for the interaction energy

When introducing the model for the multicompartment system in Section 4.1.1, we formulated the total energy for the system as

$$g_{\text{tot}} = \sum_{i=1}^{M} g(c_i) + \sigma \sum_{i=1}^{M-1} c_i c_{i+1}, \tag{7.1}$$

where the first term is the energy of individual compartments, and the second term represents the overall interaction energy. In choosing this specific form for the interaction energy, we have assumed that interaction exists only between adjacent compartments.

As a more general case, we can take into account the interaction between any pair of compartments, and use the same assumption as the nearest-neighbour interaction model, i.e. that the energy of interaction between the i-th compartment and the j-th compartment ($i \neq j$) is $\sigma_{ij} c_i c_j$, where σ_{ij} is the coefficient that measures the strength of interaction. To be consistent with the nondimensionlisation of a single compartment (2.1), σ_{ij} needs to be scaled with Ω, the enthalpy of mixing.

Now the total energy can be rewritten as

$$g_{\text{tot}} = \sum_{i=1}^{M} g(c_i) + \frac{1}{2}\mathbf{c}'\Sigma\mathbf{c}, \tag{7.2}$$

where $\mathbf{c} = [c_1, c_2, \cdots, c_M]'$ is a vector representing concentrations of the M-compartment system, and the interaction matrix

$$\Sigma = (\sigma_{ij})_{M\times M} \tag{7.3}$$

is symmetric and positive definite, and has zeros on its diagonal.

The interaction energy matrix Σ determines the pattern of lithiation/delithiation of the multicompartment system. It can be modelled from two different perspectives.

First, the sparse property of Σ specifies the range of the interaction: a full matrix means that the interaction exists between every pair of compartments, and a band matrix with bandwidth K describes K-nearest neighbour interaction. For instance, in the nearest neighbour interaction that we considered, Σ is a tri-diagonal matrix with $\sigma(i,j) = \sigma\delta_{i,j-1} + \sigma\delta_{i-1,j}$, where δ is the Kronecker delta.

Second, after choosing the matrix structure, we need to consider either the values or the functional forms for the interaction coefficient. In this chapter, we consider a simple form that

$$\sigma_{ij} = \begin{cases} \sigma d(i,j), & \text{if } i \neq j; \\ 0, & \text{if } i = j, \end{cases} \tag{7.4}$$

for both finite-range interactions and long-range interactions. In short, σ is a constant that depends on the relative strength of intra-compartment energy and inter-compartment energy, and $d(i,j) = d(j,i)$ specifies how the interaction decays with distance. Specifically, we let

$$d(i,j) = d(|i-j|) \tag{7.5}$$

depend only on the distance between two compartments, where we assume that the distance between any two compartments, indexed by i and j, is simply $|i-j|$.

Specifying a functional form for $d(|i-j|)$ is more important for long-range interactions, which we discuss in detail in Section 7.3. For a finite-range interaction model, the number of coefficients is relatively small, so that they may in principle be determined by fitting with an experimental C-V curve.

Finally, we make a slight change to the interaction structure by imposing periodic boundary conditions. In previous chapters, when we considered the nearest-neighbour interaction, the two boundary compartments, compartment-1 and compartment-M, differed from all other compartments as they only have one adjacent compartment. This non-periodic set-up complicates the equilibria structure, but it does not affect the two-stage phenomenon. Since this chapter investigates the staging phenomenon but not its equilibrium structure, we simplify the problem by imposing a periodic structure and making all compartments equivalent in terms of interaction. This means adding a few non-zero terms to the interaction matrix to make it circulant. For instance,

for the nearest-neighbour interaction, with the non-periodic interaction matrix, we change the value of $d(1, M)$ and $d(M, 1)$ to

$$\sigma_{1M} = \sigma_{M1} = \sigma, \tag{7.6}$$

so that compartment-1 and compartment-M interact with each other.

7.2 Finite K-nearest neighbour interaction

In the K-nearest neighbour interaction model, interaction happens only within a finite range, so that

$$d_{ij} = \begin{cases} d_{|i-j|} & \text{if } 1 \leq |i-j| \leq K \ ; \\ 0 & \text{otherwise.} \end{cases} \tag{7.7}$$

Without loss of generality, we let $d_1 = 1$. Therefore, there are K free parameters, including d_2, d_2, $\cdots$, d_K, as well as σ.

7.2.1 Numerical simulations with $K = 2$

As an example, we show a full lithiation/delithiation cycle found by simulating a two-nearest neighbour interaction model, using the current-control gradient flow model as in (4.8):

$$\frac{\mathrm{d}c_i(t)}{\mathrm{d}t} = -\left(1 - \frac{1}{M}\right)\frac{\partial g_{\mathrm{tot}}(t)}{\partial c_i(t)} + \frac{1}{M}\sum_{j=1, j\neq i}^{M}\frac{\partial g_{\mathrm{tot}}}{\partial c_j} + \frac{1}{M}\frac{\mathrm{d}C(t)}{\mathrm{d}t}, \tag{7.8}$$

where the total energy g_{tot} is defined in (7.2). We use illustrative parameter values $K = 2$, $\epsilon = 0.25$, $\sigma = 0.5$, $M = 100$, and $d_1 = 1$, $d_2 = 1/2$.

Figure 7.1 plots the simulation results. As in the nearest neighbour interaction model, the lithiation process can be divided into multiple distinct stages. At very low concentration, the lithiation features a uniform growth across all compartments, as in Fig. 7.1(b).

Three sub-stages of non-uniform growth follow, during which the system fills by every third compartment, as in Fig. 7.1(c-e). In the first sub-stage (c), compartments 1, 4, 7, $\cdots$, are filled; in the second sub-stage (d), compartments 3, 6, 9, $\cdots$ are filled; and in the third sub-stage (e), compartments 2, 5, 8, $\cdots$ are filled. When the system is near-full, (99% full in this simulation), uniform growth appears again.

Hence, in the range of concentration where the system is neither near-empty nor near-full, a three-stage process is clear. Generally, the M compartments are separated

into three groups, according to their values mod 3. In each stage, one of the three groups is filled. Because of the randomness in the initial distribution, as well as the equivalence of the three groups, the sequence of which group is filled first, second, or third is not fixed. In fact, in this problem, all sequences are equivalent, and they all lead to the same three-step C-V curve.

The delithiation process occurs in a similar manner to lithiation. As in the nearest-neighbour interaction model, hysteresis exists between lithiation and delithiation. First, comparing (f) and (g), we observe that the uniform growth when the system is near full occurs around $\bar{c} = 0.99$ in the lithiation process; however, in the delithiation process the uniform decrease continues around $\bar{c} = 0.9$. In addition, for the same total concentration, the concentration profile differs during lithiation and delithiation, as suggested by the comparison between (c) and (j), (d) and (i), and (e) and (g).

The total energy and the equivalent potential versus the total concentration during this lithiation/delithiation cycle are plotted in Fig. 7.2. The 3 stage process and the hysteresis are clear, and the three sub-stages of filling by every third compartment are associated with the voltage jumps at $\bar{c} = 1/3$ and $\bar{c} = 2/3$.

As in Chapter 5, the charging rate also has an impact on the pattern shown in the dynamics. Using the same parameter values as Fig. 7.1 but a different charging rate, we find that the group-by-group filling pattern is retained approximately when $\mathrm{d}C(t)/\mathrm{d}t \leq 0.1$, a uniform filling pattern occurs approximately when $\mathrm{d}C(t)/\mathrm{d}t \geq 10$, and for intermediate charging rate, a mixed pattern of group-by-group filling and uniform filling is observed.

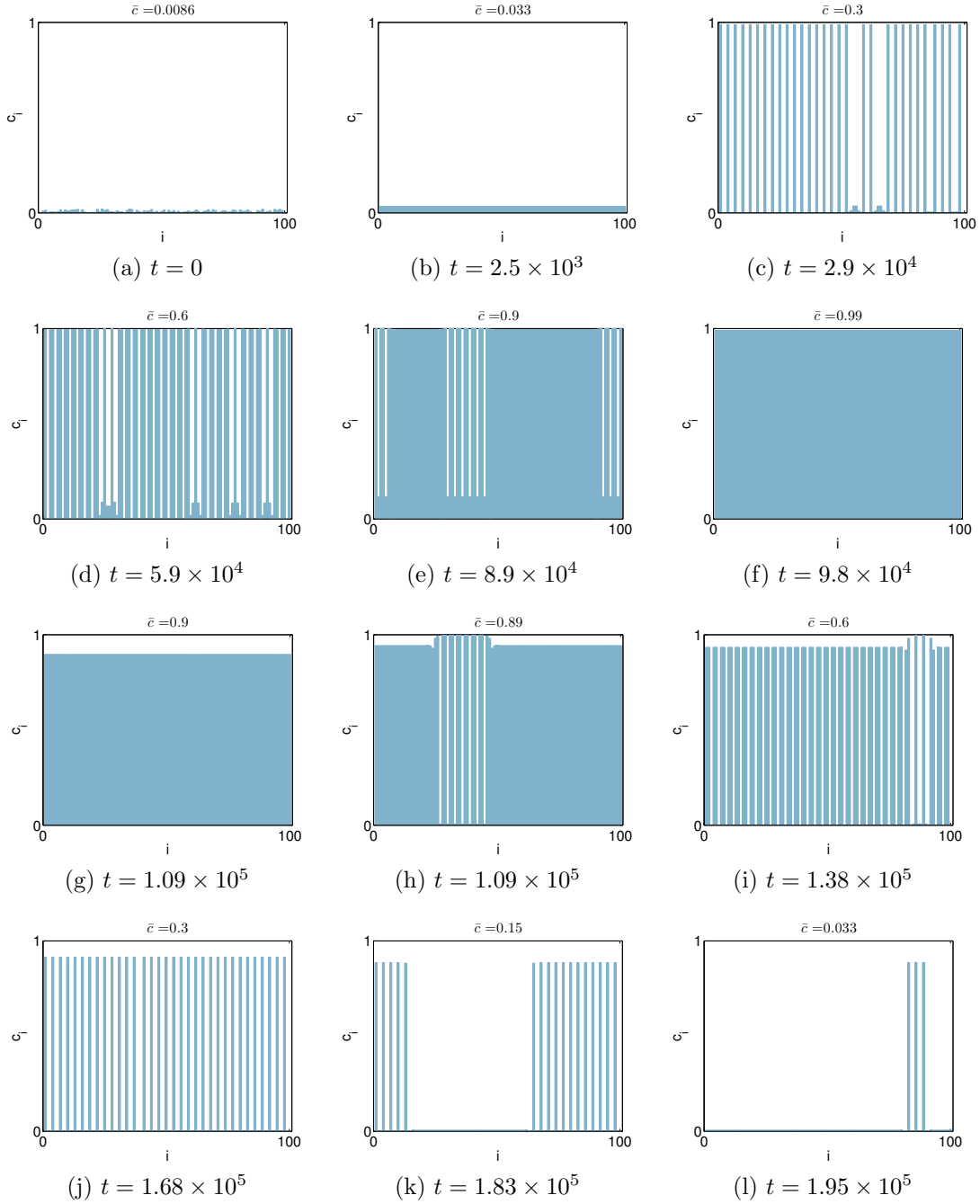
A voltage-control model with slowly-varying E generates very similar results, so we do not consider it separately.

7.2.2 General properties

The simulation results in Fig. 7.1-7.2 show that the 2-nearest neighbour interaction divides the M compartments into three groups; during lithiation/delithiation, one group needs to be nearly filled/emptied before another group can begin filling/emptying. We present a schematic representation of this process in Fig. 7.3, which shows the change of configuration before and after the filling of a single compartment from each group. By examining the change in total energy before and after such a filling, we can connect the voltage jump to the interaction coefficients.

First, the total energy of a 2-nearest neighbour interaction model is

$$g_{\mathrm{tot}} = \sum g(c_i) + \sigma \sum c_i c_{i+1} + \sigma d_2 \sum c_i c_{i+2}. \tag{7.9}$$



(a) $t = 0$ (b) $t = 2.5 \times 10^3$ (c) $t = 2.9 \times 10^4$

(d) $t = 5.9 \times 10^4$ (e) $t = 8.9 \times 10^4$ (f) $t = 9.8 \times 10^4$

(g) $t = 1.09 \times 10^5$ (h) $t = 1.09 \times 10^5$ (i) $t = 1.38 \times 10^5$

(j) $t = 1.68 \times 10^5$ (k) $t = 1.83 \times 10^5$ (l) $t = 1.95 \times 10^5$

Figure 7.1: A full lithiation/delithiation cycle of a 2-nearest neighbour interaction model found by simulating (7.8), with $\mathrm{d}C(t)/\mathrm{d}t = 10^{-3}$ for lithiation and $\mathrm{d}C(t)/\mathrm{d}t = -10^{-3}$ for delithiation. Initially the concentration of each compartment is randomly distributed in $[0, 0.02]$. (f) is the final state of lithiation as well as the initial state for delithiation, and $\bar{c}$ denotes the averaged concentration. Parameter values are $\epsilon = 0.25$, $\sigma = 0.5$, $M = 100$, and $d_1 = 1$, $d_2 = 1/2$.

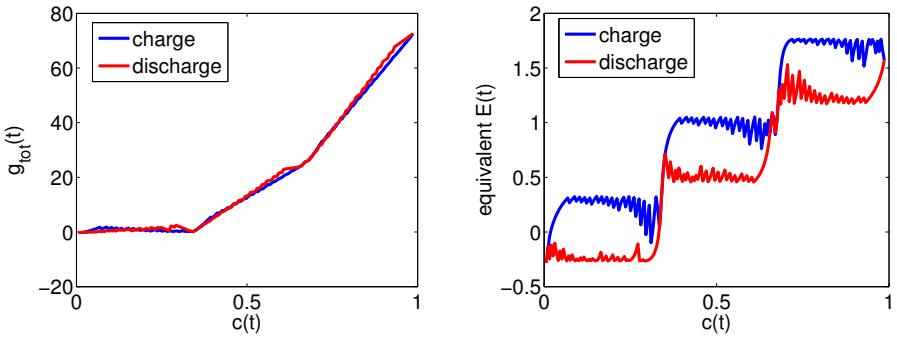
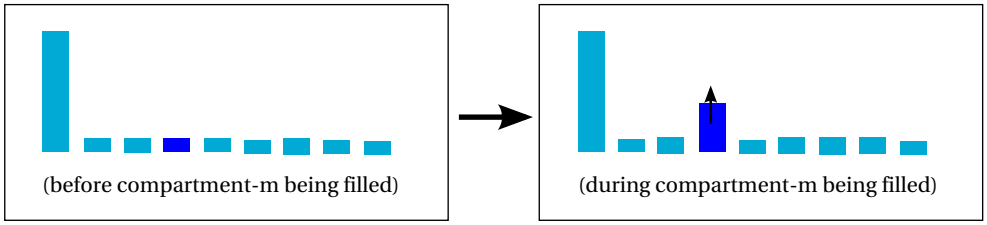
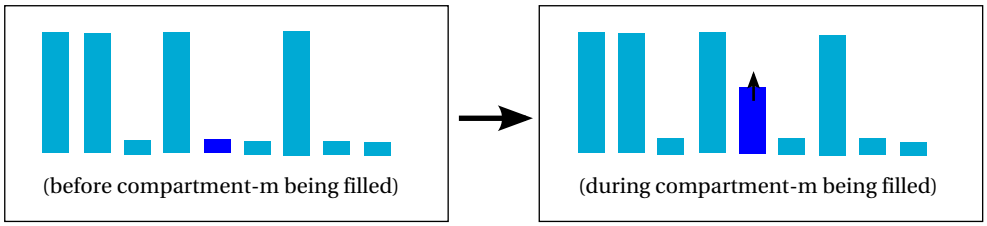


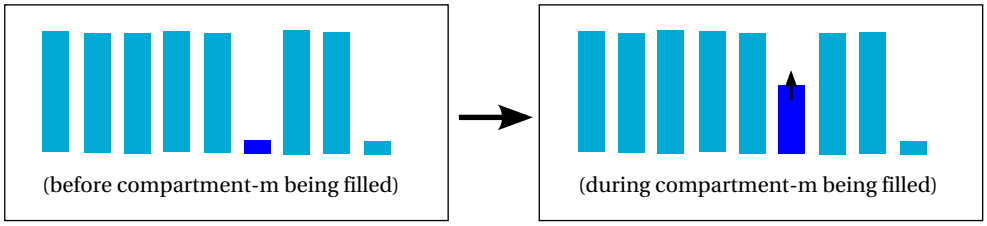
Figure 7.2: The total energy g_{tot} and the equivalent potential $E(t) = -\lambda(t)$ during the lithiation/delithiation cycle of the 2-nearest neighbour interaction model that is simulated in Fig. 7.1.



(a) The first group, m mod $3 = 1$.



(b) The second group, m mod $3 = 2$.



(c) The third group, m mod $3 = 0$.

Figure 7.3: A schematic representation of the change of configuration before and during the filling of compartment-m, which depends on m's remainder mod 3. In this plot we assume that the group of m mod $3 = 1$ is filled first, then the group of m mod $3 = 2$, and finally m mod $3 = 0$. In all panels compartment-m is plotted using a different colour from other compartments.

During the filling-up of a single compartment, which we call compartment-m, the

change in the total concentration satisfies

$$\Delta C(t) = \Delta c_m(t). \tag{7.10}$$

Meanwhile, the change in the total energy depends on the concentration of the nearest 4 neighbours of compartment-m. In this example, it depends on which group compartment-m belongs to. Assuming concentrations of other compartments instantaneously remain constant, the change in the total energy is approximately

$$\Delta g_{\text{tot}} = \begin{cases} \Delta[g(c_m)], & \text{if m is in the first group to fill up,} \\ \Delta[g(c_m)] + \sigma(1+d_2)\Delta c_m, & \text{if m is in the second group,} \\ \Delta[g(c_m)] + 2\sigma(1+d_2)\Delta c_m, & \text{if m is in the third group,} \end{cases} \tag{7.11}$$

and hence

$$\frac{\mathrm{d}g_{\text{tot}}}{\mathrm{d}C} = \begin{cases} g'(c_m), & \text{if } m \text{ is in the first group to fill up,} \\ g'(c_m) + \sigma(1+d_2), & \text{if } m \text{ is in the second group,} \\ g'(c_m) + 2\sigma(1+d_2). & \text{if } m \text{ is in the third group.} \end{cases} \tag{7.12}$$

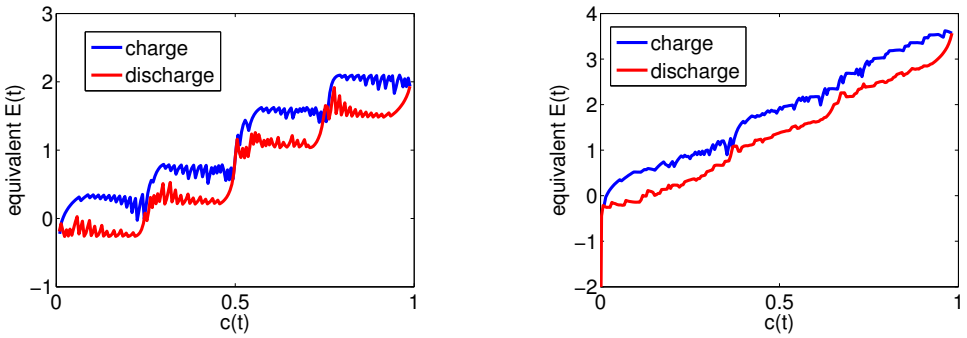
Therefore, in the 2-nearest neighbour interaction model, the distance between the two voltage plateaus must be equal, and the size of the voltage jump equals $\sigma(1+d_2)$. This is immediately verified in Fig. 7.2, as the size of the step in $E(t)$ is approximately 0.75, as predicted.

Generally speaking, a K-nearest neighbour interaction model divides all compartments into $K+1$ groups, and the current-control model predicts a sequential filling of every group in the lithiation/delithiation processes. Some of the resulting configurations correspond to compounds of an integer stage (such as stage-3 in Fig. 7.3(a)), but some are associated with a fractional stage (such as stage-2/3 in Fig. 7.3(b)) which is much less frequently observed in experiments but does exist [10].

In addition, the sequence of filling up the $K+1$ groups depends on the choice of interaction coefficients σ and $d_2, \cdots, d_K$, and does not necessarily follow the order according to their values mod $(K+1)$. In theory, the K unknown coefficients can be partly determined by fitting a C-V curve.

Generally, the group-by-group filling of $K+1$ groups leads to the $K+1$ plateaus in the C-V curve: as shown in Fig. 7.4(a), a three-nearest neighbour interaction model predicts 4 plateaus in its C-V curve. The number of plateaus therefore goes up as K increases, so that if K becomes a large number, the jumps between plateaus become difficult to discern. For example, we show the C-V curve for a 15-nearest neighbour interaction in Fig. 7.4(b). In theory, we should be able to discern 16 plateaus. However, numerical results suggest that the C-V curve exhibits a much smoother change, and the distinction between different stages is much less clear.

This observation leads us to consider a different model for longer-range interactions, which we discuss in the next section.



(a) $K = 3$ (b) $K = 15$

Figure 7.4: The equivalent voltage $E(t) = -\lambda(t)$ plotted versus the mean concentration $c(t) = C(t)/M$, found by simulating a three-nearest neighbour interaction model and a 15-nearest neighbour interaction model using (7.8), with $\mathrm{d}C(t)/\mathrm{d}t = 10^{-3}$ for lithiation and $\mathrm{d}C(t)/\mathrm{d}t = -10^{-3}$ for delithiation. Initially the concentration of each compartment is randomly distributed in $[0, 0.02]$. Parameters are $\epsilon = 0.25$, $\sigma = 0.5$, $M = 200$, and $d_i = 1/i$ for $i = 1, 2, \cdots, K$.

7.3 Long-range interaction

At the end of the previous section, we showed that when the compartments can interact over a long distance, the resulting C-V curve starts to resemble a smooth curve, instead of exhibiting apparent plateaus. This is consistent with the physical intuition that in this case, the interaction is more global than localised, and therefore that the lithiation/delithiation of the system exhibits a much more uniform behaviour.

In this section, we extend the finite K-nearest neighbour interaction to a longer range and consider the case where interactions occur between any pair of compartments. In this case, the interaction matrix Σ is a full matrix, and we retain the assumption of (7.5) that the interaction strength is only a function of distance. Hence, we need to consider only an appropriate functional form for $d(|i-j|)$. This should decay with distance, and as the simplest case, we consider a power law

$$d(|i-j|) = \begin{cases} \frac{1}{|i-j|^{\omega}} & \text{if } |i-j| \leq \frac{M}{2}, \\ \frac{1}{(M-|i-j|)^{\omega}} & \text{if } |i-j| > \frac{M}{2}, \end{cases} \tag{7.13}$$

where we assume M is an even number to enforce periodicity. When the decay factor $\omega > 1$, the interaction between two compartments decays rapidly with distance,

leading to results which are similar to the short-range interaction case. In contrast, when $\omega < 1$, the interaction decays slowly with distance, and one compartment will be affected both by its neighbouring compartments and by distant compartments.

7.3.1 Numerical simulations

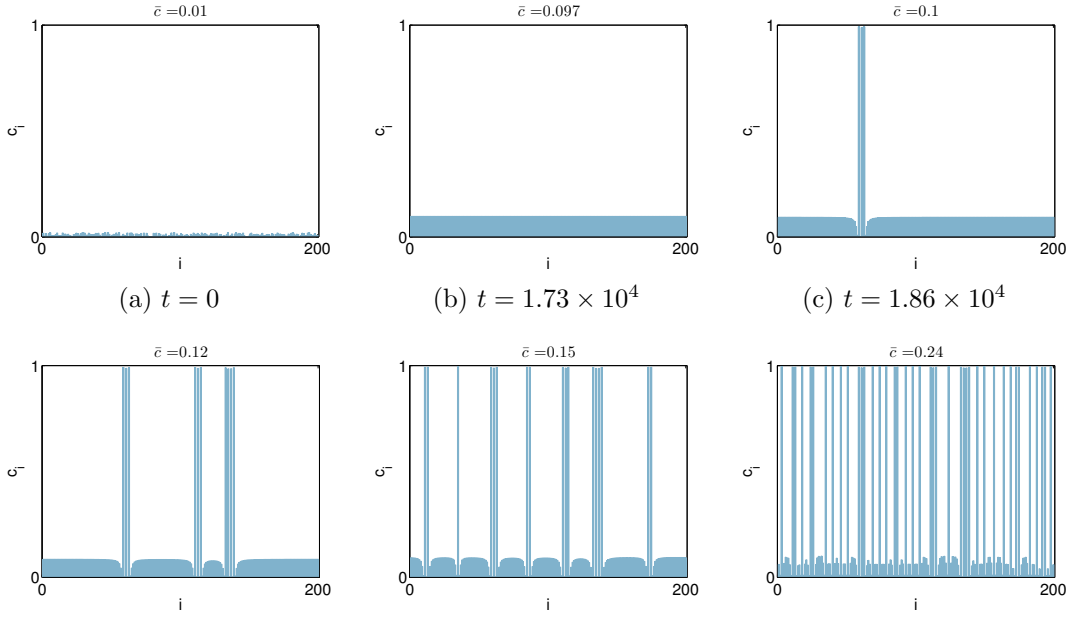
First, we perform numerical simulations to investigate the behaviour of the system under different decay factors ω. We use settings similar to those of the nearest neighbour interaction model: we use Matlab **ode23tb**, solving a system of $M = 200$ compartments using $\mathrm{d}C(t)/\mathrm{d}t = 10^{-3}$ for lithiation and $\mathrm{d}C(t)/\mathrm{d}t = -10^{-3}$ for delithiation, with $\epsilon = 0.25$ and $\sigma = 0.5$. However, with other solvers, a different set of parameters might be required to reproduce the described staging behaviour. In the beginning, each c_i $(i = 1, 2, \cdots, M)$ is randomly distributed in $[0, 0.03]$. The initial distribution is slightly higher than that we used for previous simulations (randomly distributed in $[0, 0.02]$); this is in order to assure numerical convergence, as the ODE system for the long-range interaction models appears to be more stiff than for short-range interaction in the low concentration regime.

We perform simulations with three values of ω: 2, 1, and 0.5. Time evolutions of the concentration are shown in Figs. 7.5 to 7.7. A universal pattern of the three simulations is a uniform increase of concentration across all compartments in the initial stage.

As the influx of ions continues, the uniform distribution is no longer retained, and the system switches to the filling of individual compartments. At the onset of this stage, there is apparently some randomness in picking which compartment to fill, and in the meantime a local distribution seems to have formed in the neighbourhood of the spikes, as in Fig. 7.5(c–e), Fig. 7.6(c), and Fig. 7.7(c). As the stage of filling of individual compartments continues, we find that, in the long-range model, the distance between compartments that are fully filled can vary, in contrast to the finite K-nearest neighbour model (where K is a small number), in which there is always a group-by-group filling.

Meanwhile, at low concentrations where the filling of individual compartments has just started, for instance at $\bar{c} = 0.12$ at all three plots, we see that the spikes are much more localised for $\omega = 2$, as in Fig. 7.5(d), and more evenly distributed across all compartments for $\omega = 1/2$, as in Fig. 7.7(c). This observation agrees with the physics implied in this long-range interaction model. The three simulations with different values of ω have the same intra-compartment energy and differ only

in the inter-compartment energy. In the very low concentration regime, the intra-compartment energy dominates because of the logarithmic term, so we see the same uniform increase in all three simulations. Beyond this stage, the major contribution to the total energy switches to the inter-compartment energy. When ω is small, it is markedly global. As a result, the system seeks a more global distribution to minimise the total energy, as shown when $\omega = 1/2$. In comparison, when ω is large, the inter-compartment interactions are highly local, so we see that the spikes are highly localised.



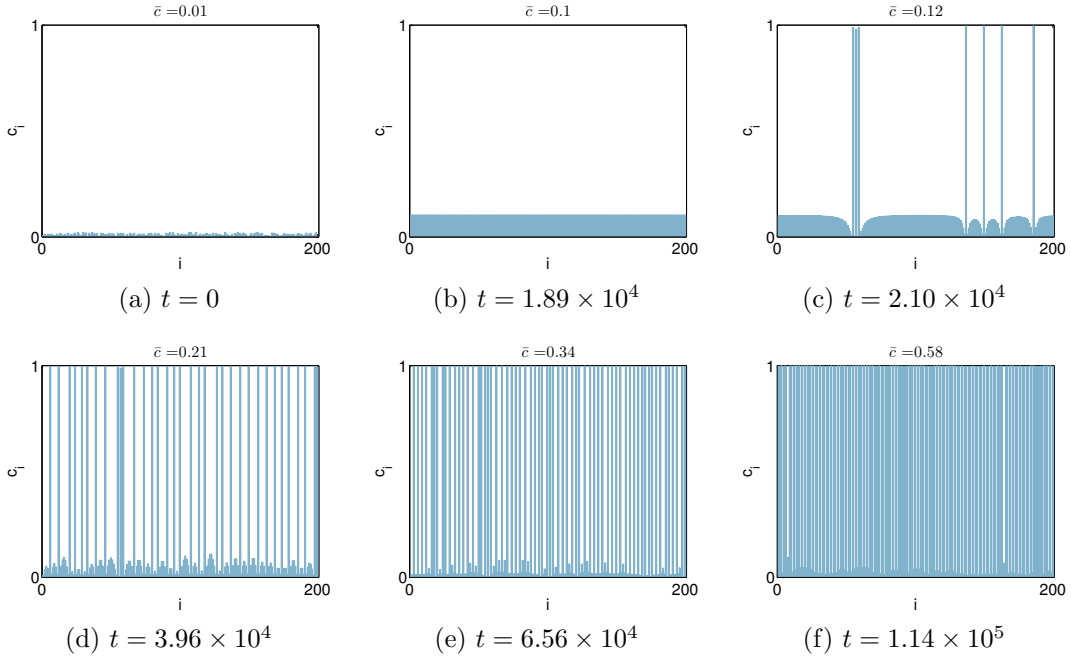
(a) $t = 0$ (b) $t = 1.73 \times 10^4$ (c) $t = 1.86 \times 10^4$

(d) $t = 2.10 \times 10^4$ (e) $t = 2.85 \times 10^4$ (f) $t = 4.58 \times 10^4$

Figure 7.5: Numerical simulation of a long-range interaction current control model (7.2), (7.4), (7.8), (7.13) with a decay factor $\omega = 2$. Initially the concentration of each compartment is randomly distributed in $[0, 0.03]$, and in lithiation we use $\mathrm{d}C(t)/\mathrm{d}t = 10^{-3}$. Parameter values are $\epsilon = 0.25$, $\sigma = 0.5$, $M = 200$.

We plot the energy-concentration dependence and the potential-concentration dependence for all three cases in Fig. 7.8 and Fig. 7.9. It is observed that the model with $\omega = 2$ predicts multiple stages over the entire process, while $\omega = 1/2$ predicts the total energy to increase smoothly, which is consistent with our earlier argument that a larger decay factor is associated with more localised behaviour, and hence resembles short-range interaction behaviour.

At the end of this section, it is worth mentioning the numerical delicacy of this problem. Actually, using the same set of parameters as Fig. 7.5-7.7, we have ob-



(a) $t = 0$ (b) $t = 1.89 \times 10^4$ (c) $t = 2.10 \times 10^4$

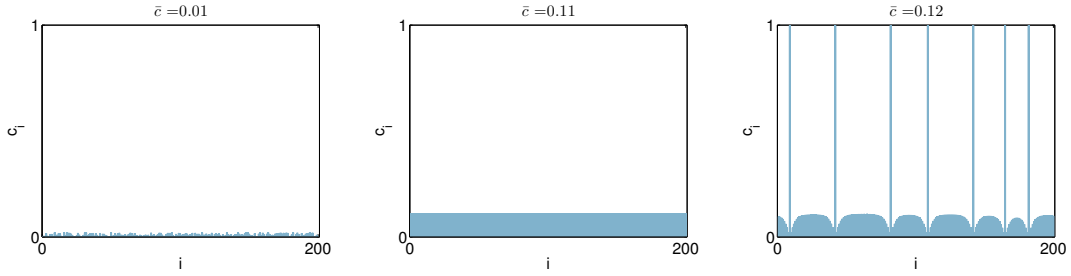
(d) $t = 3.96 \times 10^4$ (e) $t = 6.56 \times 10^4$ (f) $t = 1.14 \times 10^5$

Figure 7.6: Numerical simulation of a long-range interaction current control model (7.2), (7.4), (7.8), (7.13) with a decay factor $\omega = 1$. Initially the concentration of each compartment is randomly distributed in $[0, 0.03]$, and in lithiation we use $\mathrm{d}C(t)/\mathrm{d}t = 10^{-3}$. Parameters values are $\epsilon = 0.25$, $\sigma = 0.5$, $M = 200$.

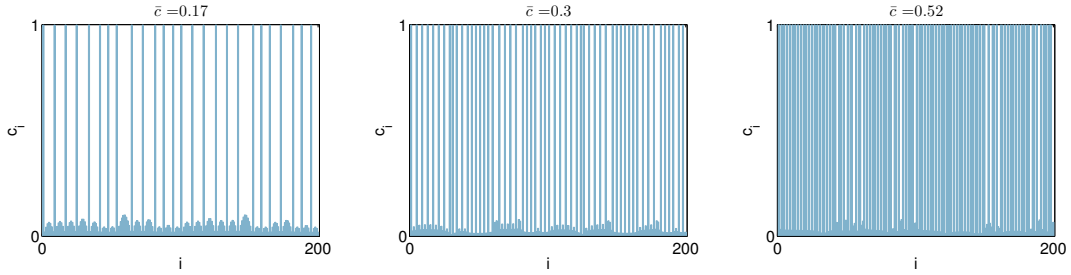
served two distinct lithiation patterns with different Matlab solvers: non-uniform growth and uniform growth. Non-uniform growth, with the appearance of spikes at intermediate concentration as illustrated in this section, occurs in simulations using **ode23tb**, **ode23t**, and a simple finite difference scheme. In contrast, a uniform growth throughout the entire lithiation process occurs in simulations using **ode15s**.

The uniform growth predicted by **ode15s** is alarming, but we suspect this is due to incorrect numerics. As found in our analysis into the nearest neighbour interaction model, the uniform distribution is not a stable equilibrium at intermediate concentration and tends to be destroyed by noise. Now with the inclusion of interaction between non-neighbouring compartments, the interaction energy associated with the uniform distribution is even higher, which makes the uniform distribution more unfavourable. We believe that in the slow charging problem considered in this section, a uniform growth pattern is unlikely.

In addition, we have two more simulation results that suggest the uniform growth predicted by **ode15s** is not a universal phenomenon and only occurs with some specific parameters. Using **ode15s**, we first simulate (7.8) using the same set of parameters as

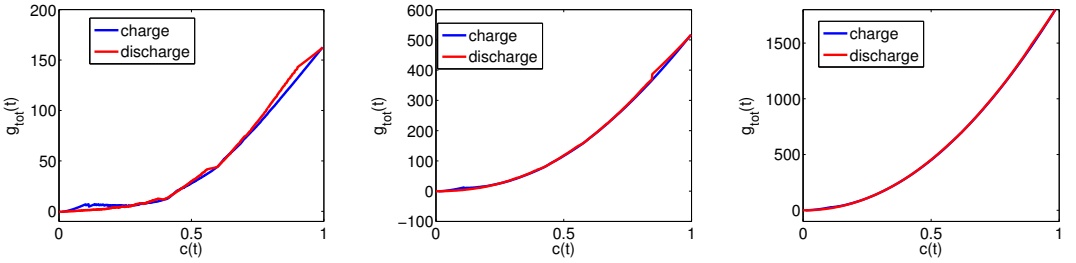


(a) $t = 0$ (b) $t = 1.98 \times 10^4$ (c) $t = 2.10 \times 10^4$



(d) $t = 3.22 \times 10^4$ (e) $t = 5.82 \times 10^4$ (f) $t = 1.01 \times 10^5$

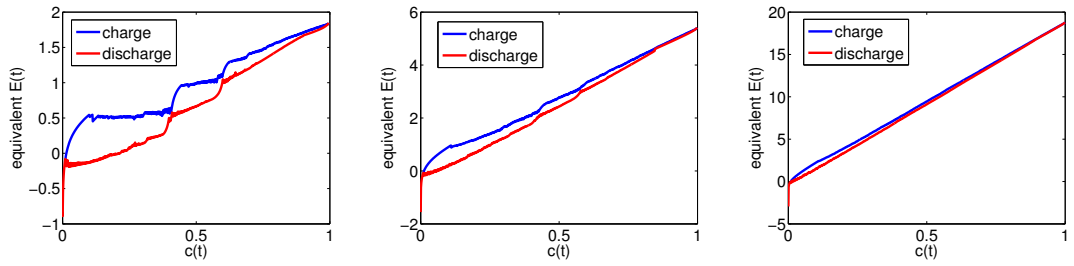
Figure 7.7: Numerical simulation of a long-range interaction current control model (7.2), (7.4), (7.8), (7.13) with a decay factor $\omega = 0.5$. Initially the concentration of each compartment is randomly distributed in $[0, 0.03]$, and in lithiation we use $\mathrm{d}C(t)/\mathrm{d}t = 10^{-3}$. Parameter values are $\epsilon = 0.25$, $\sigma = 0.5$, $M = 200$.



(a) $\omega = 2$ (b) $\omega = 1$ (c) $\omega = 0.5$

Figure 7.8: The total energy versus total concentration of the three simulations presented Figs. 7.5 – 7.7.

before except with a smaller number of compartments $M = 50$. We also reformulated (7.8) as a DAE system by keeping the control parameter explicit, i.e. solving (4.6) with the constraint that $\lambda(t)$ is explicitly given, and again simulated the DAE system with M=200. Both experiments exhibit non-uniform growth. Hence, we attribute the uniform growth observed in some simulations to numerical error and choose to present the pictures showing non-uniform growth in this section.



(a) $\omega = 2$ (b) $\omega = 1$ (c) $\omega = 0.5$

Figure 7.9: The equivalent potential versus total concentration of the three simulations presented Figs. 7.5 - 7.7.

7.3.2 A semi-continuous model

A notable feature of the simulations in Section 7.3.1 is that, in the transition from the initial uniform filling to the filling of individual compartments, the system can be treated as having nucleation spikes on top of an underlying continuous concentration. This underlying continuous concentration illuminates the semi-continuum nature of the long-range interaction.

Using Euler-Maclaurin summation [1], it is possible to turn the discrete sum of the interaction energy into a continuous expression if the interaction decays rapidly enough with distance. As the simplest case, we find that when $\omega = 2$, if the concentration near compartment-i is approximately continuous, the discrete sum can be written as

$$\sum_{j=1, j\neq i}^{M} d\left(|i-j|\right) c_j \sim \frac{1}{3}\pi^2 c(x), \tag{7.14}$$

where $c(x) = c_i$ denotes the concentration in the continuous variable x. Similar analysis can be found in [9], where it is shown that the decay factor $\omega = 1$ is a critical case, and the discrete sum can be turned into a continuous expression when $\omega > 1$. Details of the approximation (7.14) are in Appendix E.

Therefore, in a gradient flow model, away from any spikes, the concentration $c(x)$ approximately satisfies the continuous PDE

$$\frac{\partial c(x)}{\partial t} = -g'(c(x)) - \sigma\frac{\pi^2}{3}c(x) + \lambda, \tag{7.15a}$$

while in the neighbourhood of a spike, the governing equations are discrete, given by

$$\frac{\mathrm{d}c_i}{\mathrm{d}t} = -g'(c_i) - \sigma\Sigma_{ij}c_j + \lambda, \tag{7.15b}$$

where λ is the Lagrange multiplier to represent the net concentration constraint imposed on this system. In principle, a full lithiation profile may be found by matching the two regions, which offers a possible direction for future work.

7.4 Applications: the staging phenomenon of lithium graphite

This section illustrates an application of the longer-range interaction model. We use a 7-nearest neighbour interaction model to try to model a 8-4-3-2-1 transition, which is one of the many transitions proposed for lithium graphite [26]. Since our subject of study is the staging phenomenon itself, we focus only on the stage of non-uniform growth. We do not attempt to address every feature of lithiation/delithiation, such as the uniform growth stage, hysteresis, or the effect of charging speed.

To try and explain the 8-4-3-2-1 transition, our approach is to study concentration profiles that can be decomposed into a repeated periodic structure. We confine ourselves to periodic cell sizes of 8, 4, 3, and 2 compartments, corresponding to the 8-stage, 4-stage, 3-stage, and 2-stage compounds.

7.4.1 A repeated periodic structure

First of all, we compare the periodic structures with different cell sizes in terms of total energy. Given a fixed total concentration and a fixed cell size, we want to find concentrations of a basic cell that help to minimise the system energy. Then, for a fixed total concentration, we compare the periodic structures with different cell sizes and select the one with the lowest energy. We investigate how the lowest energy configuration changes with respect to the total concentration.

To find a periodic structure, we decompose the M compartments into $L = M/R$ periodic cells, assuming each cell has a period of R. Letting

$$\mathbf{x} = [x_1, x_2, \cdots, x_R]$$

be a size R row vector to represent the concentration of the R compartments that form a single cell, the total concentration column vector for the M-compartment system is hence

$$\mathbf{c} = \underbrace{[\mathbf{x}, \mathbf{x}, \cdots, \mathbf{x}]'}_{\text{repeating } \mathbf{x} \ L \text{ times}} . \tag{7.16}$$

The minimisation problem The interaction matrix Σ can be rewritten in terms of its $R \times R$ sub-blocks $(\Sigma_{ij})_{R\times R}$ as

$$\Sigma = \begin{pmatrix} \Sigma_{11} & \Sigma_{12} & \cdots & \Sigma_{1L} \\ \cdots & \cdots & \cdots & \cdots \\ \Sigma_{L1} & \Sigma_{L2} & \cdots & \Sigma_{LL} \end{pmatrix}. \tag{7.17}$$

Given the periodic structure (7.16), the interaction energy can be rewritten as

$$\begin{aligned} \frac{1}{2}\mathbf{c}'\Sigma\mathbf{c} &= \frac{1}{2}[\mathbf{x}, \mathbf{x}, \cdots, \mathbf{x}] \begin{pmatrix} \Sigma_{11} & \Sigma_{12} & \cdots & \Sigma_{1L} \\ \cdots & \cdots & \cdots & \cdots \\ \Sigma_{L1} & \Sigma_{L2} & \cdots & \Sigma_{LL} \end{pmatrix} [\mathbf{x}, \mathbf{x}, \cdots, \mathbf{x}]' \\ &= \frac{1}{2}\left[\mathbf{x}\sum_{i=1}^{L}\Sigma_{i1}, \mathbf{x}\sum_{i=1}^{L}\Sigma_{i2}, \mathbf{x}\sum_{i=1}^{L}\Sigma_{iM}\right][\mathbf{x}, \mathbf{x}, \cdots, \mathbf{x}]' \\ &= \frac{1}{2}\mathbf{x}\left(\sum_{i=1}^{L}\sum_{j=1}^{L}\Sigma_{ij}\right)\mathbf{x}'. \end{aligned} \tag{7.18}$$

Hence, for the M-compartment system, its averaged energy per compartment can be rewritten in terms of $\mathbf{x}$, the concentration vector for each cell, as

$$g_{\text{avg}}(\mathbf{x}) = \frac{1}{R}\sum_{i=1}^{R} g(x_i) + \frac{1}{2R}\mathbf{x}\left(\frac{1}{L}\sum_{i=1}^{L}\sum_{j=1}^{L}\Sigma_{ij}\right)\mathbf{x}'. \tag{7.19}$$

Because Σ is a sparse circulant matrix, it can be verified that the sum

$$A_R = \frac{1}{L}\sum_{i=1}^{L}\sum_{j=1}^{L}\Sigma_{ij} \tag{7.20}$$

is independent of L, the number of cells of the system. Instead, it only depends on the period R. To see this, we use the periodicity to obtain

$$\frac{1}{L}\sum_{i=1}^{L}\sum_{j=1}^{L}\Sigma_{ij} = \sum_{j=1}^{L}\Sigma_{1j}, \tag{7.21}$$

i.e. the equivalent interaction matrix A_R for the cell is found by summing all the $R \times R$ submatrices of the first R rows of Σ. It is straightforward to expand the matrix for a 7-nearest neighbour interaction and verify that

$$A_2 = 2\sigma \begin{pmatrix} d_2 + d_4 + d_6 & d_1 + d_3 + d_5 + d_7 \\ d_1 + d_3 + d_5 + d_7 & d_2 + d_4 + d_6 \end{pmatrix}, \tag{7.22a}$$

$$A_3 = \sigma \begin{pmatrix} 2d_3 + 2d_6 & d_1 + d_2 + d_4 + d_5 + d_7 & d_1 + d_2 + d_4 + d_5 + d_7 \\ d_1 + d_2 + d_4 + d_5 + d_7 & 2d_3 + 2d_6 & d_1 + d_2 + d_4 + d_5 + d_7 \\ d_1 + d_2 + d_4 + d_5 + d_7 & d_1 + d_2 + d_4 + d_5 + d_7 & 2d_3 + 2d_6 \end{pmatrix}, \tag{7.22b}$$

and

$$A_4 = \sigma \begin{pmatrix} 2d_4 & d_1+d_3+d_5+d_7 & 2d_2+2d_6 & d_1+d_3+d_5+d_7 \\ d_1+d_3+d_5+d_7 & 2d_4 & d_1+d_3+d_5+d_7 & 2d_2+2d_6 \\ 2d_2+2d_6 & d_1+d_3+d_5+d_7 & 2d_4+d_7 & d_1+d_3+d_5+d_7 \\ d_1+d_3+d_5+d_7 & 2d_2+2d_6 & d_1+d_3+d_5+d_7 & 2d_4+d_7 \end{pmatrix}, \tag{7.22c}$$

i.e. A_R only depends on the interaction coefficients and the period R.

Now we look for the cell concentration profile that could minimise the total energy, given an averaged concentration $\bar{c}$ and the cell size R. This is equivalent to solving the following minimisation problem:

$$\underset{\mathbf{x}}{\text{minimize}} \qquad g_{\text{avg}}(\mathbf{x}) = \frac{1}{R}\sum_{i=1}^{R} g(x_i) + \frac{1}{2R}\mathbf{x}A_R\mathbf{x}', \tag{7.23a}$$

$$\text{subject to} \qquad \sum_{i=1}^{R} x_i = R\bar{c}, \tag{7.23b}$$

$$\text{and} \qquad 0 < x_i < 1, \quad i = 1, \cdots, R. \tag{7.23c}$$

Numerical optimisation results We solve the constrained linear minimisation problem (7.23) for a 7-nearest neighbour interaction model with three values of period, $R = 2$, 3, and 4, using Matlab routine **fmincon**. This is equivalent to comparing the energy of stage-2, stage-3, and stage-4 compounds, assuming that the total concentration is prescribed.

We do not present results with $R = 8$, partly because the Matlab routine **fmincon** does not give an accurate result for $R = 8$. It should always hold that the total energy with $R = 8$ is lower than or equal to that with $R = 4$, since $R = 8$ can be obtained by repeating $R = 4$ twice. But this was violated in the numerical optimisations, indicating numerical inaccuracy for $R = 8$.

On the other hand, in the staging phenomenon of lithium graphite, the difficulties lie in the transition into a stage-3 compound from a stage-2 or stage-4 compound; therefore it suffices to consider $R = 2$, 3, and 4.

Some results are presented in Fig. 7.10. It can be seen that for very low concentration, as in (a), a uniform concentration across all compartments minimises the total concentration, which is in line with the figures. For intermediate values of $\bar{c}$, the energy minimisers with $R = 2$, 3, and 4 suggest different configurations other than a uniform concentration.

In (b) where the total concentration is $\bar{c} = 0.1$, the $R = 4$ configuration has the lowest energy among the three minimisers, with every 4-th compartment being filled.

The two minimisers with $R = 2$ and $R = 3$ suggest the same configuration with a near-uniform concentration, which has a higher energy than the $R = 4$ minimiser. This changes as $\bar{c}$ increases to 0.35. As shown in (c), in this case the $R = 3$ minimiser has lower energy than $R = 2$ and $R = 4$, suggesting a filling sequence of every third compartment. As $\bar{c}$ increases to as high as 0.5, the $R = 2$ minimiser has the lowest energy, as shown in (d). In this case the $R = 4$ minimiser has the same configuration as the $R = 2$ minimiser.

For $\bar{c}$ varying from near 0 to near 1, we plot the total energy corresponding to the three energy minimisers with periods $R = 2, 3, 4$ in the left panel of Fig. 7.11. The lowest energy of the three minimisers is selected and plotted separately in the right panel. The plot confirms that depending on the value of $\bar{c}$, the lowest energy corresponds to different values of $R = 2, 3, 4$. Note that $R = 3$ configuration has a lower energy than $R = 2$ or $R = 4$ when $\bar{c}$ is near 1/3.

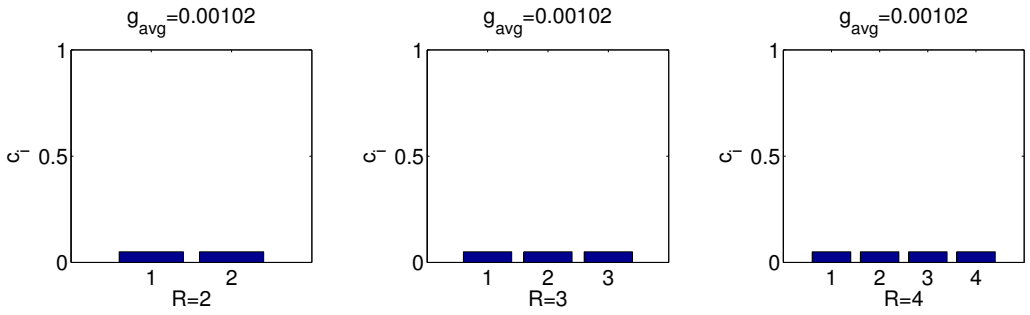
7.4.2 Numerical simulations with deterministic dynamic models

In Section 7.4.1, we have shown that a stage-3 compound can lead to lower energy than stage-2 or stage-4 compounds. However, stage-3 compounds do not seem to occur in a lithiation/delithiation process when simulated using a deterministic model.

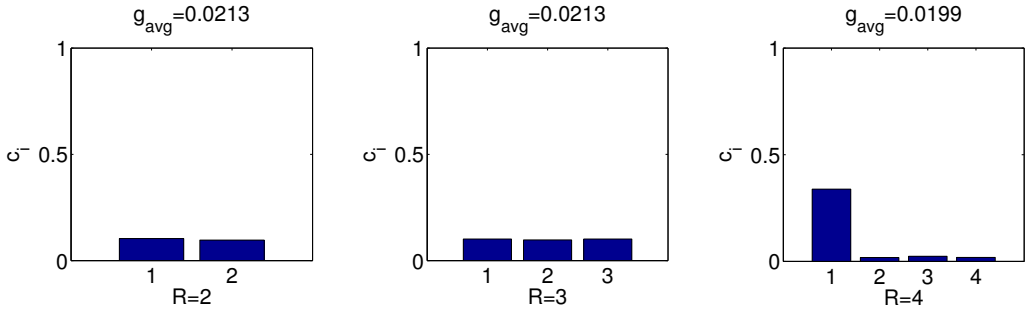
In Fig. 7.12, we plot a lithiation/delithiation cycle of a 7-nearest neighbour interaction model, using the same parameter values as applied in the numerical optimisation problem of Fig. 7.10. The simulation results confirm some of our earlier conclusions– that at very low or high concentrations the growth is uniform across all compartments, and that at the intermediate concentrations the system always fills by every eighth compartment. As a result, this 8-stage process gives rise to 8 plateaus in the C-V plot, as in Fig. 7.13.

However, in this full lithiation/delithiation cycle, no stage-3 compounds occur. Although Fig. 7.11 indicates that a stage-3 configuration is energetically favourable compared to the stage-4 or the stage-2 configuration, when the total concentration is near 1/3, Fig. 7.12(e) and (j) suggest a mixture of stage-2 compounds and stage-4 compounds instead.

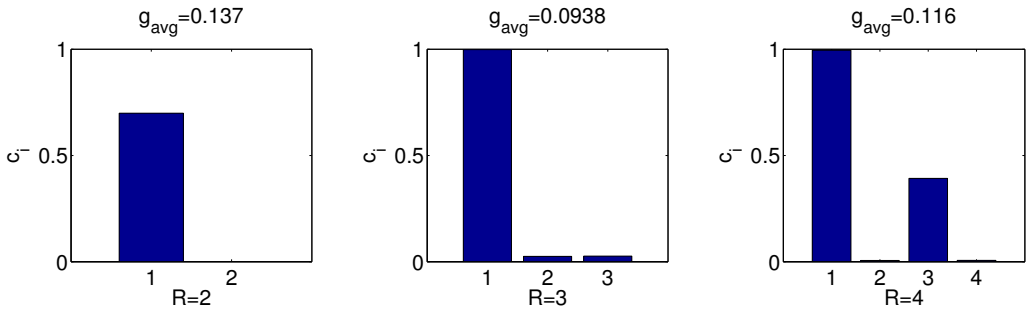
We rerun the current-control simulations with various charging speeds. We also run the voltage-control simulations with various charging speeds. However, in all simulations, we do not find stage-3 compounds: it appears difficult to obtain these with a deterministic dynamic model.



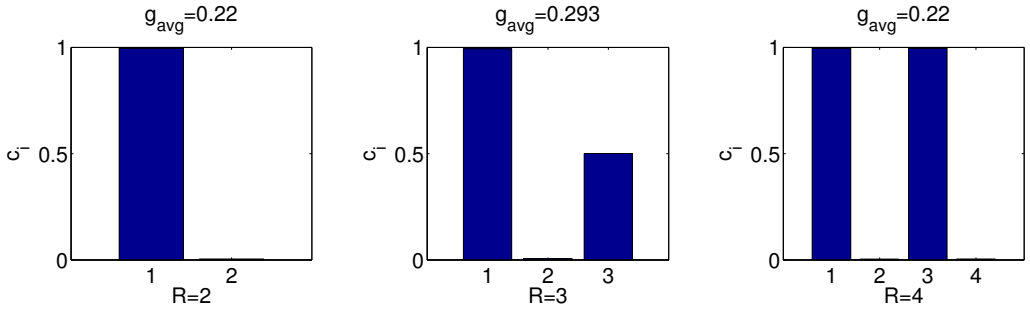
(a) $\bar{c} = 0.05$



(b) $\bar{c} = 0.1$



(c) $\bar{c} = 0.35$



(d) $\bar{c} = 0.5$

Figure 7.10: Energy minimizers with periods $R = 2, 3, 4$ by solving the minimisation problem (7.23) with Matlab **fmincon**. Parameters are $\epsilon = 0.25$, $\sigma = 0.5$, and $d_i = 1/i$ $(i = 1, 2 \cdots, 7)$ for a 7-nearest neighbour interaction model.

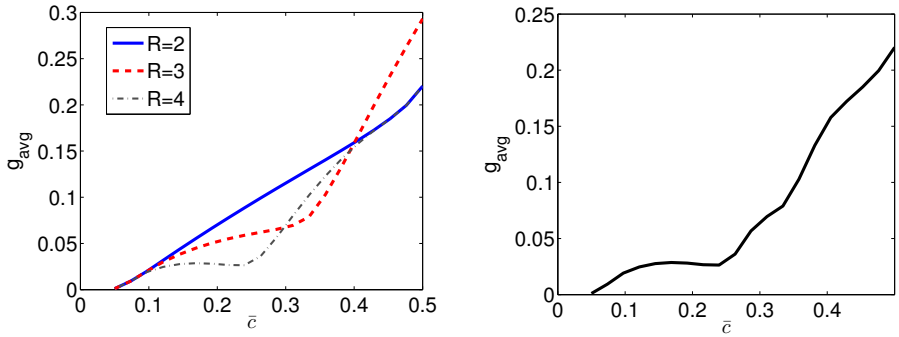


Figure 7.11: The total energy corresponds to the energy minimizers with periods $R = 2, 3, 4$ of the minimisation problem (7.23), with respect to the total concentration varying from near 0 to near 1. Parameters are the same as Fig. 7.10. The lowest energy of the three minimisers is selected out and plotted separately in the right panel.

Intuitively, a transition from stage-4/stage-2 to stage-3 requires a complete re-ordering of the filled lithium ions, and therefore can be extremely difficult to achieve in a deterministic setting as the system tends to stay in a local minimiser. However, the addition of thermal noise may lead the system to leave the local minimiser and find its global minimum, as we show in the next section.

7.4.3 Numerical simulations with thermal noise

As a preliminary investigation into the effect of noise, we time step the following process:

$$c_i(t + \Delta t) = c_i(t) + \Delta c_i(t) \tag{7.24a}$$

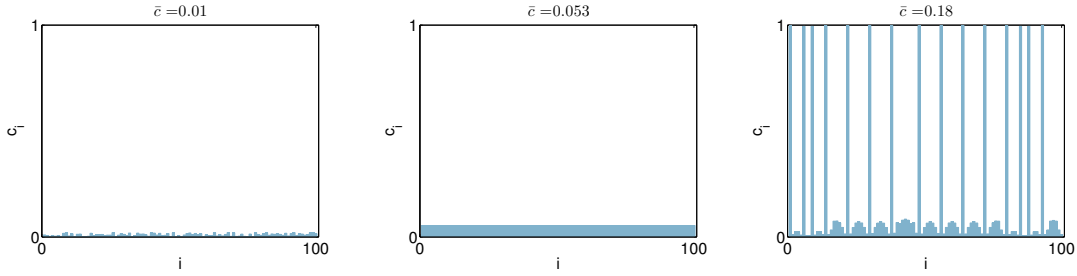
$$\Delta c_i(t) = \left[-\left(1 - \frac{1}{M}\right) \frac{\partial g_{\text{tot}}(t)}{\partial c_i(t)} + \frac{1}{M} \sum_{j=1, j\neq i}^{M} \frac{\partial g_{\text{tot}}}{\partial c_j} + \frac{1}{M} \frac{\mathrm{d}C(t)}{\mathrm{d}t} \right] \Delta t + \Delta R_i(t), \tag{7.24b}$$

where in (7.24b) the first term is a discretisation of the deterministic current-control model, and the second term represents the thermal noise.

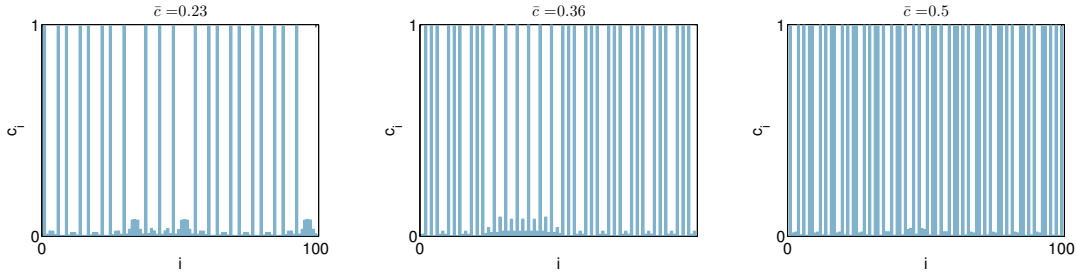
Since our primary goal is to determine whether or not thermal noise would enable the formation of stage-3 compounds, we do not use a sophisticated noise term. Instead, at each time step, we sample by

$$\Delta \bar{R}_i(t) = \upsilon \sqrt{c_i(t)} U_i(t) \sqrt{\Delta t}, \qquad i = 1, c, \cdots, M, \tag{7.25a}$$

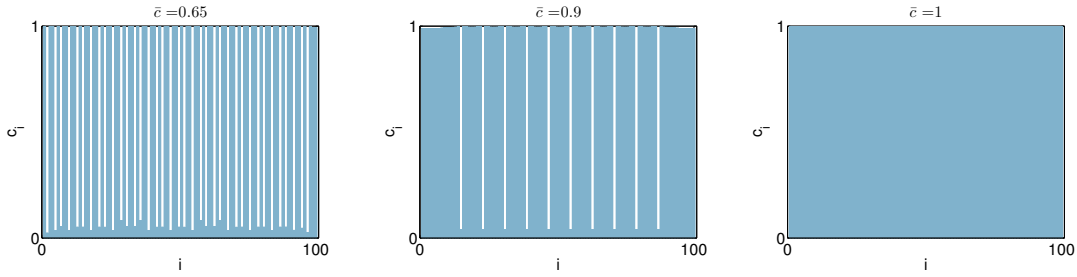
$$\Delta R_i(t) = \Delta \bar{R}_i(t) - \frac{1}{M} \sum_{i=1}^{M} \Delta \bar{R}_i(t), \qquad i = 1, c, \cdots, M. \tag{7.25b}$$



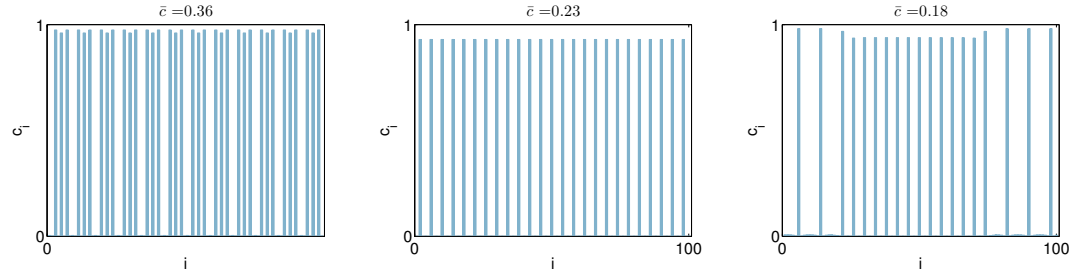
(a) $t = 0$ (b) $t = 4.4 \times 10^3$ (c) $t = 1.8 \times 10^4$



(d) $t = 2.2 \times 10^4$ (e) $t = 3.5 \times 10^4$ (f) $t = 4.9 \times 10^4$



(g) $t = 6.4 \times 10^4$ (h) $t = 8.9 \times 10^4$ (i) $t = 9.9 \times 10^4$



(j) $t = 1.61 \times 10^5$ (k) $t = 1.75 \times 10^5$ (l) $t = 1.80 \times 10^5$

Figure 7.12: A full lithiation/delithiation cycle of a 7-nearest neighbour interaction model found by simulating (7.8), with $\mathrm{d}C(t)/\mathrm{d}t = 10^{-3}$ for lithiation and $\mathrm{d}C(t)/\mathrm{d}t = -10^{-3}$ for delithiation. Parameters are the same as the minimisation problem of Fig. 7.10, with $\epsilon = 0.25$, $\sigma = 0.5$, $M = 96$, and $d_i = 1/i$ $(i = 1, 2, \cdots, 7)$. Initially the concentration of each compartment is randomly distributed in $[0, 0.02]$, and (i) is the final state of lithiation as well as the initial state for delithiation. In each panel $\bar{c}$ denotes the averaged concentration.

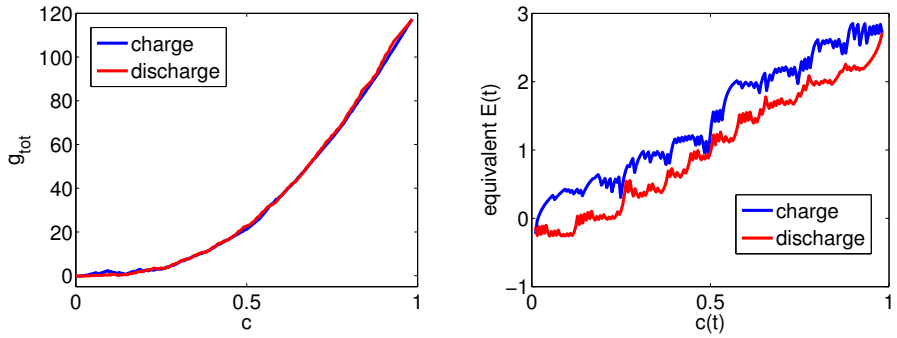


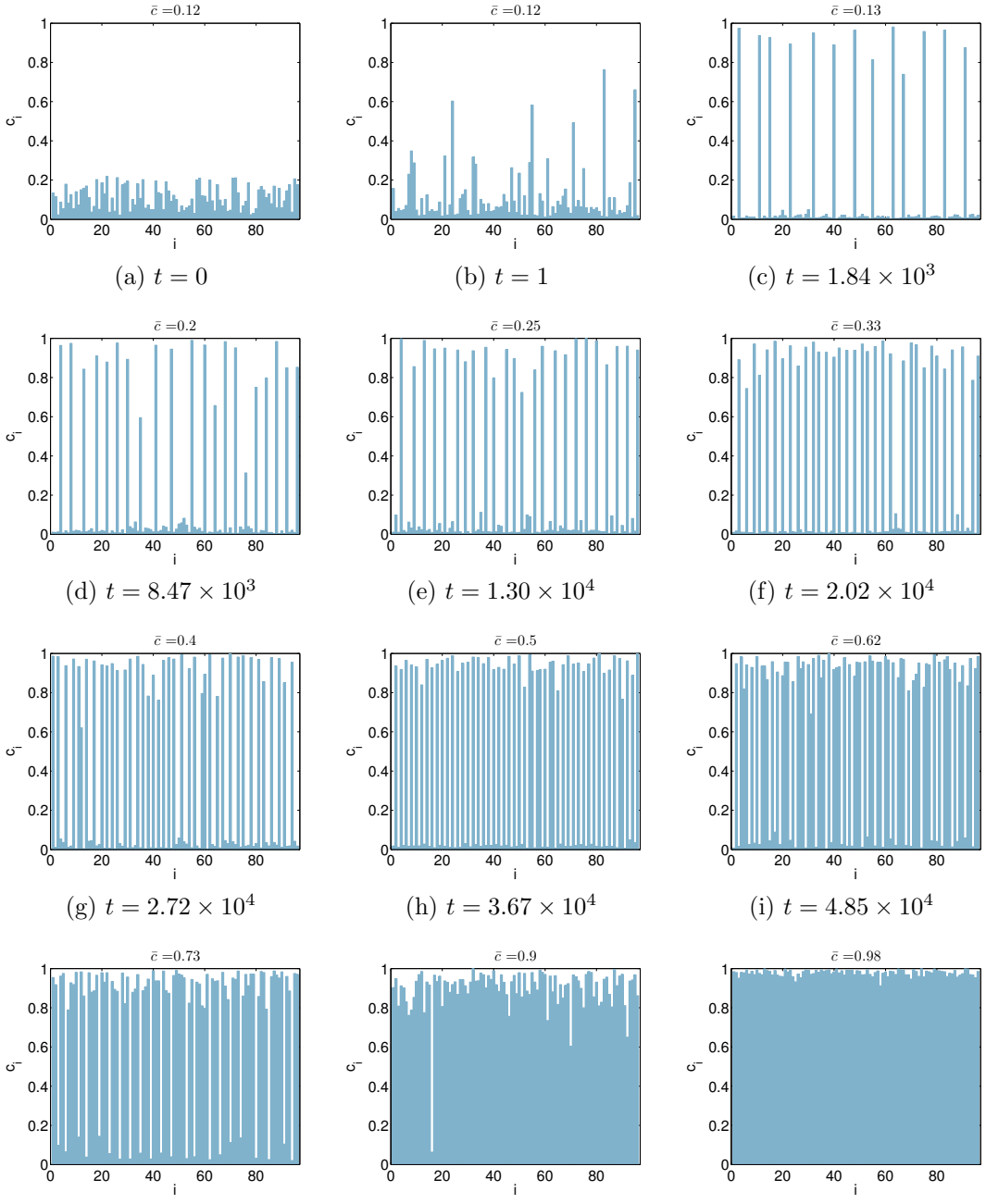
Figure 7.13: The total energy g_{tot} and the equivalent potential $E(t) = -\lambda(t)$ during the lithiation/delithiation cycle of the 7-nearest neighbour interaction model that is simulated in Fig. 7.12.

In (7.25a), υ is a scaling factor, and $U_i(t)$ is a uniform distribution in $[0, 1]$. We assume, in addition, that $\Delta\bar{R}_i(t)$ is proportional to the square root of the concentration, in order to magnify the effect of noise when the concentration is extremely low. Meanwhile, the term $\sqrt{\Delta t}$ makes the noise resemble a Brownian motion in its $\Delta t \to 0$ limit. Then in (7.25b), we subtract the noise terms sampled in (7.25a) by their average, so that $\sum \Delta R_i(t) = 0$. This ensures that the constraint on the total concentration still holds.

In theory, (7.25b) implies that the fluctuations of the concentration in each compartment are not independent, which does not have a big impact on our search for the stage-3 compound. Meanwhile, at each time step, if the sampled results make $c_i(t+\Delta t)$ exceed the range $[0, 1]$, we re-sample until it satisfies that $c_i(t+\Delta t) \in [0, 1]$, for every i.

We run a lithiation process with $\mathrm{d}C(t)/\mathrm{d}t = 10^{-3}$ and show the results in Fig. 7.14. Despite the coexistence of multiple stages in almost every figure, which can be regarded as the disorder generated by thermal noise, we do find concentration configurations that are close to the periodic structures suggested by Fig. 7.11. For instance, at $\bar{c} = 0.2$, $R = 4$ has a lower energy than $R = 2$ and $R = 3$, and in (d) the system is largely stage-4, although also stage-8, stage-6 and stage-5 coexist. Meanwhile, in (e), (f), and (g), where the energy minimiser that has the lowest energy corresponds to $R = 4$, $R = 3$, and $R = 2$, respectively, we observe a mixture of stage-4 and stage-3, a mixture of stage-3 and stage-2, and a mixture of stage-3 and stage-2. A trend of 4-3-2-1 transition is obvious, although the transition features the coexistence of multiple stages instead of a sharp change.

Finally, we show two simulations in Fig. 7.15, with a net constant concentration $\bar{c} = 1/3$, and we compare two different initial conditions. At $\bar{c} = 1/3$, a periodic



(a) $t = 0$ (b) $t = 1$ (c) $t = 1.84 \times 10^3$

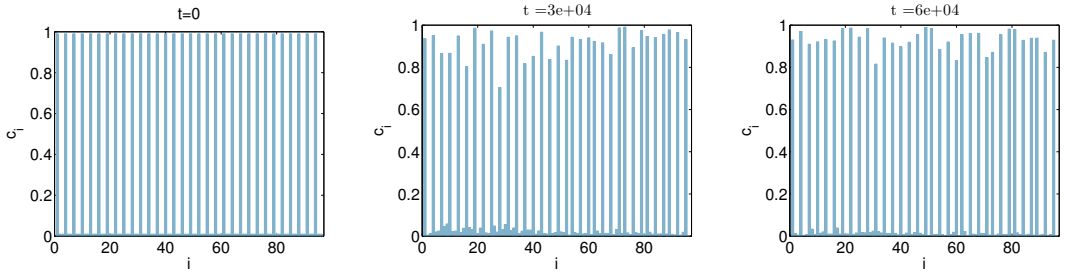
(d) $t = 8.47 \times 10^3$ (e) $t = 1.30 \times 10^4$ (f) $t = 2.02 \times 10^4$

(g) $t = 2.72 \times 10^4$ (h) $t = 3.67 \times 10^4$ (i) $t = 4.85 \times 10^4$

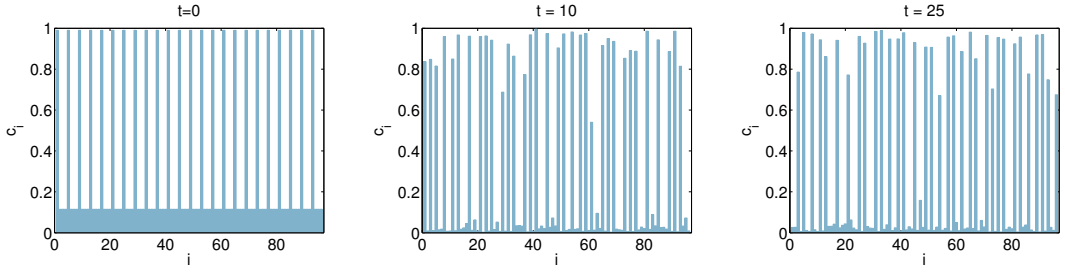
(j) $t = 5.92 \times 10^4$ (k) $t = 7.50 \times 10^4$ (l) $t = 8.29 \times 10^4$

Figure 7.14: Numerical simulations of the current control model with noise (7.24) with $\mathrm{d}C(t)/\mathrm{d}t = 10^{-3}$. The time-step is $\Delta t = 10^{-3}$, and $\bar{c}$ denotes the averaged concentration. Parameters are the same as the minimisation problem of Fig. 7.10, with $\epsilon = 0.25$, $\sigma = 0.5$, $M = 96$, $\upsilon = 0.3$, and $d_i = 1/i$ $(i = 1, 2, \cdots, 7)$, and initially the concentration of each compartment is randomly distributed in $[0, 0.2]$.

structure with $R = 3$ has lower energy than $R = 2$ or $R = 4$. In one simulation, we use the initial distribution corresponding to an $R = 3$ minimiser; in another simulation, the initial distribution corresponds to an $R = 4$ minimiser. We have run various simulations with different magnitudes of thermal noise: the simulation with an $R = 3$ initial condition always stays a mostly stage-3 structure, and the simulation with an $R = 4$ initial condition always stays a mostly stage-4 structure. The two simulations partly explain why it is difficult to find the stage-3 compounds using the deterministic model: the system tends to stay in a local energy minimum. The challenge is to add enough noise to allow the system to escape the local minimum of stage-4, but not so much that noise totally swamps the solution.



(a) Initial concentration is $R = 3$.



(b) Initial concentration is $R = 4$.

Figure 7.15: Numerical simulations of the current control model with noise (7.24) with $C(t)$ being kept constant. The time step is $\Delta t = 10^{-3}$. Parameters are the same as the simulation in Fig. 7.14, with $\epsilon = 0.25$, $\sigma = 0.5$, $M = 96$, $\upsilon = 0.3$, and $d_i = 1/i$ $(i = 1, 2, \cdots, 7)$. Initially the concentration is the energy minimiser when $R = 3$ in (a), and the energy minimiser when $R = 4$ in (b).

7.4.4 Extension: a triple well energy

In all our studies so far, we have neglected the two different possible in-plane orderings, namely close-packed in-plane ordering and hexagonally packed in-plane ordering as illustrated in Fig. 1.4. By default, we consider the close-packed in-plane ordering,

and hence we are unable to predict hexagonally packed (reduced state) stage 2 in lithium graphite. Note that, in hexagonally packed in-plane ordering, full occupation of the available sites corresponds to a 2/3 full layer in lithium graphite. One possible approach to model this would be to use a triple well potential, with an additional energy minimum at $c = 2/3$.

We examine a triple well energy model through numerics. The total energy of the system is still assumed to be a discrete sum of the intra-layer energy and the inter-layer energy, that is

$$g_{\text{tot}} = \sum_{i=1}^{M} g(c_i) + g_{\text{int}}, \tag{7.26a}$$

where the interaction energy is specified in (7.2). Now a triple well form is adopted for the intra-layer energy, in which we assume the third energy minimum to be a Gaussian, using

$$g(c) = c(1-c) + \epsilon(c\log c + (1-c)\log(1-c)) - a\exp\left(-b(c-2/3)^2\right). \tag{7.26b}$$

We adopt the Gaussian form because the depth and width of the new minimum can be conveniently adjusted using a and b. In numerics we use a triple well energy with $\epsilon = 0.3$, $a = 0.03$, and $b = 100$, which is shown in Fig. 7.16.

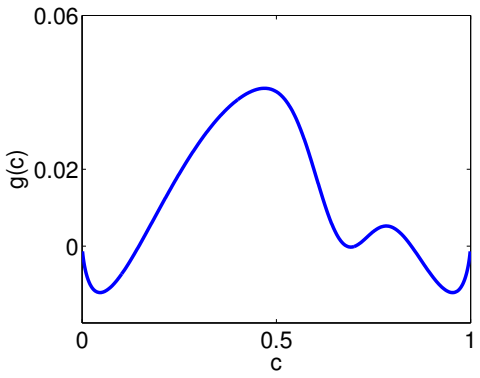
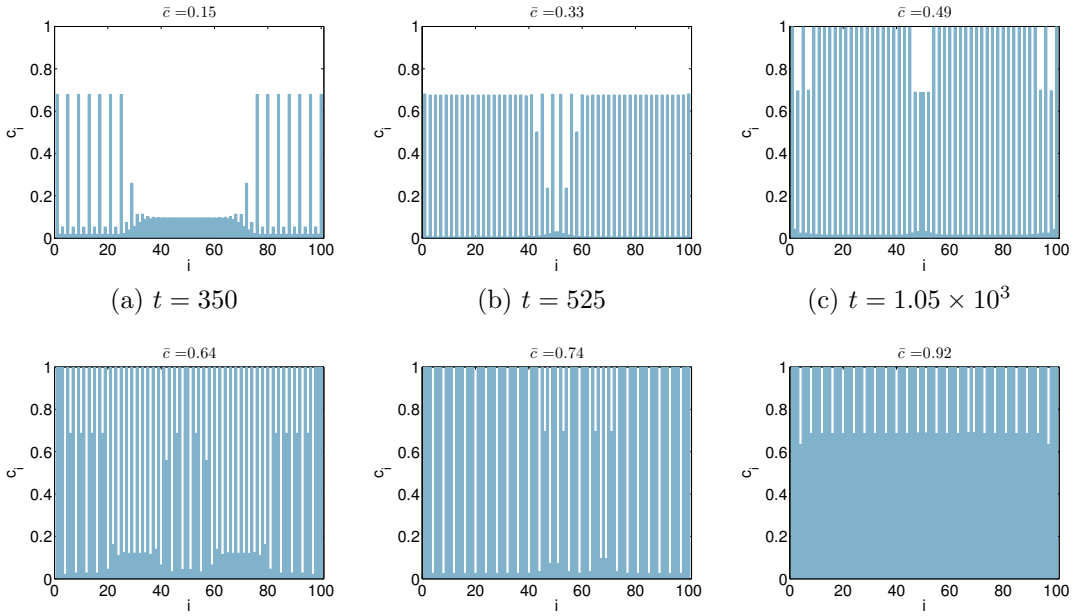


Figure 7.16: A triple well intra-layer free energy given by (7.26b), plotted with $\epsilon = 0.3$, $a = 0.03$, and $b = 100$.

We perform numerical simulations with this triple well energy, assuming voltage-control with the Butler-Volmer equation, and adopting the three-nearest neighbour interaction. Some results are presented in Fig. 7.17. In the numerics, a reduced

state stage-4 is formed first, until the averaged concentration $\bar{c}$ reaches approximately $1/4 \times 2/3 = 1/6$; it is followed in sequence by a reduced state stage-2 until $\bar{c} \approx 1/2 \times 2/3 = 1/3$, and a mixture of reduced stage-2 and normal stage-2 until $\bar{c} \approx 1/2$. After the system reaches half-full, a mixture of different in-plane patterns and different stages occurs. For instance, panel (f) suggest a configuration with two thirds of all layers in normal stage-1, and the remaining one third of all layers in the reduced stage stage-1. Such pattern has not been reported experimentally, however.



(a) $t = 350$ (b) $t = 525$ (c) $t = 1.05 \times 10^3$

(d) $t = 1.49 \times 10^3$ (e) $t = 1.59 \times 10^4$ (f) $t = 1.88 \times 10^4$

Figure 7.17: Numerical simulations of a lithiation process, using a triple-well intra-layer energy and a three-nearest neighbour inter-layer energy, with non-periodic interaction. The simulations use the Butler–Volmer equation and voltage-control, with $E(t) = 10^{-3}t$. Parameter values are $\epsilon = 0.3$, $\epsilon_2 = 0.3$, $\mu_i = 1/\sqrt{i}$, $N = 100$, $a = 0.03$, $b = 100$. Initially $t = 0$, and the concentration of each compartment is randomly distributed in $[0, 0.01]$.

The total energy and the potential associated with the simulation shown in Fig. 7.17 are plotted in Fig. 7.18. The C-V curve exhibits more steps than when using the double well energy, and some of the steps occur at unexpected concentration values.

Because the triple well intra-layer energy assumes an additional energy minimum at $c = 2/3$, the system can now take on the configuration of a reduced state stage-2 for an averaged concentration of $\bar{c} = 1/3$. Potentially, this triple well energy model can be adopted to model the phase-transition of lithium graphite where the reduced state

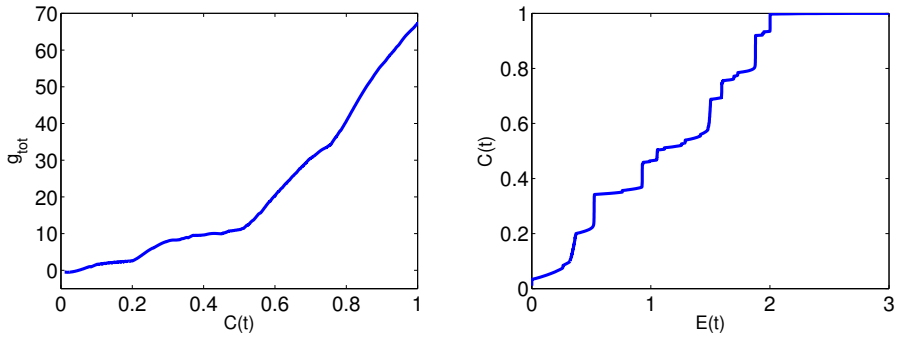


Figure 7.18: The total energy and the potential versus the total concentration, associated with the simulation presented Figs. 7.17.

stage-2 is involved. However, as illustrated in Fig. 7.18, the new triple well energy model may lead to configurations and corresponding potential jumps that are not observed experimentally. By carefully monitoring the coefficients, it may be possible to eliminate such states, and this is left for future work.

7.5 Summary

In this chapter, we investigate longer-range interaction to study the transition between multiple phases. As in Chapters 4 and 5, we assume that the interaction between any two compartments can be described by an energy term that is proportional to the concentrations of both compartments, and we further model the interaction strength to decay with distance.

In general, interactions over a finite range K divide the system into $K+1$ groups, and in lithiation/delithiation the system tends to fill/empty each group sequentially. Hence, it results in multiple phases, and the C-V curve has multiple steps, compared to the two-step C-V curve found in Chapters 4 and 5. In contrast, interactions over a much longer range lead to a global behaviour in lithiation/delithiation, so the C-V curve is somewhat smoother. Numerical simulations suggest that the system behaves as having nucleation spikes on top of an approximately continuous distribution, for which we present a preliminary semi-continuous model.

A particular focus of this chapter is to use a 7-nearest neighbour interaction to mimic the staging behaviour of lithium graphite. Although the existence of stage 3 could happen in the 7-nearest neighbour interaction model in terms of energy minimisation, in dynamic simulations, it is extremely difficult to achieve. This can be understood, as the system always prefers to stay in a local minimiser as long as the

local minimiser keeps changes to the current configuration to a minimum. Therefore, when starting from stage-4, the system tends to maintain a mixture of stage-4 and stage-2, rather than reordering the filled lithium ions to reach a stage-3 configuration.

Meanwhile, the inclusion of thermal noise enables the system to find the stage-3 minimum relatively easy compared to the simulations without the noise term. However, in this chapter, the inclusion of thermal noise into the dynamics is elementary, and we choose a reasonable form for the noise term without deducing it by connecting to the stochastic models developed in Chapters 3 and 6. This, together with the idea of using a triple well energy to model the hexagonally packed in-plane ordering of lithium graphite, can be explored in further research.

Chapter 8

Conclusions

In this thesis, we have developed various mathematical models to describe the phase-separation of a multicompartment system, assuming a homogeneous lithium concentration in each compartment. Both two-phase transitions and multiple-phase transitions have been studied, under a variety of different situations: the system may be under either voltage-control or current-control, and may evolve either in quasi-equilibrium or out-of-equilibrium; the compartments may be either coupled or decoupled; thermal noise may change the system behaviour; and the limited number of lithium ions hosted by each compartment may dominate over the double-well free energy.

In this chapter, we summarise the various models, discuss possible extensions of them, and propose possible areas for future research.

8.1 Summary of results

The basic deterministic model was presented in Chapter 2, the primary focus of which was the sudden transition between the three possible phases of a single compartment: the Li-poor phase, the Li-rich phase, and the intermediate phase. First, the equilibrium properties are directly related to the double well Gibbs free energy. Depending on the value of the applied potential, we found that there is either a single stable equilibrium close to $c = 0$, a trio of equilibria (stable equilibria near $c = 0$ and $c = 1$ and an unstable equilibrium at an intermediate value of c), or a single stable equilibrium close to $c = 1$. This led us to expect the quasi-equilibrium evolution to exhibit hysteresis of the type described in detail in [13]: we expected the lithium concentration to respond to the potential by remaining close to one stable equilibrium (either near $c = 0$ or $c = 1$) until E reached a critical value where the original stable equilibrium ceased to exist and the system was forced to jump to the remaining equilibrium.

In the dynamic problem, modelled by the Butler–Volmer equation, we found that the nonlinear relation of the Butler–Volmer equation introduced subtle changes to the equilibrium C-V relation. In Section 2.3, we considered the dynamic problem of lithium concentration responding to a potential increasing at a constant rate. From our asymptotic analysis, we found that the jump from "near-empty" to "near-full" occurs a short time *after* what would be predicted from the equilibrium analysis in Section 2.2. However, the analysis of this transition was very delicate, and it might reasonably be argued that a small amount of stochastic noise added to the deterministic model might alter the dynamics completely.

In Chapter 3, we introduced a discrete, probabilistic model of the lithium concentration in a single compartment based on the chemical master equation. A direct implication of the stochastic model is that, the quasi-equilibrium and the dynamic C-V relations are qualitatively different. We found that the stationary distribution is unique for any given value of E, and that the expected value of the concentration jumps dramatically from "near-empty" to "near-full" as E passes through zero. Thus, the equilibrium analysis of the discrete model would suggest that there is no hysteresis in the system. In Sections 3.3 and 3.4, we contrasted this equilibrium analysis with a dynamic analysis of the discrete, probabilistic model with a changing applied potential. We found that the importance of discreteness to the dynamic model is controlled by one dimensionless parameter, α, and we derived different simplified models in the case of different limits of α. When $\alpha = O(1)$, both discrete effects and continuum effects are important and we obtained the hybrid discrete-continuum model described in Section 3.3. When $\alpha \gg 1$ or $\alpha \ll 1$ we respectively obtained the discrete limit treated in Section 3.4.2 and the continuum limit treated in Section 3.4.3. In each of these three cases, we found that there was significant hysteresis in the system, although the precise value of the potential at which the jump from "near-empty" to "near-full" occurs depended on the regime we were considering (based on the value of α). In addition, our analysis showed that the continuum deterministic model for the lithiation dynamics of a nanoparticle LFP is not a bad approximation of the full stochastic model under moderate and realistic rates of charging.

In Chapter 4 and 5, we considered a system of compartments coupled together through interaction energy rising from the adjacent compartments. In Chapter 4, we assumed a linear dynamic model and imposed the constraint on the total amount of lithium of the system, or equivalently, current-control; In Chapter 5, we assumed a nonlinear dynamic model and imposed voltage-control.

The equilibrium behaviour of both the current-control problem and the voltage-control problem proves to be extremely subtle. The equilibrium of a current-control problem corresponds to the distribution of lithium ions among the multicompartment system, in order to minimise the total energy of the system. This can be studied via a detailed bifurcation analysis. A bifurcation analysis on a three-compartment system indicates that, generally, when the total concentration is extremely low or high, the equilibrium is unique, and is associated with all compartments having the same lithium concentration; and that when the total concentration is an intermediate value, the system takes on a "empty-full-empty-full" configuration, which is determined by the nearest-neighbour interaction. Such observations were also confirmed by simulating the quasi-equilibrium evolution with a linear gradient flow model. Despite the delay and memory effect during slow transition through the bifurcations, the phase-transition pattern itself has little uncertainty; we therefore did not examine in detail the dynamic problem and the effect of thermal noise in the case of the gradient flow model under current-control.

In contrast, both the equilibrium and dynamics are much more complicated in a voltage-control setting using the Butler–Volmer equation. In analysing the equilibria of a two-compartment system under voltage-control, we found that when the applied voltage was low/high enough, the two compartments were simultaneously "near-empty"/"near-full", while at an intermediate value of E, each of the two compartments could be in one of three possible phases – "near-empty", "near-full", or the intermediate phase. Meanwhile, the equilibria were subject to slight modifications as a result of the interaction.

As a result, at an intermediate value of E, multiple stable and unstable equilibria exist; and all the bifurcations concerning the appearing and disappearing of the equilibria take place in the vicinity of four critical voltages: in lithiation at $E = 1$ and $E = 1 + \sigma$, and in delithiation at $E = -1$ and $E = -1 + \sigma$.

Again, this led us to expect the quasi-equilibrium evolution to exhibit hysteresis between lithiation and delithiation. In lithiation, we expected the lithium concentration of both compartments to remain low, until the critical voltage of $E = 1$ was reached, when the equilibria associated with this "both empty" configuration ceases to exist. However, with the disappearance of the "both empty" equilibria, two stable equilibria exist: one corresponds to an "one empty, one full" configuration, and the other to the "both full" configuration. It does not immediately follows that the next stage would be the "one empty, one full" configuration, in spite of the nearest-neighbour interaction.

The same uncertainty remains in the dynamic problem. A preliminary analysis of the dynamics of a two-compartment model suggests that the choice between the 'one empty, one full" and "both full" configuration depends on the charging speed as well as the initial condition, and also that such dependence is extremely sensitive. Both the equilibrium and dynamic arguments of a two-compartment model carries over to a multicompartment system. Hence, it is necessary to consider the effect of thermal noise and find out how it would change the solution structure of the deterministic model.

Therefore, in Chapter 6, we analysed a discrete, probabilistic model for a two-compartment system. This model uses the same principles as the stochastic single-compartment model in Chapter 3, and implies the same distinction between the equilibrium and the dynamics as the single-compartment model: the hysteresis does not exist in the equilibrium, but is retained in the dynamics. Meanwhile, in the case of two interacting compartments, the stochastic model has a different implication from the deterministic model: when E is an intermediate value, the stochastic model always prefers to fill the compartments sequentially; the situation of filling all compartments at the same rate is not favourable by the stochastic model, neither in equilibrium nor dynamics. As a result, the stochastic model always predicts a two-step process.

First, the stationary distribution is unique for any given value of E, and hence the expected concentration C is single-valued with respect to E. The equilibrium C-V curve is found to be a staircase-like structure with two steps. Because of the interaction between neighbouring compartments, the expected value of the concentration jumps dramatically from "near-empty" to a half as E passes through zero, and jumps from a half to "near-full" as E passes through σ.

The C-V curve in dynamics presents a similar two-step structure, and in lithiation/delithiation is displaced from the equilibrium curve by ± 1. In addition, the dynamic C-V curve is further influenced by the parameter α, the measure of discreteness. Its implications are unchanged with respect to the single compartment case: when discreteness dominates, each compartment essentially transits between the lowest state and the highest state, so the dynamics can be analysed in a straightforward way; when the model is essentially a continuum model, the C-V curve agrees with the deterministic dynamics where a compartment-by-compartment filling sequence is selected.

We have further argued that the features of both the equilibrium and dynamics C-V curves are due to the nearest-neighbour interaction, and are hence unchanged even if the number of compartments increases.

In Chapter 7, we investigated the phase transition between multiple phases, using a free energy model that considered a longer-range interaction between the compartments. The motivation for this chapter was the phase-separation of lithium graphite, the 8-4-3-2-1 transition. Generally, by assuming that each compartment can interact with its K-nearest neighbours, we could get a C-V curve exhibiting $K+1$ jumps. Using a 7-nearest neighbour model, we found that although an 8-4-3-2-1 transition is possible, in reality it requires a reordering of all compartments, and therefore can be relatively difficult to obtain. We obtained such a transition by introducing thermal noise, which helps the system to deviate from the attraction of the current local minimum, and then find the global energy minimum of the stage-3 configuration. We also introduced a basic idea to model the different in-plane ordering by imposing a third well in the Gibbs free energy; this is associated with the energetically favourable state of every compartments being two thirds full.

8.2 Discussions and future research

Here we summarise some assumptions that might be relaxed, allowing us to describe more general behaviour.

As pointed out in Section 5.1, an underlying assumption for all the dynamic models of this thesis, is that there is no direct exchange of lithium ions between the constituent compartments. Each compartment interacts only with the electrolyte, and that any exchange of lithium ions between the two compartments has to happen via the electrolyte as the intermediate. The resulting coupling between the compartments is therefore a weak one. A stronger coupling can be captured if we assume an extra interaction pathway to account for the direct exchange of lithium ions. During the modelling of hexagonally packed in-plane ordering of lithium graphite, the change of this in-plane structure might be captured by stronger coupling between the compartments. Direct exchange between compartments might also help the system to find global energy minimum, instead of becoming stuck in local minima, as seen in Chapter 7.

Assumptions about the charging speed can be also relaxed. In all the voltage-control dynamics, a dimensionless rate of $\mathrm{d}E/\mathrm{d}t = 1$ is used, so that the voltage is assumed to vary on the intrinsic time-scale t_{int} of each compartment, that is, the time required to deplete a fully-lithiated compartment at the intrinsic current density. All the analysis and results are qualitatively similar if $\mathrm{d}E/\mathrm{d}t = \kappa$ and $\kappa = \mathcal{O}(1)$. Conclusions concerning the dynamics can therefore be applied to a general charging

problem, since the characteristic time for a nano-particle LFP with 50-nm diameter is computed to be around 17 hours, which is comparable to real-life charging/discharging time-scale.

However, as the intrinsic time depends on the material properties, such as the size, the lattice density, and the intrinsic exchange current density, it is possible that in some situations we need to consider regimes where $\kappa \gg 1$ or $\kappa \ll 1$. With the stochastic model, the limit where $\kappa \gg 1$ is found to be relatively straightforward: fast charging effectively makes the probability distribution pass through the left inner layer quickly, and hence involves fewer states in the transition of the probability distribution, making the dynamics behave similarly to the discrete limit. On the other hand, preliminary investigation into slow charging suggests a change in the solution structure: a local discrete-to-continuum model is required in the outer regions as well as in the left-inner region. Further analysis is needed here.

Another possible improvement to the model is the approach to the impact of thermal noise. The main approach adopted in this work is the chemical master equation, which we set up by reproducing the Butler–Volmer dynamics in its deterministic limit. Only in Chapter 7, in the search for the stage-3 compounds, did we present a stochastic differential equation to account for thermal noise: this model is analogous to the gradient flow model, but has an explicit stochastic term to represent thermal noise. It is possible to associate form for the stochastic term by exploiting the relation between the gradient flow model, the Butler–Volmer model, and the stochastic model using the chemical master equation. Potentially, with a stochastic differential equation that is consistent with the chemical master equation framework, we can use different methods to analyse the effects of thermal noise, and contrast the results with those of the chemical master equations.

Moreover, this thesis does not present a stochastic model based on the chemical master equation for the K-nearest neighbour interaction, M-compartment system. The analysis for such models would be formidable. However, as in the nearest-neighbour interaction, we expect the K-nearest neighbour interaction, M-compartment system to exhibit a significant degree of degeneracy, which can be used to reduce the full problem to K interacting compartments.

The improvements discussed so far concern the key electrochemical properties and neglect all the secondary effects. One secondary effect that can also be included in the model is the mechanical properties. As introduced in Section 1.1.2, mechanical effects are important practically in the novel nano-material anode. For instance, the use of silicon anodes in batteries has been limited by the large volume expansion during

lithiation. Therefore it would be useful to account for the mechanical properties in such material, and identify the new phenomena raised by the coupling between discreteness, the double-well potential, and mechanical effects.

In addition, since in a real electrode it is unlikely that all compartments will be of the same size, analysing a system of multiple compartments with varying sizes would be a natural next step.

Finally, it would be extremely helpful to incorporate the models into a full battery working simulation. In the various models developed in this thesis, the control variable is either the voltage or the concentration, with the corresponding output variable being the concentration or the voltage, respectively. Hence, a multi-step C-V curve is a result of the model.

In the common practice of higher-level modelling, however, the C-V curve is measured and fitted into a full battery working simulation. It is therefore a static curve. As we have shown, due to phase-separation at the compartment level, the static curve is insufficient to capture the dynamics of a multi-compartment system. To capture automatically the multi-step C-V curve, and also to consider the hysteresis and the initial state of the electrode system, our models could be incorporated into simulations of the full battery.

Appendix A

Simulating the one-step process as a random walk

Here we illustrate the procedure for sampling the one-step process as random walks on the concentration space, according to the chemical master equation (3.1).

Suppose at time t, the voltage $E(t)$ is known, and the random walk is in state i, the right and the left jump intensities $q_i^{\pm}$ can be computed from (3.10). Treating the jump event as a compound Poisson process, we can sample both the time and the direction of the next jump. By repeating this process, we can simulate one path for the random walk. We then obtain the overall concentration evolution by averaging over many such paths.

Initialize the starting state S_i and the voltage $E(t)$;
while *not reached final state* **do**
  calculate the jump intensity $q_i^+(t)$ and $q_i^-(t)$ associated with state S_i at time t, using equation (3.10);
  sample the time interval Δt for the next jump to happen, using a Poisson process with intensity $q_i^+ + q_i^-$;
  sample a discrete random variable X which can be ± 1, with the probability mass function $P(X = -1) = p_i^-/(p_i^- + p_i^+)$ and $P(X = 1) = p_i^+/(p_i^- + p_i^+)$;
  update with $S_{i+1} = S_i + X$ and $t = t + \Delta t$;
end

Algorithm 1: Algorithm for simulating the one-step process as a random walk.

Appendix B

Simplification of the transition probabilities

B.1 Transition probabilities in the left inner layer

In the left inner layer where $i \ll N$, the energy g_i can be expressed as

$$\begin{aligned} g_i = g(i\Delta C) &= i\Delta C(1 - i\Delta C) + \epsilon(i\Delta C)\log(i\Delta C) + \epsilon(1 - i\Delta C)\log(1 - i\Delta C) \\ &\sim i\Delta C(1 - i\Delta C) + \epsilon(i\Delta C)\log(i\Delta C) - \epsilon(1 - i\Delta C)i\Delta C \\ &= (1 - \epsilon)(i\Delta C)(1 - i\Delta C) + \epsilon(i\Delta C)\log(i\Delta C), \end{aligned} \tag{B.1}$$

giving

$$g_{i+1} \sim (1 - \epsilon)(i + 1)\Delta C(1 - (i + 1)\Delta C) + \epsilon(i + 1)\Delta C \log[(i + 1)\Delta C] \tag{B.2}$$

and

$$\begin{aligned} g_{i+1} - g_i \sim{}& (1 - \epsilon)\Delta C - (1 - \epsilon)(2i + 1)\Delta C^2 \\ &+ \epsilon\Delta C\left[(i + 1)\log(i + 1) - i\log(i)\right] + \epsilon\Delta C \log(\Delta C). \end{aligned} \tag{B.3}$$

Substituting (B.3) into the expressions for the transition probabilities (3.10), we obtain a simplified expression for the transition probabilities in the left inner layer:

$$\begin{aligned} q_i^+ &\sim \frac{1}{2\Delta C^{3/2}} \exp\left(\frac{E - 1}{2\epsilon}\right) \exp\left(\frac{1 + \alpha(2i + 1) + i\log i - (i + 1)\log(i + 1)}{2}\right) \\ &= \epsilon^{-3/2} \exp\left(\frac{E - 1}{2\epsilon}\right) f_i^+(\alpha), \end{aligned} \tag{B.4a}$$

$$\begin{aligned} q_i^- &\sim \frac{1}{2\Delta C^{1/2}} \exp\left(-\frac{E - 1}{2\epsilon}\right) \exp\left(\frac{-1 - \alpha(2i - 1) + i\log(i) - (i - 1)\log(i - 1)}{2}\right) \\ &= \epsilon^{-1/2} \exp\left(-\frac{E - 1}{2\epsilon}\right) f_i^-(\alpha), \end{aligned} \tag{B.4b}$$

where $f_i^{\pm}(\alpha)$ are defined in (3.33).

B.2 Transition probabilities in the right inner layer

Let $j = N+1-i \ll N$, we can utilise the symmetry of the double well energy $g_i = g_j$ to find the transition probabilities in the right inner layer. For $N+1-i \ll N$, it satisfies that

$$\begin{aligned} q_i^+ = q_{N+1-j}^+ &= \frac{1}{2\Delta C} \exp\left[\frac{E - \frac{g_{i+1}-g_i}{\Delta C}}{2\epsilon}\right] \\ &= \frac{1}{2\Delta C} \exp\left[\frac{E - \frac{g_{j-1}-g_j}{\Delta C}}{2\epsilon}\right] \\ &= \exp\left(\frac{E}{\epsilon}\right) q_j^-, && \text{using (3.10b)} \\ &= \epsilon^{-1/2} \exp\left(\frac{E+1}{2\epsilon}\right) f_j^-(\alpha). && \text{using (B.4b)} \end{aligned}$$

Similarly, we have

$$\begin{aligned} q_{N+1-j}^- &= \exp\left(-\frac{E}{\epsilon}\right) q_j^+, && \text{using (3.10a)} \\ &= \epsilon^{-3/2} \exp\left(-\frac{E+1}{2\epsilon}\right) f_j^+(\alpha). && \text{using (B.4a)} \end{aligned}$$

Appendix C

Equilibria of the three-compartment system

In this section, we assume $\epsilon \downarrow 0$ and find the leading order solutions to equation (4.15). As in Table 4.1, possible equilibria of the three-compartment system are listed below.

	(c_1, c_2, c_3)	equivalent solution	range of C	Section
A	$(0, 0, 0)$		exponentially small	Appx. (C.1)
B	$(0, 0, 0)$		algebraically small	Appx. (C.2)
C	$(X, 0, 0)$	$(0, 0, X)$	$C \in (0, 1)$	Appx. (C.3)
D	$(0, X, 0)$		$C \in (0, 1)$	Appx. (C.5)
E	$(X, X, 0)$	$(0, X, X)$	$C \in (0, 2)$	Appx. (C.7)
F	$(1, X, 0)$	$(0, X, 1)$	$C \in (1, 2)$	Appx. (C.8)
G	$(X, 1, 0)$	$(0, 1, X)$	$C \in (1, 2)$	Appx. (C.9)
H	$(X, 0, X)$		$C \in (0, 2)$	Appx. (C.11)
I	$(1, 0, X)$	$(X, 0, 1)$	$C \in (1, 2)$	Appx. (C.12)
J	(X, X, X)		$C \in (0, 3)$	Appx. (C.13)
K	$(1, X, X)$	$(X, X, 1)$	$C \in (1, 3)$	Appx. (C.14)
L	$(X, 1, X)$		$C \in (1, 3)$	Appx. (C.15)
M	$(1, 1, X)$	$(X, 1, 1)$	$C \in (2, 3)$	Appx. (C.16)
N	$(1, X, 1)$		$C \in (2, 3)$	Appx. (C.17)
O	$(1, 1, 1)$		$C \sim 3$	Appx. (C.18)
P	$(1, 0, 0)$	$(0, 0, 1)$	$C \sim 1$	Appx. (C.4)
Q	$(0, 1, 0)$		$C \sim 1$	Appx. (C.6)
R	$(1, 1, 0)$	$(0, 1, 1)$	$C \sim 2$	Appx. (C.10)

Table C.1: Enumeration of possible (c_1, c_2, c_3) combinations. We follow the convention of Table (4.1) and use $c_i \sim 0$, $c_i \sim 1$, and $c_i \sim X$ to denote when C is close to 0, close to 1, and in the regime inbetween, respectively. We also use $T \in (a, b)$ to indicate T is a value between a and b, but not close to a or b.

C.1 Exponentially small C

When C is exponentially small, c_1, c_2, c_3 are all exponentially small, so we rescale the problem by

$$c_1 = e^{-U_1/\epsilon}, \quad c_2 = e^{-U_2/\epsilon}, \quad c_3 = e^{-U_3/\epsilon}$$

to get the leading order equation

$$2U_1 - U_2 - U_3 \sim 0, \tag{C.1a}$$

$$-U_1 - U_2 + U_3 \sim 0. \tag{C.1b}$$

Therefore, the solution has to satisfy

$$U_1 \sim U_2 \sim U_3, \tag{C.2}$$

or equivalently,

$$c_1 \sim c_2 \sim c_3 \sim \frac{C}{3}, \tag{C.3}$$

which is the only equilibrium when C is exponentially small.

Stability To the leading order, the associated Jacobian matrix is

$$J \sim \begin{pmatrix} -\frac{\epsilon}{C} & \frac{2}{3}\sigma \\ \frac{2}{3}\sigma & -\frac{\epsilon}{C} \end{pmatrix}. \tag{C.4}$$

With exponentially small C, we have $tr(J) < 0$ and $\det(J) > 0$, so that the solution (C.3) is a **stable node**.

C.2 Algebraically small C

Assuming $\log c_1 = \mathcal{O}(\epsilon)$, $c_2 = \mathcal{O}(\epsilon)$, $c_3 = \mathcal{O}(\epsilon)$, the leading order equations are

$$(4+\sigma)c_1 - (2+\sigma)c_2 + (-2+\sigma)c_3 \sim 0, \tag{C.5a}$$

$$(-2+\sigma)c_1 - (2+\sigma)c_2 + (4+\sigma)c_3 \sim 0, \tag{C.5b}$$

$$c_1 + c_2 + c_3 = C, \tag{C.5c}$$

which admit the leading order solution

$$c_1 \sim c_3 \sim \frac{2+\sigma}{2(3+2\sigma)}C, \quad c_2 \sim \frac{1+\sigma}{3+2\sigma}C. \tag{C.6}$$

Stability We substitute the solution (C.6) into the Jacobian matrix (4.13) and compute its trace and determinant, and find a critical value

$$C_c = \epsilon \left(\frac{1}{4(1+\sigma)} - \frac{2}{2+\sigma} + \frac{27}{4(3+\sigma)} \right),$$

where the two eigenvalues λ_1 and λ_2 of the Jacobian matrix satisfy that

- when $C < C_c$, $\lambda_1 < 0, \lambda_2 < 0$, the solution is a stable node;
- when $C > C_c$, $\lambda_1 > 0, \lambda_2 < 0$, the solution is an unstable node.

C.3 $(c_1, c_2, c_3) \sim (X, 0, 0)$

Assuming $\log c_1 \sim X$, $c_2 \sim \mathcal{O}(\epsilon)$, $c_3 \sim \mathcal{O}(\epsilon)$, the leading order equations are

$$(4+\sigma)c_1 + \epsilon \log c_2 + \epsilon \log c_3 \sim 0, \tag{C.7a}$$
$$(-2+\sigma)c_1 + \epsilon \log c_2 - 2\epsilon \log c_3 \sim 0, \tag{C.7b}$$
$$c_1 + c_2 + c_3 = C. \tag{C.7c}$$

which admit the leading order solution

$$c_1 \sim C, \quad c_2 \sim e^{-(2+\sigma)C/\epsilon}, \quad c_3 \sim e^{-2C/\epsilon}. \tag{C.8}$$

Stability To the leading order, the associated Jacobian matrix is

$$J \sim \frac{\epsilon}{3} \begin{pmatrix} -e^{(2+\sigma)C/\epsilon} & -e^{(2+\sigma)C/\epsilon} + e^{2C/\epsilon} \\ -e^{(2+\sigma)C/\epsilon} & -e^{(2+\sigma)C/\epsilon} - e^{2C/\epsilon} \end{pmatrix}, \tag{C.9}$$

therefore, $tr(J) < 0$ and $\det(J) > 0$, so this is a **stable node**.

This solution exists when C is neither close to 0 nor close to 1. When C increases to close to 1, it becomes the solution branch $(1, 0, 0)$.

C.4 $(c_1, c_2, c_3) \sim (1, 0, 0)$

For $(c_1, c_2, c_3) \sim (1, 0, 0)$, the leading order equations are

$$(4+\sigma)c_1 + 2\epsilon \log(1-c_1) + \epsilon \log c_2 + \epsilon \log c_3 \sim 0, \tag{C.10a}$$
$$(-2+\sigma)c_1 - \epsilon \log(1-c_1) + \epsilon \log c_2 - 2\epsilon \log c_3 \sim 0, \tag{C.10b}$$
$$c_1 + c_2 + c_3 = C. \tag{C.10c}$$

Subtracting (C.10b) from (C.10a) gives

$$6c_1 + 3\epsilon \log(1 - c_1) + 3\epsilon \log c_3 \sim 0, \tag{C.11}$$

or

$$c_3 \sim \frac{1}{1 - c_1} e^{-2c_1/\epsilon} \sim \frac{1}{1 - c_1} e^{-2C/\epsilon}. \tag{C.12}$$

Substituting (C.12) into (C.10c) gives

$$c_2 \sim \frac{1}{1 - c_1} e^{-(2+\sigma)C/\epsilon}. \tag{C.13}$$

By letting

$$a_1 = e^{-\frac{2C}{\epsilon}}, \quad a_2 = e^{-\frac{(2+\sigma)C}{\epsilon}}, \quad a = a_1 + a_2, \tag{C.14}$$

we find that c_1 satisfies

$$\frac{a}{1 - c_1} + c_1 \sim C. \tag{C.15}$$

Therefore, depending on the relative value of $C - 1$ versus $\sqrt{a}$, we can find three different forms for the solution:

- if $C - 1 \gg \mathcal{O}(\sqrt{a})$, the solution is

$$c_1 \sim 1 - \frac{a}{C - 1}, \quad c_2 \sim \frac{a_2}{a}(C - 1), \quad c_3 \sim \frac{a_1}{a}(C - 1); \tag{C.16a}$$

- if $C - 1 = \mathcal{O}(\sqrt{a})$, we introduce a new variable t by $C - 1 = t\sqrt{a}$, and express the solution in terms of t by

$$c_1 \sim 1 + (t - \sqrt{t^2 + 4})\sqrt{a}, \quad c_2 \sim \frac{a_2}{(\sqrt{t^2 + 4} - t)\sqrt{a}}, \quad c_3 \sim \frac{a_1}{(\sqrt{t^2 + 4} - t)\sqrt{a}}; \tag{C.16b}$$

- if $1 - C \ll \mathcal{O}(\sqrt{a})$, the solution is

$$c_1 \sim C - \frac{a}{1 - C}, \quad c_2 \sim \frac{a_2}{1 - C + a/(1 - C)}, \quad c_3 \sim \frac{a_1}{1 - C + a/(1 - C)}. \tag{C.16c}$$

Stability To the leading order, the associated Jacobian matrix is

$$J \sim \frac{\epsilon}{3} \begin{pmatrix} -\dfrac{2}{1 - c_1} - \dfrac{1}{c_2} & -\dfrac{1}{c_2} + \dfrac{1}{c_3} \\ \dfrac{1}{1 - c_1} - \dfrac{1}{c_2} & -\dfrac{1}{c_2} - \dfrac{2}{c_3} \end{pmatrix}, \tag{C.17}$$

so we always have $tr(J) < 0$ and $\det(J) > 0$, and the solution is a **stable node**.

C.5 $(c_1, c_2, c_3) \sim (0, X, 0)$

In this case, to the leading order, it must satisfy that

$$c_2 \sim C.$$

The leading order equations for c_1 and c_2 becomes

$$-(2+\sigma)c_2 - 2\epsilon \log c_1 + \epsilon \log c_3 \sim 0, \tag{C.18a}$$
$$-(2+\sigma)c_2 + \epsilon \log c_1 - 2\epsilon \log c_3 \sim 0, \tag{C.18b}$$

which admit the leading order solution

$$c_1 \sim c_3 \sim \exp\left(-\frac{2+\sigma}{\epsilon}C\right), \quad c_2 \sim C. \tag{C.19}$$

Stability To the leading order, the associated Jacobian matrix is

$$J \sim \frac{\epsilon}{3}\begin{pmatrix} -\dfrac{2}{c_1} & \dfrac{1}{c_3} \\ \dfrac{1}{c_1} & -\dfrac{2}{c_3} \end{pmatrix}, \tag{C.20}$$

which suggests that the solution (C.19) is a **stable node**.

The solution (C.19) exists when C is neither close to 0 nor 1. When C increases to close to 1, it becomes the solution branch $[0, 1, 0]$.

C.6 $(c_1, c_2, c_3) \sim (0, 1, 0)$

For $(c_1, c_2, c_3) \sim (0, 1, 0)$, the leading order equations are

$$-(2+\sigma)c_2 - 2\epsilon \log c_1 - \epsilon \log(1-c_2) + \epsilon \log c_3 \sim 0, \tag{C.21a}$$
$$-(2+\sigma)c_2 + \epsilon \log c_1 - \epsilon \log(1-c_2) - 2\epsilon \log c_3 \sim 0. \tag{C.21b}$$
$$c_1 + c_2 + c_3 = C. \tag{C.21c}$$

Subtracting (C.21b) from (C.21a) gives

$$c_1 \sim c_3. \tag{C.22}$$

Substituting it into (C.21a) gives that

$$c_1 \sim \frac{e^{-(2+\sigma)/\epsilon}}{1-c_2}. \tag{C.23}$$

By letting

$$a = e^{-(2+\sigma)/\epsilon}, \tag{C.24}$$

we find that c_2 satisfies

$$c_2^2 - (C+1)c_2 + C - 2a \sim 0. \tag{C.25}$$

Therefore, depending on the relative value of $C-1$ versus $\sqrt{a}$, we can find three different forms for the solution:

- if $C - 1 \gg \mathcal{O}(\sqrt{a})$,

$$c_1 \sim c_3 \sim \frac{C-1}{2}, \quad c_2 \sim 1 - \frac{2a}{C-1}; \tag{C.26a}$$

- if $C - 1 = \mathcal{O}(\sqrt{a})$, we introduce a new variable t by $C - 1 = t\sqrt{a}$, and find the solution to be

$$c_1 \sim c_3 \sim \frac{\sqrt{a}}{\sqrt{t^2+8} - t}, \quad c_2 \sim 1 + (t - \sqrt{t^2+8})\sqrt{a}; \tag{C.26b}$$

- if $1 - C \ll \mathcal{O}(\sqrt{a})$,

$$c_1 \sim c_3 \sim \frac{a}{1 - C - (2a)/(1-C)}, \quad c_2 \sim C - \frac{2a}{1-C}. \tag{C.26c}$$

Stability To the leading order, the associated Jacobian matrix is

$$J \sim \frac{\epsilon}{3} \begin{pmatrix} -\dfrac{2}{c_1} - \dfrac{1}{1-c_2} & -\dfrac{1}{1-c_2} + \dfrac{1}{c_3} \\ \dfrac{1}{c_1} - \dfrac{1}{1-c_2} & -\dfrac{1}{1-c_2} - \dfrac{2}{c_3} \end{pmatrix}. \tag{C.27}$$

It is straightforward to verify that $\mathrm{tr}(J) < 0$ and $\det(J) > 0$, so that the solution is a **stable node**.

C.7 $(c_1, c_2, c_3) \sim (X, X, 0)$

In this case, the leading order equations are

$$(4+\sigma)c_1 - (2+\sigma)c_2 + \epsilon \log c_3 \sim 0, \tag{C.28a}$$

$$(-2+\sigma)c_1 - (2+\sigma)c_2 - 2\epsilon \log c_3 \sim 0, \tag{C.28b}$$

$$c_1 + c_2 + c_3 = C, \tag{C.28c}$$

which admit the leading order solution

$$c_1 \sim c_2 \sim \frac{C}{2}, \quad c_3 \sim e^{-C/\epsilon}. \tag{C.29}$$

Stability To the leading order, the associated Jacobian matrix is

$$J \sim \frac{1}{3}\begin{pmatrix} 2\sigma & \epsilon e^{C/\epsilon} \\ 2\sigma & -2\epsilon e^{C/\epsilon} \end{pmatrix}. \tag{C.30}$$

It is straightforward to verify that $tr(J) < 0$ and $\det(J) < 0$, so this is a **saddle**.

This solution exists in $0 < C < 2$ (but not close to 0 or 2).

C.8 $(c_1, c_2, c_3) \sim (1, X, 0)$

When $(c_1, c_2, c_3) \sim (1, X, 0)$, the leading order equations are

$$(4+\sigma) - (2+\sigma)c_2 + 2\epsilon(1 - \log c_1) + \epsilon \log c_3 \sim 0, \tag{C.31a}$$
$$(-2+\sigma) - (2+\sigma)c_2 - \epsilon(1 - \log c_1) - 2\epsilon \log c_3 \sim 0, \tag{C.31b}$$
$$c_1 + c_2 + c_3 = C, \tag{C.31c}$$

which admit the leading order solution

$$c_1 \sim 1 - e^{-\frac{2+\sigma}{\epsilon}(2-C)}, \quad c_2 \sim C - 1, \quad c_3 \sim e^{\frac{2+\sigma}{\epsilon}(2-C) - \frac{2}{\epsilon}}. \tag{C.32}$$

Stability To the leading order, the associated Jacobian matrix is

$$J \sim \frac{\epsilon}{3}\begin{pmatrix} -\dfrac{2}{1-c_1} & \dfrac{1}{c_3} \\ \dfrac{1}{1-c_1} & -\dfrac{2}{c_3} \end{pmatrix}. \tag{C.33}$$

It is straightforward to verify that this is a **stable node**.

This solution exists in $1 < C < 2$ (but not close to 1 or 2).

C.9 $(c_1, c_2, c_3) \sim (X, 1, 0)$

When $(c_1, c_2, c_3) \sim (X, 1, 0)$, the leading order equations are

$$(4+\sigma)c_1 - (2+\sigma) - \epsilon \log(1 - c_2) + \epsilon \log c_3 \sim 0, \tag{C.34a}$$
$$(-2+\sigma)c_1 - (2+\sigma) - \epsilon \log(1 - c_2) - 2\epsilon \log c_3 \sim 0, \tag{C.34b}$$
$$c_1 + c_2 + c_3 = C, \tag{C.34c}$$

which admit the leading order solution

$$c_1 \sim C - 1, \quad c_2 \sim 1 - e^{-\frac{(2+\sigma)(C-1)}{\epsilon}}, \quad c_3 \sim e^{-\frac{2(C-1)}{\epsilon}}. \tag{C.35}$$

Stability To the leading order, the associated Jacobian matrix is

$$J \sim \frac{\epsilon}{3}\begin{pmatrix} -\dfrac{1}{1-c_2} & -\dfrac{1}{1-c_2}+\dfrac{1}{c_3} \\ -\dfrac{1}{1-c_2} & -\dfrac{1}{1-c_2}-\dfrac{2}{c_3} \end{pmatrix}. \tag{C.36}$$

It is straightforward to verify that $tr(J) < 0$ and $\det(J) > 0$, so this is a **stable node**.

C.10 $(c_1, c_2, c_3) \sim (1, 1, 0)$

When $(c_1, c_2, c_3) \sim (1, 1, 0)$, the leading order solutions are

$$2 + 2\epsilon\log(1-c_1) - \epsilon\log(1-c_2) + \epsilon\log c_3 \sim 0, \tag{C.37a}$$

$$-4 - \epsilon\log(1-c_1) - \epsilon\log(1-c_2) - 2\epsilon\log c_3 \sim 0, \tag{C.37b}$$

$$c_1 + c_2 + c_3 = C. \tag{C.37c}$$

The leading order solutions are:

- when $C - 2 \gg O(e^{-1/\epsilon})$,

$$c_1 \sim c_2 \sim 1 - \frac{e^{-2/\epsilon}}{C-2}, \quad c_3 \sim C - 2; \tag{C.38}$$

- when $C - 2 \sim O(e^{-1/\epsilon})$, we introduce a new variable t by $C - 2 = te^{-1/\epsilon}$, and express the solution in terms of t by

$$c_1 \sim c_2 \sim 1 + (t - \sqrt{t^2+4})\frac{e^{-1/\epsilon}}{2}, \quad c_3 \sim \frac{2}{(\sqrt{t^2+4} - t)e^{-1/\epsilon}}; \tag{C.39}$$

- when $2 - C \ll O(e^{-1/\epsilon})$,

$$c_1 \sim c_2 \sim \frac{C}{2} - \frac{e^{-2/\epsilon}}{2-C}, \quad c_3 \sim \frac{2-C}{1+(2-C)^2e^{2/\epsilon}} \sim 2 - C. \tag{C.40}$$

Stability To the leading order, the associated Jacobian is

$$J \sim \frac{\epsilon}{3}\begin{pmatrix} -\dfrac{2}{1-c_1} - \dfrac{1}{1-c_2} & -\dfrac{1}{1-c_2}+\dfrac{1}{c_3} \\ \dfrac{1}{1-c_1} - \dfrac{1}{1-c_2} & -\dfrac{1}{1-c_2}-\dfrac{2}{c_3} \end{pmatrix}, \tag{C.41}$$

and it is straightforward to verify that $tr(J) < 0$ and $\det(J) > 0$, so this is a **stable node**.

C.11 $(c_1, c_2, c_3) \sim (X, 0, X)$

When $(c_1, c_2, c_3) \sim (X, 1, 0)$, the leading order equations are

$$(4+\sigma)c_1 - (2-\sigma)c_3 + \epsilon \log c_2 \sim 0, \tag{C.42a}$$

$$(-2+\sigma)c_1 + (4+\sigma)c_3 + \epsilon \log c_2 \sim 0, \tag{C.42b}$$

$$c_1 + c_2 + c_3 = C, \tag{C.42c}$$

which admit the leading order solution

$$c_1 \sim c_3 \sim \frac{C}{2}, \quad c_2 \sim e^{-\frac{(1+\sigma)C}{\epsilon}}. \tag{C.43}$$

Stability To the leading order, the associated Jacobian matrix is

$$J \sim \begin{pmatrix} \left(2+\frac{2}{3}\sigma\right) - \frac{1}{3}\frac{\epsilon}{c_2} & \frac{2}{3}\sigma - \frac{1}{3}\frac{\epsilon}{c_2} \\ \frac{2}{3}\sigma - \frac{1}{3}\frac{\epsilon}{c_2} & \left(2+\frac{2}{3}\sigma\right) - \frac{1}{3}\frac{\epsilon}{c_2} \end{pmatrix}. \tag{C.44}$$

It is straightforward to verify that $tr(J) < 0$ and $\det(J) < 0$, so this is a **saddle**.

This solution exists when $0 < C < 2$ (but not close to 0 or 2). When C approaches 2, it goes through another bifurcation process and merges with the solution branch $[1, 0, 1]$.

C.12 $(c_1, c_2, c_3) \sim (1, 0, X)$

When $(c_1, c_2, c_3) \sim (1, 0, X)$, the leading order equations are

$$(4+\sigma) - (2-\sigma)c_3 + 2\epsilon \log(1-c_1) + \epsilon \log c_2 \sim 0, \tag{C.45a}$$

$$(-2+\sigma) + (4+\sigma)c_3 - \epsilon \log(1-c_1) + \epsilon \log c_2 \sim 0, \tag{C.45b}$$

$$c_1 + c_2 + c_3 = C, \tag{C.45c}$$

which admit the leading order solution

$$c_1 \sim 1 - e^{-\frac{4-2C}{\epsilon}}, \quad c_2 \sim e^{-\frac{(2+\sigma)(C-1)-\sigma}{\epsilon}}, \quad c_3 \sim C - 1. \tag{C.46}$$

Stability To the leading order, the associated Jacobian matrix is

$$J \sim \frac{\epsilon}{3} \begin{pmatrix} -\frac{2}{1-c_1} - \frac{1}{c_2} & -\frac{1}{c_2} \\ \frac{1}{1-c_1} - \frac{1}{c_2} & -\frac{1}{c_2} \end{pmatrix}. \tag{C.47}$$

It is straightforward to verify that $tr(J) < 0$ and $\det(J) = \epsilon^2/[3c_2(1-c_1)] > 0$, so this is a **stable node**.

C.13 $(c_1, c_2, c_3) \sim (X, X, X)$

This is presented as an example in Section 4.3.1.

C.14 $(c_1, c_2, c_3) \sim (1, X, X)$

When $(c_1, c_2, c_3) \sim (1, X, X)$, the leading order equations are

$$(4+\sigma) - (2+\sigma)c_2 + (-2+\sigma)c_3 + 2\epsilon\log(1-c_1) \sim 0, \tag{C.48a}$$

$$(-2+\sigma) - (2+\sigma)c_2 + (4+\sigma)c_3 - \epsilon\log(1-c_1) \sim 0, \tag{C.48b}$$

$$c_1 + c_2 + c_3 = C, \tag{C.48c}$$

which admit the leading order solution

$$c_1 \sim 1 - e^{-\frac{3-C}{\epsilon}}, \quad c_2 \sim \frac{C-1}{2} + \frac{\sigma}{2(2+\sigma)}, \quad c_3 \sim \frac{C-1}{2} - \frac{\sigma}{2(2+\sigma)}. \tag{C.49}$$

Stability To the leading order, the associated Jacobian matrix is

$$J \sim \begin{pmatrix} -\frac{\epsilon}{3}\frac{1}{1-c_1} & \frac{2}{3}\sigma \\ \frac{\epsilon}{3}\frac{1}{1-c_1} & 2+\frac{2}{3}\sigma \end{pmatrix}. \tag{C.50}$$

It is straightforward to verify that $\mathrm{t}r(J) < 0$ and $\det(J) < 0$, so this is a **saddle**.

Additionally, the constraint of $0 < c_1, c_2, c_3 < 1$ requires that

$$1 + \frac{\sigma}{2+\sigma} < C < 3 - \frac{\sigma}{2+\sigma}. \tag{C.51}$$

When C approaches $3 - \frac{\sigma}{2+\sigma}$, the solution (C.49) approaches

$$c_1 \to 1 - e^{-\frac{\sigma}{\epsilon(2+\sigma)}}, \quad c_2 \to 1, \quad c_3 \to 1 - \frac{\sigma}{2+\sigma}, \tag{C.52}$$

i.e. the assumption that $c_2 \sim X$ breaks down.

C.15 $(c_1, c_2, c_3) \sim (X, 1, X)$

When $(c_1, c_2, c_3) \sim (X, 1, X)$, the leading order equations are

$$(4+\sigma)c_1 - (2+\sigma) + (-2-\sigma)c_3 - \epsilon\log(1-c_2) \sim 0, \tag{C.53a}$$

$$(-2+\sigma)c_1 - (2+\sigma) + (4+\sigma)c_3 - \epsilon\log(1-c_2) \sim 0, \tag{C.53b}$$

$$c_1 + c_2 + c_3 = C, \tag{C.53c}$$

which admit the leading order solution

$$c_1 \sim c_3 \sim \frac{C-1}{2}, \quad c_2 \sim 1 - e^{\frac{(1+\sigma)(C-1)-2-\sigma}{\epsilon}}. \tag{C.54}$$

Stability To the leading order, the associated Jacobian matrix is

$$J \sim \begin{pmatrix} \left(2+\frac{2}{3}\sigma\right) - \frac{\epsilon}{3}\frac{1}{1-c_2} & \frac{2}{3}\sigma - \frac{\epsilon}{3}\frac{1}{1-c_2} \\ \frac{2}{3}\sigma - \frac{\epsilon}{3}\frac{1}{1-c_2} & \left(2+\frac{2}{3}\sigma\right) - \frac{\epsilon}{3}\frac{1}{1-c_2} \end{pmatrix}. \tag{C.55}$$

It is straightforward to verify that $tr(J) < 0$ and $\det(J) < 0$, so this is a **saddle**.

C.16 $(c_1, c_2, c_3) \sim (1, 1, X)$

When $(c_1, c_2, c_3) \sim (1, 1, X)$, the leading order equations are

$$(4+\sigma) - (2+\sigma) + (-2-\sigma)c_3 + 2\epsilon\log(1-c_1) - \epsilon\log(1-c_2) \sim 0, \tag{C.56a}$$
$$(-2+\sigma) - (2+\sigma) + (4+\sigma)c_3 - \epsilon\log(1-c_1) - \epsilon\log(1-c_2) \sim 0, \tag{C.56b}$$
$$c_1 + c_2 + c_3 = C, \tag{C.56c}$$

which admit the leading order solution

$$c_1 \sim c_2 \sim 1 - e^{-\frac{2(3-C)}{\epsilon}}, \quad c_3 \sim C - 2, \tag{C.57}$$

Stability To the leading order, the associated Jacobian matrix is

$$J \sim \frac{\epsilon}{3}\begin{pmatrix} -\frac{1}{1-c_1} - \frac{1}{1-c_2} & -\frac{1}{1-c_2} \\ \frac{1}{1-c_1} - \frac{1}{1-c_2} & -\frac{1}{1-c_2} \end{pmatrix}. \tag{C.58}$$

It is straightforward to verify that $tr(J) < 0$ and $\det(J) = 2\epsilon^2/[9(1-c_2)(1-c_1)] > 0$, so this is a **stable node**.

C.17 $(c_1, c_2, c_3) \sim (1, X, 1)$

When $(c_1, c_2, c_3) \sim (1, X, 1)$, the leading order equations are

$$(4+\sigma) - (2+\sigma)c_2 + (-2-\sigma) + 2\epsilon\log(1-c_1) - \epsilon\log(1-c_3) \sim 0, \tag{C.59a}$$
$$(-2+\sigma) - (2+\sigma)c_2 + (4+\sigma) - \epsilon\log(1-c_1) + 2\epsilon\log(1-c_3) \sim 0, \tag{C.59b}$$
$$c_1 + c_2 + c_3 = C, \tag{C.59c}$$

which admit the leading order solution

$$c_1 \sim c_3 \sim 1 - e^{-\frac{2(3-C-2\sigma)}{\epsilon}}, \quad c_2 \sim C - 2. \tag{C.60}$$

Stability To the leading order, the associated Jacobian matrix is

$$J \sim \frac{\epsilon}{3}\begin{pmatrix} -\dfrac{2}{1-c_1} & \dfrac{1}{1-c_3} \\ \dfrac{1}{1-c_1} & \dfrac{2}{1-c_3} \end{pmatrix}. \tag{C.61}$$

It is straightforward to verify that $tr(J) < 0$ and $\det(J) > 0$, so this is a **stable node**.

When $C \uparrow 3$, the assumption that $c_2 \sim X$ breaks down. In Section 4.3.6, we show that when $C \uparrow 3$, $(1, X, 1)$ becomes with $(1, 1, 1)$.

C.18 $(c_1, c_2, c_3) \sim (1, 1, 1)$

When $(c_1, c_2, c_3) \sim (1, 1, 1)$, C is close to 3. We make the transform $y_1 = 1 - c_1,\ y_2 = 1 - c_2,\ y_3 = 1 - c_3$, and $\tau = 3 - C$ (so τ is close to 0), to get the leading order equations

$$-\sigma + (4+\sigma)y_1 - (2+\sigma)y_2 + (-2+\sigma)y_3 - 2\epsilon \log y_1 + \epsilon \log y_2 + \epsilon \log y_3 \sim 0, \tag{C.62a}$$

$$-\sigma + (-2+\sigma)y_1 - (2+\sigma)y_2 + (4+\sigma)y_3 + \epsilon \log y_1 + \epsilon \log y_2 - 2\epsilon \log y_3 \sim 0. \tag{C.62b}$$

$$y_1 + y_2 + y_3 = \tau, \tag{C.62c}$$

which admit the leading order solution

$$y_1 \sim \frac{1}{2 + e^{\sigma/\epsilon}}\tau, \quad y_2 \sim \frac{e^{\sigma/\epsilon}}{2 + e^{\sigma/\epsilon}}\tau, \quad y_3 \sim \frac{1}{2 + e^{\sigma/\epsilon}}\tau, \tag{C.63}$$

i.e.

$$c_1 \sim 1 - \frac{1}{2 + e^{\sigma/\epsilon}}(3 - C) \quad c_2 \sim 1 - \frac{e^{\sigma/\epsilon}}{2 + e^{\sigma/\epsilon}}(3 - C), \quad c_3 \sim 1 - \frac{1}{2 + e^{\sigma/\epsilon}}(3 - C). \tag{C.64}$$

To the leading order, the associated Jacobian matrix is

$$J = \frac{\epsilon}{3}\begin{pmatrix} -\dfrac{2}{y_1} - \dfrac{1}{y_2} & -\dfrac{1}{y_2} + \dfrac{1}{y_3} \\ -\dfrac{1}{y_1} - \dfrac{1}{y_2} & -\dfrac{1}{y_2} - \dfrac{2}{y_3} \end{pmatrix}, \tag{C.65}$$

which satisfies that $tr(J) < 0$ and $\det(J) > 0$, so this is a **stable node**.

In Section. 4.3.6 we show that when C grows to 3, the stable node N $(1, X, 1)$ becomes the stable node M $(1, 1, 1)$.

Appendix D

Numeric difficulties in solving the two-compartment Butler–Volmer model

Here we illustrate the numeric difficulties in solving the two-compartment Butler–Volmer equation.

First, we solve equation (5.28) for the two-compartment system,

$$\kappa \frac{\mathrm{d}X_1}{\mathrm{d}T} = \sinh\left(\frac{T + 2X_1 - \log X_1 - \sigma X_2}{2}\right), \tag{D.1a}$$

$$\kappa \frac{\mathrm{d}X_2}{\mathrm{d}T} = \sinh\left(\frac{T + 2X_2 - \log X_2 - \sigma X_1}{2}\right), \tag{D.1b}$$

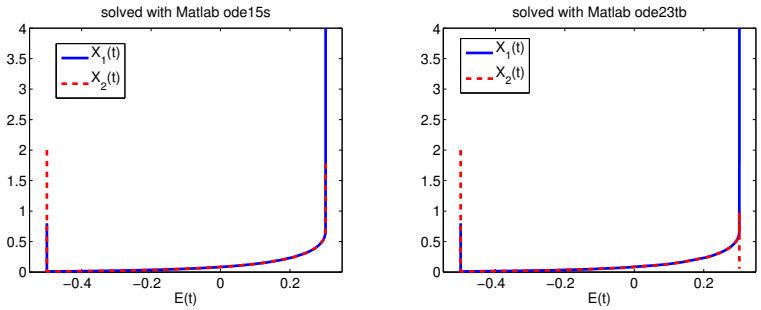
using two Matlab solvers for stiff problems, **ode15s** and **ode23tb**, and compare the results in Fig. D.1. In the case of $\kappa = 10^{-3}$, as shown in panel (a), **ode15s** predicts both X_1 and X_2 to blow up at the same rate, but **ode23tb** predicts X_1 to blow up, meanwhile X_2 to decrease to near zero. In the case of $\kappa = 10^{-5}$, as shown in panel (b), **ode15s** predicts X_1 to blow up and X_2 to decrease; however, **ode23tb** shows exactly the opposite.

We then solve the system (5.30) numerically, which approximates (5.28) in the limit of $\Delta X \ll X$, using

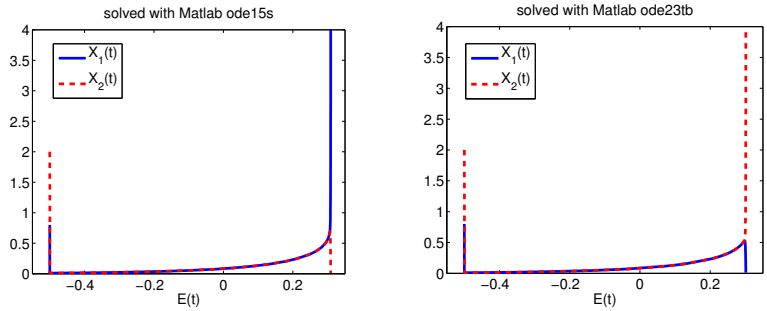
$$\kappa \frac{\mathrm{d}X_1}{\mathrm{d}T} \sim \sinh\left(\frac{T + (2-\sigma)X_1 - \log X_1}{2}\right), \tag{D.2a}$$

$$\kappa \frac{\mathrm{d}\Delta X}{\mathrm{d}T} \approx \frac{1}{2}\left(2 + \sigma - \frac{1}{X_1}\right) \cosh\left(\frac{T + (2-\sigma)X_1 - \log X_1}{2}\right) \Delta X. \tag{D.2b}$$

Again we compare the results found by the two Matlab solvers, **ode15s** and **ode23tb**, and plot the comparison in Fig. D.2. Evidently, the numerical rounding errors might determine the solution. First, ΔX computed by the two solvers differ by many orders



(a) $\kappa = 10^{-3}$



(b) $\kappa = 10^{-5}$

Figure D.1: Solving the system (D.1) with two different Matlab solvers, **ode15s** and **ode23tb**. All simulations use the same initial condition of $T_0 = -0.5/\kappa$, $E(T_0) = -0.5$, $X_1(T_0) = 0.8$, $X_2(T_0) = 2$, and $\sigma = 0.5$.

of magnitude, with **ode23tb** predicting it to be as small as 10^{-25}, much smaller than the machine epsilon 2.22×10^{-16}. Second, according to (D.2b), ΔX should not change sign, but this is not satisfied in the numerics. The broken line in plotting ΔX using the logarithmic scale suggests that ΔX is negative in some regions.

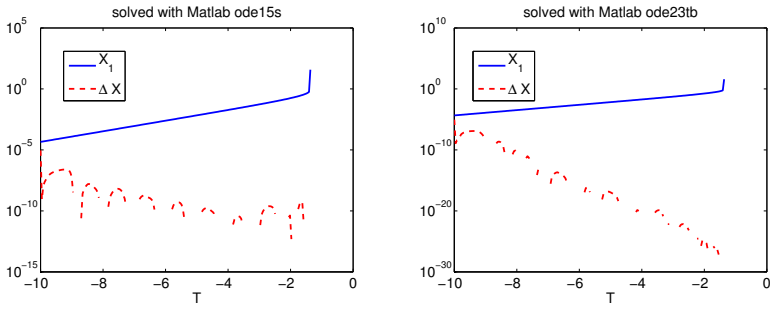


Figure D.2: Solving the system (D.2) with two different Matlab solvers, **ode15s** and **ode23tb**. Both simulations use the same initial condition of $T_0 = -10$, $X_1(T_0) = 4.5 \times 10^{-5}$, $\Delta X(T_0) = 9 \times 10^{-6}$, $\kappa = 10^{-3}$, and $\sigma = 0.5$.

Appendix E

Approximations of discrete sums

How we show show to transform the discrete sum term $\sum_{j=1,j\neq i}^{M} d\left(|i-j|\right) c_j$, where

$$d(|i-j|) = \begin{cases} \frac{1}{|i-j|^{\omega}} & \text{if } |i-j| \leq \frac{M}{2}, \\ \frac{1}{(M-|i-j|)^{\omega}} & \text{if } |i-j| > \frac{M}{2}. \end{cases} \tag{E.1}$$

In panel (c) of Figs. 7.5 to 7.7, the concentration of inner compartments ($c(i)$) away from any spikes appears to vary relatively smoothly with i. We utilise this property and assume that the concentration is approximately continuous. We also use the periodic property and assume w.l.o.g that $i > M/2$, thereby decomposing the sum into two parts

$$\sum_{j=1,j\neq i}^{M} d(|i-j|)c_j = \sum_{j=i-M/2}^{i-1} d(|i-j|)c_j + \sum_{\substack{j>i \text{ or} \\ j<i-M/2}} d(|i-j|)c_j, \tag{E.2}$$

and treat each part separately. For a number m satisfying $1 \ll m \ll M$ and denoting $\nu = \frac{m}{M} \ll 1$, the first part in the sum can be further decomposed as

$$\sum_{j=i-M/2}^{i-1} d(|i-j|)c_j = \sum_{j=i-M/2}^{i-1} \frac{c_j}{(j-i)^2} = \sum_{j=i-M/2}^{i-m} \frac{c_j}{(j-i)^2} + \sum_{j=i-m+1}^{i-1} \frac{c_j}{(j-i)^2}. \tag{E.3}$$

To transform the discrete equation to its continuous version, we first make the transformation $x_i = \frac{i}{M}$, $c(x_i) = c_i$. Then we express the first term in (E.3) by an integral term and a remainder term R with the Euler-Maclaurin formula:

$$M \sum_{j=i-M/2}^{i-m} \frac{c_j}{(j-i)^2} = \int_{x_i-1/2}^{x_i-\nu} \frac{c(x)}{(x-x_i)^2} dx + R, \tag{E.4a}$$

$$R = \frac{1}{2}(f(i-M/2) + f(i-m)) + \int_{i-M/2}^{i-m} P_1(t) f'(t) dt,$$

where $f(t) = \frac{c(t)}{(t-i)^2}$ and $|P_1(t)| = |\{t\} - \frac{1}{2}| \leq \frac{1}{2}$. It follows that

$$\int_{i-M/2}^{i-m} P_1(t) f'(t) dt \leq \frac{1}{2} \int_{i-M/2}^{i-m} f'(t) dt = \frac{1}{2}(f(i-m) - f(i-M/2)), \tag{E.5}$$

and hence the remainder

$$R = \mathcal{O}\left(\frac{1}{(i-m)^2}\right). \tag{E.6}$$

The second term in (E.3) is approximated as

$$M \sum_{j=i-m+1}^{i-1} \frac{c_j}{(j-i)^2} = \sum_{j=i-m+1}^{i-1} \frac{c(x_i) - \frac{i-j}{M} c'(x_i) + \frac{1}{2}\left(\frac{i-j}{M}\right)^2 c''(x_{\xi i})}{(j-i)^2} + \cdots. \tag{E.7}$$

Combining (E.3)-(E.7) we have

$$\begin{aligned} M \sum_{j=i-M/2}^{i-1} \frac{c_j}{(j-i)^2} &= \int_{x_i-1/2}^{x_i} \frac{c(x) - c(x_i) - (x-x_i)c'(x_i)}{(x-x_i)^2} dx + c(x_i)\left[\frac{1}{\nu} - \frac{1}{x_i} + \sum_{k=1}^{m-1} \frac{1}{k^2}\right] \\ &\quad + c'(x_i)\left[-\log x_i + \log \nu - \sum_{k=1}^{m-1} \frac{1}{k}\right] + \mathcal{O}\left(\frac{1}{(i-m)^2}\right) + \mathcal{O}\left(\frac{1}{M}\right) \\ &= \int_{x_i-1/2}^{x_i} \frac{c(x) - c(x_i) - (x-x_i)c'(x_i)}{(x-x_i)^2} dx + c(x_i)\left[\frac{M}{6}\pi^2 - \frac{1}{x_i}\right] \\ &\quad + c'(x_i)\left[-\log x_i - \log M - \gamma\right] + \mathcal{O}\left(\frac{1}{(i-m)^2}\right) + \mathcal{O}\left(\frac{1}{M}\right). \end{aligned} \tag{E.8}$$

Keeping only leading order terms, we have

$$\sum_{j=i-M/2}^{i-1} d(|i-j|) c_j \sim \frac{1}{6}\pi^2 c(x_i). \tag{E.9}$$

Using the periodic condition, we can treat the second part of (E.2) similarly and get

$$\sum_{\substack{j>i \text{ or} \\ j<i-M/2}} d(|i-j|) c_j \sim \frac{1}{6}\pi^2 c(x_i). \tag{E.10}$$

Therefore, we obtain that

$$\sum_{j=1, j\neq i}^{M} d(|i-j|) c_j \sim \frac{1}{3}\pi^2 c(x_i). \tag{E.11}$$

References

[1] M. Abramowitz and I. A. Stegun. *Handbook of Mathematical Functions with Formulas, Graphs, and Mathematical Tables.* New York: Dover Publications, 1972.

[2] A. S. Aricó, P. Bruce, B. Scrosati, J. M. Tarascon, and W. Schalkwijk. Nanostructured materials for advanced energy conversion and storage devices. *Nature Mater.*, 4:366–377, 2005.

[3] S. M. Baer, T. Erneux, and J. Rinzel. The slow passage through a hopf bifurcation: delay, memory effects, and resonance. *SIAM J. Appl. Math.*, 49:55–71, 1989.

[4] P. Bai, D. A. Cogswell, and M. Z. Bazant. Suppression of phase transformations in $LiFePO_4$ nanoparticles during battery discharge. *Nano Lett.*, 11:4890–4896, 2011.

[5] M. Bazant. Course materials for 10.626 electrochemical energy systems, spring 2011. MIT OpenCourseWare (http://ocw.mit.edu), Massachusetts Institute of Technology. Downloaded on 06 June 2012.

[6] M. Bazant. *Lithium Ion Rechargeable Batteries.* Weinheim : Wiley-VCH, 2009.

[7] J. O'M. Bockris, A. K. N. Reddy, and M. Gamboa-Aldeco. *Modern Electrochemistry 2A. Fundamentals of Electrodics.* Kluwer Academic/Plenum Publishers, 2000.

[8] P. G. Bruce, B. Scrosati, and J. M. Tarascon. Nanomaterials for rechargeable lithium batteries. *Angew. Chem. Int. Ed.*, 47:2930–2946, 2008.

[9] L. H. Cameron, J. S. Chapman, and J. R. Ockendon. Asymptotic analysis of a system of algebraic equations arising in dislocation theory. *SIAM J. Appl. Math.*, 70:2729–2749, 2010.

[10] R. Clarke, N. Wada, and S. A. Solin. Pressure-induced staging transition in KC_{24}. *Phys. Rev. Lett.*, 44:1616, 1980.

[11] C. Delmas, M. Maccario, L. Croguennec, F. Le Cras, and F. Weill. Lithium deintercalation in $LiFePO_4$ nanoparticles via a domino-cascade model. *Nat. Mater.*, 7:665–671, 2008.

[12] W. Dreyer, C. Guhlke, and M. Herrmann. Hysteresis and phase transition in many-particle storage systems. *Continuum Mech. Thermodyn.*, 23:211–231, 2011.

[13] W. Dreyer, C. Guhlke, and R. Huth. The behavior of a many-particle electrode in a lithium-ion battery. *Physica D*, 240:1008–1019, 2011.

[14] W. Dreyer, J. Jamnik, C. Guhlke, R. Huth, J. Mokon, and M. Gaberek. The thermodynamic origin of hysteresis in insertion batteries. *Nature Mater.*, 9:448–453, 2010.

[15] H. Fei, Z. Peng, Y. Yang, L. Li, A-R. Raji, E. Samuel, and J. Tour. $LiFePO_4$ nanoparticles encapsulated in graphene nanoshells for high-performance lithium-ion battery cathodes. *Chem. Commun.*, 7117:50, 2014.

[16] T. R. Ferguson and M. Z. Bazant. Phase transformation dynamics in porous battery electrodes. *Electrochim. Acta*, 146:89–97, 2014.

[17] T. F. Fuller, M. Doyle, and J. Newman. Simulation and optimization of the dual lithium ion insertion cell. *J. Electrochem. Soc.*, 141:1–10, 1993.

[18] H. Huang, S.-C. Yin, and L. F. Nazar. Approaching theoretical capacity of $LiFePO_4$ at room temperature at high rates. *Electrochem. Solid-State Lett.*, 4:A170–A172, 2001.

[19] E. M. Izhikevich. Equilibrium. *Scholarpedia*, 2:2014, 2007.

[20] N.G. Van Kampen. *Stochastic Processes in Physics and Chemistry, Third Edition.* North-Holland Personal Library, 2007.

[21] S. Krishnan, G. Brenet, E. M. Charry, D. Caliste, L. Genovese, T. Deutsch, and P. Pochet. Revisiting the domain model for lithium intercalated graphite. *Appl. Phys. Lett.*, 103:251904, 2013.

[22] L. Laffont, C. Delacourt, P. Gibot, M. Y. Wu, P. Kooyman, C. Masquelier, and J. M. Tarascon. Study of the $LiFePO_4/FePO_4$ two-phase system by high-resolution electron energy loss spectroscopy. *Chem. Mater.*, 18:5520–5529, 2006.

[23] M. Landstorfer and T. Jacob. Mathematical modeling of intercalation batteries at the cell level and beyond. *Chem. Soc. Rev.*, 42:3234, 2013.

[24] Y. Li, F. E. Gabaly, T. R. Ferguson, R. B. Smith, N. C. Bartelt, J. D. Sugar, K. R. Fenton, D. A. Cogswell, A. L. D. Kilcoyne, T. Tyliszczak, M. Z. Bazant, and W. C. Chueh. Current-induced transition from particle-by-particle to concurrent intercalation in phase-separating battery electrodes. *Nature Mater.*, 13:1149–1156, 2014.

[25] R. Mukherjeea, R. Krishnanb, T-M. Lu, and N. Koratkar. Nanostructured electrodes for high-power lithium ion batteries. *Nano Energy*, 1:518–533, 2012.

[26] T. Ohzuku, , Y. Iwakoshi, and K. Sawai. Formation of lithium-graphite intercalation compounds in nonaqueous electrolytes and their application as a negative electrode for a lithium ion (shuttlecock) cell. *J. Electrochem. Soc.*, 140:2490, 1993.

[27] B. Orvananos, T. R. Ferguson, H-C. Yu, M. Z. Bazant, and K. Thornton. Particle-level modeling of the charge-discharge behavior of nanoparticulate phase-separating Li-ion battery electrodes. *J. Electrochem. Soc.*, 161:A535–A546, 2014.

[28] A. K. Padhi, K. S. Nanjundaswamy, and J. B. Goodenough. Phospho-olivines as positive-electrode materials for rechargeable lithium batteries. *J. Electrochem. Soc.*, 144:1188–1194, 1997.

[29] Y. Qi, H. Guo, L. G. Hector, and A. Timmons. Threefold increase in the Youngs modulus of graphite negative electrode during lithium intercalation. *J. Electrochem. Soc.*, 157:A558, 2010.

[30] L. E. Reichl. *A Modern Course in Statistical Physics.* Weinheim : Wiley, 2009.

[31] Y. Reynier, R. Yazami, and B. Fultz. Thermodynamics of lithium intercalation into graphites and disordered carbons. *J. Electrochem. Soc.*, 151:422–426, 2004.

[32] S. S. Dargaville and T. W. Farrell. Predicting active material utilization in $LiFePO_4$ electrodes using a multiscale mathematical model. *J. Electrochem. Soc.*, 157:A830–A840, 2010.

[33] V. Srinivasan and J. Newman. Discharge model for the lithium iron-phosphate electrode. *J. Electrochem. Soc.*, 151:A1517–A1529, 2004.

[34] J. M. Tarascon and M. Armand. Issues and challenges facing rechargeable lithium batteries. *Nature*, 414:359–367, 2001.

[35] M. Wagemaker, J. H. Borghols, and F. M. Mulder. Large impact of particle size on insertion reactions. A case for anatase Li_xTiO_2. *J. Am. Chem. Soc.*, 129:4323–4327, 2007.

[36] M. Wechselberger. Canards. *Scholarpedia*, 2(4):1356, 2007.